

ISSN 1913-1844

MODERN APPLIED SCIENCE

**Vol. 3, No. 2
February 2009**



Canadian Center of Science and Education



Contents

Degradation of Antibiotics (Trimethoprim and Sulphamethoxazole) Pollutants Using UV and TiO ₂ in Aqueous Medium <i>Jatindra Nath Bhakta & Yukihiro Munekage</i>	3
Study on the Construction of the Internet Ecological Concept <i>Yongqing Bai</i>	14
Isolation, Stabilization and Characterization of Xanthophyll from Marigold Flower- <i>Tagetes Erecta-L</i> <i>V.B. Pratheesh, Nify Benny & C.H Sujatha</i>	19
Storm Surge Intensity Grade Classification <i>Liping Wang, Qingqing Liu, Runyu Han & Jiangen Wang</i>	29
The Investigation of Active Sites on Nickel Oxide Based Catalysts towards the <i>In-situ</i> Reactions of Methanation and Desulfurization <i>Wan Azelee Wan Abu Bakar, Mohd. Yusuf Othman, Rusmidah Ali, Ching Kuan Yong & Susilawati Toemen</i>	35
Existence of Nonoscillatory Solutions for a Class of N-order Neutral Differential Systems <i>Zhibin Chen & Aiping Zhang</i>	44
Gas Hold up in Multiple Impeller Agitated Vessels <i>Dr. Kaliannan Saravanan, Dr. Veerappan Ramamurthy & Kothandaraman Chandramohan</i>	49
Motion Control of Underwater Supercavitating Projectiles in Vertical Plane <i>Daijin Li, Yuwen Zhang, Kai Luo & Jianjun Dang</i>	60
Aging Effect to Accumulation of Lettucenin A in Lettuce after Elicitation with Various Abiotic Elicitors <i>Wen Dee Ong & Khim Phin Chong</i>	66
Effect of Polypropylene Fiber on Shrinkage Properties of Cement-stabilized Macadam <i>Zhifeng Chen</i>	71
Genetic Algorithm for Document Clustering with Simultaneous and Ranked Mutation <i>K. Premalatha & A.M. Natarajan</i>	75
Study on Cellulose-decomposed Actinomycetes in Soil in the Eastern of the Qinghai Plateau <i>Yan Cai, Quanhong Xue, Zhanquan Chen & Rong Zhang</i>	83
Illumination Compensation in Pig Skin Texture Using Local-Global Block Analysis <i>M Iqbal Sariipan, Mohd Hafrizal Azmi, Raja Syamsul Azmir Raja Abdullah & Laili Hayati Anuar</i>	89
On the PFQ-based Training Mode for the Special Force <i>Jianxin Yang, Min Yu & Fuyong Liu</i>	94
Advanced Approach in Sensitive Rule Hiding <i>Dr. K. Duraiswamy, Dr. D. Manjula & N. Maheswari</i>	98
Boundedness of Commutators on Generalized Morrey Spaces <i>Yuze Cai & Hao Zhang</i>	104
Investigation on Dielectric Constant of Zinc Oxide <i>Khalid Omar, M. D. Johan Ooi & M. M. Hassin</i>	110
Aerodynamics Simulation of Hypersonic Waverider Vehicle <i>Dingyi Wu & Hong Xiao</i>	117



Contents

The Effect of Incising Process on Copper-Chromium-Arsenic Retention in <i>Scodocarpus Borneensis</i> and <i>Kokoona</i> Spp <i>Shaharuddin Hamid, Hashim W.Samsi, Razak Wahab & Zaihan Jalaludin</i>	123
Textile Flame Retardant Review <i>Hongkun Zhang & Guoliang Sun</i>	129
A Novel Method of Image Compression Using Multiwavelets and Set Partitioning Algorithm <i>U.S.Ragupathy & A.Tamilarasi</i>	134
Polymorphism of Lactoferrin Gene with PCR - RFLP and its Association with Subclinical Mastitis in Dairy Cows <i>Changhong Zhao, Gaoming He, Yanliang Wang & Zhaoxia Zhang</i>	144
Studies on the Performance of Quarry Waste in Flowable Fly Ash-Gypsum Slurry <i>Revathi .V., Dr. Narasimha. V. L. & Dr. Jayanthi. S.</i>	147
Nanotechnology in Textiles Finishment <i>Dongxue Liu & Weiguo Dong</i>	154
Equilibrium Adsorption Isotherms of Anionic, Nonionic Surfactants and Their Mixtures to Shale and Sandstone <i>Mazen Ahmed Muherei & Radzuan Junin</i>	158
Effect of Truncation on the Performance of Busemann Inlet <i>Zhi Zhao & Wenyan Song</i>	168
The Structure and Optical Performance of InGaN/GaN Multiple Quantum Wells Grown on C-plane Sapphire <i>Xiaolei Peng, Pingjuan Niu, Xiaoyun Li, Ke Ding & Caifeng Wang</i>	172
Effect of Corner Radius and Friction Parameters on the Optimization of the Cold Forging Die Design <i>A. R. Ab-Kadir, A. R. Othman, Z. Samad, Khaleed Hussain. M. T. & A. B. Abdullah</i>	177
Analysis of the Flow Pipe Arrangement in RTM Process <i>Jinliang Liu & Xiaoqing Wu</i>	190



Degradation of Antibiotics (Trimethoprim and Sulphamethoxazole) Pollutants Using UV and TiO₂ in Aqueous Medium

Jatindra Nath Bhakta (Corresponding Author)

Department of Environmental Engineering

Faculty of Agriculture, Kochi University

B200, Monobe, Nankoku, Kochi - 783-8502, Japan

Tel: 81-88-864-5175 E-mail: lsjnbhakta@gmail.com

Yukihiro Munekage

Department of Environmental Engineering

Faculty of Agriculture, Kochi University

B200, Monobe, Nankoku, Kochi - 783-8502, Japan

Tel: 81-88-864-5175 E-mail: munekage@kochi-u.ac.jp

Abstract

Experiment was carried out in two parts to investigate the degradation profile of trimethoprim and sulphamethoxazole, antibacterial compounds in aqueous phase. In the first part of study, the effects of UV and TiO₂ on two antibiotics using the UV-water flow system (UVWFS) were examined. Obtained results revealed that trimethoprim and sulphamethoxazole pronounced 44 to 45% and 6 to 314% elevated rate of degradation in two TiO₂ doses, 0.05 and 0.1 g/l treatments with UV than only UV treatments which affords to draw a substantial conclusion that though both UV and TiO₂ have a crucial impact but the synergistic photocatalytic effects of the TiO₂ with UV attributes a rapid and higher degree of degradation of antibiotics compared to that of only UV at the same water flow rate. In this context, it may also be observed that effect of the dose of TiO₂ was very little in trimethoprim degradation but a significantly greater effects was revealed in sulphamethoxazole that indicating same number of TiO₂ molecules acted more favourably on higher number of sulphamethoxazole molecules than trimethoprim by photocatalytic activity which enhancing the rate of degradation reaction resulting in the rapid decrease of sulphamethoxazole concentration level in water. In second part of the study, three (15, 42 and 80 cc/min) water flow rates were employed using UVWFS maintaining same UV and TiO₂ dose 0.1 g/l to ascertain the effect of water flow rate in the antibiotic transformation process. The degradation efficiency in 80 cc/min water flow treatment was 113 and 61% higher in trimethoprim and 103 and 51% higher in sulphamethoxazole compared to that of 15 and 42 cc/min water flow treatments, respectively which clearly indicated that the rate of water flow is a paramount important, largely influencing the photocatalysis reaction process of TiO₂ and UV with antibiotics in water medium possibly enhancing movement velocity of their molecules. Besides it, trimethoprim degraded rapidly over sulphamethoxazole which might be inferred that higher water flow substantially increases the rate of oxidation and photocatalytic transformation of trimethoprim over sulphamethoxazole in the presence of TiO₂ and UV.

Keywords: Antibiotics, UV, TiO₂, Water flow system, Antibiotic degradation

1. Introduction

Recently, presence of antibiotic compounds in terrestrial and aquatic environment is of growing interest worldwide due to emergence as major threatened pollutants not only from environmental perspective but also from human health perspective. Antibiotics are used extensively in veterinary medicine for therapeutic purposes and as a growth promoter. In last decades, shrimp industry recognized as an important livelihood and developed rapidly because of attractive returns. A vast array of antibiotics are applied in the aquaculture especially in shrimp industry to enhance the production as well as to meet the global demand of such delicious and nutritious animal proteins in one hand and to strengthen and uplift the socioeconomic profile especially of the developing South East Asian countries. Use of antimicrobials in aquaculture essentially started with the work of Gutsell (1946), who recognized the potential usefulness of

sulphanamides for combating furunculosis. Following this, chloramphenicol, oxytetracycline, kanamycin, nifurprazine, oxolinic acid, sodium nifurstyrenate, flumequin, ciprofloxacin and others were introduced (Austin and Austin, 1993). Afterwards it appears as antibacterial, antiviral, antifungal, antiprotozoan and antimetazoan preparations, probiotics, immunostimulants, vaccines, bacterins, hormones, growth stimulants, anesthetics and bioremediators for both bioaugmentors and biostimulators.

Nowadays, antibiotic is the most common worrisome in the fish and shrimp industry that seepages through pond bottoms and discharges as wastes and effluents mixing into runoff water and crying to downstream covering tropical coastal mangroves destroying important natural habitat for shripm, fish, bird and people. Various substances in shrimp farm ponds can contaminate waters, including nutrients (nitrogen and phosphorus), metabolic wastes, antibiotics, or other medicines to protect shrimp, and suspended soil particles from erosion (Boyd and Green, 2002). Studies of fish farms have shown that the majority of antibiotics added in feed are not assimilated by fish but go into environment (Weston, 1996). Le and Munekage (2004) also reported that antibiotics residues may cause harmful effect on ecosystems in the coastal mangrove area. Once in the environment antibiotics can have a wide range of effects. Presently, indiscriminate application of antibiotics in aquaculture farms is resulting in suicidal affects due to developing mutagenic multi-antibiotic resistant viral, bacterial and fungal strains that causes boundless non preventive infectious diseases breakdown affecting aquatic organisms primarily - fishes and shrimps resulting in ultimate loss and devastation of farm. In addition to developing antibiotic resistant pathogens in surface water, it accumulates in the tissues of wild fish. According to Chua et al, (1989) if they accumulate in sediments, antibiotics may prevent natural bacterial decomposition and consequently alter the natural benthic environment. Antibiotic resistant bacteria was isolated from shrimp farm (Tendencia and de la Pena, 2001), from different shrimp farms of Viet Nam with 0.1 µg/ml antibiotic concentration (Le et al., 2005), from aquaculture sources (Akinbowale et al., 2006; Spanggaard et al., 1993) and luminous bacteria is also developing resistance to broad-spectrum antibiotics in certain shrimp culture systems of West Bengal (Sengupta et al., 2003).

On account of the above awful and trembling consequences of antibiotics, different countries have already taken up urgent steps regarding its application and removal from the environment imposing legislations and applying advanced degradation technology. Some methods have been developed concerning its degradation by means of biotic and abiotic agents that are retarded and incomplete process which further leading to contamination of environment. In this respect, some absorbents and natural zeolites have a wide variety of applications in the treatment of antibiotics using their unique adsorption and ion-exchange properties. Nowara et al. (1997) proposed that natural zeolite removes fluoroquinolone antibiotics by their high adsorptivity and sorption tendencies. According to Mansilla et al. (2007) and Herrmann (2005), photocatalytic reaction's of TiO₂ converts several classes of organic chemicals into less toxic and biodegradable compounds with the help of UV. Ozone is known to be an efficient oxidant for the degradation and removal of antibacterial agents in an aqueous state (Balcioglu and Otker, 2003; Huber et al., 2003; Ternes et al., 2004), as well as in the treatment of soils contaminated with conventional organic pollutants such as PAHs and PCBs (Nam and Kukor, 2000; Masten and Davies, 1997; Ohlenbusch et al., 1998). By considering these above mentioned facts, the goals of the present study are, to investigate the degradation capacity of widely used trimethoprim and sulphamethoxazole antibiotics employing UV-ray and TiO₂ in water phase and to determine the influence of water flow in its degradation process to reclaim aquatic environment from antibiotics troublesome situation.

2. Materials and methods

2.1 Synthesis of estuarine water

Low salinity (10 ppt) eschuarine water was prepared mixing sea water and ground water @ 1:3 ratio. According to Mark Flaherty et al. (2000) coastal shrimp farms generally, maintain pond salinity levels between 10 and 30 ppt, and commonly exchange 30 to 40% of the pond water volume each day to offset seepage or evaporation losses and maintain environmental conditions.

2.2 Antibiotic and titanium dioxide

Trimethoprim (C₁₄H₁₈N₄O₃) (Figure 1) and sulphamethoxazole (C₁₀H₁₁N₃O₃S) (Figure 2), bacteriostatic antibiotics and titanium dioxide (TiO₂) of Sigma-Aldrich Chemical GmbH, Germany was obtained from local authorized agent. Aqueous solutions of antibiotics and TiO₂ were prepared at different concentrations using distilled deionized water.

2.3 Preparation of UV-water flow system

We developed an UV-water flow system (UWFS) using a reservoir made up of stainless steel, ELEPON CR-I pump (Kitashiba Electric Co. Ltd., 50 Hz) having 10 to 100 cc/min water flow capacity and an UV lamp chamber of stainless steel (Aquapro, Model-UV 6GPM-H, ambient temperature 2 - 40°C) placed in a series and connected by pipes through which the water flows (Figure 3). Pump helps to flow the treated water of the reservoir through the UV-chamber and again recycled into the reservoir at a specific rate.

2.4 Experimental protocol

Two experiments were conducted in laboratory condition using UWFC to determine the influence of UV and TiO₂ in the degradation process of antibiotics under different water flow rates. In experiment-I, used eight UWFCs were divided into four groups with two replicates (4x2) – one groups allotted for control (C) applied no UV and remaining three employed for only UV (UV), UV plus TiO₂ @ 0.05g/l (UV+T_{0.05}) and UV plus TiO₂ @ 0.1g/l (UV+T_{0.1}) treatments, respectively, whereas three groups of UWFCs with two replicates were used for 15, 42, 80 cc/min water flow, respectively maintaining same UV and TiO₂ concentration @ 0.1g/l (herein called as UVT₁₅, UVT₄₂ and UVT₈₀). Reservoir of each UWFC was filled with 5 l of trimethoprim and sulphamethoxazole dissolved distilled water (temperature 26°C and pH 7.4) and TiO₂ of specified doses were mixed gently to the antibiotic treated water of respected treatments in both experiments. Detailed experimental conditions of experiment-I and II are given in the Table 1.

2.5 Antibiotic analysis

Water samples (100 ml) were collected from each reservoir at regular intervals using sterilized mechanical pipette and stored in neutral glass vial for the analysis of antibiotic concentration according to Samuelsen et al. (1994), Lunestad et al. (1995) and Borrego et al. (1996) with some modifications using high pressure liquid chromatography (HPLC) with Jasco liquid chromatography solvent delivery system (Tokyo, Japan, UV-2075) and Cosmosil packed column 5C18-AR-II (4.6 mm I.D x 250 mm). Sep-pak Plus PS-2 cartridge column for solid phase extraction were purchased from Waters Corporation Milford, Massachusetts USA. Used acetonitrile solvent system was of HPLC grade and obtained from Kanto Kagaku (Tokyo, Japan). Water samples (100 ml) were filtered through a 0.45 mm membrane filter and the water was applied to the sep-pack plus PS-2 solid phase extraction column at a flow rate of 1.0 ml/min and eluted with 1 ml of 60% acetonitrile solution to collect the desired fraction. Eluted 10 µl aliquot was injected into the column and HPLC was run with a flow rate of 1.0 ml/min, column temperature 40°C and detection UV-265 nm. The mobile phase to analyze trimethoprim and sulphamethoxazole consisted of acetonitrile/25 mM ammonium acetate (25:75, v/v). Antibiotic content in the water was expressed µg/l comparing with known standard antibiotic concentrations

2.6 Antibiotic degradation efficiency

The rate of reduction of antibiotic concentration in different treatments was calculated as degradation efficiency. The antibiotic degradation efficiency was written as α . δ is designated for antibiotic concentration, then initial and final concentration were represented as δ_i and δ_f , respectively. t was depicted as time, then final and initial time represented as t_f and t_i , respectively. The antibiotic degradation efficiency can also be calculated and expressed as µg/l/h using the following formula:

$$\alpha = \frac{\delta_i - \delta_f}{t_f - t_i}$$

2.7 Statistical analysis

All results obtained from each treatment were statistically interpreted. To compare the mean reduced antibiotic concentration in different treatments, a one-way ANOVA was followed. Before analysis, the assumptions of normal distributions and homogeneity of the variance were checked using Kolmogorov–Smirnov. If the main effect was found to be significant, the ANOVA was followed by a LSD (least significance difference) test. All statistical tests were performed at 5% probability level using statistical package EASE and MSTAT.

3. Results

3.1 Experiment – I

The concentration of trimethoprim varied between 0.0 and 965.7 µg/l in different treatments through out the period of experimentation. UV, UV+T_{0.05} and UV+T_{0.1} pronounced treatment dependent 73, 93 and 100% higher reduction response over the control. The lowest mean concentration 449.08 µg/l in UV+T_{0.1} showed 16 and 4% lower value than that of the UV and UV+T_{0.05}, respectively (Figure 4a). There was a significant treatment difference in the degradation efficiency (2.768 – 26.15 µg/l/h) in all treatments exhibiting 6.6 to 9.44 times higher over control (ANOVA, $P < 0.05$) (Figure 6a). Temporally, the concentration of trimethoprim exhibited a declining trend over time and reached zero level at time period 36th h in both UV+T_{0.05} and UV+T_{0.1} where as antibiotic existed in the water of UV treatments at the same time (Figure 4a).

A significant treatment dependence response was observed in the sulphamethoxazole concentration ranged from 0.0 to 887.87 µg/l (ANOVA, $P < 0.05$). The mean concentration was minimum in UV+T_{0.1} (168.58 µg/l) and maximum in C (783.62 µg/l) (Figure 4b). Though, no remarkable difference was found in the degradation efficiency (4.46 - 70.46

µg/l/h) between UV (17.83 µg/l/h) and UV+T_{0.05} (18.15 µg/l/h) but UV+T_{0.1} exhibited significantly greater value (288 - 1500%) over the treatments and control (Figure 6a). As time progressed UV and UV+T_{0.05} also showed a similar response in the sulphamethoxazole concentration reduction whereas a sharp concentration declining trend was found in case of UV+T_{0.1} during the study period (Figure 4b).

Irrespective of treatment, the concentration reduction of sulphamethoxazole was more rapid compared to that of the trimethoprim in each respective treatment.

3.2 Experiment – II

The trimethoprim content of water varied (0.0–1020.8 µg/l) significantly (ANOVA; $P < 0.05$) in all the treatments employed. The mean value was maximum (549.35 µg/l) in the UVT₁₅ exhibiting the following order of variations: UVT₁₅ > UVT₄₂ > UVT₈₀ (Figure 5a). The degradation efficiency of trimethoprim in UVT₈₀ was 113 and 61% higher compared to that of UVT₁₅ and UVT₄₂, respectively (Figure 6b). The concentration gradually decreased with time and reached at zero concentration level at the period of 36th and 48th h in UVT₈₀ and UVT₄₂, respectively, whereas UVT₁₅ showed a substantial concentration until 48th h (Figure 5a).

The concentration of sulphamethoxazole registered a significant treatment dependent response throughout the period of study (ANOVA, $p > 0.05$). The mean concentration 168.03 µg/l in UVT₈₀ was lower (68 - 150%) compared to that of UVT₁₅ and UVT₄₂ (Figure 5b). A marked difference in degradation efficiency was found in three treatments showing the following order of variation: UVT₁₅ > UVT₄₂ > UVT₈₀ (Figure 6b). Though temporal responses were similar but a sharp declining trend in the concentration of sulphamethoxazole was encountered unlike trimethoprim in all treatments and obtained zero concentration at 36th and 48th h by UVT₈₀ and UVT₄₂, respectively (Figure 5b).

Likewise, the concentration of sulphamethoxazole also showed a similar rapid reduction response compared to trimethoprim in three respective treatment in experiment - I.

4. Discussion

All findings obtained from the present study clearly demonstrated that UV, TiO₂ and water flow rate played a key operating factors in the degradation pathway of antibiotics, since final trimethoprim and sulphamethoxazole concentrations of water varied from 0.0 to 33.93 µg/l and 0.0 to 22.26 µg/l in experiment – I and II, respectively, whereas initial concentration of trimethoprim (9.1104 – 1020.8) and sulphamethoxazole (845.6 – 887.87) was available in all treatments of both experiments. In spite of that, antibiotic degradation efficiency was 6.6, 9.28 and 26.15 times in trimethoprim and 4.05, 4.2 and 1601 times in sulphamethoxazole greater values over control in experiment –I, which further strongly proved the effects of UV and TiO₂ on antibiotic degradation (Figure 6a).

Trimethoprim and sulphamethoxazole pronounced 44 to 45 % and 6 to 314% elevated rate of reduction in UV+T_{0.05} and UV+T_{0.1} over the only UV which indicating to draw a substantial conclusion that though both UV and TiO₂ have a crucial impact but the synergistic effects of the UV and TiO₂ attributes a rapid and higher degree of action on the degradation pathway of antibiotics compared to that of the only UV at the same water flow rate in experiment - I. Heterogeneous photocatalysis using TiO₂ is a procedure to promote the degradation of organic contaminants present in the aquatic environment (Pichat, 1994; Herrmann, 2005; Hoffmann et al., 1995; Mansilla et al., 2007). In trimethoprim, 34.8, 16.62 and 5.60 µg/l concentrations observed in UV, UV+T_{0.05} and UV+T_{0.1}, respectively at 36th h but complete degradation was occurred in UV+T_{0.05} and UV+T_{0.1} at 48th h, where as in sulphamethoxazole, the UV+T_{0.1} attained complete degradation (i.e., no detection limit of concentration) at 24th h when 20.28 and 5.24 µg/l concentration existed in the UV, UV+T_{0.05}. From this result it may be concluded that sulphamethoxazole degrade rapidly than trimethoprim under combined effect of UV and TiO₂ using UVWFM when time is concern. In this respect it may also be observed that influence of the dose of TiO₂ was very little in trimethoprim degradation but a significant effects was revealed in sulphamethoxazole implying that same number of TiO₂ molecules acted more favourably on higher number of sulphamethoxazole molecules than trimethoprim by photocatalytic activity which enhancing the rate of degradation reaction resulting in the rapid decrease of sulphamethoxazole concentration level in water.

In experiment – II, the degradation efficiency in UVT₈₀ was 113 and 61% higher in trimethoprim and 103 and 51% higher in sulphamethoxazole compared to that of UVT₁₅ and UVT₄₂, respectively which obviously indicated that the rate of water flow is a paramount important, largely influencing the catalytic reaction process of UV and TiO₂ with antibiotics in water medium possibly enhancing movement velocity of their molecules (Figure 6b). In consideration of degradation period, we found that when complete degradation (i.e., no detection limit of concentration) occurred at 36th and 48th h in UVT₈₀ and UVT₄₂, respectively in trimethoprim, only UVT₈₀ reached in complete degradation level at 48th h in sulphamethoxazole. Considering this result, it might be inferred that higher water flow substantially increases the rate of oxidation and photocatalytic transformation of trimethoprim over sulphamethoxazole with the help of TiO₂ and UV. Recently, advanced oxidation processes have been successfully employed on different antibiotic structures looking to transform pharmaceuticals into harmless substances (Reyes et al., 2006; Mansilla et al., 2007).

5. Conclusion and recommendations

Chemical aspects of photocatalytic reaction of TiO₂ in the presence of UV was not considered in the present study for that reasons further study is going on to determine the stoichiometry of trimethoprim and sulphamethoxazole degradation reaction as well as their end products in aqueous phase. On account of these above discussion derived from the present study affords us to draw the following conclusions and suggestions:

- 1) TiO₂ acts upon the antibiotics as a photocatalyst in the presence of UV and helps to degrade trimethoprim and sulphamethoxazole into simpler form that may be hydrocarbon of low molecular weight having no/less harmful impacts in the environment.
- 2) Synergistic and photocatalytic transformation effects of the TiO₂ and UV are higher than that of the UV only in the antibiotic degradation pathway.
- 3) Sulphamethoxazole degrades rapidly than trimethoprim under combined effect of UV and TiO₂ whereas; the effect of water flow is vice-versa in the degradation of trimethoprim and sulphamethoxazole.
- 4) Model of UV-water flow system may be a simple and low cost convenient tool can easily be used by the shrimp farmers as well as fish farmers not only in the antibiotic degradation process but also in other organic pollutants transformation to recover the ponds from suicidal effects of antibiotic troublesome situation. Under appropriate conditions mineralization of wide variety of compounds like chlorinated phenols, dyes, polyaromatic hydrocarbons and industrial effluents can be using TiO₂ and UV (Vautier et al., 2001; Yeber et al., 2000).
- 5) After each production cycle, farmers should treat water with UV and TiO₂ applying such model tools to save their precious and valuable shrimp crop and at the same time to improve the socioeconomic status by increasing profit instead of loss generally occurred by developing multi antibiotic resistant bacterial disease breakdown.
- 6) In environmental perspective, this UV-water flow treatment system imposes to the farmers to recycle the antibiotic contaminated water instead of drainage out in one hand and environment will be save from antibiotic pollutions and from rapidly development of antibiotic resistant bacterial strains on the other hand.

References

- Akinbowale, O. L., Peng, H. & Barton, M. D. (2006). Antimicrobial resistance in bacteria isolated from aquaculture sources in Australia.. *J Appl Microbiol.*, 100(5), 1103 – 1113.
- Austin, B. & Austin, D. A. (1993). Bacterial fish pathogens: Disease if farmed and wild fish. (2nd ed.). New York: Ellis Harwood, p. 384.
- Balcioglu, I. & Otker, M. (2003). Treatment of pharmaceutical wastewater containing antibiotics by O₃ and O₃/H₂O₂ processes, *Chemosphere*, 50, 85-95.
- Borrego, M., Cordoba, M., Cordoba-Dyáz, I., Bernabe, D. & Cordoba-Dyáz, (1996). Determination of norfloxacin by fluorescence in the presence of different antacids: quantification of analytical interferences. *J. Pharmaceut. Biomed. Anal.*, 41, 977-982.
- Boyd, C. E. & Green, B. W. (2002). Coastal Water Quality Monitoring in Shrimp Farming Areas, An Example from Honduras. Report prepared under the World Bank, NACA, WWF and FAO Consortium Program on Shrimp Farming and the Environment. Work in Progress for Public Discussion. Published by the Consortium. p. 29.
- Chua, T., Paw, J. & Guarin, F. (1989). The environmental impact of aquaculture and the effects of pollution on coastal aquaculture development. *Marine Pollution Bulletin*, 20, 335-343.
- Flaherty, M., Szuster, B. & Miller, P. (2000). Low salinity inland shrimp farming in Thailand. *AMBIO: A Journal of the Human Environment*, 29, 3.
- Gutsell, J. (1946). Sulfa drugs and the treatment of furunculosis in trout. *Science*, 104, 85 – 86.
- Herrmann, J.-M. (2005). Heterogeneous photocatalysis: state of the art and present applications In honor of Pr. R.L. Burwell Jr. (1912–2003), Former Head of Ipatieff Laboratories, Northwestern University, Evanston (Ill). *Topics in Catalysis*, 34(1-4), 49-65.
- Hoffmann, M., Martín, S., Choi, W. & Bahnemann, D. (1995). Environmental applications of semiconductor photocatalysis *Chem. Rev.*, 95(1), 69-96.
- Huber, M. M., Canonica, S., Park G. Y. & von Gunten, U., (2003). Oxidative treatment of pharmaceuticals during ozonation and advanced oxidation processes (AOP's), *Environ. Sci. Technol.* 37, 1016-1024.
- Le, T. X. & Munekage, Y. (2004). Residues of selected antibiotics in water and mud from shrimp ponds in mangrove areas in Viet Nam. *Marine Pollution Bulletin*, 49, 922-929.

- Le, T. X., Munekage, Y. & Kato, S. (2005) Antibiotic resistance in bacteria from shrimp farming in mangrove areas. *Sci Total Environ.*, 349(1-3), 95-105
- Lunestad, B. T., Samuelson, O. B., Fjelde, S. & Ervil, A., (1995). Photostability of eight antibacterial agents in seawater. *Aquaculture*, 134, 217-225.
- Mansilla, H. D., Mora, A., Pincheira, C., Mondaca, M. A., Marcato, P. D., Durán, N. & Freer, J. (2007). New photocatalytic reactor with TiO₂ coating on sintered glass cylinders. *Applied Catalysis B: Environmental*, 76(1-2), 57-63.
- Masten, S. J. & Davies, H. R. (1997). Efficacy of in-situ ozonation for the remediation of PAH contaminated soils, *J. Contam. Hydrol.*, 28, 327-335.
- Nam, K. & Kukor, J. J. (2000). Combined ozonation and biodegradation for remediation of mixtures of polycyclic aromatic hydrocarbons in soil, *Biodegradation*, 11, 1-9.
- Nowara, A., Burhenne, J. & Spiteller, M. (1997). Binding of fluoroquinolone carboxylic acid derivatives to clay minerals. *J. Agric. Food. Chem.*, 45, 1459-1463.
- Ohlenbusch, G., Hesse, S. & Frimmel, F. H. (1998). Effects of ozone treatment on the soil organic matter on contaminated sites, *Chemosphere*, 37, 1557-1569.
- Pichat, P. (1994). Partial or complete heterogeneous photocatalytic oxidation of organic compounds in liquid organic or aqueous phases. *Catalysis Today*, 19(2), 313-333.
- Reyes, C., Fernández, J., Freer, J., Mondaca, M. A., Zaror, C., Malato, S. & Mansilla, H. D. (2006). Degradation and inactivation of tetracycline by TiO₂ photocatalysis. *J. Photochem. Photobiol. A: Chem.*, 184, 141-146.
- Samuelson, B. O., Lunestad, B. T., Ervik, A. & Fjelde, S. (1994). Stability of antibacterial agents in an artificial marine aquaculture sediment studies under laboratory conditions. *Aquaculture*, 126, 283-290.
- Sengupta, T., Samal, D. & Jawahar Abraham, T. (2003). Antibiotic susceptibility of luminous bacteria from shrimp farm environs of West Bengal. *Indian journal of marine sciences*, 32, 334-336.
- Spanggaard, B., Jorgensen, F., Gram, L. & Huss, H. H. (1993). Antibiotic resistance in bacteria from three freshwater fish farms and an unpolluted stream in Denmark. *Aquaculture*, 115, 195-207.
- Tendencia, E. A. & de la Pena, L. D. (2001). Antibiotic resistance of bacteria from shrimp ponds. *Aquaculture*, 195, 193 – 204.
- Ternes, T., Stuber, J., Herrmann, N., McDowell, D., Ried, A., Kampmann, M. & Teiser, B. (2004). Ozonation: a tool for removal of pharmaceuticals, contrast media and musk fragrances from wastewater, *Water Res.*, 37, 1976 -1982.
- Vautier, M., Guillard, C. & Herrmann, J.-M. (2001). Photocatalytic degradation of dyes in water: case study of indigo and of indigo carmine. *Journal of Catalysis*, 201(1), 46-59.
- Weston, W. (1996). Environmental considerations in the use of antibacterial drugs in aquaculture. In: D. Baird, M. Beveridge, L. Kelly & J. Muir (Eds.), *Aquaculture and Water Resource Management* (pp. 140-165). London: Blackwell.
- Yeber, M. C., Freer, J., Martýnez, M. & Mansilla, H. D. (2000). Bacterial response to photocatalytic degradation of 6-chlorovanillin. *Chemosphere*, 41, 1257-1261.

Table 1. Experimental conditions followed in the study

Conditions	Treatments			
	C	UV	UV+T _{0.05}	UV+T _{0.1}
Experiment-I				
Water volume (l)	5	5	5	5
Water flow rate (cc/min)	42	42	42	42
Concentration of Trimethoprim ($\mu\text{g/l}$)	944.75 ± 11.75	944.75 ± 11.75	944.75 ± 11.75	944.75 ± 11.75
Concentration of Sulphamethoxazole ($\mu\text{g/l}$)	867.01 ± 17.76	867.01 ± 17.76	867.01 ± 17.76	867.01 ± 17.76
Concentration of TiO ₂ (g/l)	0	0	0.05	0.1
UV (W)	0	20	20	20
Experiment-I				
		UVT ₁₅	UVT ₄₂	UVT ₈₀
Water volume (l)		5	5	5
Water flow rate (cc/min)		15	42	80
Concentration of Trimethoprim ($\mu\text{g/l}$)		984.03 ± 21.27	984.03 ± 21.27	984.03 ± 21.27
Concentration of Sulphamethoxazole ($\mu\text{g/l}$)		877.37 ± 3.15	877.37 ± 3.15	877.37 ± 3.15
Concentration of TiO ₂ (g/l)		0.1	0.1	0.1
UV (W)		20	20	20

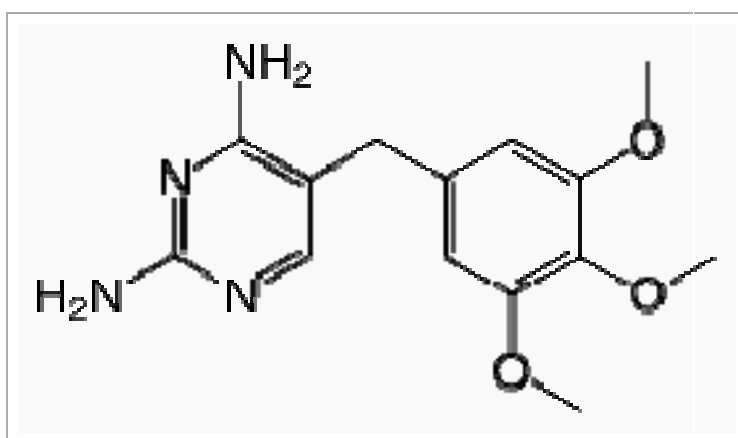


Figure 1. Chemical structure of trimethoprim

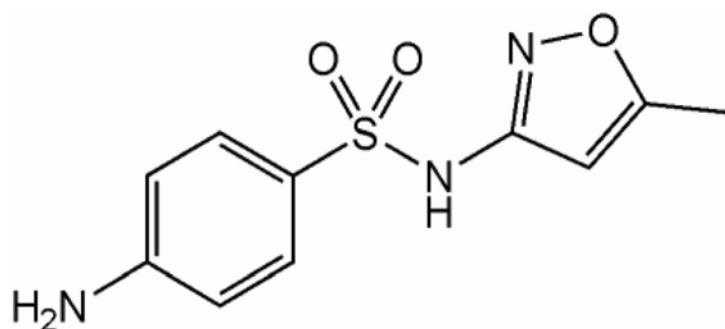


Figure 2. Chemical structure of sulphamethoxazole.

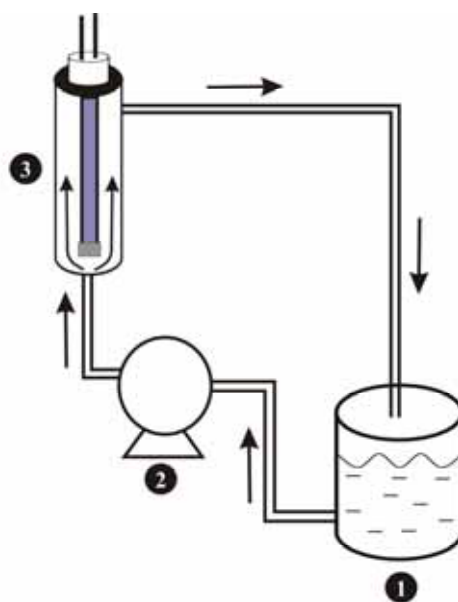


Figure 3. Schematic diagram of UV-water flow system (UWFS) used in the experiments.

1. Reservoir; 2. Pump; 3. UV chamber. (Arrow indicates water flow direction).

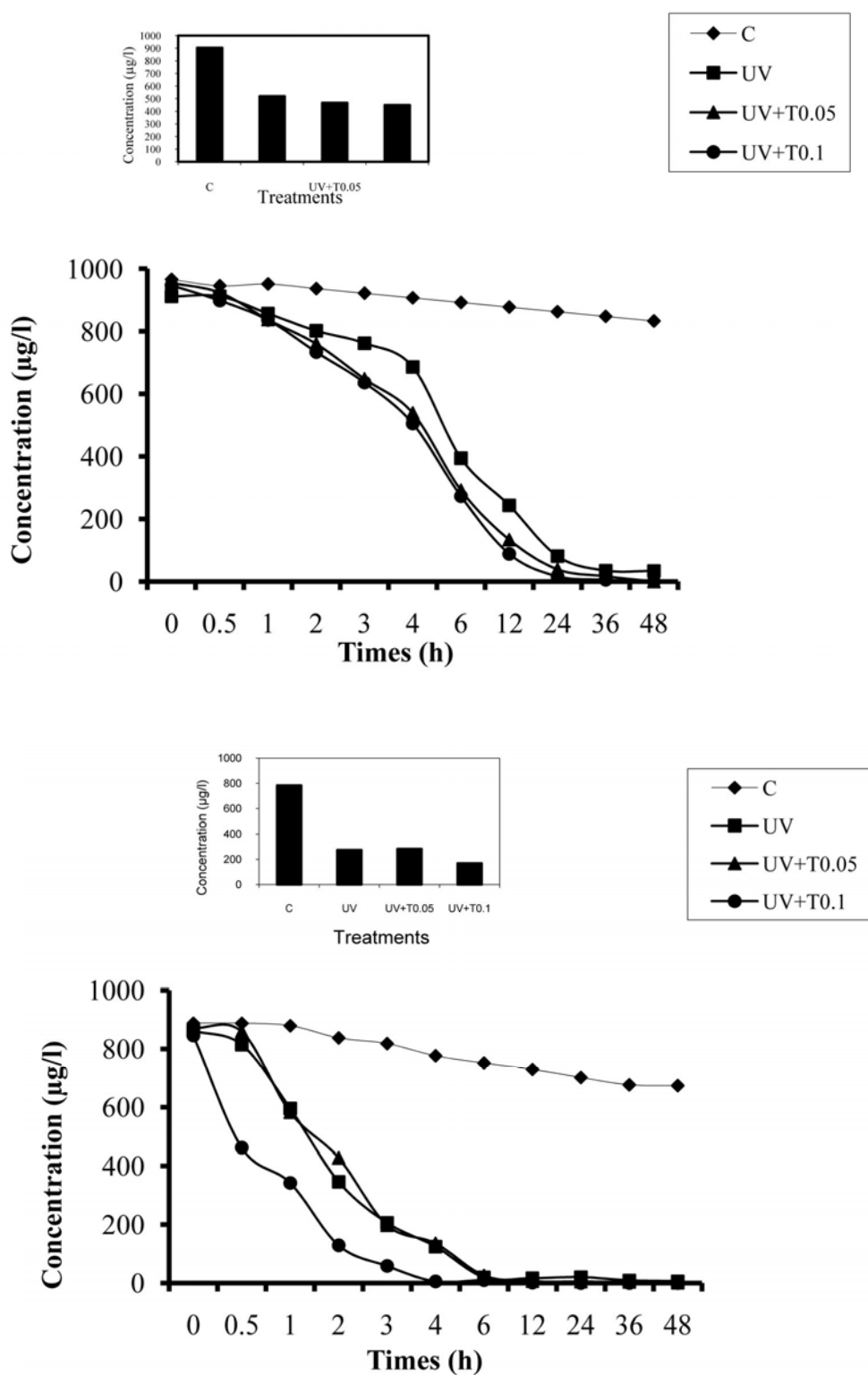


Figure 4. Temporal responses of antibiotic concentration (a) trimethoprim and (b) sulphamethoxazole in different treatments employed in experiment -I. Inset shows the mean concentration decrease.

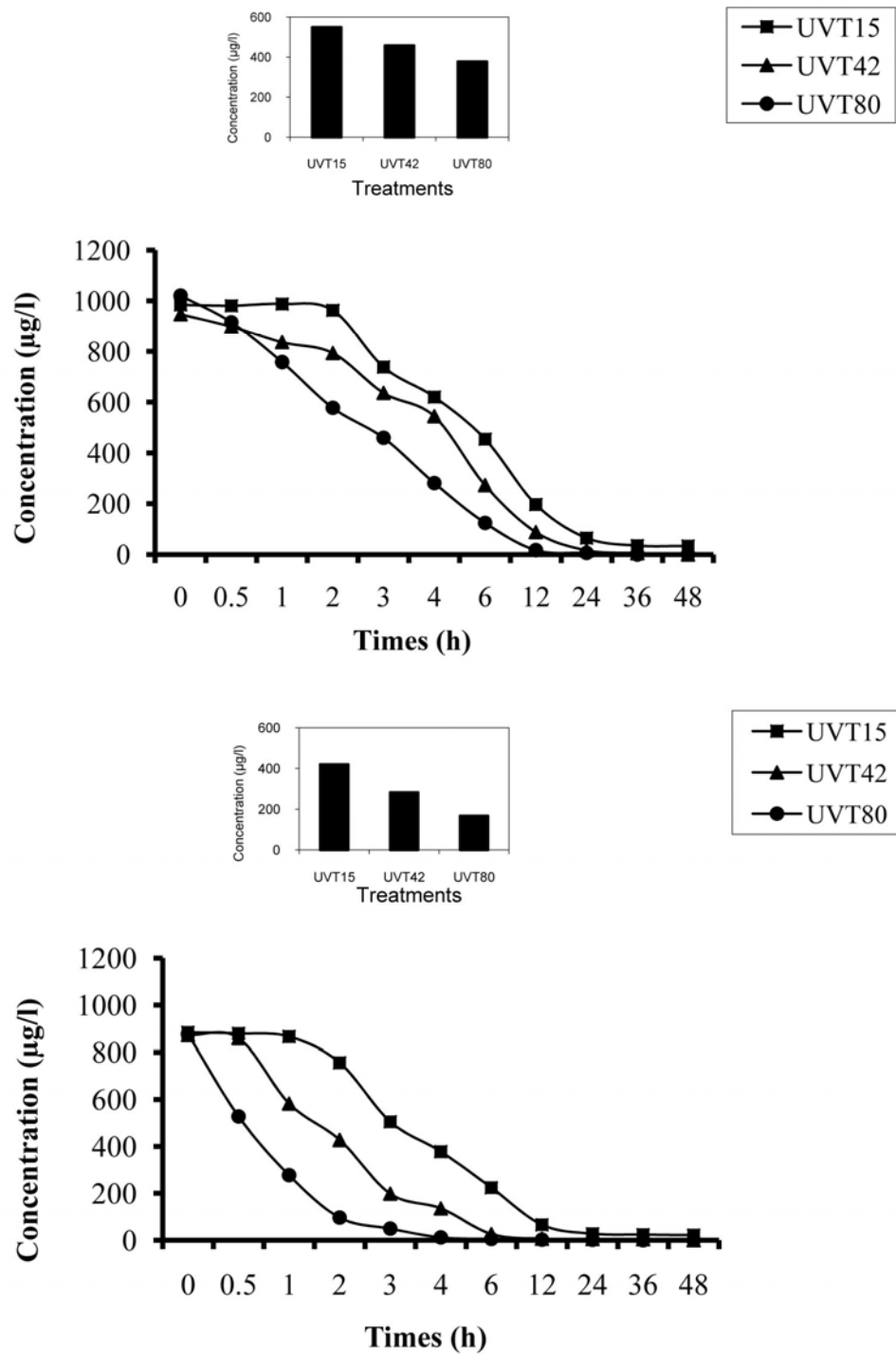


Figure 5. Temporal responses of antibiotic concentration (a) trimethoprim and (b) sulphamethoxazole in different treatments employed in experiment -II. Inset shows the mean concentration decrease.

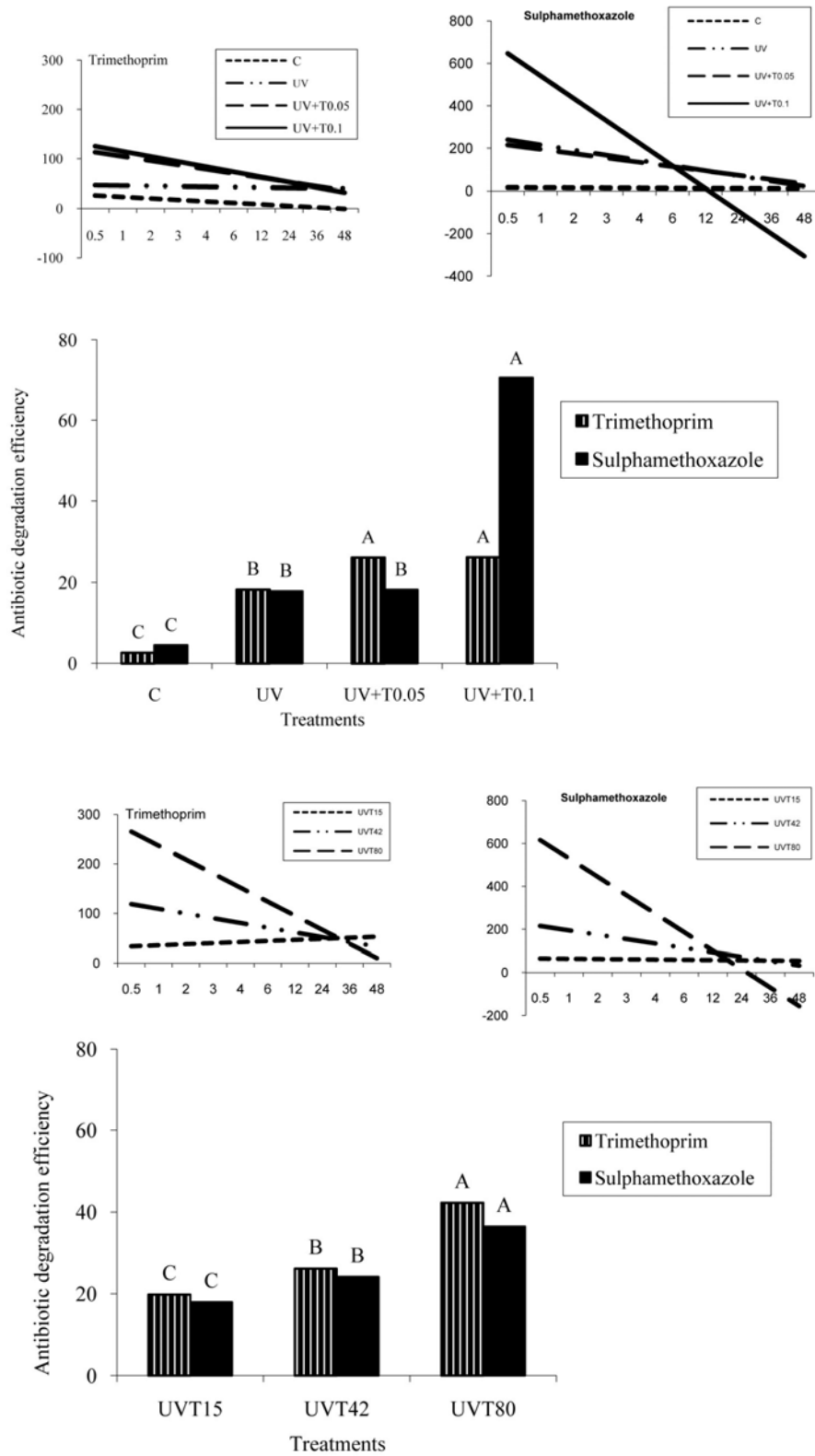


Figure 6. Antibiotic degradation efficiency of different treatments employed in experiment-I (a) and in experiment-II (b). Same script on the same bar types of different treatments revealed lack of significant difference. Inset shows the trend lines of antibiotic degradation in different treatments (X axis indicates times and Y axis indicates antibiotic degradation efficiency).



Study on the Construction of the Internet Ecological Concept

Yongqing Bai

21st Century Development Research Center of Dalian University of Technology

Dalian 116024, China

E-mail: byqda@vip.sina.com

Abstract

With the quickly development of Information Technology, the Internet has produced unprecedented influences to the human society, and the new existence space and environment for human being have been formed. Aiming at the serious social problems existing in the development of the Internet, “the Internet ecological crisis”, this article utilizes the theories such as ecology, environment management and harmonious society to primarily study the new approach to lead the healthy development of network by establishing network ecology, puts forward the network development principles such as harmonic network construction, network technology ecologization and network behavior ecologization based on the concept of network ecological concept, and expatiates on the important meanings of the network ecological concept to the healthy and harmonious development of network.

Keywords: Internet development, Internet ecosystem, Internet management, Harmonious Internet

Nowadays, the influence of the global network-Internet to the society is increasingly extensive and profound. Free and sharing network has been human new existence space, i.e. network space. Network is changing our thinking mode, work mode, study mode and amusement mode, and it is becoming into human “second living space” or “second living environment” (Qi, 2004, P.16-22). The quality of the network environment has influenced human survival and social development. “Digitization father”, Nicholas Negroponte pointed out that we had to consciously build a safe digital environment (Nicholas Negroponte, 1997, P.275). However, the Internet ecological crisis has been presented in the network environment and it has seriously harmed the healthy development of network, which have raised human extensive concerns.

1. Internet ecological crisis: new problem of Internet development

“Internet ecological crisis” means the social problem which seriously influences the Internet development, makes network ecology maladjusted and harm the security of the network because Internet abuse, misapply and pollute the network environment. It is mainly embodied in following aspects. First, information pollution, junk mails, network eroticism, network rumor and false network information which are seriously polluting the network environment, and they have been the social effects of pollution of the network space. Second, the security crisis of network occurs. The invasions of network virus, hacker behaviors and network crime have produced serious threats to the network security. Third, the privacy crisis of network occurs. Human behaviors in the network will leave “digital footprints” on the internet, and we are live in the network just like in our birthday suit, and our habited private space has been threatened. Fourth, information inflation and information resource deficiency exist together. The paradox that the useful information is difficult to be found and the information utilization rate is very low under great capacity of information exists on the Internet (Zhang, 2002, P.81-83). Fifth, the crisis of cultural diversity occurs. In the network of global integration, knowledge hegemony, cultural imperialism and “dominant culture” are easy to find their places, which will threaten the diversity of world culture. Just as the biological diversity is the important factor to sustain the biological balance, the cultural diversity is the key to protect the global cultural inheritance and sustain the cultural biological balance (Tang, 2000, P.15-20).

The Internet ecological crisis mainly possesses characters such as globality, virtuality and instantaneity.

(1) Globality. The largest character of Internet is to realize the communication all over the world. The network makes the “global village” become true, and if we say “we only have one earth”, so we can also say “we only have one Internet”, and the problems occurring in the Internet are global, and only the problem occurs at one point, it will affect the whole world, and it needs the global power to solve that problem. For example, to solve the information pollution, it is helpless that only one region or country strengthens the supervision. Therefore, the settlement of network environment problem depends on not only each region or country, but global communication and cooperation. In fact,

the international self-discipline organizations, agreements and criterions have begun to exert more and more important function in cleansing the network environment and harmonizing the network ecology.

(2) *Virtuality*. The network space is a digital space and virtual environment, and the problems existing in it still has the nature of virtuality. These problems are different to the natural environmental problems in the actuality, and they destroy the virtual information environment, and they belong to information damage and digital damage which are not same with virtual damage, and they are real damage which will directly or indirectly influence the society, and the influences are extensive and serious. Especially, because this sort of damage is not easy to be apperceived or checked in the damage process because of the virtuality of network, so when the damage is found, the very serious and irreversible aftereffects have occurred.

(3) *Instantaneity*. The development speed of Internet is infrequent in human history, and just as the development speed of Internet, the destroying speed of the network environment is very quick. Taking the computer virus as the example, before the Internet occurred, the diffusion of computer virus is mainly implemented by one to one manual mode in virtue of disk, and relatively speaking, the speed is slow, and routes are few and the range is narrow. But when the virus spreads in the network, it can automatically diffuse in the larger range, and induce serious aftereffects instantaneously. Only if hacker clicks the mouse, the report that there is website to be hacked will be spread right now. The virus of "love worm" which indulges in willful persecution all over the world induced billions dollars' losses to the world only in several days.

The essential of Internet ecological crisis is the intensification of the conflict between human and information, and that conflict is not the conflict crisis among individual factors, but it is the ecological crisis of the whole network system, network environment and network society. It is a systematic engineering to solve the problem undoubtedly, which not only needs the powers of administration, enterprise and individuals, but needs to strengthen the international cooperation. Not only the function of network technology but the function of law, ethic and morality should be emphasized. The settlement of network ecological crisis undoubtedly should depend on the technical advancement, the investment of capitals and the increase of bandwidth, but the facts proved that it is not enough only to solve the problem technically, and if we start from the views of ecology, ethic and sociology, we may be find the new approach to solve the problem.

2. Evolution of Internet ecological concept

Ecology is the science to describe the harmonious development between human and nature, and it has been the most important world view and methodology at present. The theory and method of ecology have been extensively applied in the research about social science. The "education ecology" which was raised in 1970s analyzed the education system by the ecological opinion. US scholar Regus founded the "administration ecology", and James F Muler put forward the concept of "ecology of commerce". The network ecological concept is put forward by the author based on the origin of the relationship between human and nature. And the author thinks that with the development of the network, the network has been evolved as a sort of new "humanized nature" which is called as the "network nature" (Bai, 2006, P.1-3). Traditional network cognitions are mainly centralized in the layers such as network technology, tool and establishment, but with the development of network, the network has formed a sort of new space and environment which has evolved into the new social conformation and new human ecological system. The development of network is going from tool to application, from establishment to environment, from material to humanism, and from technology to ecology.

2.1 From geographical space to network space

"US National Information Infrastructure (NII)" plan embodied a series of the geographical topics about the space relationship reform. And the plan alleged that the development of NII would change human living mode, work mode and communication mode for ever, and the future society would present the prospect of "network". This sort of "network" reminds that we have to pay attention to many new terms such as "electric space", "super space", "network space", "virtual space" and "new social space", and we have to emphasize the information communication technology (ICT) and the "geographical situations" of all participators (citizens, companies, local governments and national governments) would be changed by the technical innovation.

Traditional geographical spaces and distances exert main functions, and different places have different "values". With the occurrence of "non-geographical space", the regions are established on the based of electric network, which doesn't consider the limitations of many factors such as terrain and distance, and the high-speed transmission spanning long distance makes people can associate with any site in the world. Users can implement effective communication through the network information service, which replaces the direct contact face to face. In the non-material domain of information and data exchange, the geographical distance becomes into the instantaneous zero distance. This sort of network space essentially roots in three aspects. The first aspect is the integration of three industrial departments including computer network, telecom and TV, and various multimedia services on the Internet, which make the comprehensive transmission of voice, word, data and image possible. The second aspect is the miniaturization of new

generated terminal units such as PC, palm digital terminal and cell phone, which make the removability of information communication strengthened largely. The third aspect is that more and more organizations, units and individuals are linking with Internet in various places all over the world.

The network space is established in the interfaces of information technology and time. The network space is the “instantaneous space”, and under the organization of network, the important thing is the process to solve the problem, and it is not the place to deal with information. The communication in real society is the communication of time and space, but the network communication is the communication only under the time interface, and the space has disappeared. In the “real time”, the world is changing to be touched, and the “time control of geographical space” has become into one independent condition of globalization, and works and livings are more and more away from material and distance, and they are developing to the “fluidity in the instantaneous space” (H. Barques, 2000, P.104-111).

2.2 From network space to network society

With the continual advancement of scientific technology, the human social living domain is continually extended. From the obscurity time to the civilization time, from the agricultural society to the industrial society and to the information society, the evolutive history of human society is the process that the living domain is continually away from the natural environment and the nature. Through the humanization of nature, human make the humanized nature formed continually, and the humanized nature is continually becoming into human living territory. Network is the integration of new social activity mode and survival mode produced by the development of modern information technology, and as a new humanized nature body, it has been the new social and living territory.

The network society is a sort of undeniable “new space” in human living which really exists. As human new living domain, it has new characters which are different to the living domain formed in former human society. The material base of network society is different to the traditional society, and the mediums which form the human social relationship are largely different to traditional society. The social communication view and social scene including human life feeling are largely different to the traditional society. Comparing with past daily living domain, the network society possesses relatively independence and self-maturity, and it can be the time and space existence as an independent and self-contained sub-system, and it can co-exist with past living domain, and it can also exist with past living domain together, and in this new living domain, the living resources only include information, but in the past living domain, the living resources include information and various concrete materials.

We can say that the network space has been the new living domain of human, and the network society has been the real existence of human society, and the network existence is the new life activity form for human being. But in the back of the surprising and flourishing development speed of network, just as same as the social effects of pollution in natural environment, information pollution, network virus and garbage mails have been the public pollutions in the network environment, and the network ecological crisis occurs. Why above problems will occur? How to solve above problems? How to build healthy and harmonic network? The author thinks the ecology is the good edification. When the industrial civilization swept, many problems such as environmental pollution, resource deficiency and population explosion were induced. After experiencing one by one painful lessons, human begin to treat the important problems of human survival and look for the method to solve the problem by the ecological view. Network is the survival space and environment established by the human, and facing the serious problems in the development of network, we should study the network as viewed from the ecology, and analyze and diagnose the “network ecological crisis”.

3. Principles of the Internet ecological concept construction

The network environment should be healthy and harmonious, which is human consensus, but the “Internet ecological crisis” seriously harms the network and social development, and it is the objective requirement and proper selection to understand the network and scan the problems in the network development as viewed from the new domain of network ecology. So, based on traditional network technology concept, we should establish a sort of network cognition- network ecology concept, and we should establish the ecological value direction of network, and to rebuild the present network concept from the natural ecological concepts such as ecological system and environmental management and the social ecological concepts such as harmonic society and sustainable society.

3.1 Harmonious network

The report of “Seventeenth National Congress of the Communist Party of China” pointed out that “building harmonious culture and foresting civilized fashion, strengthening the construction and management of network culture and building good network environment”, leading and forming the concept and lively complexion of “everyone is responsible for and share harmonic network”. To establish the harmonic society is the total principle of the present social development, so to establish the harmonic network is also the total principle of the present network development.

As one important part of modern society, the network is associating with real society all the time. The establishment of the harmonic society should achieve not only the harmony of real society, but the harmony of the network society. The network and reality should be reflected each other, and the network has irreplaceable function for the establishment of

the harmonic society.

As the extension of real society, the network society offers good experiment fields for the practice of the harmonic society by right of its characters such as opening, interaction, timely nature and extension, and at the same time, the information infusion, consensus position and expression atmosphere in the Internet also react with the establishment of the harmonic society to large extent. So, it is the necessary requirement to manage and lead the Internet for the establishment of the harmonic society. However, the obvious lag and confusion of Internet management have been the unharmonious factors in the establishment of harmonic society, and to strengthen the Internet management should be the urgent task to complete the establishment of the harmonic society.

The development of Internet has its own rules which are not isolated, and these rules should be harmonized with real society, reduce and avoid the harms to the real society, and especially in the process that the Internet develops very quickly, we have to deal with various possible problems between real society and network society. The harmonic society needs harmonic network which is the important part of the harmonic society, and the harmonic network promotes the development of the harmonic society.

3.2 Ecologization of network technology

The development of network can not leave the technology, and to establish the network ecological concept, we first can not abandon the technical attributes of network. Without the technical attributes of network, it is not feasible to establish the network ecological concept. The ecologization of network technology is the principle we have to persist in to establish the network ecological concept. As the foundation of modern industrial civilization, the quick development of technology endows the industrial civilization the ability to control and conquer the nature, and endows human ability to infinitely “take” from the nature, and though human create large material fortunes because of that, but the nature is seriously destroyed, and the ecological crisis occurs. To avoid the negative effect of technology in human civilization evolvement, the technology must go to the ecologization. The technical ecologization is to use the ecological ideas to instruct the research, development and application of technology, lead and standardize the technical system by the ecological law, and make the ecological technology better server for the harmonic evolvement of human and nature. According to the requirement of ecological theory, we have to persist in the tenet of “technology benefits human”, implement technical research, application, development and management, take the ecologization (including natural ecology and social ecology) as the standards, fully advocate the development of network technology which accords with the ecologization, and gradually wash out the network technology which doesn't accord with the ecological development.

3.3 Ecologization of network behavior

The network is supported by the technology, but human network behaviors decide the application and consequence of network technology, so we have to establish corresponding network behavior rules.

First, the “harmless rule” should be required. Any network behaviors should be harmless to others and network environment. Human should not utilize the network technology to induce direct or indirect harms to other network bodies and network space, which is the ecological base line of network behaviors and the basic moral standard to evaluate the network behaviors. It is very helpful to analyze the moral paradox in the domain of network technology, for example, the network virus and hacker behaviors are behaviors which seriously disobeys the harmless rule (Richard, 1999, P.54).

Second, we should persist in the “public rule”. Network is the network of all human and the network of the whole world, and it is a global ecological system. When you enjoy the Internet, you should take care of others' existence, feelings, public benefits and public orders, and you should not pollute and destroy the network environment. Network is not our own network, and it is also our unborn network, and we have to leave clean and beautiful network space for our offspring.

Third, we should persist in the “respect rule”. Network is the humanism network, and it is not the network of machine. Professor Lucas D. Inrona (2002) of British Lancaster University pointed out that the network was human itself, and it was the support of human existence (Lucas, 2002, P.220-221). Whatever the network achieves high technology and virtual effect, it is not the “place without human”, and it is the relationship network among human beings, and it is the communication space among human beings, and the main body of network is not the real human and the “virtual human” and the machine, so the network behaviors should accord with human characters and social standards and requirements. Network main bodies should respect each other, and they should not regard others as pure “digital” symbol which can be operated and computed at will. The protection of privacy is the basic behavior rule, and individual information should not been issued and diffused at will, and both the right that human control their private information and the respect that others face the private information should be emphasized, so the status of the respect rule is more important in the network. In the popular “free service” of network, service suppliers always think they have infinite and absolute rights, and they rarely consider and respect service receptors' rights, and in fact, that is the representation of

householder idea, and its abuses have been early condemned in social ethic, life ethic and medical ethic.

4. Signification of the Internet ecological concept construction

The network is the space full of paradox, and the existence of paradox induce the settlement of network environment be in a dilemma. For example, should we supervise the network? If we let it along, many anarchism behaviors will run riot, and if we supervise too strictly, the essential of the network will be harmed, and the characters such as opening, freedom and sharing of network will lose, and we can not image the separatist and blanked network is still the network.

US scholar Baird (2003) (Zoe Baird, 2000, P.26-29) pointed out that the internet management was the real challenge in the future, and the internet management should be the part of the mainstream management, and it should be the management which governments, enterprises and individuals all participated in. The internet management has been the global challenge what we have to face at present. The ecology and relative theories are the most effective approaches and means to study and solve problems under the present topics of “harmonic society” and “sustainable development”, and the network has been evolved to a sort of new human ecological system from early simple technology and tool. So it is the objective requirement to establish the network ecological concept for the development and management of internet, and that is the guidance to establish harmonic and healthy network, and one important part to establish the harmonic society.

The Internet ecological concept is a sort of new network development concept, and it is the confirmation and spread of new network view under the scientific development view, the sustainable development view and harmonic society view, and it is the transformation of pattern for the network world view from “technical” pattern to the “ecological” pattern of the integration of “technology- information- society”. The network ecological concept can lead human to form overviews and ultimate opinions, i.e. the network ecological view, based on ecology. The network ecological view is a sort of new network development view in the frame of the scientific development view, and it is the enhancement and integration of original network tool view, network technology view, network information view and network society view, and it is the objective requirement and essential reflection of present network and society, and it is the necessary tendency of network and human social development, and it is one of important contents of modern ecological civilization for human society.

References

- Bai, Yongqing & Wang, Ziyang. (2006). The Impacts of Network Nature on Human Society. *Science Technology and Dialectics*. No.4. P.1-3.
- H. Barques & Luzi. (2000). The Change Tendency from Geographical Space to Geographical Network Space. *Acta Geographica Sinica*. No.1. P.104-111.
- Lucas D. Introna. (2002). The question concerning information technology: thinking with Heidegger on the essence of information technology. John D. Haynes. Internet management issues: a global perspective. *Idea Group Pub*. P.220-221.
- Nicholas Negroponte, interpreted by Huyong & Fan, Haiyan. (1997). *Digital Survival*. Haikou: Hainan Press. P.275.
- Qi, Aimin. (2004). The Attribute of Cyberspace as well as Its Influence on the Laws Related. *Journal of Guizhou University (Social Science)*. No.2. P.16-22.
- Richard A. Spinello. (1999). *Century Morality: the Ethic Aspect of Information Technology*. Beijing: Central Compilation & Translation Press. P.54.
- Tang, Yizhi & Lilun. (2000). The Network Ecological Crisis and Network Ecological Ethic. *Journal of Social Science of Hunan Normal University*. No.6. P.15-20.
- Zhang, Xinzhi. (2002). An Antinomy of Communication in the Internet Age. *Journal of China Agricultural University (Social Science Edition)*. No.3. P.81-83.
- Zoe Baird. (2000). Managing Network: Government, Business Circles and Non-profit Organizations. *Digest of Social Sciences*. No.3. P.26-29.



Isolation, Stabilization and Characterization of Xanthophyll from Marigold Flower- *Tagetes Erecta-L*

V.B. Pratheesh, Nify Benny & C.H Sujatha

Department of Chemical Oceanography

CUSAT. Kochi-16, Kerala, India

Tel: 91-0484-238-2131 Fax: 91-484-374164

E-mail: dr.sujathach@gmail.com

Abstract

The present paper deals with the chemistry, isolation, separation, characterisation and stabilisation of the Marigold oleoresin and its application as a natural food colorant. Marigold (*Tagetes Erecta L*), an ornamental plant belonging to the composite family, has a rich source of natural antioxidant-Lutein. A natural pigment, xanthophylls offer an alternative to synthetic dyes as a food colorant, due to its non-toxicity. Chromatographic separations of saponified and unsaponified oleoresin were performed and Trans-Lutein identified as the major constituent. Well-preserved flowers exhibit a high yield of Xanthophyll content (105.19 g/Kg) in contrast to the unpreserved flower sample (54.87 g/Kg), emphasizing the significance of flower preservation in the extraction of xanthophyll. The stability and amount of xanthophyll also increased from 105.19 g/Kg to 226.88 g/Kg on saponification and subsequent purification with Ethylene Dichloride.

Keywords: Antioxidant Activity, Colorants, Extraction / Separation, HPLC, Natural Products, Pigments

1. Introduction

Since the early civilizations and in the beginning of the food industry, pigments –natural or synthetic, were used to give an attractive presentation, perception of freshness, taste, and quality of food. Saffron and other plant species were used to provide characteristic color and flavor in food. Today, natural colorants are emerging globally due to the perception of its safer and eco-friendly nature. Nowadays, a trend towards “naturalness” represents a challenge for food manufacturers, because of its pharmacological applications. Synthetic dyes received faster acceptability due to a wide range of applications in various fields like food (Torgils et al. 1998), cosmetic (Calnan 1976), and more importantly in textile (Savarino et al. 1999, Paisan et al. 2002) due to ease in dyeing, and reproducibility in shades and overall cost factor. Natural food colorants can be originally present in the foodstuff, or may be added as an extract to enhance the natural color. Quality of food is associated with many aspects –color, flavor, and texture, but color can be considered the most important of them, because of its appealing nature. Color as well gives the key to catalogue a food as safe, with good aesthetic and sensorial characteristics: the undesirable colors in meat, fruits, and vegetables warn us about a potential danger or at least of the presence of undesirable flavors, among other reactions. The food industry is therefore, interested in gaining a better understanding of color generation and color stabilization during the various steps of food processing. The processed food constitute 60- 65% of total food and the need for the food additives and its improved shelf life is also increasing. There are some 2500 chemicals that function as food additives that give rise to some 5000 trade name products on a worldwide basis (Scotter.M.J & Castle.L. 2004). However, the natural pigments that are permitted for human foods are very limited, and the approval of new sources is difficult, because the U.S. Food and Drug Administration (FDA) considers the pigments as additives, and consequently pigments are under strict regulations (Delgado-Vargas et al.2000).

A high quality of food and beverages is vital to our physical and mental well being. Of all the food additives in use, none gives rise to greater controversies than food colors. The readily available coloring matter based on natural products is of considerable importance since the United States have banned the use of synthetic coloring in foods. In ancient times tinted amaranth has been used to extract the coloring matter, which is hydrophilic in nature and was used for the dyeing of drinks, food and other products in Mexico, Bolivia and Ecuador (Gladis et al. 2000). In India and Mexico, for facial rouge the woman used amaranth juice. This pigment belongs to the group of betacyanines (Attoe. L.J. & Von Elbe, J.H. 1985, Mabry T.J & Drieding, A.S.1968) and the betanine have been used as colorants in many types of food (Pasch, J. H. & von Elbe, J. H .1979). Some of the important plant pigments are carotenoids, Anthocyanins, and

betalains. Carotenoids are compounds comprised of eight Isoprenoid units (Ip) whose order is inverted at the molecule center (Delgado-Vargas et al.2000) (Figure: 1). Carotenoids are classified by their chemical structure as: (i) carotenes that are constituted by carbon and hydrogen; (ii) oxycarotenoids or xanthophylls that have carbon, hydrogen, and, additionally, oxygen. Also, Carotenoids have been classified as primary or secondary. Primary carotenoids group those compounds required by plants in photosynthesis (β -carotene, violaxanthin, and Neoxanthin), whereas secondary Carotenoids are localized in fruits and flowers (α -carotene, β -cryptoxanthin, zeaxanthin, antheraxanthin, capsanthin, capsorubin). Anthocyanins are the most important group of pigments, after chlorophyll, which is visible to the human eye (Harborne et al.1988). Chemically, Anthocyanins (Greek word *anthos* means a flower, and *kyanos*, dark blue) are flavonoids. Anthocyanins (Figure: 2) are substituted glycosides of salts of phenyl-2- benzopyrylium (anthocyanidins). Chemically, betalain definition embraces all compounds with structures based on the general formula (Figure 3) therefore, they are ammonium derivatives of betalamic acid (Strack et al.1993).

Carotenoids are abundant in fruits and plants and are widely used as an antioxidant and may be useful in the prevention of diseases including cancer. The consumption of lutein and zeaxanthin reduces 40 % of the age related macular degeneration (Seddon 1994). The xanthophylls because of their yellow to orange-red coloration and natural occurrence in human foods, also find its use as a food colorant. Therefore there exists a high demand for the significantly pure Xanthophyll that can be used as a food colorant and a nutrient supplement. Flowers such as *Tagetes* comprise different species about 33 in number, helenium, helianthus, sunflower, dandelion and many others. Of these, the most concentrated source of xanthophylls is of the order 4500mg/lb (Verghese, 1998b) in the petals of *Tagetes Erecta* L (African marigold, Aztec marigold, Zempasuchil). Marigold flower petals are a significant source of the Xanthophyll and have a much higher concentration of this pigment compared to other plant materials (Verghese, 1998a). Marigold flower (*Tagetes Erecta* L) is a hardy annual branching herb about 60 to 90 cm tall and erect, grown in certain parts of India- Tamil Nadu, Andhra Pradesh, Karnataka as well as in other parts of the World; and is extensively cultivated in temperate climate. It prefers nourishing soil of pH 7.0 to 7.5 with good water-holding capacity and well-drained fertile sandy loamy soil as well as a sunny climate. Mexicans use marigold flower as a traditional medicine and to Romans, an inexpensive food colorant, a substitute for saffron and it was they who introduced it to other parts of Europe. Now a days, the marigold flower is exclusively used for the Malayali festival "Onam" in Kerala, India and all over the world to make "pookalam" (flower carpet) (Figure: 4), due to its exotic combination with other vibrant colored flowers.

Depending on the varieties, cultivar and horticulture practices, the yield of flower showed remarkable variations in number and in flower weight (from 11 to 30 ton/hectare). Although flower is made up of petals, calyx pedicel, seeds etc., approximately 40% to 50% of the flower consist of petals. Extraction studies of petals and total flower with hexane showed that only flower petals contain xanthophylls. Calyx contains chlorophyll which in-turn affects absorption of xanthophylls by broilers and layers (Verghese. J 1998b). Hence, only the petals are used for the isolation of oleoresin. The main coloring component of Marigold flower is lutein ($C_{40}H_{56}O_2$). Free Lutein hardly exists in the flower and it naturally occurs in the acylated form (Figure 5). The Lutein ester concentration in fresh Marigold flowers varies from 4 mg/Kg in greenish yellow flowers to 800 mg/Kg in orange brown flowers (Sowbhagya et al. 2004). Dark-colored flowers contain about 200 times more Lutein esters than the light-colored flowers. Xanthophyll content varies in the range of 9 to 11 g/Kg. The concentration of Lutein varies in different shades of marigold flowers, viz.; greenish yellow to bright yellow and orange brown (Gregory et al.1986). Total Lutein esters have been reported to be in the range of 3.8 to 791 mg/Kg of flower (Sowbhagya et al. 2004). Lutein palmitate is the major ester in the flower. The other esters of lutein identified in the flower are dimyristate, myristate palmitate, palmitate stearate, and distearate (Table: 1). A purified extract of marigold petals mainly containing Xanthophylls dipalmitate is marketed as an ophthalmologic agent (Sowbhagya et al. 2004, Gau et al. 1983). Lutein is stable in pH range 3 to 9. At extreme pH and in the presence of light, lutein undergoes isomerization resulting in color loss. Lutein structure consists of conjugated bonds, which when react with the oxygen present in air, cause oxidation to take place and lead to color loss. Oxidation products of xanthophylls are mono and di-epoxides, carbonyls, alcohols etc. and extensive oxidation results in bleaching of carotenoid pigments. To minimize color loss, it is safe to pack lutein-containing products in tin or opaque containers. Enzymes like lipoxygenase hasten oxidative degradation, which occurs by direct mechanisms. Enzymes first react with unsaturated or saturated fatty acids producing peroxides, which react with lutein xanthophylls and lead to oxidative degradation. "Blanching" (98°C/5 min) exhibits an apparent increase in xanthophylls content due to inactivation of lipoxygenase and also enhances pigment extraction (Sowbhagya et al. 2004, Alam et al. 1968).

Marigold carotenoids have potential as a natural food colorant. The status of marigold, as a source of natural carotenoids, has been reviewed (Verghese. J 1998a, 1998b). Temperature, pH, light, activity in water is all factors which affect the stability of the pigment (Pasch, J. H. & von Elbe, J. H. 1979). Stability of Xanthophyll pigment extracted from marigold has been studied by saponifying. Xanthophylls are usually esterified which produces additional analyses complications and requires both separation and identification. Saponification obtains less complex mixtures when only non-esterified pigments appear. Another advantage of saponification is chlorophyll destruction in the saponified samples (Delgado-Vargas et al.2000). Since commercial extracts are valued by their Xanthophyll and

trans-lutein content, concentration of lutein fatty acid esters in the extract can be enhanced by purification. Xanthophyll content can be boosted by phase partition between 70% and 90% of hexane, acetone, methanol and ethanol. When marigold extract was subjected to precipitation using isopropanol removes 65% of the lipids in the extract are removed. The precipitated fraction contained 51.3% lutein esters and a second precipitation from isopropanol-petroleum ether (80:20) resulted in a product of much higher purity, more than 65% pure (Sowbhagya et al. 2004). Since the availability of marigold flower is seasonal, flower preservation becomes vital in the extraction of marigold oleoresin. If flowers are not properly stored and preserved, Xanthophyll content will decrease. The extraction of xanthophylls (oleoresin) from marigold flower involves the following stages: ensilage, pressing and drying, Hexane extraction, and saponification. Of these, the ensilage is considered important in determining the efficiency of the overall process. Studies were conducted to obtain a relationship between the xanthophylls extraction yield and the efficiency of marigold flower ensilage (Navarrete-Bolanos et al. 2003). It was reported that during the ensilage, structural cell-wall degradation of the marigold petals by saprophytic microorganisms associated with the flower resulted in increased mass transfer during the extraction stage. Such an increase is associated with the level of cellulose synthesized by these microorganisms.

Numerous methods have been proposed in order to improve both xanthophylls extraction and purification efficiency (Ausich and Sanders 1997, Khachik 1995, Philip 1997). But many of them have the drawback of high temperature requirement and long processing times, which can result in the degradation and formation of unwanted isomeric components (Levi 2001, Madhavi & Kagan 2002). Enzymatic treatment has also been proposed as an alternative stage to enhance xanthophylls extraction from marigold flower (Delgado-Vargas. F.& Paredes-López. O. 1997, Navarrete-Bolanos JL.2004). But it too had practical limitations, due to the use of expensive commercial enzyme. It was reported that solid-state fermentation process of marigold flower showed improved yield efficiency (Soboleva 1978). Marigold extracts have been commercialized internationally and are used as additives for poultry feed, as they provide bright colors in egg yolks, skin, and fatty tissues. Marigold extract also finds application in coloring foods like edible oils, mustard and other salad dressings, cakes, ice cream, yogurt, and dairy products. The extract with only the purified form with a lutein content of known concentration and a pure crystalline lutein isolated from marigold flower is allowed for food use. *Tagetes* meal and extract has been listed with a color index of 75125, and it is allowed in chicken feed only to a maximum limit of 1% (Vernon-Carter 1996).

2. Material and methods

2.1 Reagents and equipment

All the reagents used were of A.R. grade or the best quality available and milli-Q water was used throughout in the analysis. A UV-Visible spectrophotometer with 1 cm quartz cell was used for the absorbance measurements and HPLC was used for the separation and analytical measurements.

2.2 Experimental

The method involved in this study was extraction, saponification, separation, identification, and quantification.

2.2.1 Isolation of Oleoresin- Extraction:

The raw sample- marigold flower was provided by Synthite Industrial chemicals Ltd, Kolenchery, Kerala, where the experimental part have been carried out. The experiment was carried out with two set of flowers (A1 & A2) - one stored without preservation and the other with proper preservation technique. For processing, the full-blown marigold flowers having minimum calyx portion are taken and was then laden in a room. It was then compressed and sprayed with lactic bacterial culture, covered with a layer of lime and covered with black tarpaulin. This will induce lactic acid fermentation under anaerobic condition. Under this condition, the material can be stored for 3 to 4 months. By this technique, it was reported that xanthophylls are stabilized and preserved. The water from the raw material was removed and then dried in a drier for 8 to 10 hour under controlled conditions at a temperature lower than 60- 65°C to a moisture level of 8% to 10%. The dried flowers are powdered to a particle size of 0.5 mm and then extracted. Of the solvents, hexane, acetone, ether, isopropyl ether, methylenechloride, 1, 2- dichloroethane, chloroform, hexane- acetone and hexane- acetone-toluene; hexane was found to be the efficient solvent (Verghese.J 1998b) for better yield of xanthophylls. The powdered marigold flowers were then packed in a column and were eluted using analytical grade hexane under mild conditions (30°C, for 15 min). The extract (miscella) so obtained was distilled, under controlled conditions until the desired quantity of the solvent in the oleoresin was achieved. In order to prevent the degradation of xanthophylls, 0.1 to 0.3 % of ethoxyquin was mixed to the final product with stirring at a temperature less than 45°C.

2.2.2 Saponification

Most carotenoids including xanthophyll are stable under alkaline treatments; thus, the use of methanolic solutions of potassium hydroxide is a common method of saponification, which de-esterifies the pigment to free xanthophylls, sometimes at room temperature or by heating. Saponification was accomplished with 40% methanolic KOH by 20 minute treatment at 56°C. Enhanced stability of xanthophylls was obtained when the esters are partially saponified, then

neutralized with weak acid - acetic acid, propionic or lauric acid etc, so that the final product with pH greater than 8 contains about 10 to 20% by weight of unsaponified original xanthophylls esters. Oleoresins initially containing 12.5 % xanthophylls esters saponified to 85% and 100%, after 75 days of storage at 40°C drops down to 5.2% and 33% respectively (Verghese.J 1998b) and this result established the merit of selective, incomplete saponification in conferring the stability. The alkali treated xanthophylls can be either incorporated to poultry feed itself or as the solution of the concentrate in vegetable oil and other oils.

2.2.3 Separation

Separation methods can be classified as non-chromatographic and chromatographic. Non-chromatographic method uses mainly phase partition, by using petroleum ether and aqueous methanol (90%) or ethylene dichloride (EDC) and chromatographic methods adsorbents used are sucrose, silica gel etc. The product obtained after extraction was then washed with EDC. The solvent was removed and dried.

2.2.4 Characterization

The most important technique in xanthophylls (carotenoid) analyses is UV-visible spectroscopy, which gives information about the presence of rings, carbonyl groups, and isomeric effects. In this analysis, absorption maxima, form, and fine structure of spectra are characteristic of the molecule's chromophore. The purity of compounds is obtained with a diode array detector (DAD), which makes the HPLC a versatile technique due to greater sensitivity, resolution, reproducibility, speed of analysis and flexibility to use at inert conditions.

2.3 Analysis of pigment

The oleoresin was analyzed by AOAC method to determine the total xanthophylls concentration and by HPLC-high-performance liquid chromatography (Hellish, 1990) to determine the profiles of the main components (Dietmar 2005). The xanthophyll esters obtained are unstable and are stabilized by saponification, which also resulted in the boosting of xanthophylls content. About 0.05g of oleoresin was transferred into a 100 ml amber colored volumetric flask and added 30 ml extractant (Hexane, 10 ml + Acetone, 7ml+ Absolute alcohol, 6ml + Toluene, 7ml). 2ml, 40% methanolic KOH was added and shaken for a minute. The flask was then kept in a water bath (56°C) for 20 minutes. Cooled and kept in the dark for an hour. Added 30 ml of hexane, shaken for 1 minute and was then diluted with 10% Na₂SO₄ and kept in dark for an hour. The upper phase was 50 ml and with this part absorbance and chromatographic analysis were carried out.

2.3.1 Spectrophotometric method

0.5 ml of the upper phase was transferred into a 50 ml flask and made up to mark with hexane. Absorbance was measured at 474nm using hexane as reference.

Total xanthophylls = $(A_{474} \cdot D) / (W \cdot 236)$; Where

A_{474} = absorbance at 474nm

D = Dilution factor

W = sample weight

236 = specific absorbivity of Trans- lutein (g/L)

2.3.2 Chromatographic separation-HPLC

Aliquots of the *Tagetes* extract obtained from the hexane extraction were isocratically separated using HPLC, over a C18 column in a normal mode. The colored fraction was separated using a mobile phase of a mixture of hexane and ethyl acetate (65:35). About 1 ml of the upper layer was diluted with hexane and 20 µL of it was injected to the column and was eluted at 1.0 ml/ min at room temperature. The pigments were monitored at 447 nm. The components profile was obtained using the relative percentage of HPLC chromatogram area.

3. Results and discussion

Both saponified and unsaponified extracts of marigold were analyzed and from the chromatogram it was observed that in both cases, the main component of oleoresin was Trans-Lutein. Saponification converts Xanthophyll esters to its free form and more peaks are found in the chromatogram of saponified product. Chromatogram peaks were identified by comparison to the retention time of standards and the peaks obtained were analogous to Cryptoxanthin, Cis-Lutein, Trans-Lutein, Trans-Zeaxanthin and some epoxides (Figure: 6, 7).

If the flowers are not properly stored and preserved or else are of poor quality, then assay show a low xanthophyll content. In the first run of the experiment, carried out using an unpreserved flower sample (A1), the yield and xanthophylls content was 4.62% and 54.87 g/Kg respectively. Higher value was observed when the experiment was repeated with well preserved (sample-A2) flowers (Table: 2). Xanthophyll isolation by solvent extraction method in contradictory to the new studies (enzyme based flower preservation, solid state fermentation etc) showed a less efficient

result due to the high temperature involved in isolation step and degradation of the component. The extracted oleoresin was enriched from 105.19 g/Kg Xanthophyll content to 226.88 g/Kg Xanthophyll content, by saponification and subsequent extraction with ethylene dichloride.

Although marigold flower is a cheaper source as a starting material for the isolation of lutein, its storage in seasonal times is very important. From the present work, it was found that, the sample without proper preservation had a diminution in the xanthophylls deduce the implication of preservation technique. A suitable technique for storage enhances the stability of the pigment in the flower and hence an exhaustive study in this area is required. This study involved an anaerobic and lactic acid treatment for the preservation of marigold flowers. Xanthophyll can retain some of the solvent from which they are isolated and purified. The solvents can be easily removed by drying the oleoresin at higher temperature, but in some instances the solvent hardly escapes from it. The traces of toxic organic solvents in the oleoresin makes it unfit for the human consumption as a food colorant. Still another disadvantage of this solvent extraction process is the hazardous organic wastes that face disposal problem.

4. Conclusion

The toxicological effects of the synthetic dyes in the food industry gave way to a renewed interest in the isolation of natural pigments. With the growing legislative restrictions on the use of synthetic colors, a reappraisal of natural plant pigments is taking place with a view to use them as possible colorants in foods. With the application of new innovations, natural pigments can become more cost effective, increase their competitiveness against certified dye, and dye products. According to the Code of Federal Regulations, marigold oleoresin should pursue the prescribed specification and only purified lutein can be used in food applications for human consumption. The antioxidant property of the lutein crafts it application even in making organic tea, which claims great medicinal value. Since large quantities of pesticides are used in the cultivation of marigold flower, the toxic components may be present in the marigold oleoresin. With the more studies of marigold extracts, showing its safety and non-toxicity, marigold flowers can be good source of natural orange colorant in food applications. Advanced biotechnology can improve the novel varieties of marigold having higher Lutein content to elevate Xanthophyll yield. As a food colorant, toxicity determination is valuable and hence the evaluation of solvents used and the study of toxicants in oleoresin are being in the experimental stage. The quantification of some of the toxicants-pesticides and trace metals, in the marigold flower and its oleoresin is also under study to scrutinize the use of marigold oleoresin as a natural food colorant without any impairment.

References

- Attoe, E. L. & von Elbe, J. H. (1985). Oxygen involvement in betanine degradation: effect of antioxidants, *Journal of Food Science.*, 50: 106–110.
- Ausich, RL, Sanders, DJ . (1997). Process for the formation, isolation and purification of comestible xanthophyll crystals from plants. US Patent 5, 648, 564.
- Calnan, C.D. (1976). Quinazoline yellow SS in cosmetics. *Contact Dermatitis*, 2(3), 160- 166.
- Delgado-Vargas, F. and Paredes-Lopez, O. (1997). Effects of enzymatic treatments of marigold flowers on lutein isomeric profiles, *Journal of Agricultural and Food Chemistry*, 45(4): 1097–1102.
- Delgado-Vargas, F, Paredes-Lopez, O, Jimenez, A.R. (2000). Natural Pigments: Carotenoids, Anthocyanins, and Betalains — Characteristics, Biosynthesis, Processing, and Stability. *Critical Reviews in Food Science and Nutrition*, 40(3):173–289.
- Dietmar, E, Breithaupt, Jorg Schlatterer. (2005). Lutein and Zeaxanthin in new dietary supplements — analysis and quantification. *European Food Research and Technology* 220: 648–652.
- Gau, W., Plosche, H. J., Wunsche, C. (1983). Mass spectrometric identification of xanthophyll fatty acid esters from Marigold flowers (*Tagetes Erecta*) obtained by high performance liquid chromatography and counter current distribution. *Journal of Chromatography*, 262: 277–284.
- Gladis Ester Scoles, Silvia Haydee Pattacini, Guillermo Federico Covas. (2000). Separation of the pigment of an Amaranth. *Molecules*, 5: 566,567.
- Gregory, G.K.; Chen, T.S.; Philip, T. (1986). Quantitative analysis of lutein esters in marigold flowers by high performance liquid chromatography. *Journal of Food Science*, 51: 1093–1094.
- Harborne, J. B., Marbry, T. J., And Marbry, H., (1988), *The Flavanoids*. London. Chapman & Hall.
- Helrich, K. (1990). A.O.A.C. Official Methods of Analysis. 15th ed. Arlington, Virginia, 1048–1049.
- Khachik, F . (1995). Process for isolation, purification, and recrystallization of lutein from saponified marigold oleoresin and uses thereof. US Patent 5, 382, 714.

- Levi, LW . (2001). Trans-xanthophyll ester concentrates of enhanced purity and methods of making same. US Patent 6,191, 293.
- Mabry, T.J; Drieiding. A.S. (1968). The Betalaines. In *Recent Advances in Phytochemistry*, (1968).
- Madhavi, DL, Kagan DI . (2002). Process for the isolation of mixed carotenoids from plants. US Patent 6, 380, 442.
- Navarrete-Bolanos, JL, Jimenez-Islas, H, Botello-Alvarez, E, Rico- Martinez, R. (2003). Mixed culture optimization for marigold flower ensilage via experimental design and response surface methodology. *Journal of Agricultural and Food Chemistry*. 51: 2206–2211.
- Navarrete-Bolanos, Jose Luis, Jimenez-Islas Hugo, Botello-Alvarez Enrique, Rico- Martinez Ramiro, Paredes-Lopez, Octavio. (2004). An optimization study of solidstate fermentation: xanthophylls extraction from marigold flowers *Applied Microbiology & Biotechnology*, 65:383–390.
- Paisan, K, Aroonsiri, S, Nontalee, C. (2002). Thermodynamics of adsorption of laccic acid on silk, 53(2): 179–185.
- Pasch, J. H. and von Elbe, J. H.. (1979). Betanine stability in buffered solutions containing organic acids, metal cations, antioxidants, or sequestrants, *Journal of Food Science*, 44: 72–74,81.
- Philip, T . (1997). Purification of lutein-fatty acid esters from plant materials. US Patent 4, 048, 203.
- Savarino, P, Viscardi, G, Quagliotto, P, Montoneri, B.E. (1999). Reactivity and effects of cyclodextrins in textile dyeing. *Dyes and Pigments*, 42(2):143–147.
- Scotter, M.J, Castle, L. (2004). *Food Additives and Contaminants*, 21: 93–124.
- Seddon. (1994). *Journal of American Medical Association*, 272 (18): 1413-1420.
- Soboleva, M. I., Selezneva, G. D., Bondareva, E. S. (1978). Improvement of quality and shelf life of butter creams. *Izvestiya-vyssikh- Uchebyki- zavenii, Pishchevanya Tekhnologiya*. 2: 99–101.
- Sowbhagya. H. B, S. R. Sampathu, Krishnamurthy. (2004). Natural Colorant from Marigold-Chemistry and Technology *Food reviews International*, 20(1): 33–50.
- Strack, D., Steglich, W., Wray, V., (1993). Betalains. In: *Methods in Plant Biochemistry Vol. 8*, Academic Press, Orlando, 421–450.
- Torgils, F, Luis, C, Oyvind, M.A. (1998). Colour and stability of pure anthocyanins influenced by pH including the alkaline region. *Food Chemistry*, 63(4): 435–440.
- Verghese, J. (1998a). Focus on xanthophylls from *Tagetes Erecta* L the giant natural complex-I. *Indian Spices* 33(4): 8–13.
- Verghese, J. (1998b). Focus on xanthophylls from *Tagetes Erecta* L the giant natural color complex-II. *Indian Spices* 34(1&2): 13–16.
- Vernon-Carter, E. J., Gomez, S. A., Beristain, C. I., Mosqueira, G., Pedroza-Islas, R., and Moreno- Terrazas, R. C. (1996). Color degradation and coalescence kinetics of Aztec marigold oleoresin-in-water emulsions stabilized by mesquite or Arabic gums and their blends, *Journal of texture studies*, 27: 625–641.

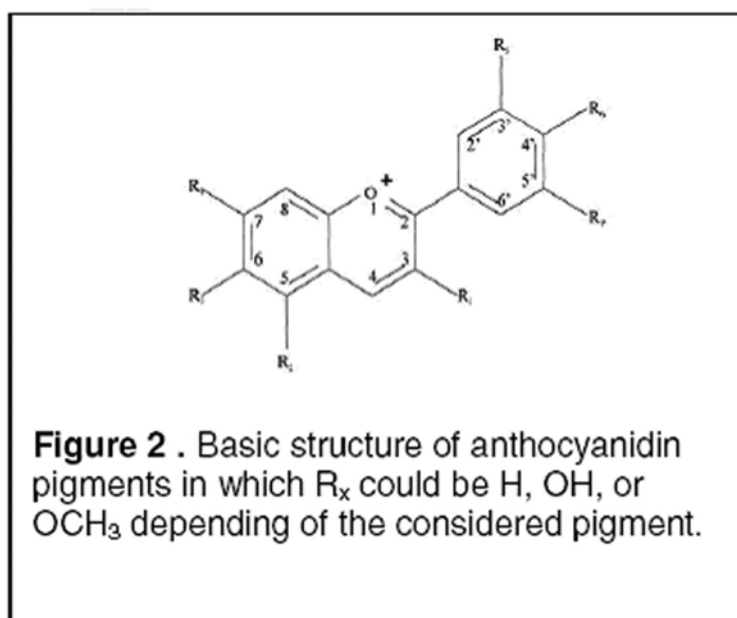
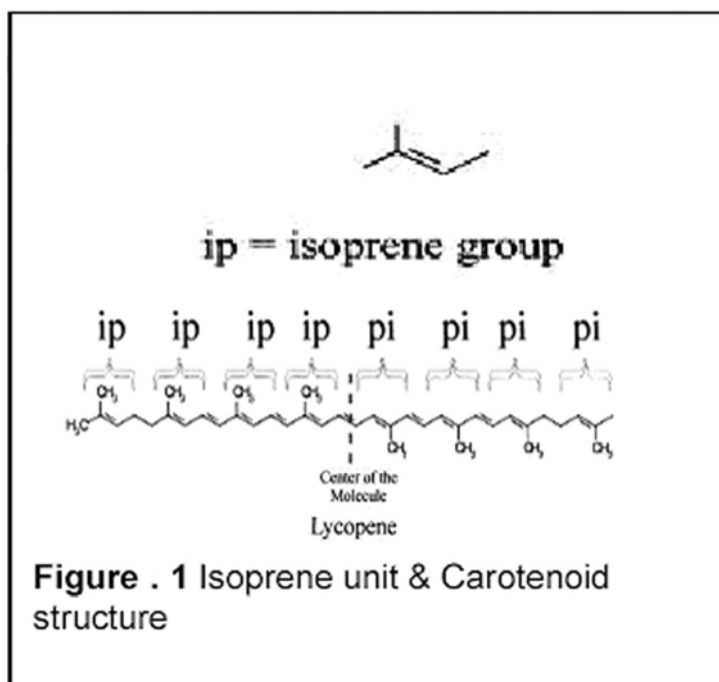
Table 1. Composition of lutein fatty acid esters (%)

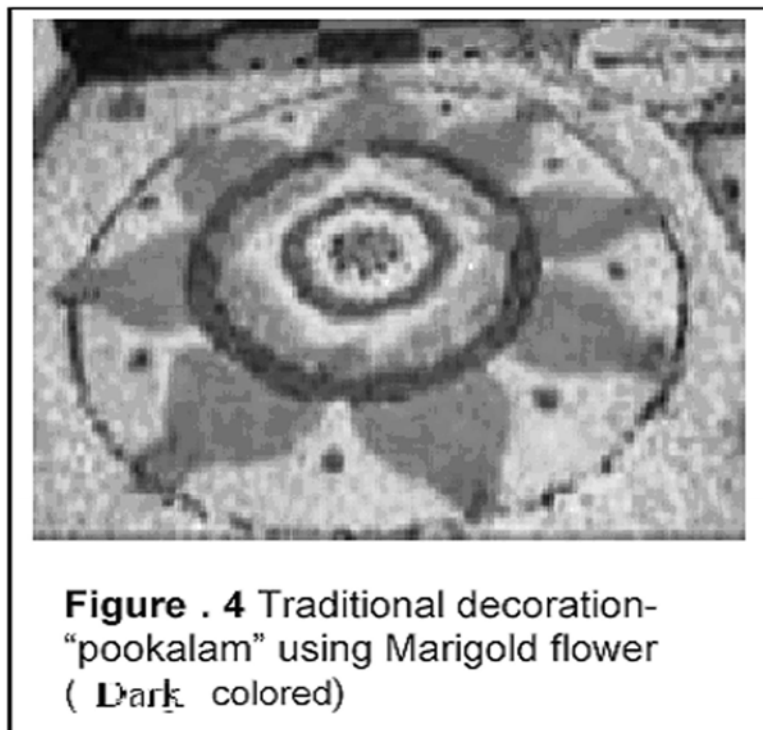
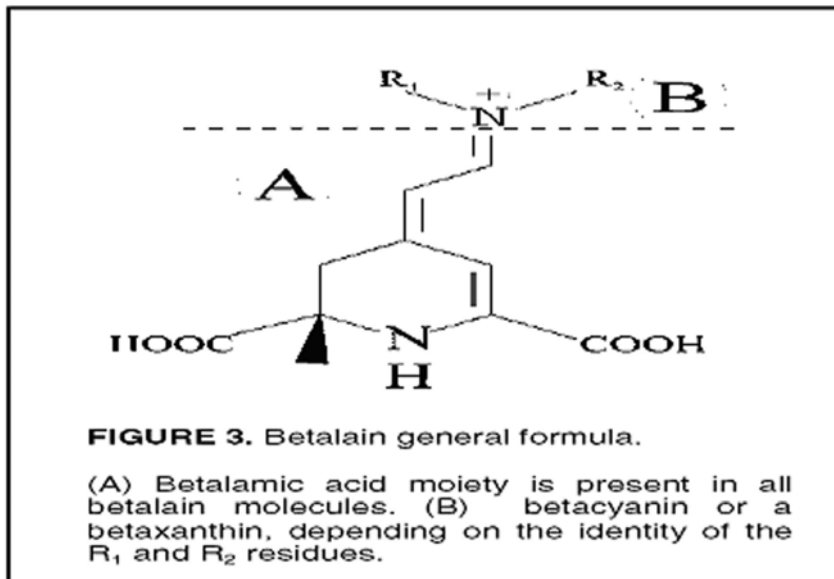
(Ref: Sowbhagya et al. 2004)

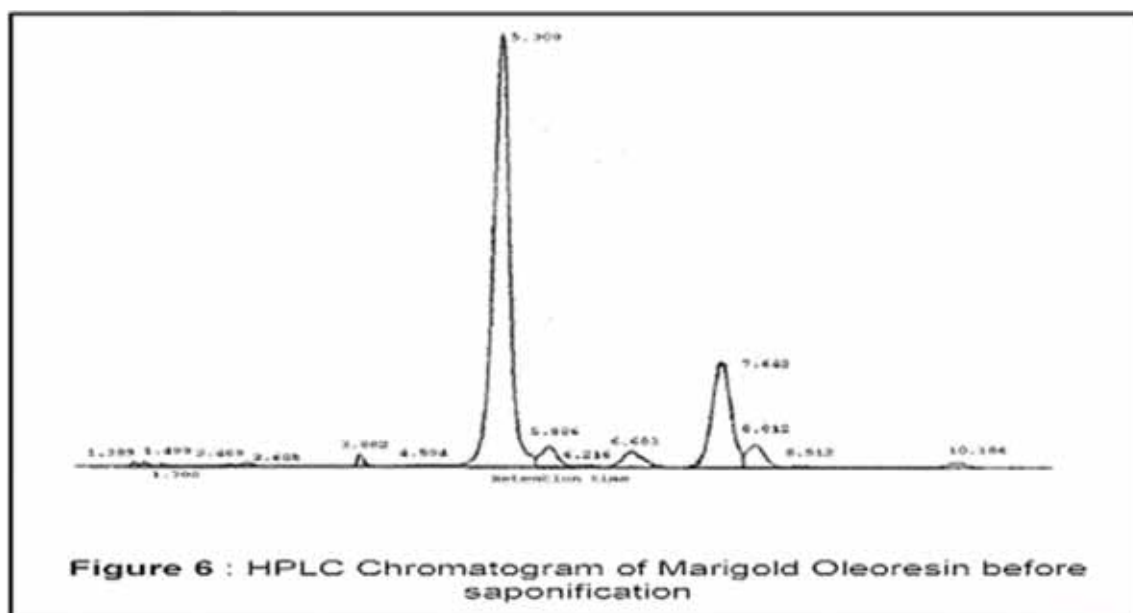
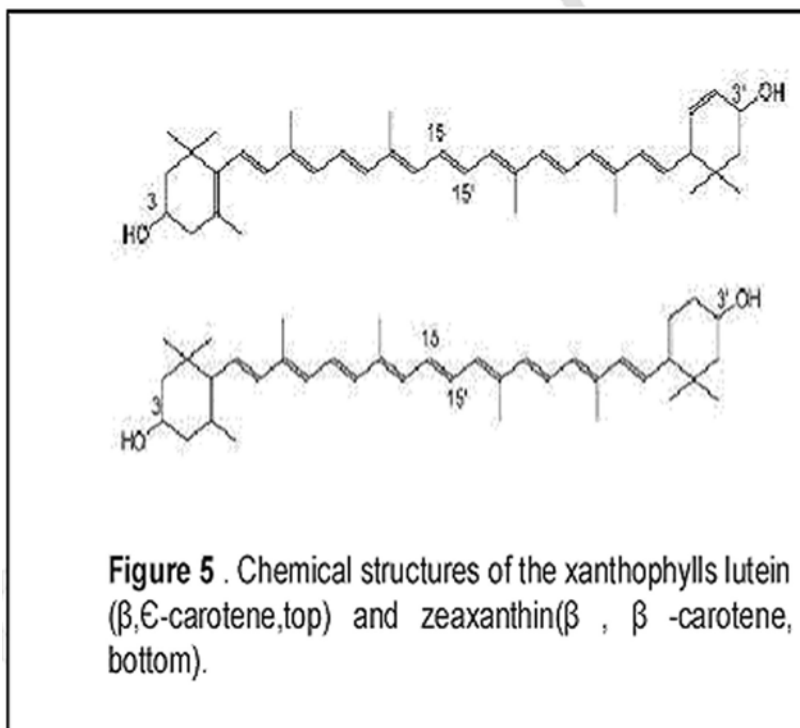
Xanthophyll Type	Gau et al	Helrich et al
Dipalmitate	35.5	37.57
Dimyristate	12.6	11.57
Myristate - palmitate	24.7	24.23
Palmitate-stearate	14.4	15.55
Di-stearate	2.4	3.63

Table 2. Comparative results of sample A1 and A2
(Xt – Xanthophyll content)

Sample	Moisture of flower (%)	Oleoresin Yield (%)	Xt (g/Kg)	T-Lutein in Xanthophyll (%)
A1	10.0	4.62	54.87	36.62
A2	12.1	9.12	105.19	70.28







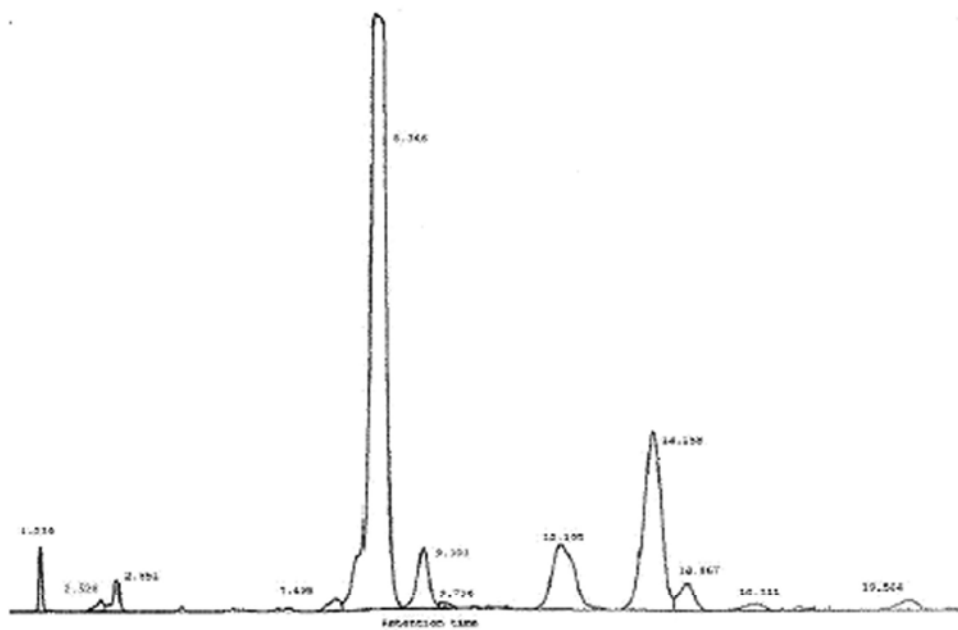


Figure .7 HPLC chromatogram of the saponified marigold oleoresin obtained as final product



Storm Surge Intensity Grade Classification

Liping Wang, Qingqing Liu & Runyu Han

College of Mathematical Science

Ocean University of China

Qingdao 266071, China

Tel: 86-532-8590-1990 E-mail: wlpjsh@163.com

Jianguan Wang

Department of Computer Science

Guangdong Radio & TV University

This work was supported by Natural Science Foundation of China (No. 40776006) and Innovation Program Item in Postgraduate Education (SDYC08008)

Abstract

In order to accurately describe and predict the intensity of the typhoon storm surge, the paper builds up Poisson—Maximum Entropy Compound Extreme Value Distribution model, and estimates the return period of typhoon storm surge on the basis of observed samples from main storm surge processes in a certain observation station of QingDao from 1963 to 1989. The conclusion verified that the calculating result of new model is similar to other models, but it is relatively stable and can overcome the shortcomings of the traditional methods in the situation of lack of observed material.

Keywords: Poisson—Maximum Entropy Compound Extreme Value Distribution, Typhoon Storm Surge, Intensity, Return period

1. Put forward the question

Typhoon Storm Surge refers to the phenomenon of abnormal rise and fall of surface caused by intense weather system such as tropic cyclone, temperate zone cyclone, the strong wind affecting of cold front and the radical change of air pressure. It is also called Strom Surge or Weather Tsunami. Typhoon storm surge is a huge ocean disaster phenomenon. Accompanying with gale and billow, storm surge can make surface hoik in a short time, ruin seawalls, devour docks and factories, flood farms and buildings and destroy vessels, so that materials can't be moved , people and livestock can't survive ,consequently it results in a great disaster. Once storm surge encounters astronomical tide, because of superposing their high tide, the tide will rise sharply, simultaneously as more intense storm surge and high tide superpose, it must result in greater disaster. From March 3, 2007 to wee hours of March 5.2007, affected by the strong cold air in the north and the cyclone in the Yellow Sea, the strong extratropical storm surge occurred in Bohai Bay. The direct economic loss of marine disasters of LiaoNing, HebBei, and ShanDong Province summed to 4,065 billion. There were 4 tide stations where coastal water level uplift exceeded 100 cm, and the highest was 202cm which occurred in Yangjiaogou tide station in Laizhou Bay; The water levels in Yangjiaogou tide station, Longkou tide station and Yantai tide station were over local alert tide, among these, the water level in Yantai tide station was more 49cm than the local alert tide. In Shandong Province, 7 persons were killed, raft-cultures of more than 6700 hectares were damaged, shrimp ponds and fish ponds of more than 2000 hectares were washed away, breakwater of 10 km collapsed, 1900 vessels were destroyed, all in all, the direct economic loss of marine disaster amounted to 2.1 billion.

With the weather warming and sea-level rising, the storm surge disaster has occurred more frequently in coastal regions of China in recent years (see Figure 1). According to the statistics of the State Oceanic Administration, China annual direct economic losses caused by marine disasters such as the storm surge, storm waves, severe sea ice, sea fog and strong wind at sea rose from more than 2 billion to more than 8 billion, and about 500 people were killed. Of all

economic losses, storm surge nearby the coast damaged most severely. Storm surge disaster has become the greatest marine disaster in China.

To further improve the moisture-resistance and disaster reduction of the marine, and reduce the losses caused by disasters, it is necessary to accurately describe the intensity of storm and the size of the disaster and find the way of forecasting, in the hope of helping the authorities deploy the kinds of losses as far as possible. Therefore, the research for the storm surge disaster classification to identify is important and urgent.

At present, the existing classification of the storm surge intensity are the following: 1. Based on the level of the setup of water accompanying with storm surges (Gan, Yuming. 1991.), this standard counts water level uplift of storm surge as the first hazard factor of storm surge. 2. Synthesizing the intensity of water level uplift of the storm surge, we know that storm surge is not an isolated occurrence, which takes effect together with astronomical tide in the coastal areas. Floods, runoff and other factors also play a part in the estuary area. They codetermine the actual water level or water level uplift. This method refers the water level uplift caused by various factors above mentioned as the standard for classification; 3. Based on the highest tide of the storm surge, mainly according to the difference between the local alert tide and forecasting value of the highest tide in the course of typhoon. That is, if the highest tide reaches or surpasses the alert tide, we believe that the storm surge disaster will occur and then release storm surge disaster forecasting; otherwise, we believe no storm surge disaster (Li, Peiwei. 1996.). 4. classifying the intensity of storm surge based on combined tide and waves (Dong, Sheng, Yu, Haijing & Hao, Xiaoli. 2005.) Dongsheng and others promoted compound extreme value with a single variable, considered the occurrence of typhoon, built a compound extreme value distribution model with two-dimensional, and discussed the return period of storm surge according to the water level of storm surge and the significant height of wave; 5. Classifying disaster grade based on the degree of disasters. This method is based on disaster losses such as: the number of death and economic losses, and then establish the disaster grade.

According to the above classification, we find that the methods which calculate the return tide and storm surge of many years are all based on Pearson III model, Gumbel model and so on. But as the numerical model used is apriority, so its own accuracy is not good. On the basis of these models, the early warning to storm surge disaster will be inevitably different from the real situation.

In view of the above, this paper gives a compound extreme value distribution consisting of Poisson distribution and the maximum entropy distribution. Through statistically calculating return period of storm surge based on the samples of maximum wave height in an observation post from 1987 to 1963, and comparing to the results got from other methods, we can see that the result from this paper is similar to others, but more stable under the condition of short observed time. At the same time, this method can solve the problems existing in other methods, and because of the nature of maximum entropy function, it can overcome the shortcomings of the other traditional models. Then comparing with the existing materials of marine disasters, this paper puts forward the standard of classifying the intensity grade of the storm surge hazard, and refers it as the criterion of the disaster degree of the future storm surge. This model will be very valuable for the socio-economic risk assessment of storm surge.

2. Theory of Poisson—Maximum Entropy Compound Extreme Value Distribution

Theorem: Let ξ, η be random vectors. Their distribution function are $G(x), Q(x)$ respectively. Let ξ_i be the i -th observed value of ξ and n be a random variable which is independent of ξ, η and nonnegative integer. The distribution function of n is

$$P\{n = k\} = p_k, \quad k = 0, 1, \dots, \quad \sum p_k = 1. \quad (1)$$

Define random vector ζ

$$\zeta = \begin{cases} \eta, & \text{when } n = 0, \\ \text{Max}\{\xi_i\}, & \text{when } n \geq 1, \end{cases} \quad (2)$$

And then the distribution function of ζ is

$$F(x) = \sum_{k=0}^{\infty} p_k [G(x)]^k - p_0 [1 - Q(x)] \quad (3)$$

The proof is as follows:

$$\begin{aligned}
 F(x) &= P\{\zeta < x\} = P\{\zeta < x, n = 0\} + \sum_{k=1}^{\infty} P\{\zeta < x, n = k\} \\
 &= P\{\zeta < x |_{n=0}\}P\{n = 0\} + \sum_{k=1}^{\infty} P\{\zeta < x |_{n=k}\}P\{n = k\} \\
 &= P\{\eta < x\}p_0 + \sum_{k=1}^{\infty} P\{\text{Max}_{1 \leq i \leq n} \{\zeta_i\} < x\}p_k \\
 &= p_0Q(x) + \sum_{k=1}^{\infty} p_k[G(x)]^k \\
 &= \sum_{k=0}^{\infty} p_k[G(x)]^k + p_0[1 - Q(x)]
 \end{aligned}$$

Therefore theorem is proved.

Let

$$F_0(x) = \sum_{k=0}^{\infty} p_k[G(x)]^k \tag{4}$$

Then we can see $F_0(x)$ is not only compound extreme distribution consisted of the distribution n and the distribution of ζ mentioned above, but also decided entirely by ζ and η .

In actual application, the primary problem is solving Equation (5) when $R(0 < R < 1)$ is given

$$F(x) = R \tag{5}$$

Let $P = 1 - R$ (P is design frequency)

$$T = \frac{1}{P} = \frac{1}{1 - R} \tag{6}$$

(T is called return period). If x_R agrees with equation(5), (that is $F(x_R) = R$), then x_R is the return value of T years.

If n agrees with Poisson distribution

$$p_k = \frac{\lambda^k}{k!} e^{-\lambda}, \quad k = 0, 1, \dots, \quad T = \frac{1}{P} = \frac{1}{1 - R}$$

Then

$$F_0(x) = e^{-\lambda[1 - G(x)]} \tag{7}$$

$$G(x) = 1 + \frac{1}{\lambda} \ln R \tag{8}$$

In formula (8) $G(x)$ can be any type of univariate continuous distribution.

3. Application

First of all, we compare the results of Gumbel distribution and the maximum entropy distribution fitting extremum wave height with the histogram respectively (Figure 2). We can see from the comparison, that the difference between Gumbel distribution and the histogram is larger when the extremum wave height is greater, while the maximum entropy distribution is better no matter when the extremum wave height is greater or smaller. Obviously, the maximum entropy is more applicable.

In the past, the calculation of return period was based on distribution function such as Pearson III, Gumbel distribution function. So it inevitably was apriori and also had some subjective factors as a result of a variety of other reasons. In this paper, the maximum entropy function manages to avoid the problems above. The maximum entropy theory is following:

Theory of maximum entropy: Let X is continuous random variable. $H(X)$ (natural unit) is the information entropy of X and is defined as

$$H(X) = - \int_{-\infty}^{+\infty} f(x) \ln f(x) dx$$

In this formula, $f(x)$ is the probability density function of X . From information theory, we know $H(X)$ is the disordered measure of X , that is people measure X with ignorance. Accordingly, Jaynes put forward the theory of maximum entropy. In 1975, Ulry and Thomas applied the maximum entropy theory to the spectroscopy analysis of wave, and in his article he narrated: we use a designed probability density function to describe the given information, but to maintain the

greatest ignorance for the unknown information. Consequently this function must possess the maximum entropy.

When $G(x)$ is the distribution function of the maximum entropy, formula (8) becomes

$$\int_0^x f(t)dt = 1 + \frac{1}{\lambda} \ln R \tag{9}$$

In formula (9)

$$f(x) = \begin{cases} \alpha x^\gamma e^{-\beta x^\xi}, & x \geq 0 \\ 0, & x < 0 \end{cases} \tag{10}$$

Then:

$$\int_0^x \alpha t^\gamma e^{-\beta t^\xi} dt = 1 + \frac{1}{\lambda} \ln R \tag{11}$$

In formula (11), α , β , γ , ξ can be got from the following equations:

$$\left. \begin{aligned} \frac{\Gamma^2(\frac{\gamma+2}{\xi})}{\Gamma(\frac{\gamma+1}{\xi})\Gamma(\frac{\gamma+3}{\xi})} &= \frac{A_1^2}{A_2} \\ \frac{\Gamma(\frac{\gamma+2}{\xi})\Gamma(\frac{\gamma+4}{\xi})}{\Gamma^2(\frac{\gamma+3}{\xi})} &= \frac{A_1 A_3}{A_2^2} \\ \beta &= \left(\frac{\Gamma(\frac{\gamma+2}{\xi})}{\Gamma(\frac{\gamma+1}{\xi})} / [A_1 \Gamma(\frac{\gamma+1}{\xi})] \right)^\xi \\ \alpha &= \frac{\xi \beta^{\frac{\gamma+1}{\xi}}}{\Gamma(\frac{\gamma+1}{\xi})} \end{aligned} \right\} \tag{12}$$

A_m can be estimated from the following formula, in the actual applicaton.

$$\tilde{A}_m = \frac{1}{n} \sum_{i=1}^n x_i^m \quad m = 1, 2, \dots, n \tag{13}$$

Under the condition of the storm surge disaster occurred, this paper sums up the past researches on return period and early-warning method of storm surge, then gives a series of $R(0 < R < 1)$ value .we can get x_R from formula(6) and formula(11). x_R is the return value of T years.

In the formula (11), λ is the annual average of the times of typhoon affecting this sea region, that is,

$$\lambda = \frac{\text{the total times of typhoon affecting sea region}}{\text{the total years}} = \frac{82}{26} = 3.1538$$

Formula(11) has four parameters α , β , γ , μ , and from formula (12)and formula(13),we can see these parameters only relate to the original state ,so this method can fit the observed samples more acutely and perfectly. In addition, this function has simple form and has parameters which can be calculated from the observed samples easily, thereby it is more applicable.

In order to test the quality of Possion-the maximum entropy compound extreme value distribution, we take the course of the typhoon hazard occurring in Qingdao since 1963 for example. We use a designed return period to calculate the extreme wave height of storm surge and compare with Possion-Gumbel compound extreme value distribution (Table 1). The table shows that, when the samples observed is less, the results of Possion-maximum entropy compound extreme value distribution model are still very stable.

For 26 years' (1963~1989) samples of main extremum wave height in a observation station of QingDao ,we give the grade classification (Table 2) of storm surge disasters intensity, according to the formula (11) that is the size of the return period of extremum wave height of Poisson-maximum entropy compound extreme value model.

We have selected the samples from some storm surge disasters in QingDao to calculate the return period and the results are in Table 3.From the following table, we can see that the calculation of the intensity grade of the storm surge is basically consistent with the actual situation. It should be noted that due to other factors, the calculation of typhoon No. 9216 has great difference with the actual situation (the result is serious disaster while the actual situation is very serious disaster and is the return situation of a hundred years).

4. Conclusion

This paper builds up a model of Poisson-maximum entropy compound extreme value distribution and then applies it to the classification of typhoon surge intensity. From the above argument, we can see:

(1) The model of Poisson-maximum entropy compound extreme value distribution is based on the theory of maximum entropy and the concrete form of maximum entropy probability function entirely determined by parameters not artificial factors, so this model can overcome the shortcomings of other traditional methods and more accurately reflect the relation between extremum wave height and disasters.

(2) This paper statically analyses the extremum wave height in the course of main storm surge in QingDao area since 1963. From the example, despite the short observed time, the result is still stable. So this model is more applicable in coastland where samples are relatively shorter than other areas.

(3) In order to further improve the assessment model and the accuracy of assessing disasters. It is necessary to deeply and quantitatively analyse and research the relation between disaster and other random factors affecting disasters such as the regional economic situation, the conditions of disaster prevention and disaster resist, and the land feature and landform of disaster areas.

References

Dong, Sheng, Yu, Haijing & Hao, Xiaoli. (2005). Typhoon surge intensity grade classification based on combination of wave height and tide level. *Periodical of Ocean University of China*. 2005. Vol. 35, No.1, 152-156.

Gan, Yuming. (1991). The identity and judgment of storm surge. In Disaster preventing association of China(Eds). *Exploring the disaster reduction and development of the coastland*. Earthquake Press. pp. 322-327.

Li, Peiwei. (1996). Exploring the forecast of storm surge in QingDao area. *Marine Forecasts*. 1996. Vol. 13, No. 1, 53-57.

State Oceanic Administration. Oceanic disaster communiqué of China in 2007. [Online] Available: <http://www.soa.gov.cn/hyjww/index.htm>.

Zhang, Lizhen & Xu, Delun. A new maximum entropy probability function about nonlinear displacement of sea wave surface.

Table 1.

Calculation	Time of material (start-stop time)	Number of material	Extreme value wave height(m)				
			10	30	50	100	200
Poisson-Gumbel	1963~1989	82	3.38	4.53	5.05	5.75	6.44
Poisson-maximum entropy	1963~1989	82	3.29	4.45	4.97	5.67	6.34
	1963~1976	47	3.52	4.67	5.18	5.88	6.58
	1976~1989	35	3.22	4.37	4.89	5.59	6.28

Table 2. storm surge intensity grade

Grade	1	2	3	4
Disaster intensity	weak	a little strong	strong	very strong
Return period(year)	0~10	10~30	30~50	50~200

Table 3. the disaster situation of storm surge in QingDao area

Typhoon number	Significant wave height	Return period	Calculating storm surge intensity
8509	5.5	80	Very strong
9005	1.8	10	weak
9216	5.0	50	strong*
9414	2.2	10	weak
9415	4.4	30	A little strong

Figure 1 Times of the storm surge disaster occurring in China for 26 years (1989-2006)

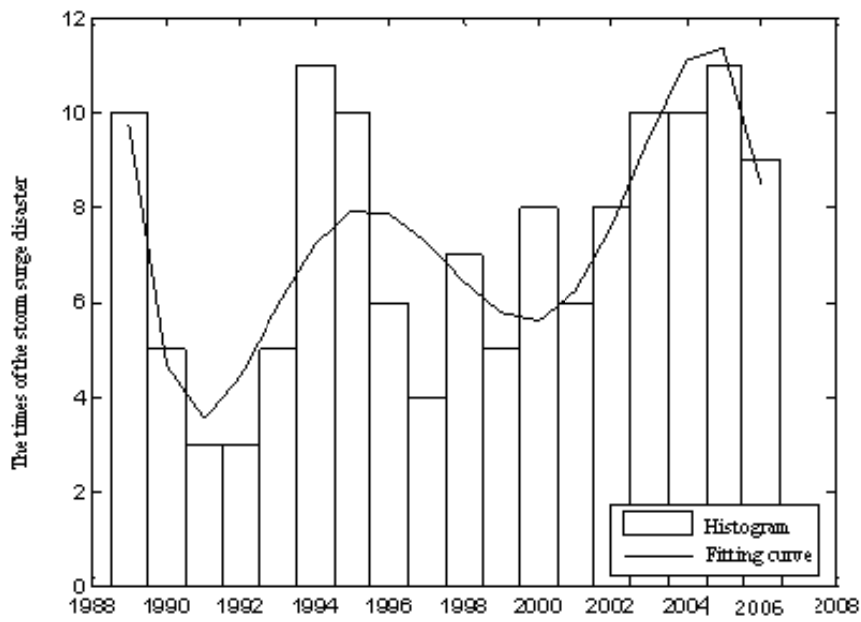
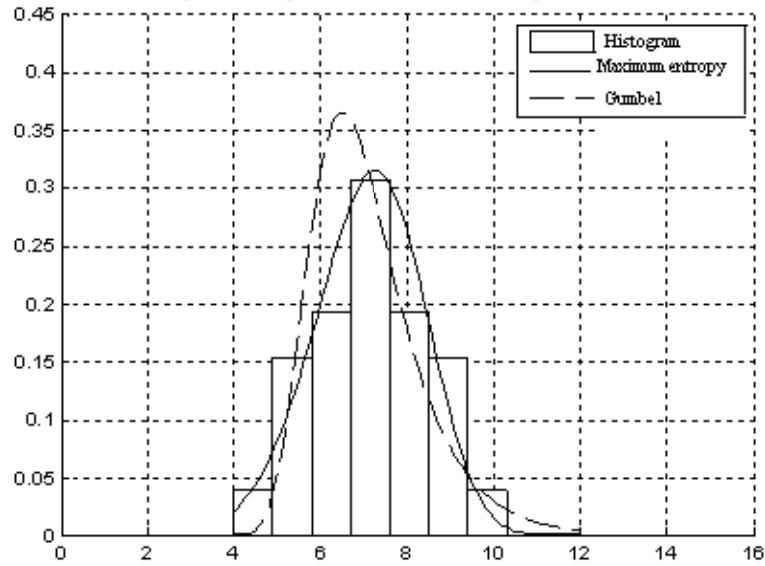


Figure 2 Histogram of extremum wave height distribution





The Investigation of Active Sites on Nickel Oxide Based Catalysts towards the *In-situ* Reactions of Methanation and Desulfurization

Wan Azelee Wan Abu Bakar, Mohd. Yusuf Othman, Rusmidah Ali

Ching Kuan Yong & Susilawati Toemen

Department of Chemistry, Faculty of Science

Universiti Teknologi Malaysia

81310 UTM Skudai, Johor, Malaysia

Tel: 60-13-746-6213 E-mail: wanazelee@yahoo.com

The research is financed by Universiti Teknologi Malaysia and Ministry of Science, Technology and Innovation, Malaysia through IRPA Vot 79252

Abstract

Supported nickel oxide based catalysts of Fe/ Co/ Ni (10: 30: 60)-Al₂O₃ and Pr/ Co/ Ni (5: 35: 60)-Al₂O₃ that were prepared by wetness impregnation method showed potential catalysts for the in-situ reactions of H₂S desulfurization and CO₂ methanation from ambient temperature up to 300 °C. X-ray Photoelectron Spectroscopy revealed Ni₂O₃ and Fe₃O₄ as the surface active components on the Fe/ Co/ Ni (10: 30: 60)-Al₂O₃ catalyst, while Ni₂O₃ and Co₃O₄ on the Pr/ Co/ Ni (5: 35: 60)-Al₂O₃ catalyst. Energy Dispersive X-ray analysis indicated the presence of 2.7 % and 0.9 % of sulfur on the spent Fe/ Co/ Ni (10: 30: 60)-Al₂O₃ and Pr/ Co/ Ni (5: 35: 60)-Al₂O₃ catalysts, respectively. N₂ adsorption-desorption analysis showed reduction of 5.5 % on the surface area of the spent Fe/ Co/ Ni (10: 30: 60)-Al₂O₃ catalyst. However, the surface area of the spent Pr/ Co/ Ni (5: 35: 60)-Al₂O₃ catalyst increased by 8.6 %.

Keywords: Active site, Methanation, Desulfurization, Nickel oxide, Catalyst

1. Introduction

Sour crude natural gas is usually contaminated by the presence of carbon dioxide (CO₂) and hydrogen sulfide (H₂S). Catalysts for the CO₂ methanation have been extensively studied because of their application in the conversion of CO₂ gas in the presence of hydrogen to produce methane, which is the major component in natural gas. However, in real natural gas, there is also presence of H₂S which in the invention of methanation catalyst, its presence should be considered, since it could cause poisoning of the nickel catalyst.

The essential requirement for the correct selection of the oxide system is its ability to accept and to activate CO₂ and H₂S. The acidic nature of CO₂ and H₂S necessitates the employment of a catalytic system with Lewis basic properties such as Group VIII metals. According to Miao et al. (1997), the activity and selectivity of the catalysts are most probably related to the changeable valence of M⁰/ M²⁺. The major reasons for the much slower development of the catalysts science of mixed metal oxide is its significantly complexity compared with metal based catalysts e.g. possible presence of multiple oxidation states, variable local coordination, coexisting bulk and surface phases as well as different surface termination functionalities such as M-OH, M=O or M-O-M [Wachs et al., 2005].

According to Inui et al. (1979), the CO₂ methanation activity of the nickel based composite catalyst from the substrates of iron group metals following this order: Ni > Co > Fe. Nickel based catalysts are generally considered as reference methanation catalysts and proven to eliminate H₂S by desulfurization process. Song et al. (1998), who studied on the amorphous Ni-Zr alloys for methanation activity, detected Ni₂O₃ as the major Ni-containing species on the oxidized Ni₃₆Zr₆₄ surface at 250 °C. Wojcieszak et al. (2004), who worked on the mesoporous molecular sieves supported nickel catalyst for the hydrogenation of benzene, also found out the dominant nickel form on the surface of Ni impregnated AIMCM-41 catalyst was Ni₂O₃. El-Shobaky et al. (2003) observed a significant increment in the catalytic activity of NiO/ MgO system due to treatment with small amount of CoO. Souma et al. (1995) investigated that methanation seems to be accelerated by the absorption of H₂ on metallic Ni or Co. Methane formation from carbon was easier on Co (001) than on Fe (110).

In addition, it had been found by Curtis et al. (1999) that sulfur at levels above 2000 ppm would bring about poisoning effect for the supported cobalt Fischer-Tropsch catalyst. Medina et al. (2000) concluded that carbon dioxide hydrogenation on Fe has the advantage of no catalyst deactivation. Based on the mechanism of the Fischer-Tropsch synthesis involving unreduced iron catalyst [Blanchard et al., 1982], it is attractive to consider the oxidized state of iron

as the active phase in Fischer-Tropsch synthesis. It is of interest to note that the partially pre-reduced catalyst containing Fe_3O_4 as a major phase was more active than the catalyst pre-reduced to $\alpha\text{-Fe}^{2+}$. Previous research showed that Pr_6O_{11} is the most active oxide among rare earth metals because praseodymium possesses stable multiple oxidation state [Wang et al., 2002]. The addition of increasing amounts of Pr_6O_{11} caused the conversion rate of side product to decrease with an apparent minimum.

The objective of this research is to assign the active sites of the nickel oxide based catalysts. The nickel oxide based catalysts should be capable to achieve both low temperature and high conversion of sour gases to be applicable in gas industry. At low temperature, application of the novel catalyst in gas industry is more likely. It is a challenge to propose the active sites for in-situ reactions of methanation and desulfurization to facilitate future studies.

2. Materials and Methods

2.1 Preparation of Catalysts

$\text{Ni}(\text{NO}_3)_2 \cdot 6\text{H}_2\text{O}$ produced by GCE Laboratory Chemicals was dissolved with minimum amount of distilled water. Mixed catalysts solution was prepared by mixing appropriate amount of metal nitrate salts. Wet impregnation method was used to prepare Al_2O_3 supported catalyst by impregnating the catalyst solution on Al_2O_3 beads (MERCK Eurolab) support for 15 minutes. It was then dried at 80°C for 24 hours and calcined in air at 400°C for 5 hours.

2.2 Characterization of catalysts

XPS analysis was done by using Kratos instrument XSAM HS surface analysis spectrometer with Mg $K\alpha$ X-ray source (1253.6 eV). Sample was introduced into the spectrometer in flowing argon atmosphere, and evaporated at least 6×10^9 Torr before spectrum was recorded. The spectrum was taken at 10 mA and 14 kV energy source at 2 sweeps. For EDX analysis, sample was scanned using Zeiss Supra 35 VP FESEM operating of 15 kV couple with EDX analyzer. The catalyst sample was bombarded by electron gun with tungsten filament under 25 kV resolution. N_2 adsorption-desorption isotherms for the catalysts were measured by Micromeritics ASAP 2010. All samples were evacuated at 120°C prior to the measurement.

3. Results and Discussion

3.1 Characterization of Catalysts

3.1.1 X-ray Photoelectron Spectroscopy (XPS)

XPS is a unique surface sensitive technique for chemical analysis. Figure 1 shows the XPS spectra resulted from wide scan in the region of 0-1100 eV, while Figure 2 reveals high resolution XPS spectra obtained over fresh and spent Pr/Co/Ni (5: 35: 60)- Al_2O_3 catalysts. Table 1 depicts the parameters obtained by deconvolution of XPS spectra for these two catalysts.

1.57 % of Ni was detected in the surface composition of fresh Pr/Co/Ni (5: 35: 60)- Al_2O_3 catalyst. The binding energies of Ni ($2p$) were characteristic of NiO at the E_b of 854.21 eV ($2p_{3/2}$) and 871.72 eV ($2p_{1/2}$), similar assignment of NiO to the data obtained made by Lorenz et al. (1979) who studied XPS on NiO/ SiO_2 and NiO- Al_2O_3 / SiO_2 catalysts; and Nefedov et al. (1975) who investigated on some coordination compounds. E_b value of 529.41 eV resulted from the deconvolution of O ($1s$) also confirmed the existence of NiO. However, the existence of Ni ($2p$) peak at E_b of 856.83 eV ($2p_{3/2}$) and 874.30 eV ($2p_{1/2}$) is attributed to the existence of Ni^{3+} in Ni_2O_3 . According to Nascente who worked on Ni/ Pd thin metallic film, E_b of 856 eV was corresponding to Ni_2O_3 . Alumina supported nickel oxide calcined at 350°C also revealed the characteristic peak corresponding to Ni^{3+} at $E_b = 856.9$ eV [Salagre et al., 1996]. The most intense peak at E_b of 531.52 eV resulted from deconvolution of O ($1s$) over the fresh catalyst also referred to the existence of Ni_2O_3 and Al_2O_3 . Ni^{3+} showing a higher binding energy because the E_b of the metal increases when the covalency decreases [Vederine et al., 1978]. In other words, as the ionic radius of $\text{Ni}^{2+} > \text{Ni}^{3+}$ and furthermore the covalency of Ni^{3+} decreases compare to Ni^{2+} . Ni^{3+} is known to be more reactive than Ni^{2+} due to its higher metallic property. Ni_2O_3 is suggested to be responsible as active site for this catalyst. By observing $2p_{3/2}$ peak area, the existence of NiO was observed as 31 % more than Ni_2O_3 . When NiO was more dominant on the fresh Pr/Co/Ni (5: 35: 60)- Al_2O_3 catalyst, low catalytic activity was observed. It is presumed that the lower H_2S desulfurization activity over Pr/Co/Ni (5: 35: 60)- Al_2O_3 catalyst at reaction temperature below 200°C was due to lack of Ni_2O_3 , which is an oxygen rich compound. Ni_2O_3 structure is believed to play an important role in the nickel cation reduction and the oxygen release process [Yoon et al., 2006]. This suggestion is further supported when the dominant nickel form on the surface of Ni impregnated AlMCM-41 catalyst was found out to be Ni_2O_3 [Wojcieszak et al., 2004]. This oxidized phase served as a matrix which decreased the Ni atoms agglomeration.

After exposure towards the catalytic testing environment, the surface composition of Ni^{3+} was increased to 2.28 %. The existing peaks were attributed to Ni^{3+} in Ni_2O_3 species at the E_b value of 856.80 eV ($2p_{3/2}$) and 874.32 eV ($2p_{1/2}$). NiO was disappeared in the spent catalyst. This was also supported by 59 % reduction of peak area on the O ($1s$) peak at 529.73 eV. It is believed that NiO was transformed into Ni_2O_3 during prolong catalytic testing process. Similar

phenomenon was also reported by Djaidja et al., (2000) where NiO phase was disappeared in their used Ni/ Sm₂O₃ and Ni/ La₂O₃ catalysts. They suggested that Ni₂O₃ phase is necessary in the oxidative transformation of methane reaction course. Dong et al., (1998) had also observed the growth of Ni₂O₃ layers on the surface of Ni particles after exposure in a mixture of H₂ and Ar gas atmosphere of 760 Torr. No NiO phase was detected by them. The absence of NiO is presumably responsible for the increasing of the catalytic performance over this catalyst at maximum study temperature of 300 °C.

There was 0.49 % of Co revealed in the surface composition of fresh Pr/ Co/ Ni (5: 35: 60)-Al₂O₃ catalyst. Binding energies of 779.79 eV (*2p*_{3/2}) and 793.96 eV (*2p*_{1/2}) suggesting the presence of spinel compound, Co₃O₄, on the surface of the catalyst. This is in good agreement with Kim (1975) who studied the electronic structure of cobalt oxides and Zeng et al. (1995) who worked on the effect of ZrO₂ matrix on surface Co₃O₄-CO position. The presence of Co₃O₄ is supported by the O (1s) peak at *E*_b value of 529.41 eV, which was also suggested by Natile and Glisenti (2003) who studied on NiO/ Co₃O₄ nanocomposite catalyst. NO₂ formed during the decomposition of Co(NO₃)₂•6H₂O during preparation could oxidize Co²⁺ to Co³⁺ even at low calcination temperature. Once oxidized, the Co ions have a high tendency to form Co₃O₄ [Arnoldy and Moulijn et al., 1985]. The existence of the spinel compound in the catalyst is presumed to be good for the catalytic efficiency as it provides more active sites for the reaction and also it could be easily changed forms according to the environment; whether it is more to Co²⁺ or Co³⁺. After catalytic testing, the Co (*2p*) peaks shifted to a higher *E*_b of 781.70 eV (*2p*_{3/2}) and 796.11 eV (*2p*_{1/2}), but indicating no changes of Co oxidation state on the surface of the catalyst. The O (1s) peak remained in the same region, at *E*_b of 529.73 eV, with 59 % reduction of peak area. This peak is attributed to the existence of Co₃O₄ only. This reduction on peak area was due to the disappearance of NiO. 0.48 % of Co was still observed on the spent catalyst surface. In this stage, an optimum amount of Co spinel compound is presumed to be the reason for the increasing of the catalytic activity [Zhang et al., 2002].

There are two Al (*2p*) peaks obtained from the fresh Pr/ Co/ Ni (5: 35: 60)-Al₂O₃ catalyst, indicating the existence of Al in two different environments. At *E*_b value of 74.70 eV, it is attributed to Al₂O₃. The O (1s) peak at 531.52 eV also referred to the existence of Al₂O₃. When Al atom is on the outermost surface, the influence of the surrounding chemical environment on Al *2p* spectrum is significant. On the outer surface, alumina is in contact with atmosphere and absorbed water. Therefore, the surrounding chemical environment of alumina on the outer surface is different from that in inner layer [Zheng et al., 2008]. This contributed to the formation of Al³⁺-OH which was shown at *E*_b of 76.63 eV. As the binding energy increases, so does the ionic character of the bonding. Wojcieszak et al. (2004) also observed similar XPS result from their AIMCM-41 support. Al₂O₃ (*E*_b 75 eV) was assigned to framework aluminium species and to extra framework Al³⁺ (*E*_b 77.5 eV). The extra framework Al³⁺ species is easily affected by the surrounding environment. Adsorbed water on the catalyst surface or Al³⁺ with the surface hydroxyl was observed at the O (1s) *E*_b value of 533.19 eV. However, only one peak was detected at *E*_b value of 74.11 eV on the spent catalyst. It is attributed to the existence of Al₂O₃. The detected weight percentage of Al also decreased in the spent catalyst compared to the fresh catalyst; in agreement with the only peak existed in the spent catalyst. After exposure to the catalytic testing environment, the increment of O (1s) peak area at 533.62 eV is due to the adsorbed water on the surface, one of the products from methanation reaction.

From the surface composition detected by XPS, 0.09 % of Pr was revealed on the surface of fresh Pr/ Co/ Ni (5: 35: 60)-Al₂O₃ catalyst. After catalytic activity measurement, the percentage of Pr was reduced to 0.02 %. This reduction would be either due to the deposition of sulfur, or agglomeration of other elements that forced the Pr element to move into the bulk of the catalyst.

Figure 3 depicts XPS spectra resulted from wide scan in the region of 0 - 1100 eV and the high resolution XPS spectra over fresh Fe/ Co/ Ni (10: 30: 60)-Al₂O₃ catalyst is shown in Figure 4. The atomic concentration of Ni detectable by XPS was low (0.93%), indicating the partial surface encapsulation of Ni in the alumina support [Salagre et al., 1996]. The Ni (*2p*_{3/2}) and Ni (*2p*_{1/2}) peaks at *E*_b = 856.67 eV and 874.37 eV are registered in the XPS spectra of Ni *2p* level of the fresh Fe/ Co/ Ni (10: 30: 60)-Al₂O₃ sample, respectively. This assignment is similarly as been suggested by Nascente (2005) and Salagre (1996). The O (1s) peak at *E*_b = 531.77 eV over fresh Fe/ Co/ Ni (10: 30: 60)-Al₂O₃ catalyst is attributed to the existence of O²⁻ in Ni₂O₃. Ni₂O₃ could act as an active site for oxidation reaction because its oxygen storage property is needed for the H₂S desulfurization reaction. It is known that the presence of Ni³⁺ may enhance the p-type character (oxygen rich) of the catalyst.

0.66 % of Fe was revealed in the surface composition. The oxides of α-Fe₂O₃, γ-Fe₂O₃ and Fe₃O₄ have almost identical core binding energies, but the absence of satellite peak had confirmed that the *E*_b at 711.45 eV (*2p*_{3/2}) and 725.09 eV (*2p*_{1/2}) is due to Fe₃O₄. This is also supported by the appearance of O 1s peak at *E*_b of 530.05 eV. This assignment is in good agreement with McIntyre and Zetaruk (1977), who studied iron oxides with XPS and Yamashita and Hayes (2007), who had analyzed XPS spectra of Fe²⁺ and Fe³⁺ ions in oxide materials. It is believed that spinel compound of Fe₃O₄ is good for the catalytic reaction as it able to provide more active sites. Based on the mechanism of the Fischer-Tropsch

synthesis involving unreduced iron catalyst [Blanchard., 1982], it is attractive to consider the oxidized state of iron as the active phase in Fischer-Tropsch synthesis. It is of interest to note that the partially pre-reduced catalyst containing Fe_3O_4 as a major phase was more active than the catalyst pre-reduced to $\alpha\text{-Fe}^{2+}$. According to Iyer et al. (2006), Fe_3O_4 was also reported as active phase in their enhanced hydrogen production integrated with CO_2 separation.

There are two peaks indicating Al^{3+} in Al_2O_3 ($E_b = 74.11$ eV) and $\text{Al}^{3+}\text{-OH}$ ($E_b = 76.30$ eV) on the fresh Fe/ Co/ Ni (10: 30: 60)- Al_2O_3 catalyst. When Al is on the outermost surface, it is in contact with atmosphere and absorbed water thus resulting in higher E_b .

Merely 0.08 % of cobalt was revealed in the surface composition compared to 0.66 % of iron. Similar condition was also detected by Kozhukharov et al. (2003), where the Co $2p$ partial contribution was not well expressed when there was presence of iron. It is believed that Co ions react with the substrates during the calcination and sintering process. Part of them being high chemical mobility and reactivity are incorporated into the bulk of the support. Furthermore, previous study suggested that the sorption affinity of cations depends not only on the valence of the cations but also on their radius. The ionic radii of Co^{2+} and Co^{3+} are 74 pm and 61 pm while Fe^{2+} and Fe^{3+} are 78 and 65 pm [Weast and Selby, 1966]. The smaller radii of the Co ions could disperse highly into the matrix and penetrate deeper into the support. Therefore, results in lower surface concentration of Co. The synthesis of highly dispersed Co catalysts requires the initial formation of very small CoO or Co_3O_4 crystallites. The formation of these small oxide clusters in turn requires strong interactions between the support and the Co precursor [Iglesia, 1997]. Because the mean free path of electrons in solids is very small, the detected electrons originate from only the top few atomic layers. While ionization occurs to a depth of a few micrometers, only those electrons that originate within tens of angstroms below the solid surface can leave the surface without energy loss [Moulder et al., 1992].

3.1.2 Energy Dispersive X-ray Analysis (EDX)

As shown in Table 2, there was presence of 0.94 % of sulfur on the spent Pr/ Co/ Ni (5: 35: 60)- Al_2O_3 catalyst. Lower percentage of sulfur deposited on the catalyst demonstrated less deactivation effect over this catalyst compared to the Fe/ Co/ Ni (10: 30: 60)- Al_2O_3 catalyst. This also indicates that Pr/ Co/ Ni (5: 35: 60)- Al_2O_3 catalyst is more resistance to sulfur poisoning. Only 0.04 % of Pr was revealed on the fresh Pr/ Co/ Ni (5: 35: 60)- Al_2O_3 catalyst. After catalytic testing, the surface composition of Pr increased to 0.12 %. NiO was known to appear over the fresh catalyst from XPS analysis. At this stage, it is believed that NiO with larger ionic radii accommodated on the surface. Pr and Ni_2O_3 are presumed to be located in the deeper bulk structure. Therefore, the overall surface composition of Pr was revealed in small percentage. On the spent catalyst, depletion of Ni^{2+} to Ni^{3+} pushed the Ni migrated into the bulk structure. Hence, Pr could be revealed in larger surface composition when NiO was transformed into Ni_2O_3 . Although there is deposition of 0.94 % of sulfur, Pr still can be revealed as higher percentage. The catalytic activity over this catalyst is believed to be increased dramatically when NiO had been transformed into Ni_2O_3 .

EDX analysis shows that the composition of Fe on the fresh Fe/ Co/ Ni (10: 30: 60)- Al_2O_3 catalyst is 3.12 %, higher than Co that composed of 2.26 % only (Table 3). Theoretically, the surface composition of Co should be higher than Fe by referring to the loading of metal with ratio of Fe: Co: Ni = 10: 30: 60. This phenomenon was also observed from the XPS analysis. 0.66 % of Fe was revealed while only 0.08 % of Co was detected on the fresh Fe/ Co/ Ni (10: 30: 60)- Al_2O_3 catalyst by XPS. It is believed that Co ions with higher chemical mobility and reactivity were incorporated into the bulk of the support and Fe ions with higher atomic radii were stayed on the surface of the catalyst. Besides that, Co is presumed to be dispersed homogeneously into the bulk matrixes. From EDX analysis over the spent Fe/ Co/ Ni (10: 30: 60)- Al_2O_3 catalyst, 2.13 % reduction on the surface composition of Fe was revealed. It is believed that the deposition of 2.68 % of sulfur suppressed the agglomeration of Fe on the catalyst surface, as such forced Fe to migrate into the bulk matrixes. In addition, the surface composition of Ni and Co also shows reduction of 1.00 % and 0.45 %, respectively. Sulfur is known to poison the catalyst and lead to the deactivation effect. The catalytic activity over this catalyst gradually decreased after maximum conversion of 16 % of CO_2 at 120 °C. Al from the support dominated the surface area. This means that the catalyst was not distributed evenly on the surface or had been absorbed into the pores of the support due to the high surface area and porosity of Al_2O_3 support.

3.1.3 Nitrogen Adsorption Analysis

From Table 4, the surface area of the spent Pr/ Co/ Ni (5: 35: 60)- Al_2O_3 catalyst is 8.6 % higher than the surface area of its fresh catalyst. As such for this catalyst, it can be concluded that the increment of the surface area, did increase the catalytic activity of the Pr/ Co/ Ni (5: 35: 60)- Al_2O_3 catalyst at higher temperature (300 °C). By referring to the XPS analysis, it was known that Co ions with high mobility were incorporated into the bulk of the support when there was presence of Fe ions. For the Pr/ Co/ Ni (5: 35: 60)- Al_2O_3 catalyst, Co ions were detected as spinel compound of Co_3O_4 on the surface. Therefore, Co_3O_4 is presumed to give contribution on the increment of surface area over this catalyst. Besides that, NiO was present in the fresh Pr/ Co/ Ni (5: 35: 60)- Al_2O_3 catalyst but disappeared after catalytic testing. The transformation of NiO into Ni_2O_3 is believed to be able to generate new active sites for the in-situ reactions of methanation and desulfurization. Consequently, the surface area is increased when there is generation of new active

sites. The average pore diameter of Pr/ Co/ Ni (5: 35: 60)-Al₂O₃ catalyst, increases in accordance with the increased in surface area. The enlargement of pore diameter over the spent catalyst is believed to be resulted by from the collapsed of pores during the in-situ reactions of CO₂ methanation and H₂S desulfurization.

However, the BET surface area over the spent Fe/ Co/ Ni (10: 30: 60)-Al₂O₃ catalyst shows 5.5 % reduction. This reduction is believed to be resulted from the deposition of sulfur on the catalyst surface or collapsed of the pores during prolong catalytic reaction. The smaller pore diameter shown by spent catalyst also proved the blockage of the pores by sulfur. Catalytic activity over this catalyst also decreased after reaching maximum 16.5 % conversion of CO₂ at 120 °C. The BET surface area is presumed to be reduced when there is no generation of new active sites. No transformation of active species occurred during the catalytic reaction as reported by XPS analysis.

4. Conclusion

XPS analysis, suggested that Ni₂O₃ and Co₃O₄ are the probable active sites on the Pr/ Co/ Ni (5: 35: 60)-Al₂O₃ catalyst. Meanwhile, Ni₂O₃ and Fe₃O₄ acted as the active phases on the Fe/ Co/ Ni (10: 30: 60)-Al₂O₃ catalyst. However, further investigation is still needed to support the present postulation of the active sites which are responsible to catalyze high CO₂ methanation rate at low temperature in the presence of H₂S, which is a deactivation source.

References

- Arnoldy, P. and Moulijn, J.A. (1985). Temperature-programmed reduction of CoO/ Al₂O₃ catalysts. *Journal of Catalysis*. 93, 38-54.
- Blanchard, F., Reymond, J.P., Pommier, B. and Teichner, S.J. (1982). On the mechanism of the Fischer-Tropsch synthesis involving unreduced iron catalyst. *Journal of Molecular Catalysis*. 17, 171-181.
- Curtis, V., Nicolaides, C.P., Coville, N.J., Hildebrandt, D. and Gilasser, D. (1999). The effect of sulfur on supported cobalt Fischer-Tropsch catalysts. *Catalysis Today*. 49, 33-40.
- Djaidja, A., Barama, A. and Bettahar, M.M. (2000). Oxidative transformation of methane over nickel catalysts supported on rare-earth metal oxides. *Catalysis Today*. 61, 303-307.
- Dong, X.L., Zhang, Z.D., Jin, S.R., Sun, W.M. and Chuang, Y.C. (1998). Surface characterizations of ultrafine Ni particles. *Nano Structured Materials*. 10 (4), 585-592..
- El-Shobaky, G.A., El-Molla, S.A. and Ali, A.M.I. (2003). Catalytic promotion of NiO/MgO system by doping with some transition metal cations. *Applied Catalysis A: General*. 253, 417-425.
- Iglesia, E. (1997). Design, synthesis, and use of cobalt-based Fischer-Tropsch synthesis catalysts. *Applied Catalysis A: General*. 161, 59-78.
- Inui, T., Funabiki, M., Suehiro, M. And Sezume, T. (1979). Methanation of CO₂ and CO on supported nickel-based composite catalysts. *Journal of the Chemical Society, Faraday Transaction*. 75, 787-802.
- Iyer, M., Ramkumar, S. and Fan, L.S. (2006). Enhanced hydrogen production integrated with CO₂ separation in a single type of report. *Annual Technical Progress Report*. United States of America: The Ohio-State University.
- Kim, K.S. (1975). X-ray photoelectron spectroscopic studies of the electronic structure of CoO. *Physical Review B*. 11 (6), 2177-2187.
- Kozhukharov, V., Machkova, M. and Brashkova, N. (2003). Sol-gel route and characterization of supported perovskites for membrane applications. *Journal of Sol-Gel Science and Technology*. 26, 753-757.
- Lorenz, P., Finster, J., Wendt, G., Salyn, J.V., Žumadilov, E.K. and Nefedov, V.I. (1979). ESCA investigations of some NiO/ SiO₂ and NiO-Al₂O₃/ SiO₂ catalysts. *Journal of Electron Spectroscopy and Related Phenomena*. 16, 267-276.
- McIntyre, N.S. and Zetaruk, D.G. (1977). X-ray photoelectron spectroscopic studies of iron oxides. *Analytical Chemistry*. 49 (11), 1521-1529.
- Medina, J.C., Butala, S.J., Bartholomew, C.H. and Lee, M.L. (2000a). Iron-catalyzed CO₂ hydrogenation as a mechanism for coalbed gas formation. *Fuel*. 79, 89-93.
- Miao, Q., Xiong, G., Sheng, S., Cui, W., Xu, L. and Guo, X. (1997). Partial oxidation of methane to syngas over nickel-based catalysts modified by alkali metal oxide and rare earth metal oxide. *Applied Catalysis A: General*. 154, 17-24.
- Moulder, J.F., Stickle, W.F., Sobol, P.E. and Bomben, K.D. (1992). *Handbook of X-ray Photoelectron Spectroscopy*. United States of America: Perkin-Elmer Corporation.
- Nascente, P.A.P. (2005). Materials characterization by X-ray photoelectron spectroscopy. *Journal of Molecular Catalysis A: Chemical*. 228, 145-150.

- Natile, M.M. and Glisenti, A. (2003). New NiO/ Co₃O₄ and Fe₂O₃/ Co₃O₄ nanocomposite catalysts: Synthesis and characterization. *Chemistry of Materials*. 15, 2502-2510.
- Nefedov, V.I., Gati, D., Dzhurinskii, B.F., Sergushin, N.P. and Salyn, Ya.V. (1975). Simple and coordination compounds. *Russian Journal of Inorganic Chemistry*. 20, 2307-2314.
- Salagre, P., Fierro, J.L.G., Medina, F. and Sueiras, J.E. (1996). Characterization of nickel species on several γ -alumina supported nickel samples. *Journal of Molecular Catalysis A: Chemical*. 106, 125-134.
- Song, Z., Bao, X., Wild, U., Muhler, M. and Ertl, G. (1998). Oxidation of amorphous Ni-Zr alloys studied by XPS, UPS, ISS and XRD. *Applied Surface Science*. 134, 31-38.
- Souma, Y., Ando, H., Fujiwara, M. and Kieffer, R. (1995). Catalytic hydrogenation of carbon dioxide to hydrocarbons. *Energy Conversion and Management*. 36 (6-9), 593-596.
- Vederine, J.C., Hollinger, G. and Minh, O.T. (1978). Investigations of Antigorite and Nickel Supported Catalysts by X-ray Photoelectron Spectroscopy. *The Journal of Physical Chemistry*. 82, 1515.
- Wachs, I.E. (2005). Recent conceptual advances in the catalysis science of mixed metal oxide catalytic materials. *Catalysis Today*. 100, 79-94.
- Wang, W.D., Lin, P.Y., Fu, Y.L. and Cao, G.Y. (2002). Redox properties and catalytic behavior of praseodymium-modified (Ce-Zr)O₂ solid solutions in three- way catalysts. *Catalysis Letters*. 82, 19-27.
- Weast, R.C. and Selby, S.M. (Eds.) (1966). *Handbook of Chemistry and Physics*. (47th ed.) Ohio: The Chemical Rubber Co.
- Wojcieszak, R., Monteverdi, S., Mercy, M., Nowak, I., Ziolk, M. and Bettahar, M.M. (2004). Nickel containing MCM-41 and AlMCM-41 mesoporous molecular sieves. Characteristics and activity in the hydrogenation of benzene. *Applied Catalysis A: General*. 268, 241-253.
- Yamashita, T. and Hayes, P. (2007). Analysis of XPS spectra of Fe²⁺ and Fe³⁺ ions in oxide materials. *Applied Surface Science*. doi: 10.1016/j.apsusc.2007.09.063.
- Yoon, W.S., Hanson, J., McBreen, J. and Yang, X.Q. (2006). A study on the newly observed intermediates structures during the thermal decomposition of nickel-based layered cathode materials using time-resolved XRD. *Electrochemistry Communications*. 8, 859-862.
- Zeng, H.C., Lin, J. and Tau, K.L. (1995). Memory effect of ZrO₂ matrix on surface Co₃O₄-CO position. *Journal of Material Research*. 10, 3096-3105.
- Zhang, Y.Q., Jacobs, G., Sparks, D.E., Dry, M.E. and Davis, B.H. (2002). CO and CO₂ hydrogenation study on supported cobalt Fisher-Tropsch synthesis catalysts. *Catalysis Today*. 71, 411-418.
- Zheng, H.Y., An, M.Z. and Lu, J.F. (2008). Surface characterization of the Zn-Al-Al₂O₃ nanocomposite coating fabricated under ultrasound condition. *Applied Surface Science*. 254, 1644-1650.

Table 1. Parameters obtained by deconvolution of XPS spectra for fresh and spent Pr/ Co/ Ni (5: 35: 60)-Al₂O₃ catalysts.

Catalyst	Phase	Ni 2p _{3/2}	Ni 2p _{1/2}	Co 2p _{3/2}	Co 2p _{1/2}	Al 2p	O 1s
Pr/ Co/ Ni (5:35:60)-Al ₂ O ₃ (Fresh)	NiO	854.21	871.72				529.41
	Ni ₂ O ₃	856.83	874.30				531.52
	Co ₃ O ₄			779.79	793.96		529.41
	Al ₂ O ₃					74.70	531.52
	Al ³⁺ -OH					76.63	533.19
	Surface water						533.19
Pr/ Co/ Ni (5:35:60)-Al ₂ O ₃ Spent	Ni ₂ O ₃	856.80	874.32				531.78
	Co ₃ O ₄			781.70	796.11		529.73
	Al ₂ O ₃					74.11	531.78
	Surface water						533.62

Table 2. Comparison of elemental composition over the fresh and spent Pr/ Co/ Ni (5: 35: 60)-Al₂O₃ catalysts through EDX analysis.

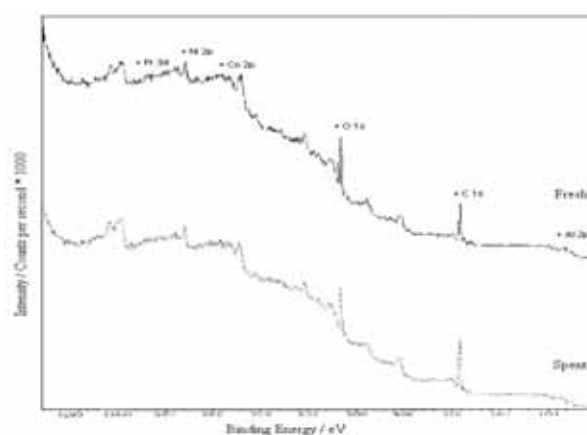
Catalyst	Atomic ratio (%)					
	Pr	Co	Ni	Al	O	S
Pr/ Co/ Ni (5: 35: 60)-Al ₂ O ₃ (Fresh)	0.04	2.34	3.51	30.35	60.08	-
Pr/ Co/ Ni (5: 35: 60)-Al ₂ O ₃ (Spent)	0.12	2.36	3.15	27.31	62.84	0.94

Table 3. Comparison of elemental composition over the fresh and spent Fe/ Co/ Ni (10: 30: 60)-Al₂O₃ catalysts through EDX analysis.

Catalyst	Atomic ratio (%)					
	Fe	Co	Ni	Al	O	S
Fe/ Co/ Ni (10: 30: 60)-Al ₂ O ₃ (Fresh)	3.12	2.26	4.66	25.16	60.77	-
Fe/ Co/ Ni (10: 30: 60)-Al ₂ O ₃ (Spent)	0.99	1.81	3.66	24.74	64.01	2.68

Table 4. BET surface area and BJH desorption average pore diameter of the fresh and spent forms of Fe/ Co/ Ni (10: 30: 60)-Al₂O₃ and Pr/ Co/ Ni (5: 35: 60)-Al₂O₃ catalysts.

Catalyst	Condition	S _{BET} (m ² g ⁻¹)	d (nm)
Fe/ Co/ Ni (10: 30: 60)-Al ₂ O ₃	Fresh	175.01	9.24
Fe/ Co/ Ni (10: 30: 60)-Al ₂ O ₃	Spent	165.37	5.12
Pr/ Co/ Ni (5: 35: 60)-Al ₂ O ₃	Fresh	166.22	5.63
Pr/ Co/ Ni (5: 35: 60)-Al ₂ O ₃	Spent	180.45	5.88

Figure 1. XPS spectra resulted from wide scan of fresh and spent Pr/ Co/ Ni (5: 35: 60)-Al₂O₃ catalysts.

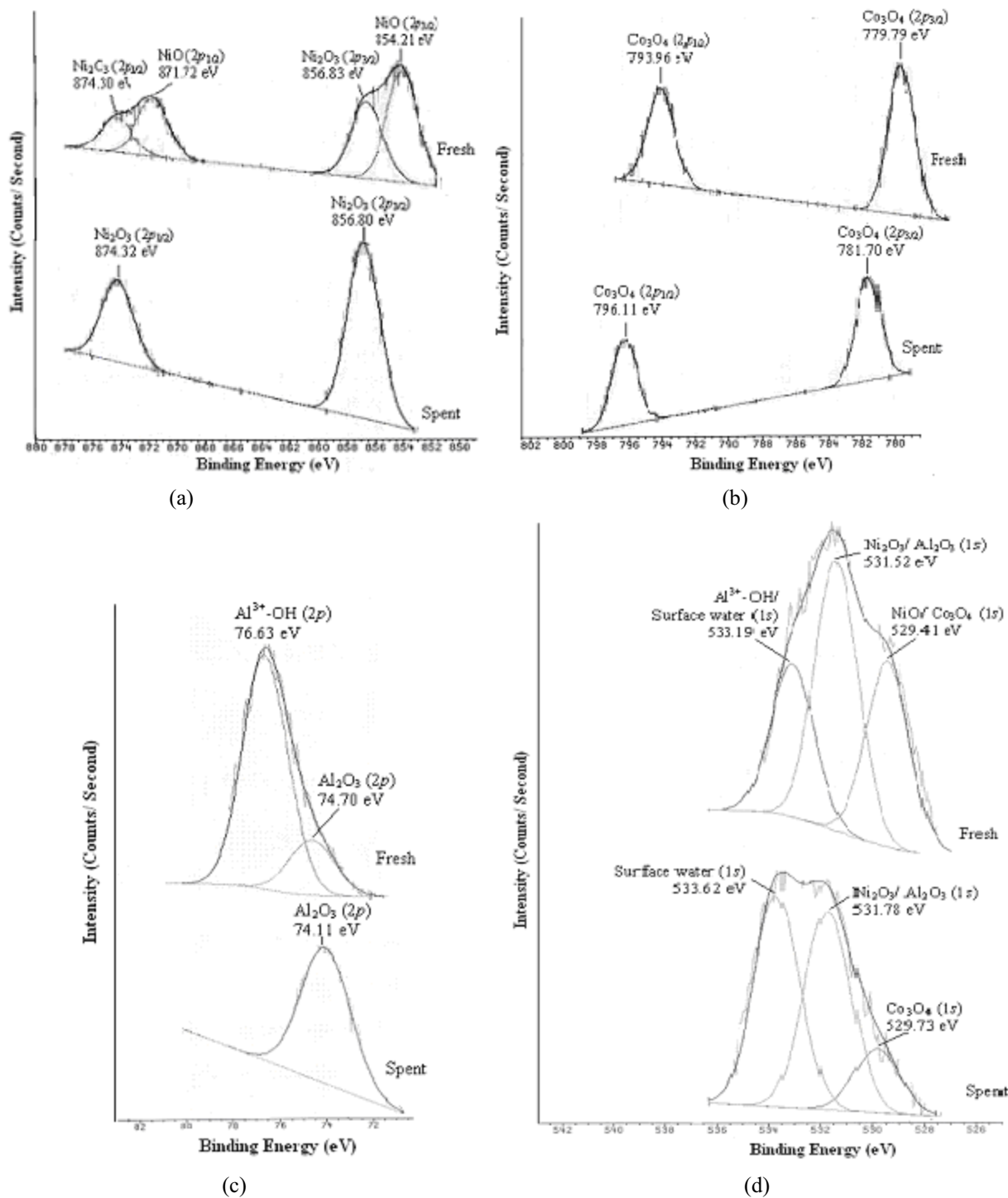


Figure 2. High resolution (a) Ni 2p; (b) Co 2p; (c) Al 2p; and (d) O 1s XPS spectra obtained from fresh and spent Pr/Co/Ni (5: 35: 60)-Al₂O₃ catalysts.

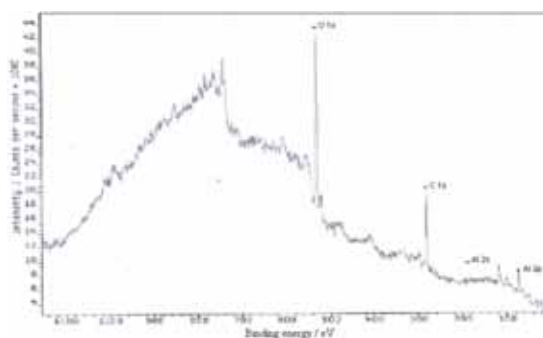


Figure 3. XPS spectra resulted from wide scan of fresh Fe/ Co/ Ni (10: 30: 60)-Al₂O₃ catalyst

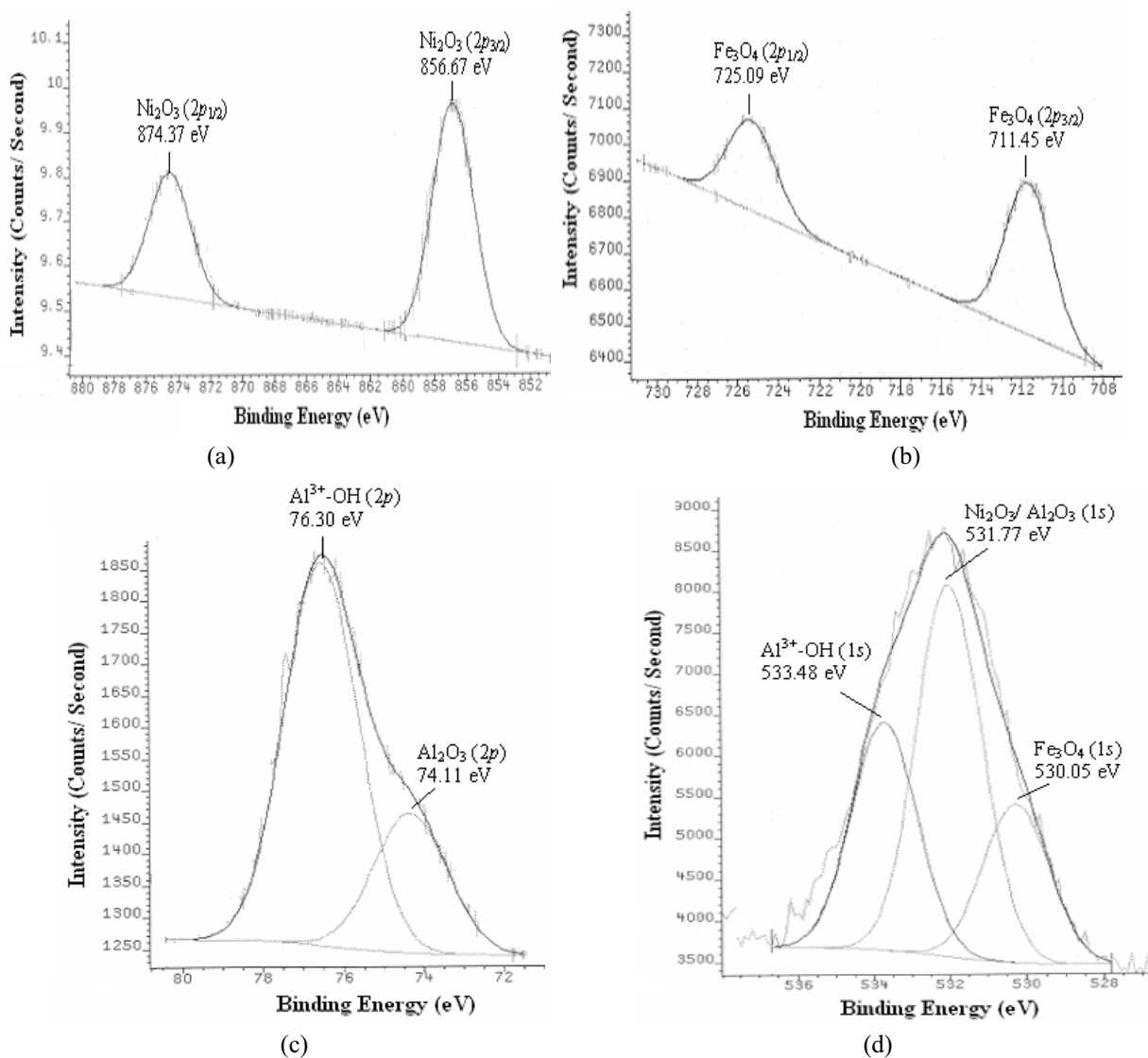


Figure 4. High resolution (a) Ni 2p; (b) Fe 2p; (c) Al 2p; and (d) O 1s XPS spectra obtained from fresh Fe/ Co/ Ni (10: 30: 60)-Al₂O₃ catalyst.



Existence of Nonoscillatory Solutions for a Class of N-order Neutral Differential Systems

Zhibin Chen & Aiping Zhang
Department of Information Engineering
Hunan University of Technology
Hunan 412000, China
E-mail: chenzhibinbin@163.com

The research is financed by Hunan Province natural sciences fund project (NO. 060D74).

Abstract

Using fixed point theorem through the method of structural compression mapping on set of bounded continuous function, this paper qualitative studies the existence of nonoscillatory solutions for a class of n-order neutral differential systems, and obtains some sufficient conditions of nonoscillation existence of solution for this class systems.

Keywords: Neutral, Differential system, Nonoscillatory solution, Compression mapping, Fixed point theorem

1. Introduction

Consider the existence of nonoscillatory solutions for n-order neutral differential systems

$$[x(t) - \sum_{i=1}^l p_i(t)x(t - \tau_i(t))]^{(n)} + (-1)^{n+1} \sum_{j=1}^r Q_j(t) f_j(t, x(\sigma_j(t))) = 0 \quad (1.1)$$

where n is a positive integer and the followings are always satisfied:

$$(A_1) \ p_i(t), Q_j(t) \in C[[t_0, \infty), R^+], \tau_i(t), \sigma_j(t) \in C[[t_0, \infty), R], \lim_{t \rightarrow \infty} (t - \tau_i(t)) = +\infty,$$

$$\lim_{t \rightarrow \infty} \sigma_j(t) = +\infty \quad (i = 1, 2 \dots l; j = 1, 2 \dots r).$$

$$(A_2) \ f_j(t, y) \in C[[t_0, \infty) \times R, R], \text{for enough big } t, \text{ when } y \neq 0, \ y f_j(t, y) > 0, (j = 1, 2 \dots r) \text{ holds.}$$

$$(A_3) \ \text{Function } f_j(t, y) \text{ satisfies local Lipschitz condition for } y, \text{ i.e. exists constant } L > 0 \text{ and } \delta > 0, \text{ which agrees that } |f_j(t, y_1) - f_j(t, y_2)| \leq L |y_1 - y_2| \text{ when } -\delta < y_1, y_2 < \delta, (j = 1, 2 \dots r).$$

The equation (1.1) solution is oscillatory, if it has arbitrary big zero; Otherwise, it is nonoscillatory.

On the century 90's, it appeared many papers (Yan, Jurang. 1990.)(Wang, Zhibin. 1995.)(Wang, Lianwen. 1995.)(Li, Guanghua, Yu, Yuanhong, & Lin, ShiZhong. 1997)(Wang, Guangpei. 2000.)(Li, Hongfei, & Wang, Zhibin. 2000.) about oscillatory solutions for higher order neutral differential equation. These articles have given some solution oscillatory conditions. However, there have few researches for nonoscillatory solution. The most earliest research is discussed by Zhang Binggen in paper (Zhang, Binggen. 1996.) for the existence of nonoscillatory solution

$$[x(t) - h(t)x(\tau(t))]^{(n)} + \sum_{i=1}^m p_i(t)x(g_i(t)) = 0 \quad (1.2)$$

Afterwards, Shen Jianhu, Yu Jianshe studies the more generaler equation than (1.2) in paper (Shen, Jianhua, & Yu,

Jianshe. 1996.):

$$[x(t) - p(t)x(\tau(t))]^{(n)} + f(t, x(t - \sigma_1(t)), \dots, x(t - \sigma_m(t))) = 0 \tag{1.3}$$

This paper established the sufficient condition for bounded positive solution existence of equation (1.3) when neutral item $p(t) \equiv 1$ and $P(t) \equiv p \neq 1$. In recent years, papers (Tang, Xianhua, & Yu, Jianshe. 2000.) (Liu, Kaiyu. 2000.) have considered the special situation of equation (1.3)

$$[x(t) - p(t)x(t - \tau)]^{(n)} + Q(t)x(t - \sigma) = 0 \tag{1.4}$$

which established the sufficient condition of solution existence of equation (1.4) when neutral item $p(t)$ has initial change among 1.

This paper uses *Banach* compression reflection principle, discusses nonoscillation existence of solution for the generaler equation than equation (1.1) of papers (Zhang, Binggen. 1996.) (Shen, Jianhua, & Yu, Jianshe. 1996.) (Tang, Xianhua, & Yu, Jianshe. 2000.) (Liu, Kaiyu. 2000), and obtains the sufficient conditions of nonoscillation existence of solution for this class systems, whose conclusions are different from papers (Zhang, Binggen. 1996.) (Shen, Jianhua, & Yu, Jianshe. 1996.) (Tang, Xianhua, & Yu, Jianshe. 2000.) (Liu, Kaiyu. 2000).

2. Conclusions and Proof

Lemma 2.1: (*Banach* compression mapping principle) Supposes mapping $A: \Omega \rightarrow \Omega$ is a compression mapping in the complete distance space $(\Omega, \|\bullet\|)$, then A must exist only a fixed point $x \in \Omega$ satisfying $Ax = x$.

Theorem 2.1: Suppose $(A_1), (A_2), (A_3)$ hold, and exist positive constant c and nonnegative number k which satisfying

$$\limsup_{t \rightarrow \infty} \left[\sum_{i=1}^l P_i(t) e^{k\tau_i(t)} + \frac{L e^{kt}}{(n-1)!} \sum_{j=1}^r \int_t^{\infty} (s-t)^{n-1} Q_j(s) e^{-k\sigma_j(s)} ds \right] < 1 \tag{2.1}$$

,then the equation exists eventually positive solution $x(t)$ and $0 < x(t) \leq c e^{-kt}$.

Proof: From theorem, there are $T > t_0$ and $0 < \alpha < 1$ satisfying the following equation when $t \geq T$

$$t - \tau_i(t) \geq t_0, \sigma_j(t) \geq t_0, \quad (i = 1, 2 \dots l; j = 1, 2 \dots r)$$

$$\sum_{i=1}^l P_i(t) e^{k\tau_i(t)} + \frac{L e^{kt}}{(n-1)!} \sum_{j=1}^r \int_t^{\infty} (s-t)^{n-1} Q_j(s) e^{-k\sigma_j(s)} ds < \alpha \tag{2.2}$$

Denote set $C_B = \{x(t) : [t_0, \infty) \rightarrow R\}$ is a bounded continuous function set in $[t_0, \infty) \rightarrow R$, and define $\|x(t)\| = \sup_{t \geq t_0} |x(t)|$

in C_B , then C_B is a *Banach* space.

Denote $\Omega = \{x(t) \in C_B : 0 \leq x(t) \leq 1, t > t_0\}$.

the following proof is that the set Ω is a bounded closed convex subset in C_B .

It is obvious that Ω is boundary.

For arbitrary $x, y \in \Omega$, since $0 \leq ax(t) + (1-a)y(t) \leq 1, a \in [0, 1], \Omega$ is a convex set.

If $x_n \in \Omega$ and $\lim_{n \rightarrow \infty} \|x_n - x_0\| = 0$, when $n \rightarrow \infty$, we have

$$|x_0| \leq |x_0 - x_n| + |x_n| \leq \|x_0 - x_n\| + 1 \rightarrow 1, 0 \leq x_n \leq \|x_n - x_0\| + x_0 \rightarrow x_0$$

Hence, $x_0 \in \Omega$. From the above, Ω is a bounded closed convex subset in C_B .

Define mapping in Ω

$$(Ax)(t) = \begin{cases} \sum_{i=1}^l p_i(t)e^{k\tau_i(t)}x(t-\tau_i(t)) + \frac{e^{kt}}{c(n-1)!} \sum_{j=1}^r \int_t^\infty (s-t)^{n-1} Q_j(s) \\ f_j(s, ce^{-k\sigma_j(s)}x(\sigma_j(s)))ds, t \geq T; \\ 1 - \frac{t}{T} + \frac{t}{T}(Ax)(T), t_0 \leq t \leq T, \end{cases} \tag{2.3}$$

where c, k, δ satisfy inequality $0 < ce^{-kt} < \delta$.

The following will prove that mapping A is self and compressive .

(1)For arbitrary $x(t) \in \Omega$ and $t > T$, from (2.2)and (2.3), we have

$$\begin{aligned} (Ax)(t) &= \sum_{i=1}^l p_i(t)e^{k\tau_i(t)}x(t-\tau_i(t)) \\ &+ \frac{e^{kt}}{c(n-1)!} \sum_{j=1}^r \int_t^\infty (s-t)^{n-1} Q_j(s) f_j(s, ce^{-k\sigma_j(s)}x(\sigma_j(s)))ds \\ &\leq \sum_{i=1}^l p_i(t)e^{k\tau_i(t)} + \frac{Le^{kt}}{(n-1)!} \sum_{j=1}^r \int_t^\infty (s-t)^{n-1} Q_j(s) e^{-k\sigma_j(s)} ds \\ &< \alpha \\ &< 1. \end{aligned} \tag{2.4}$$

When $t_0 \leq t \leq T$, we have

$$(Ax)(t) = 1 - \frac{t}{T} + \frac{t}{T}(Ax)(T) \leq 1. \tag{2.5}$$

The above indicates $A(\Omega) \in \Omega$, i.e. A is a self mapping in Ω .

(2)Without loss generality, suppose $x_1(t), x_2(t) \in \Omega$, and when $t \geq T$, from equation(2.3), we have

$$\begin{aligned} |(Ax_1)(t) - (Ax_2)(t)| &\leq \sum_{i=1}^l p_i(t)e^{k\tau_i(t)} |x_1(t-\tau_i(t)) - x_2(t-\tau_i(t))| \\ &+ \frac{e^{kt}}{c(n-1)!} \sum_{j=1}^r \int_t^\infty (s-t)^{n-1} Q_j(s) \\ &|f_j(s, ce^{-k\sigma_j(s)}x_1(\sigma_j(s))) - f_j(s, ce^{-k\sigma_j(s)}x_2(\sigma_j(s)))| ds \\ &\leq \left(\sum_{i=1}^l p_i(t)e^{k\tau_i(t)} + \frac{Le^{kt}}{(n-1)!} \sum_{j=1}^r \int_t^\infty (s-t)^{n-1} Q_j(s) e^{-k\sigma_j(s)} ds \right) \|x_1 - x_2\| \\ &\leq \alpha \|x_1 - x_2\|. \end{aligned} \tag{2.6}$$

When $t_0 \leq t \leq T$, we have

$$\begin{aligned} |(Ax_1)(t) - (Ax_2)(t)| &\leq \frac{t}{T} |(Ax_1)(T) - (Ax_2)(T)| \\ &\leq \alpha \|x_1 - x_2\|. \end{aligned} \tag{2.7}$$

The above indicates that $(Ax)(t)$ is a compressive mapping. Therefore it exists fixed point $x^*(t) \in \Omega$ satisfying $(Ax^*)(t) = x^*(t)$, namely

$$x^*(t) = \begin{cases} \sum_{i=1}^l p_i(t)e^{k\tau_i(t)}x^*(t-\tau_i(t)) + \frac{e^{kt}}{c(n-1)!} \sum_{j=1}^r \int_t^\infty (s-t)^{n-1} Q_j(s) \\ f_j(s, ce^{-k\sigma_j(s)}x^*(\sigma_j(s)))ds, t \geq T; \\ 1 - \frac{t}{T} + \frac{t}{T}(Ax^*)(T), t_0 \leq t \leq T. \end{cases} \tag{2.8}$$

Taking $x(t) = cx^*(t)e^{-kt}$ ($t > t_0$), from (2.8) we have

$$\begin{aligned}
 x(t) &= \sum_{i=1}^l p_i(t) c e^{-k(t-\tau_i(t))} x^*(t-\tau_i(t)) \\
 &+ \frac{1}{(n-1)!} \sum_{j=1}^r \int_t^\infty (s-t)^{n-1} Q_j(s) f_j(s, c e^{-k\sigma_j(s)} x^*(\sigma_j(s))) ds \\
 &= \sum_{i=1}^l p_i(t) x(t-\tau_i(t)) \\
 &+ \frac{1}{(n-1)!} \sum_{j=1}^r \int_t^\infty (s-t)^{n-1} Q_j(s) f_j(s, x(\sigma_j(s))) ds, (t \geq T).
 \end{aligned}
 \tag{2.9}$$

Derivate equation (2.9) n times, equation (1.1) is gotten. So $x(t) = c x^*(t) e^{-kt}$ is the eventually positive solution of equation(1.1) and $0 < x(t) \leq c e^{-kt}$. The proof is completed.

Corollary 2.1: If conditions $(A_1), (A_2), (A_3)$ are satisfied and inequalities

$$\sum_{i=1}^l p_i(t) \leq c, 0 < c < 1, \tag{2.10}$$

$$\int_t^\infty s^{n-1} Q_j(s) ds < \infty, j = 1, 2 \dots r \tag{2.11}$$

hold, then the equation(1.1) exists eventually positive solution.

Proof: From(2.10),(2.11), we have

$$\limsup_{t \rightarrow \infty} \sum_{i=1}^l p_i(t) \leq c < 1, \tag{2.12}$$

$$\lim_{t \rightarrow \infty} \sum_{j=1}^r \int_t^\infty (s-t)^{n-1} Q_j(s) ds = 0. \tag{2.13}$$

Then when $K=0$, we have

$$\begin{aligned}
 &\limsup_{t \rightarrow \infty} \left[\sum_{i=1}^l p_i(t) e^{k\tau_i(t)} + \frac{L e^{kt}}{(n-1)!} \sum_{j=1}^r \int_t^\infty (s-t)^{n-1} Q_j(s) e^{-k\sigma_j(s)} ds \right] \\
 &= \limsup_{t \rightarrow \infty} \left[\sum_{i=1}^l p_i(t) + \frac{L}{(n-1)!} \sum_{j=1}^r \int_t^\infty (s-t)^{n-1} Q_j(s) ds \right] \\
 &< 1
 \end{aligned}$$

From theorem 2.1, it is obtained that the equation(1.1) exists eventually positive solution.

Corollary 2.2 When conditions $(A_1), (A_2), (A_3)$ hold, if positive constants k, p_i, τ_i, σ_i satisfy $p_i(t) \leq p_i, Q_j(t) \leq Q_j, \tau_i(t) \leq \tau_i, \sigma_j(t) \geq t - \sigma_j, (i = 1, 2 \dots l; j = 1, 2 \dots r)$, and the inequality

$$k^n (1 - \sum_{i=1}^l p_i e^{k\tau_i}) > L \sum_{j=1}^r Q_j e^{k\sigma_j} \tag{2.14}$$

hold, then equation(1.1) exists eventually positive solution.

Proof From condition (2.14) in Corollary 2.1,

$$\begin{aligned}
 &\limsup_{t \rightarrow \infty} \left[\sum_{i=1}^l p_i(t) e^{k\tau_i(t)} + \frac{L e^{kt}}{(n-1)!} \sum_{j=1}^r \int_t^\infty (s-t)^{n-1} Q_j(s) e^{-k\sigma_j(s)} ds \right] \\
 &\leq \limsup_{t \rightarrow \infty} \left[\sum_{i=1}^l p_i e^{k\tau_i} + \frac{L e^{kt}}{(n-1)!} \sum_{j=1}^r \int_t^\infty (s-t)^{n-1} Q_j e^{-k(s-\sigma_j)} ds \right] \\
 &= \sum_{i=1}^l p_i e^{k\tau_i} + \frac{L}{k^n} \sum_{j=1}^r Q_j e^{k\sigma_j} < 1.
 \end{aligned}$$

Then equation (1.1) exists eventually positive solution by theorem 2.1.

In equation(1.1), when $f_j(t, x(\sigma_j(t))) = x(\sigma_j(t))$, equation

$$[x(t) - \sum_{i=1}^l p_i(t) x(t-\tau_i)]^{(n)} + (-1)^{n+1} \sum_{j=1}^r Q_j(t) x(\sigma_j(t)) = 0. \tag{2.15}$$

is gotten.

Corollary 2.3 When condition (A_1) is satisfied, and if there exists constant $k \geq 0$, the inequality

$$\limsup_{t \rightarrow \infty} \left[\sum_{i=1}^l p_i(t) e^{k\tau_i(t)} + \frac{e^{kt}}{(n-1)!} \sum_{j=1}^r \int_t^{\infty} (s-t)^{n-1} Q_j(s) e^{-k\sigma_j(s)} ds \right] < 1$$

holds, then equation (2.15) exists eventually positive solution.

Example: Suppose $k > 0$ and $\frac{d^n}{dt^n} \left[x(t) - \frac{\sin^2 t}{e^k (1 + \sin^2 t)} x(t-1) \right] + (-1)^{n+1} (a(t)x(t) + b(t)x(t-1)) = 0$. When $t \geq t_0$, $a(t) + e^k b(t) < \frac{k^n}{1 + \sin^2 t}$, $a(t) > 0, b(t) > 0$, whether the equation does have the eventually positive solution?

Solution: Since $0 \leq p(t) = \frac{\sin^2 t}{e^k (1 + \sin^2 t)} \leq e^{-k} < 1$, from theorem 1.1, we have

$$\begin{aligned} & \limsup_{t \rightarrow \infty} \left[\sum_{i=1}^l p_i(t) e^{k\tau_i(t)} + \frac{e^{kt}}{(n-1)!} \sum_{j=1}^r \int_t^{\infty} (s-t)^{n-1} Q_j(s) e^{-k\sigma_j(s)} ds \right] \\ &= \limsup_{t \rightarrow \infty} \left[p(t) e^k + \frac{e^{kt}}{(n-1)!} \int_t^{\infty} (s-t)^{n-1} [a(s) e^{-ks} + b(s) e^{-k(s-1)}] ds \right] \\ &< \limsup_{t \rightarrow \infty} \left[\frac{\sin^2 t}{1 + \sin^2 t} + \frac{k^n}{(1 + \sin^2 t)(n-1)!} \int_t^{\infty} (s-t)^{n-1} e^{-k(s-t)} ds \right] \\ &\leq \limsup_{t \rightarrow \infty} \left[\frac{\sin^2 t}{1 + \sin^2 t} + \frac{1}{1 + \sin^2 t} \right] = 1, \end{aligned}$$

Which indicates this equation has eventually positive solutions.

References

- Li, Guanghua, Yu, Yuanhong, & Lin, ShiZhong. (1997). Oscillation of solutions for higher order nonlinear functional differential equation. *Mathematics in practice and theory*, 27(3), 262-265.
- Li, Hongfei, & Wang, Zhibin. (2000). Oscillation for higher order nonlinear time lag differential equations of variable coefficients. *Journal of engineering mathematics*, 17(3), 121-124.
- Liu, Kaiyu. (2000). Existence of boundary positive solutions for high order neutral differential equation. *Journal of Hunan University*, 27(2), 11-16.
- Shen, Jianhua, & Yu, Jianshe. (1996). Existence of positive solutions for high order neutral differential equation, *Acta Mathematica Sinica*, 39(2), 145-155.
- Tang, Xianhua, & Yu, Jianshe. (2000). Existence of positive solutions for high order neutral differential equation. *Journal of Hunan University*, 27(4), 7-9.
- Wang, Guangpei. (2000). Oscillation theorem of a kind of higher order nonlinear neutral equation. *Mathematics in practice and theory*, 30(4), 433-435.
- Wang, Lianwen. (1995). Oscillation condition for higher order nonlinear neutral equation. *Journal of Shandong University*, 30(2), 126-133.
- Wang, Zhibin. (1995). Oscillation and gradation for higher order neutral equation of variable coefficients. *Acta Mathematica Applicatae Sinica*, 8(1), 38-43.
- Yan, Jurang. (1990). Oscillation and gradation of solutions for n-order nonlinear time lag differential equations solutions. *Acta Mathematica Sinica*, 33(4), 537-543.
- Zhang, Binggen. (1996). Positive solutions for a kind of neutral equations, *Acta Mathematica Applicatae Sinica*, 19(2), 222-230.



Gas Hold up in Multiple Impeller Agitated Vessels

Dr. Kaliannan Saravanan

Department of Chemical Engineering

Kongu Engineering Collage

Erode-638 052, India

Tel: 91-4294-226-600 E-mail: rumisivaesh@yahoo.com

Dr. Veerappan Ramamurthy

Department of Chemical Engineering

Anna University

Chennai-600025, India

Tel: 91-44-235-5373 E-mail: ramamur1951@yahoo.co.in

Kothandaraman Chandramohan (Corresponding author)

Department of Chemical Engineering

Kongu Engineering College

Erode-638 052, India

Tel: 91-4294-226-600 E-mail: kcmohan_2005@yahoo.co.in

Abstract

Gas hold up was measured in mechanically agitated vessels fitted with dual impellers. Different impellers like Pitched blade turbine and Disc turbine were used. 5 different combinations of dual impellers were used. A tank of 0.45 m internal diameter with an impeller diameter of 0.15m was used. Superficial gas velocity was varied from 0.005m/sec to 0.01 m/ sec. Correlations are proposed for gas hold ups for different combinations of impellers. Optimum combination of dual impellers for maximum gas hold up has been identified. The effect of bottom clearance, inter impeller clearance and physical properties like surface tension on gas hold up were also studied for the optimum combination of impellers

Keywords: Multiple impeller vessels, Gas hold up, Power per unit volume

1. Introduction

Mixing is an important unit operation and has extensive applications in chemical, bio chemical and pharmaceutical industries. Mixing means taking two or more phases such as two fluids or a fluid and solid and randomly distributing one in another.

1.1 Equipment

Mixing can be accomplished in a wide variety of equipment. Mechanically agitated vessels or stirred tank reactors are popularly used for gas liquid contacting including gas dispersion, solid suspension, crystallization, polymerization, fermentation, waste treatment etc.

1.2 Multiple Impellers

Vessels with single impeller are used when height to diameter ratio is low. Multiple impellers are used in vessels having a large height to diameter ratio. Multiple impellers are preferred over single impellers to provide better gas utilization, narrow spread in the residence time distribution in the flow systems and higher surface area per unit volume for heat transfer. They also provide low shear compared to single impellers due to overall lower speed of operation at equal power levels. They can also control the dispersed phase hold up and residence time. They have plug flow characteristics and consume lower power per impeller compared to single impeller. High gas hold up and good gas distribution are the

major benefits. Multiple impellers are thus preferred in shear – sensitive micro organism- enriched fermentation reactors.

2. Definitions and Objective of the Study

2.1 Superficial gas velocity (V_G):

It is a velocity at which gas passes upwards through (liquid filled) stirred tank. It is calculated as follows.

$$\text{Superficial gas velocity (m / sec)} = \frac{\text{Volumetric flow rate of gas (m}^3\text{/sec)}}{\text{Cross sectional area of the stirred tank (m}^2\text{)}}$$

2.2 Gas hold up (ϵ_G):

It is the ratio of gas phase volume to total volume. Gas holdup is an important hydrodynamic parameter and is a basic measure of gas-liquid contacting in mechanically agitated tanks. Gas hold up is governed by average bubble size, population of bubbles and bubble velocity. The interfacial area and mass transfer rate are dependent on holdup. Holdup also indicates the volume fraction of gas phase and mean residence time of the gas phase in the vessel. It also governs the velocity or flow field in the vessel, turbulence characteristics in the individual phases and the energy dissipation rates. Thus a study of gas holdup is important for scaling up and design of stirred tank reactors.

2.3. Measurement

Gas hold up was measured by visual method. A graduated graph paper was pasted on the outside of the vessel in between two baffles. By noting the difference between level with and without aeration the hold up was found out. The following equation was used.

$$\epsilon_G = (H_G - H) / H_G$$

Where H_G = Height of liquid after aeration (m), H = Height of clear liquid without aeration (m) and ϵ_G = (fractional) gas hold up. It is a dimensionless quantity. Its value generally ranges from 0 to 0.20.

2.4 Objective

The objective of this study is to identify the optimum combination of dual impellers that will give the maximum gas hold up for a given specific power input – power / unit volume. (Watt / m³)

3. Experimental Set-up

3.1 Details of Agitated Vessel

Experiments were conducted in a vertical cylindrical acrylic vessel having a flat bottom. The diameter (T) of the vessel was 0.45 m and the height of the vessel 1.2 m. The tank is provided with four equally- spaced vertical baffles of width $T / 10$, fixed along the wall of the vessel. A vertical shaft (stirrer) attached to a variable speed DC motor helps to mix the contents of the vessel. Two impellers were mounted on the shaft. The diameter of each of the impeller D was equal to $T/3$. The distance between the lower impeller and the bottom of the vessel – bottom clearance C_1 was equal to $T / 3$. The distance between the lower and upper impeller – inter - impeller clearance was equal to D (diameter of the impeller). The speed of revolution of the stirrer was varied by means of a speed controller. The vessel was filled with tap water up to a height equal to two times the diameter of the vessel. Air was admitted to the bottom of the vessel using a ring sparger having a diameter equal to that of the impeller. The diameter of the sparger was 6.0 mm and there were eight holes through which air was admitted to the vessel.

Three different types of impellers were used. PTD– Pitched Blade Down pumping, PTU – Pitched Blade Up pumping and DT- Disc Turbine. At any point of time two (dual impellers) were used. In all five combinations of impellers were employed.

PTD – PTU means Pitched Blade Turbine Down pumping at the bottom, Pitched Blade Turbine Up pumping at the top. Similarly DT – PTD means Disc turbine at the bottom and Pitched Blade Turbine Down pumping at the top. PTD – PTD, PTD – DT and DT – DT are other combinations.

Superficial gas velocities used were 0.005 m / sec, 0.008 m / sec and 0.01 m/ sec Stirrer speed was varied from 150 to 1200 rpm. The experiments were conducted at room temperature at about 30 to 31 °C.

The details of experimental set up are given in Table 1. Table 2 and 3 give the details of impellers

4. Results and Discussions

4.1 Optimum Combination of impellers

The experimental data were plotted in the form of graphs. In Figure.2 the gas holdup was plotted against power per unit volume for different combinations of dual impellers. As the gas holdup increases, the power per unit volume also increases. Thus there is proportionality between holdup and power per unit volume. It is also noted that of all the

combinations DT-PTD combination gives the highest gas holdup. PTD-PTD gives the second highest holdup followed by DT –DT, PTD –DT and PTD-PTU combinations. Thus DT-PTD combination was found to be optimum for getting maximum gas holdup for a given power per unit volume.

4.2 Behaviour of DT –PTD combination

In the case of DT-PTD combination the upper impeller-pitched blade down pumping turbine -produces a downward flow. This together with the radial stream produced by the lower disc turbine increases the axial velocity in downward direction. This acts against the movement of raising air bubbles and thus helps in the recirculation of air in the upper regions of the vessel. The upper impeller is responsible for gas dispersion and recirculation. In this case, the upper impeller is PTD. Mishra *et al* (1994) have reported that PTD has a higher pumping effectiveness compared to other impellers like DT. Hence the gas holdup increases significantly. The DT-PTD combination thus gives highest gas holdup

Figure 3 and 4 exhibit the same trend at higher superficial gas velocities of 0.008m/s and 0.01m/s.

4.3 Effect of superficial gas velocity

Figure.5 represents the effect of superficial gas velocity on the gas holdup. The gas holdup increases as the superficial gas velocity increases. This is understandable, as the volume of air increases a large population of raising bubbles tends to increase the hold up.

4.4 Effect of bottom clearance

The distance from the bottom of the impeller to the bottom of the tank is called the bottom clearance. Normally the value of this bottom clearance equals 1/3 (T) where T is the tank diameter. In this study the bottom clearance was varied and the effect of this variation on gas holdup was studied. Figure.6 shows the effect of bottom clearance on gas hold up. The holdup was significantly lower when bottom clearance was T/2 compared to the holdup when the clearance was T/3. The holdup was lowest when the clearance was T/6.

This is because the pumping effectiveness of the lower impeller decreases with an increase in the bottom clearance. Also if the clearance is decreased to a low value of T/6 the gas holdup falls significantly. A low clearance leads to changed flow pattern with high resistance to flow .The holdup thus decreases. This is in line with the observations reported by Saravanan *et al* (1994).

4.5 Effect of Inter- Impeller Clearance

The inter impeller clearance is defined as the distance between the centre line of the two impellers. Normally, this distance is kept equal to the diameter of the impeller. Above this value each impeller sets up its own liquid circulation loops which do not mix with that produced by other impeller. In this study the effect of inter impeller clearance on gas holdup was studied. The distance between the impeller was kept at 1.5 D, and 2.0 D and gas hold up was measured. It was observed that the gas hold up decreases with an increase in the impeller clearance. The gas holdup values for 1.5 D were significantly lower than that for 1.0 D. Gas hold up values for 2.0 D were lowest. See Figure 7. This is also in line with the findings reported by Mishra and Joshi (1994) using LDA (Laser Doppler Anemometry) method.

4.6 Effect of Physical properties on gas hold up

The physical properties of the liquid in the vessel, like density, viscosity and surface tension affect the gas hold up. As a bubble raises up its size and velocity are affected by the physical properties of the liquid through which it raises. Surface tension does play a part and its effect on gas holds was studied. Figure .8 indicates the effect of surface tension on gas hold up for a system with air – ethanol and T equal to 0.45m, D equal to 0.15m. Impeller speed was 1200rpm and superficial gas velocity 0.01m/sec. As the surface tension increases the gas holdup falls, because the size of the bubble and its upward velocity increase. If the surface tension is lower the bubble size and its upward velocity decrease leading to higher gas holdup. This is in conformity with the findings reported by Loisseau *et al* (1977).

4.7 Correlation

Based on the data obtained from experiments the following type of empirical correlation is proposed.

$$\epsilon_G = a (P / V)^b (V_G)^c \text{ -----(1)}$$

ϵ_G = Gas hold up –Dimensionless quantity

P = Power consumed by impeller in aerated condition (w)

V = Volume of liquid in the vessel (m³)

V_G = Superficial gas velocity (m/sec)

a, b, c = Constants

The values of all constants a , b and c obtained by regression of experimental data are presented in Table 4. The values of constants obtained in this work are much lower than that reported by Moucha *et al* (2003). This is due to the fact that the latter measured hold up in electrolytic solutions whereas the present work was conducted with air – water systems. The effect of electrolytic solutes on the gas hold up is due to the property of coalescence. The solutes inhibit coalescence and thus the hold up increases in the presence of electrolytic solutes.

4.8 Comparison of Correlations

The present work is also compared with that of Vasconceles *et al* (2000). See Figure 9. The gas holdup values reported by the latter are higher than that reported in the present work. The latter conducted the experiments in a tank of diameter of 0.39 m whereas a tank of 0.45 m diameter was used in the present work. The gas hold up is dependent on the tank diameter. As the tank diameter increases the hold up decreases significantly.

4.9 Parity Plots

Figures 10 and 11 compare the experimental values with that of theoretical values of gas hold up obtained using the correlation proposed in this work. Such plots are called Parity Plots. It is noted that the difference between the two values is less than 15%

5. Conclusions

The gas holdup of dual impeller combination in agitated vessel was studied in detail. Five different dual impeller combinations - PTD/PTU, PTD/PTD, PTD/DT, DT/PTD, and DT/DT were studied. It was found that DT/PTD combination gave maximum gas holdup compared to other combinations. The effects of bottom clearance, inter-impeller clearance and surface tension on gas hold up for the optimum impeller combination were studied. It was found that a bottom clearance of $T/3$ gave the maximum holdup followed by $T/2$, and $T/6$. It was also found that the gas hold up was maximum when inter-impeller clearance was D . At values of clearance $1.5D$ and $2.0D$ the gas hold up was much lower. It was found that gas hold up falls as the surface tension increases.

References

- Calderbank P.H. (1958). Physical rate processes in industrial fermentation Part I: The interfacial area with gas liquid contacting with mechanical agitation, *Transactions of Institute of Chemical Engineers*, 36, 443– 460.
- Foust H.C, Mack D.C. (1964). – Gas liquid contacting in mixtures, *Industrial Engineering Chemistry*, 36, 517 – 522.
- Hudcova, Machon .V & Nienow .A.W. (1999). Gas liquid dispersion with dual Rushton Turbine impellers *Bio Technology Bio Engineering*, 34, 617 – 628.
- Loiseau B.N, Midoux. N & Charpentier J.C (1997). Some Hydrodynamics and power input data in mechanically agitated gas liquid contactors, *American Institute of Chemical Engineers Journal*, 23, 931-935.
- Miller DW. (1974). Scale up of agitated vessels – Gas liquid mass transfer – *American Institute of Chemical Engineers journal* – 20, 445 – 453.
- Mishra B.P, Joshi J.B. (1994). Flow generated by disc turbines –Multiple impellers. *Chemical Engineering Research Design*. 73 (5), 657-668.
- Rushton JH & Bimbinet JJ. (1968). Hold up and flooding in air liquid mixing – *Canadian journal of Chemical Engineering*, 46, 16 – 21.
- Saravanan K, Mondale V.D & Joshi J.P. (1994). Gas inducing type of mechanically agitated contactors – *Industrial Engineering Chemistry Research*, 33, 2228 – 2242.
- Vasconcelos J.M, Alves SS & Barata J.M (1995). Mixing in Gas liquid contactors agitated by multiple turbines – *Chemical Engineering Science*, 50, 2343 – 2354.

Table 1. Details of experimental set up

Diameter of the vessel	0.45 m
Height of the vessel	1.2 m
Diameter of the Impeller	0.15 m
Bottom Clearance	0.15 m
Inter impeller clearance	0.15 m
No. of Baffles	4
Height of water in the vessel	0.9 m
Width of Baffles	0.045 m
Type of sparger	Ring Sparger
Diameter of the sparger	0.006 m
No. of holes	8
Drive used	2 H.P DC motor with variable speed controller
Type of impellers used	PTD Pitched Blade Turbine Down pumping PTU. Pitched Blade Turbine Up pumping DT – Disc turbine

Table 2. Combinations of dual impellers

Sl.No.	Nomenclature	Bottom	Top
1	PTD – PTD	Pitched Blade Turbine Down pumping	Pitched Blade Turbine Down pumping
2	PTD- PTU	Pitched Blade Turbine Down pumping	Pitched Blade Turbine Up pumping
3	PTD – DT	Pitched Blade Turbine Down pumping	Disc Turbine
4	DT – PTD	Disc Turbine	Pitched Blade Turbine Down pumping
5	DT – DT	Disc Turbine	Disc Turbine

Table 3. Details of Impellers

Sl.No.	Type	No. of Blades	Blade angle	Imp. Diameter	Blade width
1	PTD	6	45 °	0.15 m	0.0375 m
2	PTU	6	45 °	0.15 m	0.0375 m
3	DT	6	-	0.15 m	0.0375 m

Table 4. Values of Constants a, b and c in equation 1

Sl.No.	Type	a	b	C	Square of correlation coefficient
1	DT-PTD	0.02	0.478	0.4910	0.980
2	PTD-PTD	0.047	0.433	0.6097	0.990
3	DT-DT	0.07135	0.4244	0.6904	0.981
4	PTD-DT	0.0596	0.4459	0.6971	0.974
5	PTD-PTU	0.0768	0.4235	0.7116	0.965

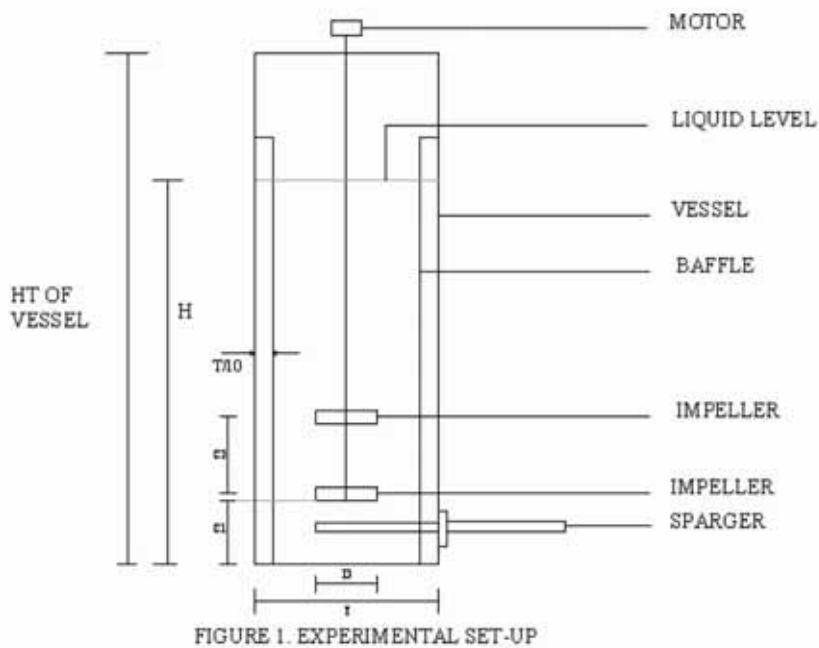


FIGURE 1. EXPERIMENTAL SET-UP

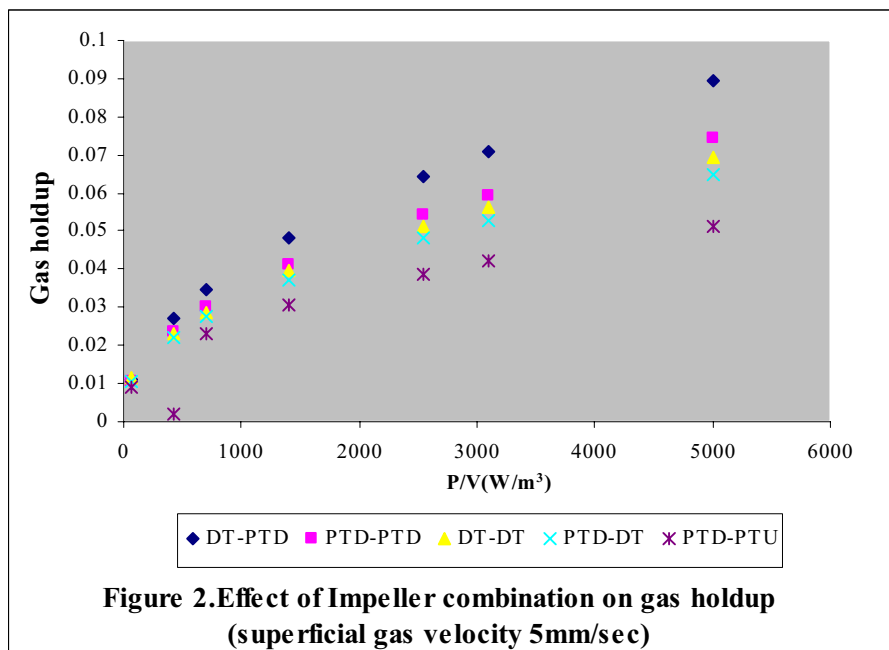
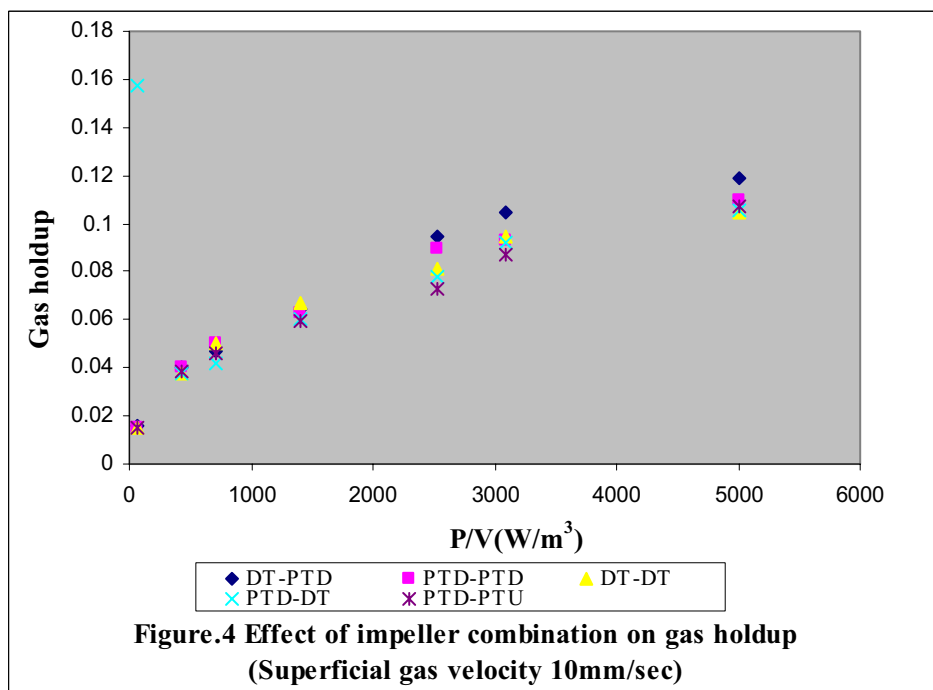
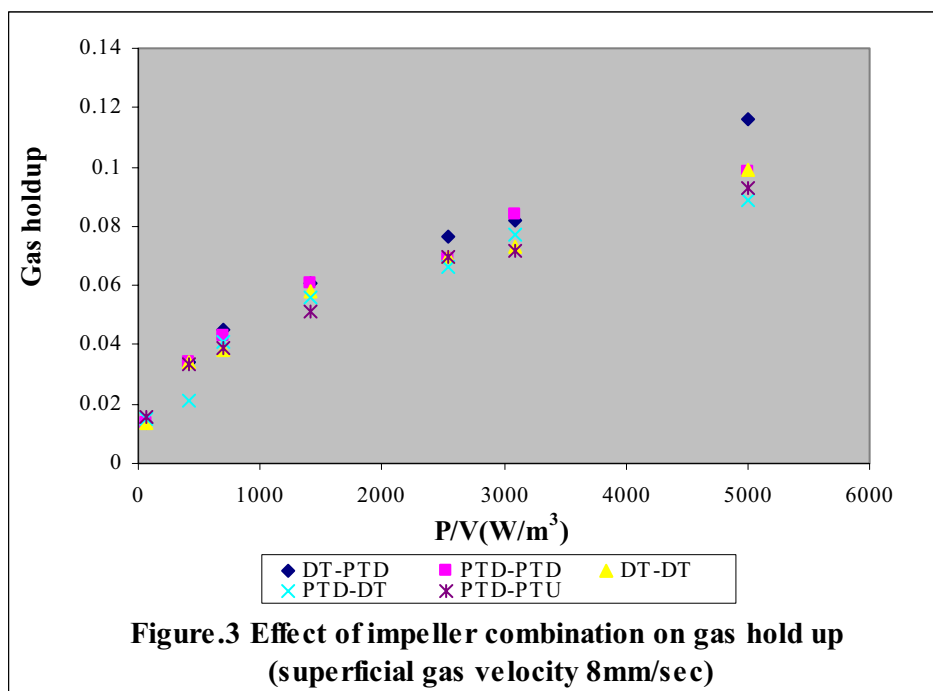
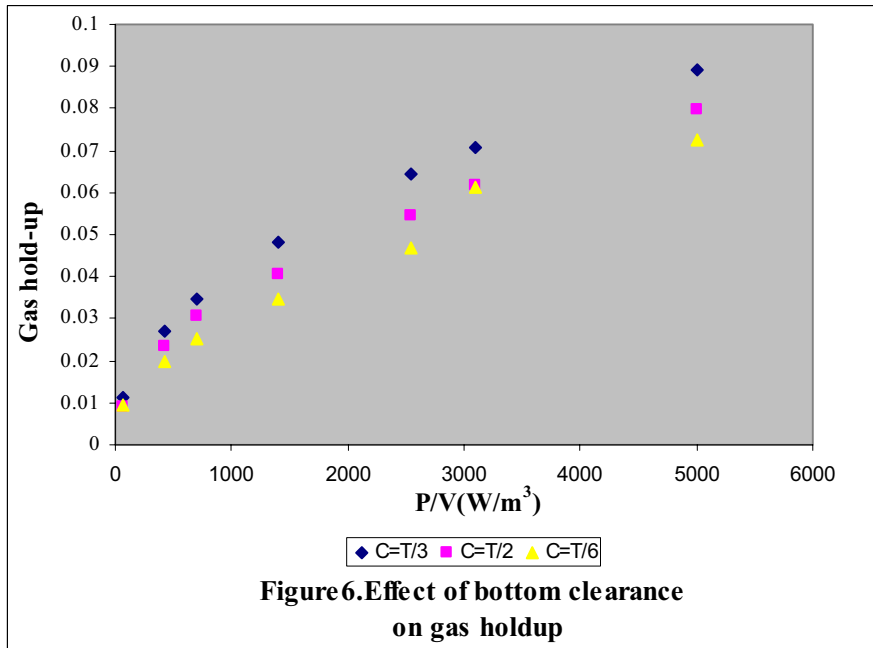
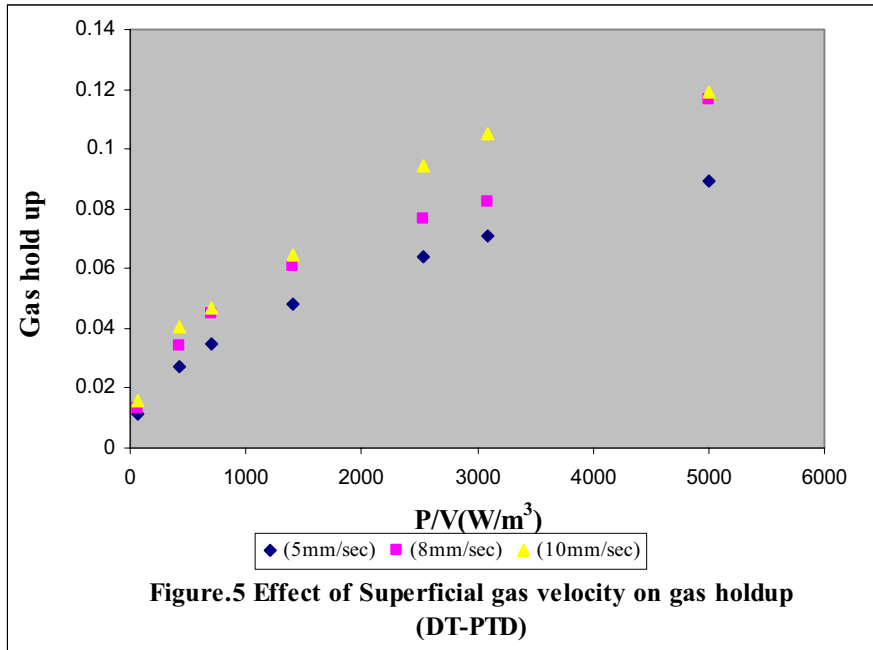
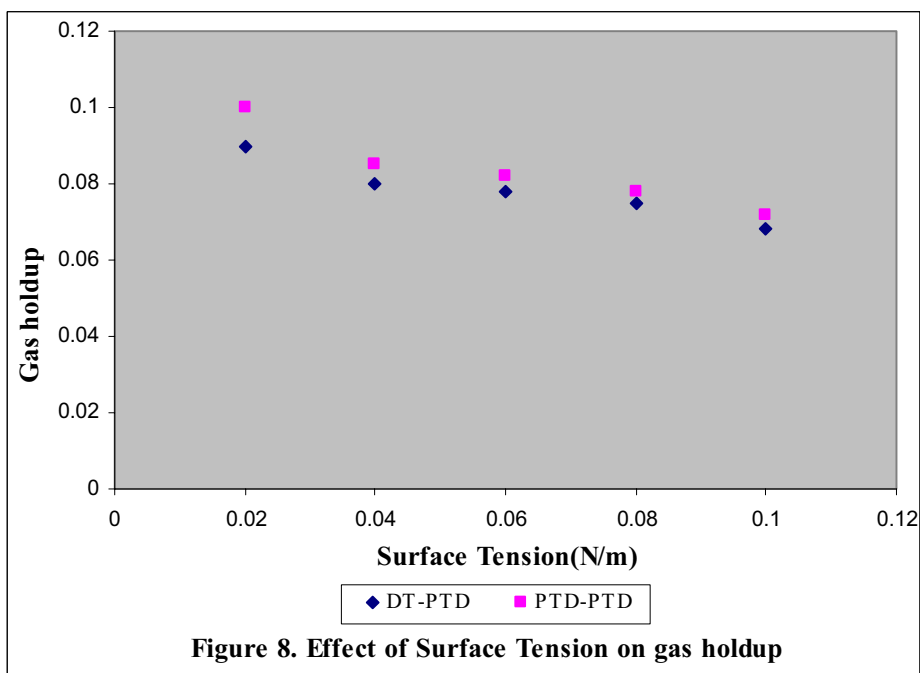
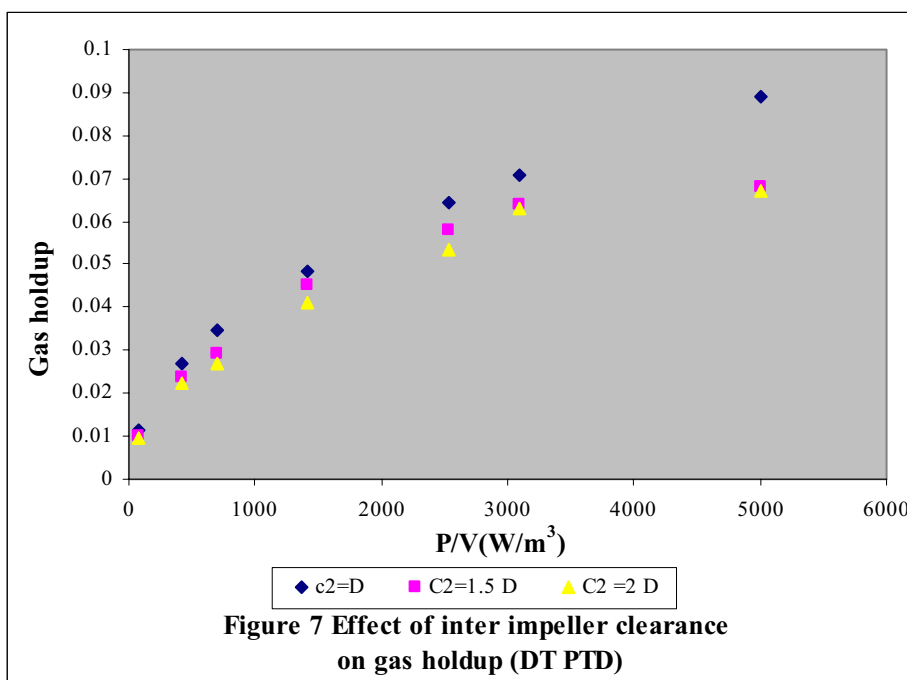
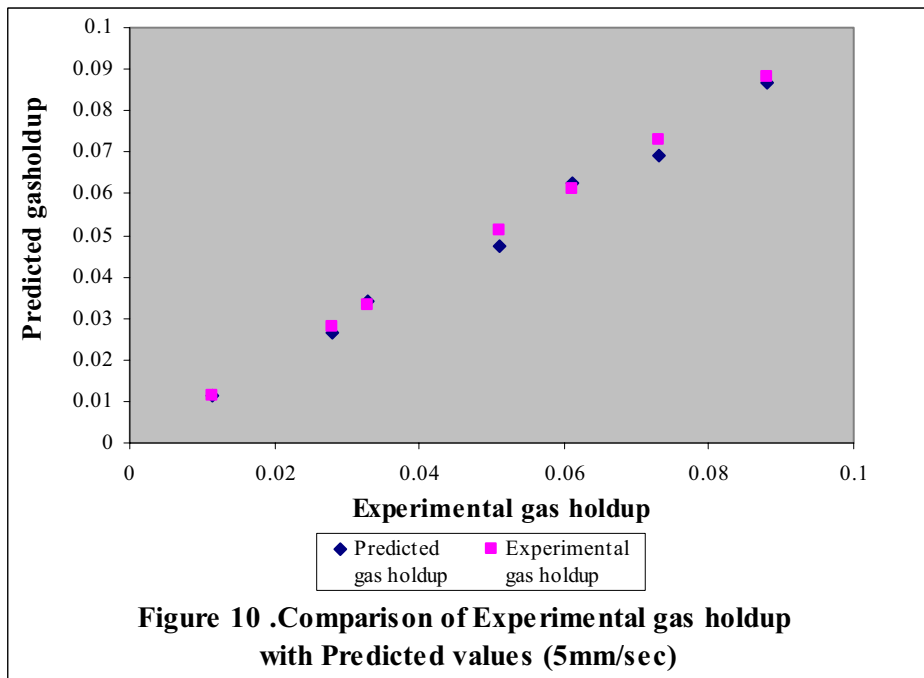
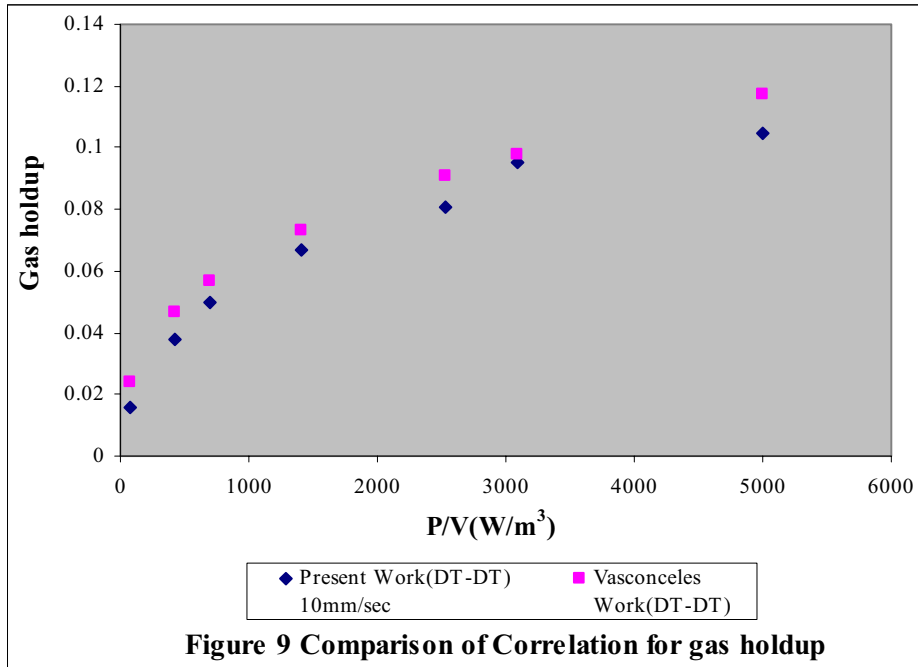


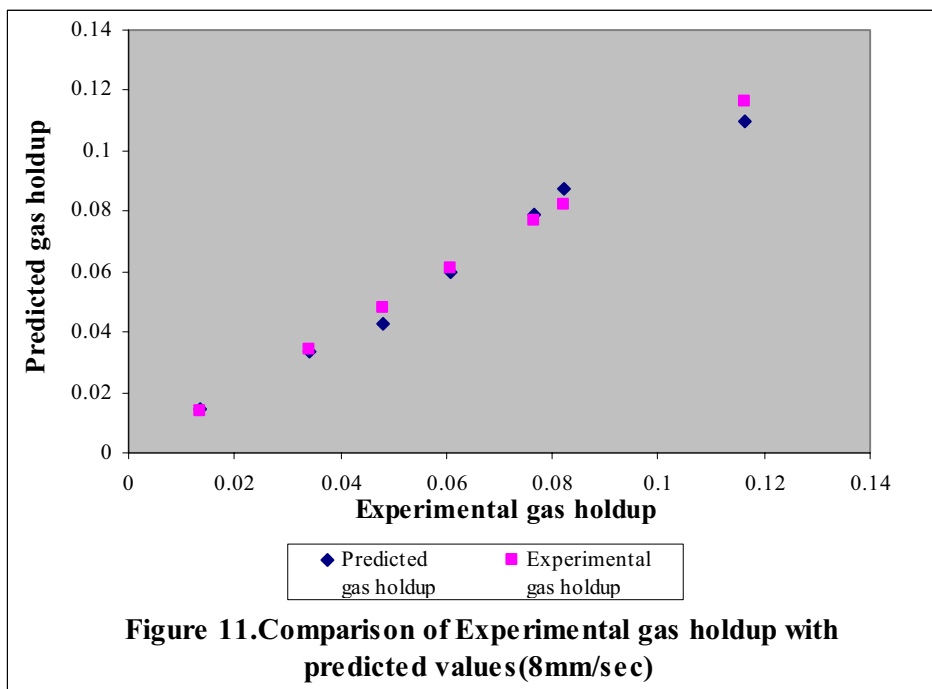
Figure 2. Effect of Impeller combination on gas holdup (superficial gas velocity 5mm/sec)













Motion Control of Underwater Supercavitating Projectiles in Vertical Plane

Daijin Li, Yuwen Zhang, Kai Luo & Jianjun Dang

Collage of Marine Engineering

Northwestern Polytechnical University

Xi'an 710072, China

Abstract

Supercavitating projectiles are characterized by substantially reduced hydrodynamic drag from the fully wetted underwater projectiles. Drag is localized at the nose of the projectile, where a cavitator generates a cavity that completely envelops the body (supercavity). While a supercavitating projectile moving in cruise phase, its motion modes is different from that of a usual wetted projectiles. Based on the motion characteristics, an indirect fixed-depth control via controlling the pitch angle feedback schemes adopting the margin steering control method is put forward. The control method is robust and easy to implement. The research may be useful for designing the control system of supercavitating projectiles.

Keywords: Supercavitating projectiles, Vertical plane, Motion control

CLC number: TP13; TJ630.1 *Document code:* A

1. Introduction

When underwater projectiles such as torpedoes and submarines move through water at sufficient speed, the fluid pressure drops locally below the level that sustains the liquid phase, and a low-density gaseous cavity forms. Flows exhibiting cavities entirely enveloping the moving body are called "supercavitating". (S. S. Ahn and M. Ruzzene, 2006, p.967-976).

In supercavitating flows, the liquid phase does not contact the moving body over most of its length, thus making the skin drag almost negligible. (John Dzielski and Andrew Kurdila, 2003, p.791-804). Several new and projected supercavitating underwater projectiles exploit supercavitation as a means to achieve extremely high submerged speeds and low drag. (Miller D, 1995, p.61-63). The size of existing or notional supercavitating high-speed bodies ranges from that of projectiles to heavyweight full-scale torpedoes. (Ashley S, 2001, p.52-53). Although extensive efforts have been devoted in the past to the analysis of the fluid dynamic characteristics of supercavitating projectiles (Harkins TK, 2001, p.7-11), very little research has been dedicated so far to the evaluation of the fixed-depth control of slender elastic bodies traveling underwater at high speed in supercavitating regimes. Much of the previous and current studies on guidance, control and stability have considered supercavitating projectiles as rigid bodies (Kirschner IN, Fine NE and Uhlman JS, 2001; Kirschner IN and Imas LG, 2002; Vasin AD, 2001). And scarcely any have addressed the hydrodynamic characteristics of the water/cavity system. (Semenenko VN, 2001). The small wetted surface area results in a significant reduction of drag. The projectile may be controlled through a combination of the deflection of the cavitator and control surface, and planning. The control of these bodies presents a number of significant challenges. Depending on the shape of the cavitator and the size and immersion of the control surfaces, the body may be inherently stable or unstable. If the body is unstable, active control of the cavitator or control surface in the aft of the projectile is required to achieve stability. Even if the body is designed to be stable, it is not guaranteed that the projectile will be stable when in contact with the cavity. Since the cavity wall causes a very large restoring force and the time that the projectile is in contact with the cavity wall is very short, suppressing these contacts requires very high performance actuators.

The goal of this paper is to investigate the dynamic characteristics of supercavitating bodies, then present a fixed-depth control method. The paper is organized in six sections. In the first section a brief introduction is given. Section 2 outlines the formulation for the equations of motion for the longitudinal or pitch-plane dynamic model. Section 3 presents a control-algorithm of indirect depth control via controlling the pitch angle feedback. Section 4 describes margin steering control method to put the control-algorithm into effect. Section 5 gives numerical simulation results, while Section 6 summarizes the main results of the work and gives recommendations for future research.

2. A longitudinal kinematics model for a supercavitating projectile

To derive the equations of motion, the following assumptions are made:

- The motion of the projectile is confined to a plane.
- The effect of rolling angular is negligible.
- The effect of added mass on the dynamics of the projectile is negligible.
- The motion of the projectile is not influenced by the presence of gas, water vapour or water drops in the cavity.
- The velocity and cavitation number are confined fixed values.

The supervacitating projectiles longitudinal plane kinematics equation, make up the system model:

$$mv\dot{\Theta} = A^d k + A^\alpha \alpha + A^\omega \omega_z - G \tag{3}$$

$$J_z \dot{\omega}_z = M^d k + M^\alpha \alpha + M^\omega \omega_z \tag{4}$$

$$\dot{\theta} = \omega_z \tag{5}$$

$$\dot{y} = v\Theta \tag{6}$$

$$\Theta = \theta - \alpha \tag{7}$$

Where m is the mass of the projectile; Θ is the obliquity of the trajectory; θ is the pitch attitude; and J_z is the moment of inertia about z axis. The combined coefficients $A^d, A^\alpha, A^\omega, M^d, M^\alpha, M^\omega$ are given by

$$A^d = 0.5C_D^d(\sigma, \alpha_N)\rho A_d v^2 \tag{8}$$

$$A^\alpha = 0.5C_D^\alpha(\sigma, \alpha_N)\rho A_b v^2 \tag{9}$$

$$A^\omega = 0.5C_D^\omega(\sigma, \alpha_N)\rho A_b v^2 \tag{10}$$

$$M^d = 0.5\rho v^2 A_d L m_d^d \tag{11}$$

$$M^\alpha = \begin{cases} 0.5\rho v^2 A_b L m_{bs}^\alpha, & |\alpha| \leq \alpha_s \\ 0.5\rho v^2 A_b L m_{bB}^\alpha, & |\alpha| > \alpha_s \end{cases} \tag{12}$$

$$M^\omega = 0.5m_b^\omega \rho A_b L^2 v \tag{13}$$

In Eq. (3) and (4), balanceable angle of attack and balanceable rudder angle can be gotten:

$$\alpha_0 = GM^d / (A^\alpha M^d - A^d M^\alpha) \tag{14}$$

$$d_0 = -GM^\alpha / (A^\alpha M^d - A^d M^\alpha) \tag{15}$$

Generally speaking, $|\alpha_0| \leq \alpha_s$, so M^α should be fixed under the condition of $|\alpha| \leq \alpha_s$. Because damping derivatives m_{bs}^α is negative, near by the α_0 . The projectile is of static stable. While $|\alpha| > \alpha_s$ (For example, the control system of the projectile dose not work.), m_{bs}^α would become to positive number. The projectile loses static stability. (Jou-Yong Choi, 2006, p.1360-1370).

It is necessary to investigate the motion characteristics of the projectiles on a vertical plane in order to controlling the depth and the attitude. Under the fixed depth control mode, the condition of $|\alpha| > \alpha_s$ is not allowed. So the study should focus on motion characteristics of projectile in the case of $|\alpha| \leq \alpha_s$. Also, the active control of the angle of nose rudder should be paid more attention for keeping from the condition of $|\alpha| > \alpha_s$ while moving in cruise phase. (Kirschner IN, Kring DC and Stokes AW, 2002, p.219-2).

The benchmark problem focuses exclusively on the vertical plane dynamics of the body which currently appear to present the most severe challenges. (John Dzielski and Andrew Kurdila, 2003, p.791-804).

Under the condition of $|\alpha| \leq \alpha_s$, the transfer function of the system can be gotten striking a balance from the parameter of a_0 and d_0 :

$$\alpha(s) = G(s)(J_z s - M^\omega) / \bar{X}(s) + d(s) \cdot (-A^d J_z s + A^d M^\omega - A^\omega M^d + mvM^d) / \bar{X}(s) \tag{16}$$

$$\omega_z(s) = G(s)M^\alpha / \bar{X}(s) + d(s) \cdot (mvM^d s + A^\alpha M^d - A^d M^\alpha) / \bar{X}(s) \tag{17}$$

$$\theta(s) = \omega_z(s) / s \tag{18}$$

$$y(s) = -v[\theta(s) - \alpha(s)] / s \tag{19}$$

$$\bar{X}(s) = mvJ_z s^2 + (A^\alpha J_z - mvM^\omega)s + A^\omega M^\alpha - A^\alpha M^\omega - mvM^\alpha \tag{20}$$

In the functions, not only d is the importer, which can be controlled, but G which is disturbance quantity. While a supercavitating projectiles moving in cruise phase, G is reducing with monotone curvature, according to the propellant reduction. So G can be treated as a steady negative slope signal, labeled:

$$G(s) = -k_G / s^2 \tag{21}$$

Where slope k_G represents \dot{m}_f which is the propellant consumption per seconds.

3. The control-algorithm design

As obliquity of the trajectory Θ and angle of attack α are not easy to be measured in fact, (May A, 1974, p.75-2), the direct depth feedback control is impossible to achieve. So the other indirect depth control via controlling the pitch angle feedback should be discussed.

Transfer function of the control system (containing electric-actuator) can be expressed as follows:

$$G_c^y(s) = k(s) / (y_c(s) - y(s)) \tag{22}$$

Where, y_c is expectant depth. And transfer function of the closed-loop is given as:

$$y(s) = \frac{1}{\bar{M}_4 s^4 + \bar{M}_3 s^3 + \bar{M}_2 s^2 + 1} y_c(s) + \frac{M^\alpha}{(\bar{M}_4 s^4 + \bar{M}_3 s^3 + \bar{M}_2 s^2 + 1) s^2} \frac{(M^k A^\alpha - M^\alpha A^k) G_c^y(s)}{G(s)} \tag{23}$$

Where, \bar{M} is combinatorial coefficient. y is superposition output response for both y_c and G . For the output response of y_c , y achieves no-steady-state error tracking whatever $G_c^y(s)$ forms, because there are two integral actions in the transfer function forward channel. While, for the output response of G , which inputs in form of ramp, its steady-state error is given as:

$$\lim_{t \rightarrow \infty} y(s) = \lim_{s \rightarrow 0} \frac{M^\alpha - (J_z s - M^\omega)s}{(\bar{M}_4 s^4 + \bar{M}_3 s^3 + \bar{M}_2 s^2 + 1) s^2} \frac{(M^k A^\alpha - M^\alpha A^k) G_c^y(s)}{G(s)} k_G s \tag{24}$$

$$= \lim_{s \rightarrow 0} \frac{M^\alpha k_G}{(M^k A^\alpha - M^\alpha A^k) G_c^y(s) s}$$

Eq. (24) will tend to infinity, if there is no integral action in $G_c^y(s)$. Therefore, there are two choices to control $G_c^y(s)$, PI or PID.

Controlling $G_c^y(s)$ with PI control method, transfer function would add a negative real zero and a real zero-pole in the forward channel, else root locus curve would always has two branches in the right half plane, which can not guarantee system security. Root locus curve adjusted is shown as Figure 1.

Controlling $G_c^y(s)$ with PID control method, the control-algorithm is given as:

$$G_c^y(s) = k_p + T_D s + 1 / T_I s \tag{25}$$

Where, k_p is Proportional gain; T_D is differential time and T_I is integral time. Transfer function would add a negative real zero and a pair of real zero-pole in the forward channel. Root locus curve adjusted is shown as Figure 2. Amplitude frequency curve cross the $0dB$ by $-20dB/dec$. Amplitude gain and phase margin are both abundant. System would keep stable controlling the gain not too large.

4. Margin steering control

To simplify the system and get better robustness, implement the fixed-depth control with limit rudder model could be considered, which is easy to achieve. (Liu Yun-Gang, 2007). From Eq.(25), the control-algorithm of fixed-depth can be gotten:

$$k_c = k_0 + \Delta k \cdot \text{sign} \left(k_p \Delta \theta + T_D \omega_z + \frac{1}{T_I} \int_0^t \Delta \theta dt \right) \quad (26)$$

Where, k_c represents command angle of the head rudder; k_0 is balanced angle of the head rudder; Δk is change angle of the head rudder; and $\Delta \theta$ is represents depth deviation. In order to reduce the depth deviation, the expectant pitch attitude angle can be set to the estimated value of the balanced attack angle.

In addition, considering $|\alpha| > \alpha_s$ is not allowed in the control process, overshoot of step-response system φ , and response gain $k_{k\alpha}$ from α to k are defined. Then restriction of Δk is as follows:

$$\Delta k \leq (\alpha_s - \alpha_0) / [k_{k\alpha} (1 + 2\varphi)] \quad (27)$$

5. Numerical simulation

The following values have been used in the numerical simulation:

- Mass of the projectile $m = 100kg$.
- Depth of firing beneath the water surface $= 3m$.
- Sailing time $= 4s$.
- Shooting speed $= 44m/s(t = 0)$.
- When $t = 0.23s$, the projectile achieves invariable speed $= 203Kn$.
- Thrust of solid rocket motor $= 25KN/0.5s$, specific impulse $= 220s$.
- Thrust misalignment angle of solid rocket motor $= 0.4^\circ$ (in the horizontal plane).
- Initial transverse-roll angle $= 20^\circ$.
- With indirect fixed-depth control (pitch attitude control mode).
- Conversion time of limit rudder angle of the head rudder $= 20ms$.
- Sampling period of pitch attitude control $= 240ms$.

Based on control-algorithm Eq.(26), simulation of projectile motion is shown in Figures 3 and 4. Figure 3 shows the characteristics of the head rudder and depth with PI control. Figures 4 shows the characteristics with PID control.

From the result of system simulations, it can be seen that both of the indirect depth control via controlling the pitch angle feedback are efficacious. Generally speaking, both the PI and PID control methods are well implemented with little range of projectile. While the range of the projectile is large, the system counteracts the variety of gravity vigorously with the PID control method. (Zhu ji-hua, Su Yu-min, Li Ye and Tian Yu, 2007).

With the indirect depth control via controlling the pitch angle feedback, the system running steady intensifies consumedly. (Yu Jian-cheng and Zhang Ai-qun, 2007). The system security can be ensured. The superiority of the control method is proved by experimentation. The system constitution and controlling algorithm is simple and well implemented.

6. Conclusion

The conclusion can be obtained from the analysis and example above: (1) The simple control algorithm should be designed to enlarge the sampling frequency for the stability of supercavitating projectiles motion characteristics on vertical plane; (2) Under the condition of lack of damp, attention should be paid to that attack angle must not exceed the limit restrictions in control process. And the control force can not be too violent; (3) The nicer control quality is not easy acquired by fixed-depth control directly; (4) The lag of system that is brought by the too slow respond speed of the head rudder drive machine will enlarge the regulation overshoot and dithering.

The control algorithm described in this paper is simple, robust and the capability and realization are good. (Yu Jian-cheng and Zhang Ai-qun, 2007). The results presented herein are intended to provide design guidelines which will help estimating the motion stability limits for the considered class of projectiles. Further investigations on how to construct the basis function vectors and somewhat simply the structure of the stabilizing functions, typically in high-order systems, may be needed in the future practical applications.

Acknowledgements

This work was supported by Foundation of China Shipbuilding Industry Corporation.

References

- Ashley S. Warp-drive underwater. *Scientific American*, May 2001.
- Harkins TK. Hydroballistics: development, theory and some test results. *19th international symposium on ballistics. Nterlaken*. Switzerland, May 2001, 7–11.
- John Dzielski, Andrew Kurdila. A benchmark control for supercavitating projectiles and an initial investigation of solutions. *Journal of Vibration and control*. 2003, 9: 791-804.
- Jou-Yong Choi, Massimo Ruzzene. Stability analysis of supercavitating underwater projectiles with adaptive cavitator. *International Journal of Mechanical Sciences*. 48 (2006). 1360-1370.
- Kirschner IN, Fine NE, Uhlman JS, Kring DC. Numerical modeling of supercavitating flows. *RTO AVT lecture series on supercavitating flows*. Brussels, Belgium: Von Karman Institute; February 2001.
- Kirschner IN, Imas LG. Plume-supercavity interactions. *The international summer scientific school "high-speed hydrodynamic"*. Cheboksary, Russia, June 2002.
- Kirschner IN, Kring DC, Stokes AW, Fine NE, Uhlman JS. Control strategies for supercavitating projectiles. *Journal of Vibration and Control* 2002; 8: 219–42.
- Liu Yun-Gang. Output-feedback adaptive control for a class of nonlinear system with unknown control directions. *Acta Automatica Sinica*. Vol. 33, No.12, Dec, 2007.
- May A. Water entry and the cavity-running behavior of missiles. *Naval Sea Systems Command*. Arlington, VA, SEAHAC TR 75-2; 1974.
- Miller D. Going to war in a bubble. *International Defense Review*. 1995; 61–63.
- S. S. Ahn, M. Ruzzene. Optimal design of cylindrical shells for enhanced buckling stability: Application to supercavitating underwater projectiles. *Finite Elements in Analysis and Design*. 42(2006) 967-976.
- Semenenko VN. Dynamic processes of supercavitation and computer simulation. *RTO AVT lecture series on supercavitating flows*. Brussels, Belgium: Von Karman Institute; February 2001.
- Vasin AD. Some problems of supersonic cavitation flows. In: *Proceedings of the fourth international symposium on cavitation*. Pasadena CA. June 20–23, 2001.
- Yu Jian-cheng, Zhang Ai-qun. Direct adaptive control of underwater projectiles based on fuzzy neural networks. *Acta Automatica Sinica*. Vol. 33, No.8, Aug, 2007(In Chinese).
- Zhu ji-hua, Su Yu-min, Li Ye, Tian Yu. Integral variable structure control and simulation for near-surface moment of AUV. *Journal of System simulation*. Vol. 19, No.22, Nov, 2007(In Chinese).

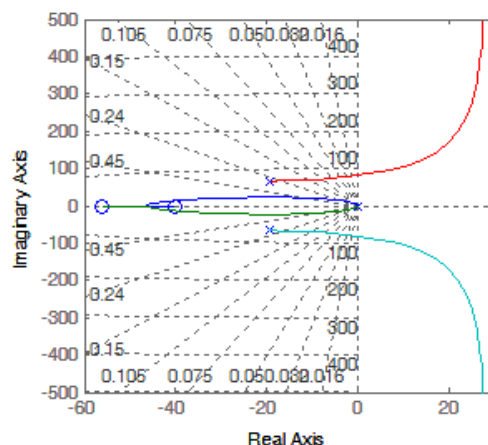


Figure 1. Root locus of depth by PI control

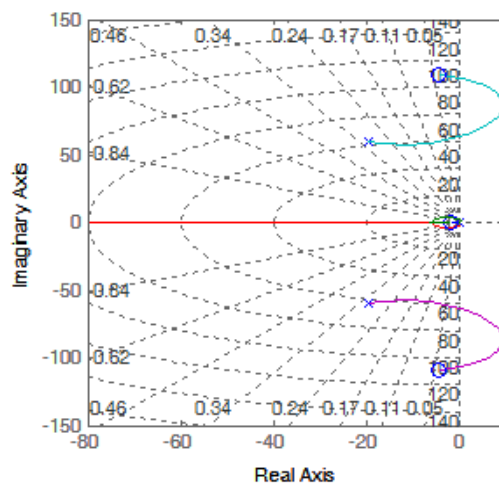


Figure 2. Root locus of depth by PID control

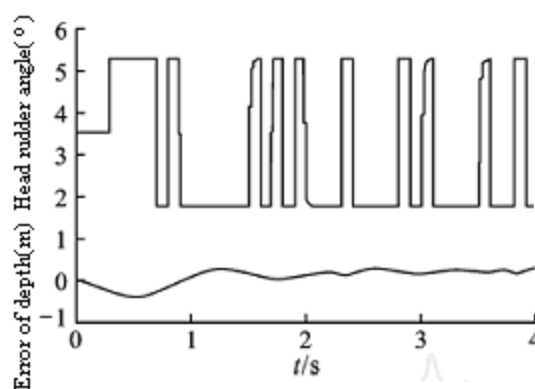


Figure 3. Characteristics of the head rudder and depth with PI control

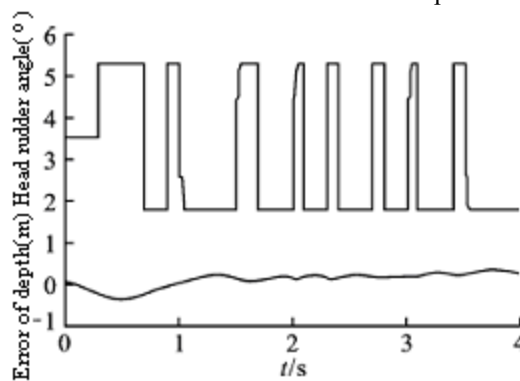


Figure 4. Characteristics of the head rudder and depth with PID control



Aging Effect to Accumulation of Lettucenin A in Lettuce after Elicitation with Various Abiotic Elicitors

Wen Dee Ong

School of Science and Technology

Universiti Malaysia Sabah

88999, Kota Kinabalu, Sabah, Malaysia

E-mail: wendy_young2004@yahoo.com

Khim Phin Chong (Corresponding author)

School of Sustainable Agriculture

Universiti Malaysia Sabah

88999, Kota Kinabalu, Sabah, Malaysia

Tel: 60-88-320000 x5655 E-mail: chongkp@ums.edu.my

Abstract

A series of experiments were conducted to study the effect of age to accumulation of lettukenin A in lettuce (*Lactuca sativa*) after various elicitations. Lettuces were challenged with four different types of elicitation method; spray with silver nitrate (AgNO_3) or copper sulfate (CuSO_4), ultraviolet irradiation and freeze-thawed. Lettukenin A, a type of phytoalexin in lettuce accumulated with a higher concentration after challenged with chemical elicitors, silver nitrate (AgNO_3) and copper sulfate (CuSO_4). Physical elicitation with irradiation of short wavelength (254nm) ultraviolet radiation and freeze-thawed were also effective in eliciting the production of lettukenin A. However, the amounts were considerably lower compared to those elicited by chemical elicitors. Ultraviolet radiation and freeze-thawed stimulated lettuce to produce lettukenin A at a concentration of 1.52 $\mu\text{g/ml}$ and 0.49 $\mu\text{g/ml}$ respectively while AgNO_3 and CuSO_4 contributing to accumulation of 4.27 $\mu\text{g/ml}$ and 4.26 $\mu\text{g/ml}$ respectively. The elicitations of lettukenin A were both dependent on types of elicitor and the age of the plant. Treatments with AgNO_3 and ultraviolet radiation both showed the same pattern production of lettukenin A. Lettukenin A accumulation increased significantly from week nine to the maximum at week twelve before it decreased to minimum at week eighteen. There is a week relation ($R^2 = 0.69$) between the accumulation of lettukenin A with the age of the lettuce with elicitation of silver nitrate. However, there is no relation with induction with ultraviolet radiation. Our results suggest lettuce produces the highest amount of lettukenin A after elicitation with chemical elicitors at twelve weeks old throughout the series of trial.

Keywords: Lettukenin A, Silver nitrate, Cooper sulphate, UV

1. Introduction

Lettuce (*Lactuca sativa*) is one of the most popular vegetable after tomato, citrus and potato in the world (Ryder, 1979). It contributes a lot for diet purpose as it provides little protein, fat, starch or sugar resulting in low energy value and the presence of the β -carotene make them more important among the salad (Siemonsma and Piluek 1994). The major problem in growing lettuce is the occurrence of disease such as downy mildew, powdery mildew, anthracnose, corky root rot, lettuce mosaic virus and many others (Peirce, 1987). The diseases are not only reducing the quality appearance of the lettuce but also affecting the growth and the yield when it involved large scale of vegetable production (Peirce 1987; Ryder 1979). Great economy loses encouraged researches to be conducted in understanding lettuce's defense mechanisms. Plants are constantly live under uncertainty environment with the mercy of wind, rain, UV radiation, herbivores and pathogens attack. To impede to this different uncertainties they need special defence mechanisms. Some plants may produce some antimicrobial compounds after pathogen attack such as secondary metabolites being known as phytoalexins. These compounds have demonstrated a striking activity *in vitro* against potential pathogens (Chong et. al. 2006). Lettukenin A, the phytoalexin in lettuce was first found and isolated by Takasugi et. al. in 1985. The finding of

lettucenin A is considered new at that time compared to others phytoalexins that found in soya bean, pea and many other plants. Although there were research to study the response of lettuce in production of lettucenin A, but most of them are concentrated on the effect after biotic elicitation. In an experiment conducted by Bestwick et. al. 1995. using lettuce seedlings with red spot disorder, the accumulation of lettucenin A was reported vary in different time (days) after sowing. It is apparent that changes take place in the aging of plant tissues that render them to become more resistant to attack and conversely more susceptible to attack. In this study we studied the accumulation of lettucenin A in respond to different types of abiotic elicitor and the relation of lettucenin A production to different time of elicitation (weeks).

2. Research methods

2.1 Plants

Lettuce seeds were sown using top soil with mixture of compost to maintain the moisture of the soil. Seeds were grown in room temperature with 25°C. The lettuce seeds were first grown in trays before transferred to pots after two weeks old. Organic fertilizer was added at week three to enhance their growth.

2.2 Silver nitrate ($AgNO_3$) elicitation

Solution of $AgNO_3$ was prepared at the concentration of 10 mM (1%). The lettuces were sprayed with solution of $AgNO_3$ when they reached to their respective week before maintained for another three days (Mert-Turk et. al. 2003). For control, plants were placed in 25°C under normal growing condition for three days before undergo extraction.

2.3 Copper sulfate ($CuSO_4$) elicitation

Solution of 50 mM (5%) of $CuSO_4$ was prepared and the whole plant was sprayed with the solution at the respective weeks (Al-Barwani and Eltayeb 2004). Control plants were not sprayed with $CuSO_4$. All plants were then incubated for three days under the normal growing condition.

2.4 Ultraviolet radiation elicitation

Lettuces were irradiated under the short wavelength 254nm. Lettuces were placed 10 cm from the UV source for 30 minutes (Al-Barwani and Eltayeb 2004), removed and incubated in dark at room temperature for one and a half days followed by another one and a half day in the normal growing condition. Plants for control were not subjected to irradiation but only incubated under the same condition as those irradiated.

2.5 Freeze- thawed treatment

Plants are kept under the temperature of -65°C for five minutes. These partially frozen plants were later thawed by incubating them at 25°C in dark (Hargreaves and Bailey 1978). Control plants were incubated in dark but not subjected to freeze-thaw treatment. A total of three replications were done for each of the elicitations mentioned above section 2.2-2.5).

2.6 Extraction of Lettucenin A

Treated leaf samples were first homogenized using mortar and pestle before addition of 60% methanol with a ratio of 10 ml of solvent per gram of tissue and left overnight in dark at room temperature. The homogenate was then filtered through Whatman No.1 filter paper and the residue was again re-extracted as described before. The extracts were pooled and evaporated at 45°C using a rotary evaporator to about 30% from the total volume. The concentrate was then extracted three times with chloroform. The extract was filtered again through Whatman No.1 filter paper before concentrated to a volume of 2ml (Bennett et. al. 1994).

2.7 Detection of Lettucenin A

Detection of lettucenin A was done using High Performance Thin Layer Chromatography (HPTLC) plates. Methanolic extracts of treated tissue were applied onto 1 cm origin on pre-coated HPTLC plates (Merck Kiesel 60F₂₅₄) and developed in chloroform:methanol (98:2,v/v) (Bennett et. al. 1994) the plates were later taken out and air-dried. The chromatograms were examined under UV with wavelength of 365 nm where a greenish yellow fluorescent spot (Takasugi et. al. 1985) was observed. Chromatograms were sprayed with 2,4-dinitrophenylhydrazine reagent (DNP) which reacts with lettucenin A to give a pinkish red coloration (Bennett et. al. 1994)

2.8 Quantification of Lettucenin A

A Varian Cary 50 Win UV was used to estimate the concentration of lettucenin A. The spectrophotometer was adjusted to 446 nm, the maximum absorption wavelength of the lettucenin A (Takasugi 1985) Absorbance of the methanolic lettucenin A were recorded. The final concentrations were adjusted to µg/ml.

3. Results and discussion

3.1 Accumulation of lettucenin A after different abiotic elicitation

Accumulation of lettucenin A was significantly different after elicited by the four different methods of elicitation

(Figure 1). Silver nitrate elicited the highest accumulation of lettuceenin A (4.27 $\mu\text{g/ml}$) but not significantly different with copper sulfate which induced the production of 4.26 $\mu\text{g/ml}$ (Figure 1). This followed by ultraviolet radiation contributed to 1.52 $\mu\text{g/ml}$ of lettuceenin A and freeze-thawed method induced the lowest production of lettuceenin A with only 0.49 $\mu\text{g/ml}$ (Figure 1). Results showed that accumulation of lettuceenin A was higher in elicitation using chemical elicitors compared to non-chemical elicitor. The higher accumulation of lettuceenin A elicited with chemical elicitors may due to release of plant's constitutive elicitors from the cell wall surrounding the damage cells caused by the elicitation or the increased activities of the enzymes that could be intermediates in the accumulation of phytoalexin in surrounding cells (Darvill and Albersheim 1984). In addition, Loschke et al. 1983 also reported the induction of PAL activities and other specific proteins by chitosan when tissues were challenged with biotic and abiotic inducer. The minimum productions of lettuceenin A were obtained when lettuce is subjected to freezing injury compared to other three abiotic elicitors. This may due to the delay of *de novo* synthesis of phytoalexin. The *de novo* synthesis is required for the occurrence of the irreversible membrane damage (IMD) and for the onset of hypersensitive (HR) reaction (Gottlieb 1970; Woods et. al. 1988). Woods et al. 1989, in their experiments to investigate the effect of heat-shock on IMD occurring during the HR reaction of *Lactuca sativa* L. to infection of *Bremia lactucae* Regel demonstrated the application of heat shock would affect the protein synthesis by inhibiting the translation of mRNA other than those newly synthesis. The temporary suppression of the protein synthesis results in delay both the occurrence of IMD and also the onset of HR reaction. Temperature stress on lettuce might have causes the reduced in protein synthesis that might be essential to the biosynthesis of lettuceenin A (Hess et. al. 1988).

3.2 Accumulation of Lettuceenin A at different age (weeks)

Among the four different weeks tested, twelve weeks-old lettuce accumulated the highest amount of lettuceenin A in both silver nitrate elicitation and UV radiation. The accumulation of lettuceenin A significantly increased at week nine to week twelve and significantly decreased to the minimum at week eighteen. Plants elicited with silver nitrate accumulated lettuceenin A with 2.30 $\mu\text{g/ml}$ at week nine and drastically increased to 4.28 $\mu\text{g/ml}$ at week twelve. This was followed with a decrease to the lowest concentration of lettuceenin A at the age of eighteen weeks with only 1.57 $\mu\text{g/ml}$. Elicitation using non-chemical abiotic elicitor, such as UV radiation increased the production of lettuceenin A from week nine; 0.55 $\mu\text{g/ml}$ to the highest at week twelve (1.52 $\mu\text{g/ml}$) and decreased drastically to 0.66 $\mu\text{g/ml}$ at week fifteen. The lowest accumulation of lettuceenin A was at week eighteen with 0.54 $\mu\text{g/ml}$. Throughout the experiment all controls showed no production of lettuceenin A. The accumulation of lettuceenin A at different weeks of elicitation is shown in Figure 2. There is a week relation ($R^2 = 0.69$) between the accumulation of lettuceenin A with the age of the plant after elicitation with silver nitrate. However, for non-chemical elicitor, there is no relation with R^2 below 0.5. Different age of plant produces different amount of phytoalexins (Bestwick et. al. 1995; Daniel and Purkayartha, 1995; Paxton and Chamberlain 1969). The present study showed an increase in the accumulation of lettuceenin A until it reaches maturity stage (10-12 weeks) (Siemonsma, and Piluek 1994; Splittstoesser 1979; Tindall 1983) and started to decrease later to the late stage of the plant growth. The increase in the production of lettuceenin A in the early stage may due to increase in resistance of lettuce (Daniel and Purkayartha 1995) while the decrease in the late growing stage may due to the resistance of other defense mechanisms such as morphological barriers and production of other antimicrobial compounds that took over the role of lettuceenin A in defending lettuce against whatever invasion (Chong et. al. 2007). The results in this research also suggesting the older the tissues, the ability for them to produce phytoalexins decreases (Lazarovits 1981). The finding suggesting, the production of lettuceenin A in lettuce start to decrease gradually after week twelve and the increase in accumulation of lettuceenin A only at the first half of the growing period. The outcome from this support the postulation by Paxton and Chamberlain 1969 which they proposed to the resistance of soya beans that may contributed by the production of phytoalexin which plays a role at the early stage of the plant growth and the other resistance occurs in older plant tissue which the production of phytoalexin are greatly reduced.

4. Conclusion

In conclusion, this study demonstrated a positive relation between the ages of plant (weeks) in the production of lettuceenin A with the use of chemical abiotic elicitor but there is no significant different with non-chemical elicitors. Our results suggest lettuce produces the highest amount of Lettuceenin A after elicitation with chemical elicitors at twelve weeks old throughout the series of trial.

References

- Al-Barwani, F.M., & Eltayeb, E.A. (2004). Antifungal compound from induced *Conium maculatum* L. plants. *Biochemical Systematics and Ecology*, 32, 1097-1108.
- Bailey, J.A., & Deverall, B.J. (1983). *The Dynamics of Host Defence*; Academic Press Inc, Australia.
- Bennett, M.H., Gallagher, M.D.S., Bestwick, C.S., & Rossiter, J.T. (1994). The phytoalexin response of lettuce to challenge by *Botrytis cinerea*, *Bremia lactucae* and *Pseudomonas syringae* pv. *Phaseolicola*. *Physiological and Molecular Plant Pathology*, 44, 321-333.

- Bestwick, L., Bennett, M.H., Mansfield, J.W., & Rossiter, J.T., (1995). Accumulation of phytoalexins lettucein A and changes in 3-hydroxy-3-methylglutaryl coenzyme a reductase activity in lettuce seedlings with the red spot disorder. *Phytochemistry*, 39, 775-777.
- Chong, K. P., Kee, K. C., & Desyi. A. N. (2007). Comparison of Aging Effect on Accumulation of Sakuranetin in Paddy and Camalexin in *Arabidopsis thaliana* after Elicited by Silver Nitrate. *Asian Journal of Microbiology Biotechnology and Environmental Sciences*, 9, 3, 463-467.
- Chong, K. P., Mansfield, J. W., Bennett, M. H., & Rossiter, J. F. (2006). Detection of antifungal compounds in *Arabidopsis thaliana* and *Brassica oleracea* by Thin Layer Chromatography. *ASEAN Journal on Science and Technology for Development*, 23, 1&2, 123-131.
- Daniel, M., & Purkayartha, R.P. (1995). *Handbook of Phytoalexin Metabolism and Action*. Marcel Dekker, Inc, America.
- Darvill, A.G., & Albersheim, P. (1984). Phytoalexins and their elicitors. *Annual Review Plant Physiology*, 35, 243-275.
- Gottlieb, D., & Shaw, P.D. (1970). Mechanisms of action of antifungal antibiotics. *Annual Review of Phytopathology*, 8, 371-402.
- Hammerschmidt, R., Lamport, D.T.A., & Muldon, E.P. (1984). Cell wall hydroxypoline enhancement and lignin deposition as an early event in the resistance of cucumber to *Cladosporium cucumerum*. *Physiological Plant Pathology*, 20, 43-47.
- Hargreaves, J.A., & Bailey, J.A. (1978). Phytoalexin production by hypocotyls of *Phaseolus vulgaris* in response to constitutive metabolites released by damaged bean cells. *Physiological Plant Pathology*, 13, 89-100.
- Hess, W.M., Singh, R.S., Singh, U.S., & Weber, D.J. (1988). *Experimental and Conceptual. Plant Pathology*, Volume 3. Oxford and IBH Publishing Co. Pvt. Ltd, India.
- Lazarovits, G., Stossel, R., & Ward, E.W.B. (1981). Age-related changes in specificity and glyceollin production in the hypocotyl reaction of soyabeans to *Phytophthora megasperma* var. *sojae*. *Phytopathology*, 71, 94-97.
- Loschke, D.C., Hadwiger, L.A., & Wagoner, W. (1983). Comparison of mRNA population coding for phenylalanine ammonia lyase and other peptides from pea tissue treated with biotic and abiotic phytoalexin inducers. *Physiological Plant Pathology*, 23, 163-173.
- Maclean, D.J., & Tommerup, I.C. (1979). Histology and physiology of compatibility and incompatibility between lettuce and the downy mildew fungus, *Bremia lactucae* Regel. *Physiological Plant Pathology*, 14, 291-312.
- Mert-Turk, F., Bennett, M.H., Mansfield, J.W., & Holub, E.B. (2003). Camalexin accumulation in *Arabidopsis thaliana* following abiotic elicitation or inoculation with virulent or avirulent *Hyaloperonospora parasitica*. *Physiological and Molecular Plant Pathology*, 62, 137-145.
- Paxton, J.D., & Chamberlain D.W. (1969). Phytoalexins production and disease resistance in soyabeans as affected by age. *Phytopathology*, 59, 775-778.
- Peirce, L.C. (1987). *Vegetables: Characteristic, Production and Marketing*; Library of Congress Cataloging in Publication Data, America.
- Ryder, E.J. (1979). *Leafy Salad Vegetables*. Avi Publishing Company Inc, America.
- Siemonsma, J.S., & Piluek, K. (1994). *Plant Resources of South-East-Asia*. No.8. Vegetables Prosea Foundation, Indonesia.
- Splittstoesser, W.E. (1979) *Vegatables growing handbook*. AVI publishing company Inc, United States of America.
- Takasugi, M., Okinaka, S., Katsui, N., Masamune, T., Shirata, A., & Ohuchi, M. (1985). Isolation and structure of lettucein A, a novel guaianolide phytolaexin from *Lactuca sativa* var. *capitata* (Compositae). *Journal of The Chemical Society*, 10, 621-622.
- Tindall H.D. (1983). *Vegetables in the tropics*. Macmillian Education Ltd, Hong Kong.
- Woods, A.M., Fagg, J., & Mansfield, J.W. (1988). Fungal development and irreversible membrane damage in cells of *Lactuca sativa* undergoing the hypersensitive reaction to the downy mildew fungus *Bremia lactucae*. *Physiological and Molecular Plant Pathology*, 32, 483-497.
- Woods, A.M., Fagg, J., & Mansfield, J.W. (1989). Effect of heat-shock and inhibitors of protein synthesis on irreversible membrane damage occurring during the hypersensitive reaction of *Lactuca sativa* L. to *Bremia lactucae* Regel. *Physiological and Molecular Plant Pathology*, 34, 531-544.

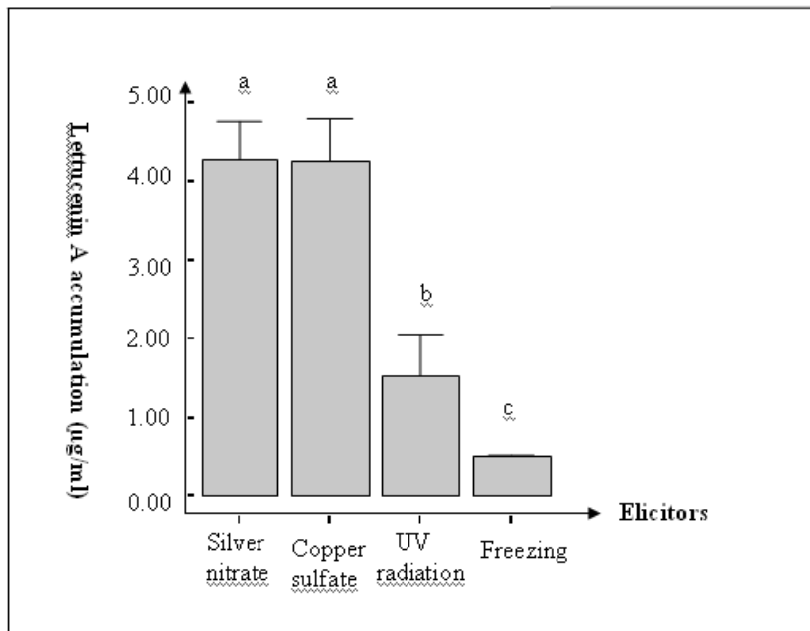


Figure 1. The concentration of lettukenin A accumulated in respond to different type of elicitors. Bar represented means of three replicates with 15g of lettuce leaves per replicate.

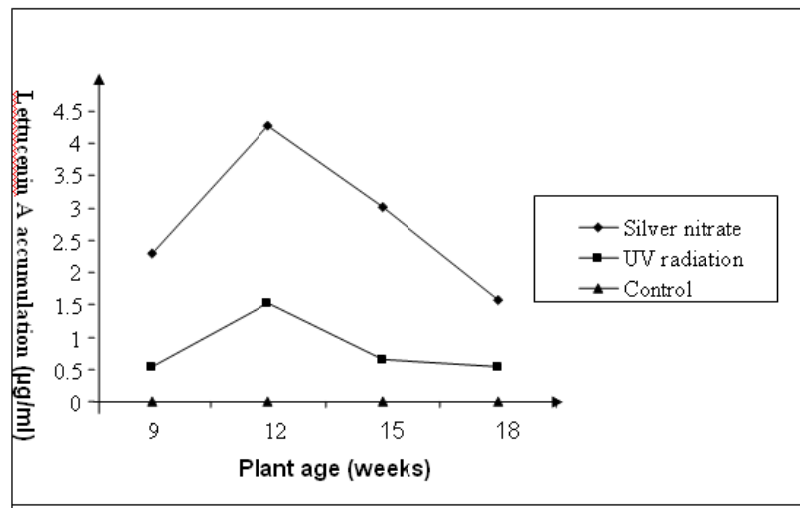


Figure 2. Accumulation of lettukenin A in lettuce at different age (weeks) after elicited by silver nitrate (AgNO_3) and ultraviolet radiation at 254nm. Data represent means of three independent experiments with 15g of lettuce leaves per treatment.



Effect of Polypropylene Fiber on Shrinkage Properties of Cement-stabilized Macadam

Zhifeng Chen

Highway Survey and Design Institute of Zhoukou

Zhoukou 466000, China

Abstract

A parametric experimental study has been conducted to investigate the effect of polypropylene fiber on the shrinkage of cement-stabilized macadam. By means of the micrometer gauge method and the strain gauge method, the dry shrinkage coefficient and thermal shrinkage coefficient of cement-stabilized macadam were measured respectively. The results indicate that polypropylene fiber can effectively decrease the average dry shrinkage coefficient and average thermal shrinkage coefficient of cement-stabilized macadam. The average dry shrinkage coefficient of long curing period is smaller than that of short curing period, while the average thermal shrinkage coefficient of long curing period is much larger than that of short curing period. When the fiber volume fraction is not beyond 0.1%, the average dry shrinkage coefficient and average thermal shrinkage coefficient are gradually decreasing with the increase in fiber volume fraction. Furthermore, polypropylene fiber appears to be highly effective in controlling dry and thermal shrinkage cracking of cement-stabilized macadam.

Keywords: Cement-stabilized macadam, Polypropylene fiber, Dry shrinkage, Thermal shrinkage, Average shrinkage coefficient

1. Introduction

As a kind of material of semi-rigid base course in asphalt pavements, compared with other semi-rigid base course materials, cement-stabilized macadam is characterized by its advantages, such as higher strength and rigidity and more excellent wholeness and water stability. Therefore, it has been used as the main base course material of high-grade highways with semi-rigid base courses and asphalt surface layers for a long period in China. However, this material also presents some disadvantages such as high brittleness, poor resistance to deformation and high shrinkage rate, so it is prone to crack when it is subjected to the changes of temperature and humidity.

Some research has indicated that polypropylene fiber can improve the resistance to deformation and anti-cracking property of cement-stabilized macadam effectively, while the strength of cement-stabilized macadam will decrease a little after mixing with polypropylene fiber. Accordingly, polypropylene fiber has better application prospect in cement-stabilized macadam to control shrinkage cracks. However, the above-mentioned polypropylene fibers applied in cement-stabilized macadam are all long fibers, the length of which is from 50 to 70 mm. Currently only a limited number of documents are found on the properties of cement-stabilized macadam reinforced with polypropylene short fiber. However, none of the other phases have been studied the dry and thermal shrinkage properties of cement-stabilized macadam reinforced with polypropylene fiber. Therefore, we conducted this parametric study to investigate the effects of polypropylene short fiber on the mechanical properties and shrinkage properties of cement-stabilized macadam. In this study, the length of the polypropylene short fiber is from 10 to 20mm. The properties of dry shrinkage and thermal shrinkage are evaluated with the indices of average dry shrinkage coefficient and average thermal shrinkage coefficient respectively.

2. Materials and Experimental Methods

2.1 Materials used

The polypropylene fiber used in this investigation was bunched single short fiber, which was manufactured by mixing modified polypropylene short fiber with different lengths and section shapes together in proportion in special production techniques. The basic physical properties of polypropylene fiber in this study are shown in Table 1. Four fiber volume fractions were adopted (0.04, 0.06, 0.08 and 0.1%). The cement used was the Class 42.5R Ordinary Portland cement with the content of 5%. The macadam used was composed of five kinds of aggregates with different size ranges. The aggregate has a maximum size of 30mm, and the aggregate with a minimum size of 2.5mm was replaced by river sands. The fineness modulus of the river sands is 2.73. The composite gradation of the aggregate

referred to the median of the gradation range prescribed for cement-stabilized base course materials of high-grade highway in the Chinese standard (JTJ 014-97, 2001). The gradation of the macadam adopted in this investigation is shown in Table 2.

2.2 Preparation of specimens

A series of beam specimens with the size of 100×100×400 mm were used to determine the average dry and thermal shrinkage coefficients. The beam moulds for the preparation of beam specimens were self-made steel moulds, which were designed referring to the preparing principle of cylinder specimens in the Chinese Standard (JTJ 057-94, 2004). All the specimens were prepared by compacting at their respective maximum dry density and optimum moisture content, and the compacting and stripping of the specimens were both carried out by pressure testing machine. Before being stripped, the specimens were covered by plastic sheets and allowed to stand for 4-5 h. After stripping, the specimens sealed in plastic sheets were cured at 100% relative humidity and controlled temperature ($21 \pm 2^\circ\text{C}$) before testing. In order to compare the effect of polypropylene fiber, besides the four sets of specimens of polypropylene fiber cement-stabilized macadam, another set of specimens without mixed fibers was prepared.

2.3 Dry shrinkage test

Dry shrinkage test was carried out in the constant temperature box with the constant temperature of 40°C . The specimen was supported by several glass bars with the same diameter on a pallet fixed in a bracket, and two micrometers with dial indicators were fixed in the bracket to measure the dry shrinkage deformation. After the testing began, the additional specimen was weighed every 2 h until the last two weights were equal. Finally, the final numerical reading shown in the micrometer with dial indicator was noted. The dry shrinkage coefficient can be computed as follows:

$$\alpha_d = \frac{\varepsilon}{\omega_2 - \omega_1} \quad (1)$$

$$\varepsilon = \frac{\Delta_2 - \Delta_1}{L} \quad (2)$$

where, α_d , dry shrinkage coefficient, $\mu\text{e}/\%$; ε , dry shrinkage strain, μe ; Δ_1 , Δ_2 , initial and final numerical reading shown in the micrometer with dial indicator respectively, mm; ω_1 , ω_2 , initial and final moisture contents of the specimen respectively, %; L , length of the specimen, mm. For dry shrinkage tests, each set includes 3 specimens, and the average value of 3 data was computed as the final result.

2.4 Thermal shrinkage test

Thermal shrinkage test was carried out in the Hi-Lo temperature experimental box with the temperature range of 40 to -20°C . The thermal strain was measured by resistance strain gauges (Hu, 2004). The initial temperature of the experimental box was set to be 40°C , and the initial strain was read after the temperature was kept unchanged for 4 h. Then the temperature was lowered from 40 to -20°C at the rate of $0.5^\circ\text{C}/\text{min}$, and the final strain was read after the temperature of -20°C was kept unchanged for 4 h. The thermal shrinkage coefficient can be computed as follows:

$$\alpha_t = \frac{\varepsilon_2 - \varepsilon_1}{T_2 - T_1} + \beta \quad (3)$$

where, α_t , thermal shrinkage coefficient, $\mu\text{e}/^\circ\text{C}$; ε_1 , ε_2 , initial and final thermal strain respectively, μe ; T_1 , T_2 , initial and final temperature in the experimental box respectively, $^\circ\text{C}$; β , thermal shrinkage coefficient of the temperature compensation plate, $\mu\text{e}/^\circ\text{C}$. For thermal shrinkage tests, each set also includes 3 specimens, and the average value of 3 data was computed as the final result.

3. Experimental Results and Discussion

3.1 Effect of polypropylene fiber volume fraction on dry shrinkage property

Fig. 1 shows the varying rule of the average dry shrinkage coefficient of non-fibrous cement-stabilized macadam and polypropylene fiber-reinforced cement-stabilized macadam as the volume fraction of fiber varies. From the figure, it can be seen that polypropylene fiber can effectively restrain the dry shrinkage of cement-stabilized macadam. For instance, when the volume fraction of polypropylene fiber is 0.1%, compared with non-fibrous cement-stabilized macadam, the average dry shrinkage coefficient (28d) decrease 42%. After polypropylene fibers were mixed into cement-stabilized macadam, as the binding material of the sands and macadam, cement also bonds a large number of fine and short fibers. So the area of water loss of the cement-stabilized macadam will be reduced, and the water inside the matrix is difficult to move, which will decrease the capillary tension produced by the shrinkage for water loss of capillaries. Meanwhile, there are interface cohesive strength and mechanical interlocking action between the matrix and

the fiber. Therefore, the average dry shrinkage coefficient was evidently decreased after polypropylene fibers were mixed into cement-stabilized macadam. When the curing period is 7d, the comprehensive action of the capillary tension, the intermolecular force of the adsorbed water and the shrinkage force of the interlayer water inside cement-stabilized macadam is much smaller than that of 28d, and therefore the average dry shrinkage coefficient of 7d is higher than that of 28d (Zhang, 2006). However, whether the curing period is 7d or whether the curing period is 28d, there is a tendency of decrease in the average dry shrinkage coefficient of cement-stabilized macadam with the increase of polypropylene fiber volume fraction within the range of the fiber dosage in this study, which is not beyond 0.1%. As the volume fraction of polypropylene fiber increases, the number of randomly distributed fibers in cement-stabilized macadam mixture increases. According to the fiber spacing theory (Nemkumar, 2006, pp. 1263-1267), the confinement force of fibers on the mixture and cement paste will increase if the spacing between two adjacent fibers decreases, so the restriction of fibers on dry shrinkage of the mixture is strengthened. As a result, the average dry shrinkage coefficient will have a tendency of decrease as the volume fraction of polypropylene fiber increases.

3.2 Effect of polypropylene fiber volume fraction on thermal shrinkage property

Fig. 2 shows the contrast relationship between the average thermal shrinkage coefficient of non-fibrous cement-stabilized and polypropylene fiber-reinforced cement-stabilized macadam with different fiber dosages. From the figure, it can be seen that the addition of polypropylene fiber can decrease the average thermal shrinkage coefficient effectively. For instance, when the volume fraction of polypropylene fiber is 0.1%, the average thermal shrinkage coefficient (28d) decreases from $8.0 \mu\epsilon/^\circ\text{C}$ (non-fibrous cement-stabilized macadam) to $6.3 \mu\epsilon/^\circ\text{C}$, and it is reduced by 21%. The cement-stabilized macadam reinforced with polypropylene fiber can be regarded as a kind of composite material, and its thermal properties depend upon the comprehensive action of the matrix and the fibers. The thermal coefficient of polypropylene fiber is very small, which is only about 10% of that of cement-stabilized macadam, and therefore when the composite material is subjected to drops in temperature, it is not sensitive to the temperature variation. Moreover, the polypropylene fibers distributed in cement-stabilized macadam are in three-dimensional and disordered directions, and they will form a network structure by overlapping each other. Therefore, polypropylene fiber can obviously decrease the average thermal coefficient of cement-stabilized macadam. At the early stage of the curing period, the ratio of various binding materials and hydrates with higher thermal coefficient in the whole composite material is much smaller, and the ratio will increase with the running of various chemical reactions inside the mixture. As a result, the average thermal shrinkage coefficient of polypropylene fiber-reinforced cement-stabilized macadam of 28d is higher than that of 14d. However, when the fiber dosage is not beyond 0.1%, whether the curing period is 14d or whether the curing period is 28d, the inhibit function of the fibers on the thermal shrinkage of cement-stabilized macadam is strengthened with the increase of polypropylene fiber volume fraction, and accordingly, the average thermal shrinkage coefficient of cement-stabilized macadam is decreasing gradually.

4. Summary and Conclusions

This paper reported experimental results of dry and thermal shrinkage studies conducted on cement-stabilized macadam reinforced with polypropylene fiber. The following conclusions can be draw from the results presented in this paper:

- 1) Polypropylene fiber is highly effective in controlling the dry and thermal shrinkage of cement-stabilized macadam. A 0.1% dosage of fibers (by volume fraction) resulted in a 42% decrease in the dry shrinkage coefficient and a 21% decrease in the thermal shrinkage coefficient of cement-stabilized macadam (28d). The decrease in the dry and thermal shrinkage coefficients will improve the anti-cracking performance of cement-stabilized macadam base course obviously.
- 2) With the increase of polypropylene fiber volume fraction, and accordingly, there is a tendency of decrease not only in the average dry shrinkage coefficient but also in the average thermal shrinkage coefficient of cement-stabilized macadam, and consequently, the crack resistance of cement-stabilized macadam base course will be increased gradually.

References

- Hu, Liqun. (2004). *Research on structural characteristic and component design methods for semi-rigid base course material*. Ph.D. dissertation, Chang'an University.
- JTJ 014-97. (2001). *Specifications for design of highway asphalt pavement*. Beijing: China Communications Press.
- JTJ 057-94. (2004). *Test methods of materials stabilized with inorganic binders for highway engineering*. Beijing: China Communications Press.
- Nemkumar, Banthia and Rishi, Gupta. (2006). Influence of polypropylene fiber geometry on plastic shrinkage cracking in concrete. *Cement and Concrete Research*, 36(7), 1263-1267.
- Zhang, Gazhi. (2006). *Mix design and road performance of cement and flyash stabilized crushed-stones roadbases*. Ph.D. dissertation, Chang'an University.

Table 1. Physical properties of polypropylene fiber

Density (g/cm ³)	Linear density (dtex)	Fiber length (mm)	Tensile strength (MPa)	Elastic modulus (MPa)	Melting point (°C)
0.91	10~20	10-20	≥ 450	≥ 4100	160~170

Table 2. Gradation of the macadam

Sieve size (mm)	31.5	19	9.5	4.75	2.36	0.6	0.075
Percentage passing of aggregate (%)	100	94.3	67.64	41.96	26.9	9.68	0.26

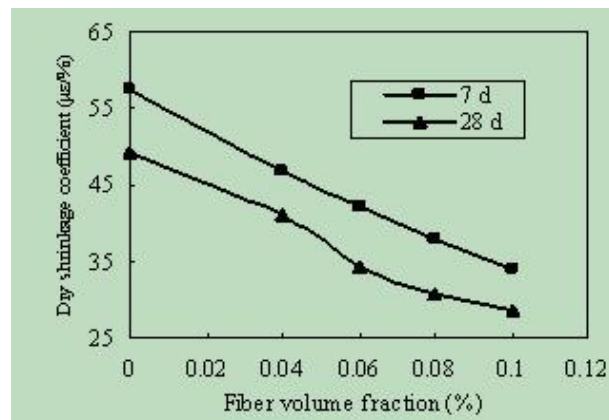


Figure 1. Effect of fiber volume fraction on dry shrinkage coefficient

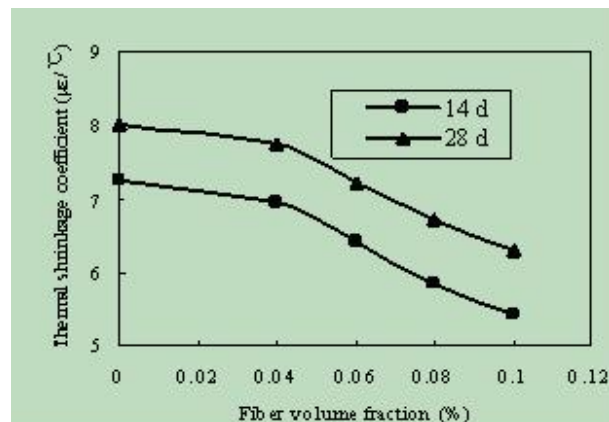


Figure 2. Effect of fiber volume fraction on thermal shrinkage coefficient



Genetic Algorithm for Document Clustering with Simultaneous and Ranked Mutation

K. Premalatha (Corresponding Author)

Kongu Engineering College

Perundurai, Erode, TN, India

E-mail: kpl_barath@yahoo.co.in

A.M. Natarajan

Bannari Amman Institute of Technology

Coimbatore, TN, India

Abstract

Clustering is a division of data into groups of similar objects. Each group, called cluster, consists of objects that are similar between themselves and dissimilar to objects of other groups. The clustering algorithm attempts to find natural groups of components, based on some similarity. Traditional clustering algorithms will search only a small sub-set of all possible clustering and consequently, there is no guarantee that the solution found will be optimal. This paper presents the document clustering based on Genetic algorithm with Simultaneous mutation operator and Ranked mutation rate. The mutation operation is significant to the success of genetic algorithms since it expands the search directions and avoids convergence to local optima. In each stage of the genetic process in a problem, may involve aptly different mutation operators for best results. In simultaneous mutation the genetic algorithm concurrently uses several mutation operators in producing the next generation. The mutation ratio of each operator changes according to assessment from the respective offspring it produces. In ranked scheme, it adapts the mutation rate on the chromosome based on the fitness rank of the earlier population. Experiments results are examined with document corpus. It demonstrates that the proposed algorithm statistically outperforms the Simple GA and K-Means.

Keywords: Genetic algorithm, Clustering, Tf-idf, Convergence, K-means, Simultaneous and Ranked mutation

1. Introduction

Document clustering is an automatic grouping of text documents into clusters so that documents within a cluster have high similarity in comparison to one another, but are dissimilar to documents in other clusters. Unlike document classification (Wang, K., Zhou, S., & He Y. 2001), no labeled documents are provided in clustering; hence, clustering is also known as unsupervised learning. Document clustering is widely applicable in areas such as search engines, web mining, Information retrieval and topological analysis. Many clustering techniques have been developed and they can be applied to clustering documents. (Jain A.K., M.N. Murthy, P.J. Flynn. 1999) contain examples of using such techniques. A Genetic Algorithm (GA) is a computational abstraction of biological evolution that can be used to solve some optimization problems (John Holland. 1975.) (Goldberg). In this paper, the documents are clustered based on Genetic algorithm with dynamic mutation operator and adaptive mutation rate for faster convergence. The proposed system is an iterative process applying a series of genetic operators such as selection, crossover and mutation to a population of elements. These elements, called chromosomes or individuals represent possible solutions to the problem; the initial chromosomes are selected randomly from the solution space. Genetic operators combine the genetic information of the elements to form new generations of the population; this process is known as reproduction and mutation. Each chromosome has an associated fitness value which quantifies its value as a solution to the problem- a chromosome representing a better solution will have a higher fitness value. The chromosomes compete to reproduce based on their fitness values, thus the chromosomes representing better solutions have a higher chance of survival

2. Review of Related works

While a lot of work has focused on clustering of numeric data only a limited number of studies have focused on categorical clustering; these include STIRR (Gibson D, J. Kleinberg, and P. Raghavan. 1998.), ROCK (Guha S, R.

Rastogi, K. Shim. 1999.) CACTUS (Ganti V, J. Gehrke, and R. Ramakrishnan. 1999.) COOLCAT (Barbara D, Y. Li, and J. Couto. 2002.), kmodes (Huang Z. 1997.) and others more (Cristofor D, D. Simovici. 2002.)(Zhang. Y, A. Fu, C. Cai, P. Heng. 2000.) Other works have focused more narrowly on binary or transactional data (Ordonez C. 2003.)(Wang, K., Zhou, S., & He Y. 2001.) , on a framework to compress high dimensional categorical datasets (KoyutÄurk M , A. Grama. 2003.) and on using hypergraph partitioning to cluster itemsets (Han E, G. Karypis, V. Kumar, B. Mobasher. 1997.). For document clustering the recent studies have shown that partitioning clustering algorithms are more suitable for clustering large datasets due to their relatively low computational requirements (Makagonov, P., Alexandrov, M., Gelbukh, A. 2002.)(Zhao Y, Karypis G. 2004.). In the field of clustering, K-means algorithm is the most popularly used algorithm to find a partition that minimizes mean square error (MSE) measure. Although K-means is an extensively useful clustering algorithm, it suffers from several drawbacks. The objective function of the K-means is not convex and hence it may contain local minima. Consequently, while minimizing the objective function, there is possibility of getting stuck at local minima (also at local maxima and saddle point) (Selim SZ, Ismail MA. 1984.). The performance of the K-means algorithm depends on the initial choice of the cluster centers. Besides, the Euclidean norm is sensitive to noise or outliers. Hence K-means algorithm should be affected by noise and outliers (Wu KL, Yang MS. 2002.)(Jones G, Robertson A, Santimetvirul C, Willett P. 1995.).

There are earlier works that apply GA and evolutionary programming to clustering. Some of them deal with clustering a set of objects by assuming that the appropriate value of k is known (Goldberg.)(Chu S.C., Roddick J.F., Pan J.S. 2002.) (Murthy C.A., Chowdhury N. 1996.)(Merz P., Zell A. 2002.)(Lucasius C.B., Dane A.D., Kateman G. 1993.). However, in [23] an evolutionary programming-based clustering algorithm is proposed that groups a set of data into an optimum number of clusters. It is based on the well known K-means algorithm. They use two objective functions that are minimized simultaneously: one gives the optimum number of clusters, whereas the other leads to proper identification of each cluster's centroids. (Casillas, M. T. Gonzalez de Lena, and R. Martinez) used only one objective function at the same time both aspects of the solution is calculated: an approximation to the optimum. k value, and the best grouping of the objects into these k clusters. In (Makagonov, P., Alexandrov, M., Gelbukh, A. 2002.) discusses other heuristics to split the dendrite in an optimal way without fixing the number of clusters.

In this work, a method is proposed for the clustering a set of documents using Genetic algorithm with simultaneous mutation operator with ranked mutation rate. The main aim is to provide the best grouping of the objects into k clusters. The remainder of the paper is organized as follow: Section 3 presents the Simple Genetic Algorithm. Section 4 describes the proposed genetic algorithm with simultaneous and ranked mutation for document clustering. Section 5 describes the experiments and their results.

3. Simple Genetic Algorithm

Genetic Algorithms are a family of computational models inspired by evolution. These algorithms encode a potential solution to a specific problem on a simple chromosome-like data structure and apply recombination and mutation operators to these structures so as to preserve critical information. An implementation of a genetic algorithm begins with a population of (usually random) chromosomes. One then evaluates these structures and allocates reproductive opportunities in such a way that those chromosomes which represent a better solution to the target problem are given more chances to reproduce than those chromosomes which are poorer solutions. The goodness of a solution is typically defined with respect to the current population. Usually there are only two main components of genetic algorithms that are problem dependent: the problem encoding and the fitness function (objective function / evaluation function). A problem can be viewed as a black box with different parameters: The only output of the black box is a value returned by an evaluation function indicating how well a particular combination of parameter settings solves the optimization problem. The goal is to set the various parameters so as to optimize some output. In more traditional terms that to maximize (or minimize) some function $F(X_1, X_2, \dots, X_m)$

The first assumption that is typically made is that the variables representing parameters can be represented by strings and the evaluation function is usually given as part of the problem description. The genetic algorithm can be viewed a two stage process. It starts with the current population. Selection is applied to the current population to create an intermediate population. Then recombination and mutation are applied to the intermediate population to create the next population. The process of going from the current population to the next population constitutes one generation in the execution of a genetic algorithm. (Goldberg) refers to this basic implementation as a Simple Genetic Algorithm (SGA)

In the first generation the current population is also the initial population. There are a number of ways to do selection. After selection has been carried out the construction of the intermediate population is complete and recombination can occur. This can be viewed as creating the next population from the intermediate population. Crossover is applied to randomly paired strings with a probability denoted P_c . (The population should already be sufficiently shuffled by the random selection process) Pick a pair of strings with probability P_c recombine these strings to form two new strings that are inserted into the next population. After recombination, mutation operator is applied. For each bit in the population, mutate with some low probability P_m . Typically the mutation rate is applied with less than 1% probability.

In some cases mutation is interpreted as randomly generating a new bit in which case, only 50% of the time will the mutation actually change the bit value. After the process of selection, recombination and mutation, the next population can be evaluated. The process of evaluation, selection, recombination and mutation forms one generation in the execution of a genetic algorithm.

Algorithm

- 1) Generate an initial, random population of chromosomes.
- 2) Test the fitness of each chromosome in the population.
- 3) Select parents as the most fit members of the population.
- 4) Reproduce from selected parents to produce a new population.
- 5) Mutate according to some probability.
- 6) Test the fitness of each chromosome in the new population.
- 7) Evaluation
- 8) Iterate steps 3 to 7 until termination criterion is met.

To successfully apply a GA to solve a problem one needs to determine the following:

- 1) How to represent possible solutions, or the chromosomal encoding;
- 2) What to use as the fitness function which accurately represents the value of the solution;
- 3) Which genetic operators to employ; and
- 4) The parameter values (population size, probability of applying operators, etc.) which are suitable.

4. GA With Simultaneous and Ranked Mutation

The algorithm begins with the initial solutions population of the problem. This population is generated randomly. Each one of these solutions must be evaluated by means of a fitness function; the result of this evaluation is a measure of individual adaptation. The individuals with the best adaptation measure have more chances of reproducing and generating new individuals.

4.1 Problem Formulation

The objective of optimization is to seek value for set of parameters that maximize or minimize objective functions subject to certain constraints. A choice of values for the set of parameters that satisfy all constraints is called a feasible solution. Feasible solutions with objective function value as good as the values of any other feasible solutions are called optimal solutions.

The objective function of the document clustering problem is given as follows:

$$f = \frac{\sum_{i=1}^{N_c} \frac{\sum_{j=1}^{P_i} m_{ij} \cdot O_j}{\|m_{ij}\| \cdot \|O_j\|}}{N_c} \quad (1)$$

The function f should be maximized.

- where
- m_{ij} : j th document vector belongs to cluster i
 - O_i : Centroid vector of the i^{th} cluster
 - P_i : stands for the number of documents, which belongs to cluster C_i ;
 - N_c : number of clusters.

4.2 Document Vectorization

It is necessary to convert the document collection into the form of document vectors. Firstly, to determine the terms that is used to describe the documents. Extraction of all the words from each document.

- 1) Elimination of the stopwords from a stopword list generated with the frequency dictionary of (Kucera, H., & Francis, N. 1967.)
- 2) Stemming the remaining words using the Porter Stemmer which is the most commonly used stemmer in English
- 3) Formalizing the document as a dot in the multidimensional space and represented by a vector d , such as $d = \{w_1, w_2, \dots, w_n\}$, where w_i ($i = 1, 2, \dots, n$) is the term weight of the term t_i in one document. The term weight value represents the significance of this term in a document. To calculate the term weight, the occurrence frequency of the term within a

document and in the entire set of documents must be considered. The most widely used weighting scheme combines the Term Frequency with Inverse Document Frequency (TF-IDF). The weight of term i in document j is given in equation (2)

$$W_{ji} = tf_{ji} \times idf_{ji} = tf_{ji} \times \log_2 (n/df_{ji}) \quad (2)$$

where tf_{ji} is the number of occurrences of term i in the document j ; df_{ji} indicates the term frequency in the collections of documents; and n is the total number of documents in the collection.

4.3 Chromosome Representation

The algorithm uses chromosomes which codify the whole partition P of the data set in a vector of length n , where n is the size of the dataset. Thus, each gene of the chromosome is the label where the single item of the dataset belongs to; in particular if the number of cluster is k each gene of the chromosome is an integer value in the range $\{1, \dots, K\}$. An example of chromosome is reported in Figure 2.

4.4 Initial Generation

At the initial stage, each individual randomly chooses k different document vectors from the document collection as the initial cluster centroid vectors. For, each individual, a gene assigns a document vector from the document collection to the closest centroid cluster. The allele of gene represents the cluster where the document is present. The objective function for each individual can be calculated based on the equation (1).

4.5 Selection

In selection the offspring producing individuals are chosen. The first step is fitness assignment. Each individual in the selection pool receives a reproduction probability depending on the own objective value and the objective value of all other individuals in the selection pool. This fitness is used for the actual selection in the step afterwards. The simplest selection scheme is roulette-wheel selection, also called stochastic sampling with replacement. The proposed system employs roulette-wheel selection method.

4.6 Crossover

The interesting behavior happens from genetic algorithms because of the ability of the solutions to learn from each other. Solutions can combine to form offspring for the next generation. Occasionally they will pass on their worst information, but doing crossover in combination with a powerful selection technique perceives better solutions result. Crossover occurs with a user specified probability called, the crossover probability P_c . Many crossover techniques exist for individual. In single point crossover, a position is randomly selected at which the parents are divided into two parts. The parts of the two parents are then swapped to generate two new offspring.

4.7 Simultaneous and Ranked Mutation

The purpose of mutation is to diversify the search direction and prevent convergence to the local optimum. Mutation is a genetic operator that alters one or more gene values in a chromosome from its initial state. This can result in entirely new gene values being added to the gene pool. With these new gene values, the genetic algorithm may be able to arrive at better solution than was previously possible. Mutation is an important part of the genetic search as help to prevent the population from stagnating at any local optima. It prevents local searches of the search space and increases the probability of finding global optima. Mutation occurs during evolution according to a user-definable mutation probability P_m

4.7.1 Simultaneous Mutation Operator

The proposed algorithm at once uses several mutation operators in producing the next generation. The mutation ratio of each operator changes according to evaluation results from the respective offspring it produces (Tzung-Pei Hong, Hong-Shung Wang, Wei-Chou Chen. 2000.). Thus, the appropriate mutation operators can be expected to have increasingly greater effects on the genetic process. It automatically chooses a proper mutation operator, or to handle situations in which different operators are suitable for different genetic stages. Initially, the mutation ratios are the same for all operators. After a new generation or several generations, the mutation ratio of each operator is automatically and dynamically adjusted. The mutation ratios of suitable operators (evaluated according to fitness values) are increased and the mutation ratios of unsuitable operators are decreased. The highly effective mutation operators will have increasingly greater effects on the genetic process.

Assume N mutation operators are applied in the proposed algorithm. Initially, the mutation ratios of all available mutation operators are set equal ($1/N$ of the total mutation ratio for the problem). Each mutation operator is then applied according to its assigned probability, and offspring fitness is evaluated. The mutation operators that result in higher average fitness values then have their control ratios increased. The mutation operators that result in lower average fitness values then have their control ratios decreased. Finally, the most suitable mutation operator stands out and

controls almost all the mutation behavior in the population. The dynamic mutation genetic algorithm is then theoretically better than most genetic algorithms that use only single mutation operators.

Algorithm

Calculate the average growth value $P(M_i)$ $I = 1$ to m (the number of applied mutation operators), given by each mutation operator. Assume a parent p is chosen by a mutation operator to produce a child a . the progress value of the mutation operator for this operation is calculated is given in equation (3)

$$P = \max(f(p), f(a)) - f(p) \quad (3)$$

$f(p)$ – Fitness function selected for Parent

$f(a)$ – Fitness function for a

Assume r parents are chosen by this mutation operator in this generation. The progress value $P(M_i)$ of this mutation operator M_i is then the average of the r values. The Mutation ratio is calculated as follows (4) :

$$M_r = \frac{P(M_i)}{\sum P} \times N \quad (4)$$

M_r = Mutation Ratio

N – Number of Parents selected for Mutation

4.7.2 Ranked Mutation Rate

In this study, different mutation rates are assigned to each chromosome based on the fitness rank of the earlier population.

$$P_m = \left(\text{Max} - \frac{\text{Max} - \text{Min}}{\text{NOI}} \times T \right) \times \frac{\text{rank}}{R}$$

Max = Maximum Mutation rate

Min = Minimum Mutation rate

NOI = Number of Iterations

T = Time epoch (or) Iteration number

R = Total number of Ranks

4.8 Evaluation

After producing offspring they must be inserted into the population. This is especially important, if less offspring are produced than the size of the original population. Another case is, when not all offspring are to be used at each generation or if more offspring are generated than needed. By a reinsertion scheme is determined which individuals should be inserted into the new population and which individuals of the population will be replaced by offspring. The used selection algorithm determines the reinsertion scheme. The elitist combined with fitness-based reinsertion prevents this losing of information and is the recommended method. At each generation, a given number of the least fit parent is replaced by the same number of the most fit offspring. Fig 3 shows the proposed system.

5. Experiment Results

The proposed system experimented on some common datasets CISI, Cranfield and ADI available at the Glasocow [http://www.dcs.gla.ac.uk/idom/ir_resources/test_collections/]. The number of individuals selected for each generation is 20 for 3 clusters. Random and Boundary mutation operators are preferred for simultaneous mutation. In K-Means algorithm the clusters reformed such that the sum of square errors to be minimal. The main goal of the system is to maximize the fitness value and fastening the convergence to near global optimal solution. Figure 4 shows the fitness value obtained from GA with random mutation operator, GA with boundary mutation operator, GA with simultaneous random and boundary mutation operators with ranked mutation rate and K-Means algorithm.

CONCLUSION

The objective of this paper is to present the potential power of the mutation operator in Genetic algorithm to solve the combinatorial optimization problems, which has a variety of applications in the real world. The proposed technique markedly increased the success of the document clustering problem. Two models were used in comparison, namely the Simple GA and K-Means. The proposed model was outperformed by the Simple GA and K-Means regarding a comparison of the best optima found. Yet, the proposed system had a marginally faster convergence than Simple GA and K-Means due to simultaneous and ranked nature of mutation operator.

References

- Barbara D, Y. Li, and J. Couto. (2002). Coolcat: an entropy-based algorithm for categorical clustering. In ACM Press, pages 582-589.
- Casillas, M. T. Gonzalez de Lena, and R. Martinez, Document Clustering into an unknown number of clusters using a Genetic Algorithm.
- Chu S.C., Roddick J.F., Pan J.S.: "An Incremental Multi-Centroid, Multi-Run Sampling Scheme for k-medoids-based Algorithms-Extended Report". Proceedings of the Third International Conference on Data Mining Methods and Databases, Data Mining III, (2002), 553–562.
- Cristofor D, D. Simovici.(2002). An information-theoretical approach to clustering categorical databases using genetic algorithms. In *2nd SIAM ICDM, Workshop on clustering high dimensional data*.
- Estivill-Castro V., Murray A.T.: "Spatial Clustering for Data Mining with Genetic Algorithms". *Proceedings of the International ICSC Symposium on Engineering of Intelligent Systems*, EIS-98, (1998).
- Ganti V, J. Gehrke, and R. Ramakrishnan. CACTUS: Clustering categorical data using summaries. In ACM SIGKDD Int'l Conference on Knowledge discovery in Databases, 1999.
- Gibson D, J. Kleinberg, and P. Raghavan. (1998). Clustering categorical data: An approach based on dynamical systems. In 24th Int'l Conference on Very Large Databases.
- Goldberg. D Genetic Algorithms in Search Optimization and Machine Learning, Reading, MA: Addison Wesley.
- Guha S, R. Rastogi, K. Shim.(1999). Rock: A robust clustering algorithm for categorical attributes. In International Conference on Data Engineering.
- Han E, G. Karypis, V. Kumar, B. Mobasher.(1997). Clustering based on association rule hypergraphs. In *Research Issues on Data Mining and Knowledge Discovery*.
- Holland. J, Adaptation In Natural and Artificial Systems, University of Michigan Press, 1975.
- Huang Z. (1997). A fast clustering algorithm to cluster very large categorical data sets in data mining. In *SIGMOD Workshop on Research Issues on Data Mining and Knowledge Discovery*, Tucson, AZ, 1997.
- Jain A.K., M.N. Murthy, P.J. Flynn. (1999). Data Clustering : A Review ACM Computing Surveys, 31(3): 264-323.
- John Holland. Adaptation in Natural and Artificial Systems. University of Michigan Press, 1975.
- Jones G, Robertson A, Santimetrovirul C, Willett P. (1995). Non-hierarchical document clustering using a genetic algorithm. *Information Research*, 1(1).
- KoyutÄurk M, A. Grama. (2003). Proximus: A framework for analyzing very high-dimensional discrete attributed datasets. In *Proceedings of the Ninth ACM SIGKDD Intl. Conf. on Knowledge Discovery and Data Mining (KDD 2003)*, pages 147 - 156.
- Kucera, H., & Francis, N. (1967). Computational analysis of present-day American English. Providence, RD: Brown University Press.
- Lucasius C.B., Dane A.D., Kateman G.: "On k-medoid clustering of large data sets with the aid of Genetic Algorithm: background, feasibility and comparison". *Analytica Chimica Acta*, Elsevier Science Publishers B.V. 283(3), (1993) 647–669.
- Makagonov, P., Alexandrov, M., Gelbukh, A.: "Selection of typical documents in a document flow". *Advances in Communications and Software Technologies*, WSEAS Press (2002). 197–202.
- Merz P., Zell A.: "Clustering Gene Expression Profiles with Memetic Algorithms". *Lecture Notes in Computer Science* 2439, Springer-Verlag Berlin (2002). 811–820.
- Murthy C.A., Chowdhury N.: "In search of Optimal Clusters Using Genetic Algorithms". *Pattern Recognition Letters*, 17(8), (1996), 825–832.
- Ordonez C. (2003). Clustering binary data streams with k-means. In *Proceedings of DMKD*, pages 12 -19.
- Sarkar, M., Yegnanarayana, B., Khemani, D.: "A clustering algorithm using an evolutionary programming-based approach". *Pattern Recognition Letters*, 18, (1997). 975–986.
- Selim SZ, Ismail MA. (1984). K-means Type Algorithms: A Generalized Convergence Theorem and Characterization of Local Optimality, *IEEE Transaction on Pattern Analysis and Machine Intelligence*, 6, 81-87.
- Tzung-Pei Hong, Hong-Shung Wang, Wei-Chou Chen, Simultaneously Applying Multiple Mutation Operators in Genetic Algorithms, *Journal of Heuristics*, 6: 439–455, (2000).

Wang K , C. Xu, B. Liu. (1999). Clustering transactions using large items. In *CIKM*, pages 483 -490.

Wang, K., Zhou, S., & He Y. (2001, Apr.). Hierarchical classification of real life documents. *SIAM International Conference on Data Mining, SDM'01*, Chicago, United States.

Wu KL, Yang MS. (2002). Alternative C-means Clustering Algorithms. *PatternRecognition*, 35, 2267-2278.

Zhang. Y, A. Fu, C. Cai, P. Heng. (2000). Clustering categorical data. In *Proceedings of the ICDE*, page 305.

Zhao Y, Karypis G (2004). Empirical and Theoretical Comparisons of Selected Criterion Functions for Document Clustering, *Machine Learning*, 55(3), 311-331.

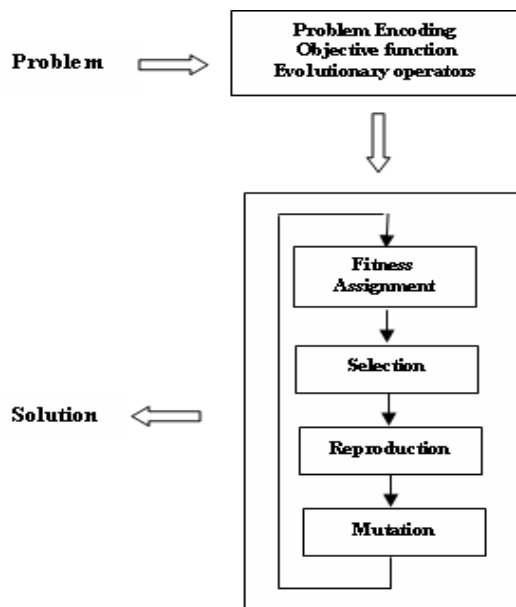


Figure 1. Simple Genetic algorithm

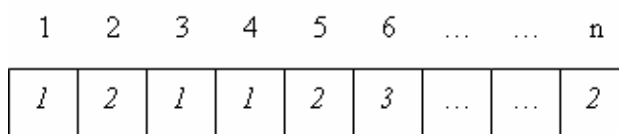


Figure 2. Chromosome representation

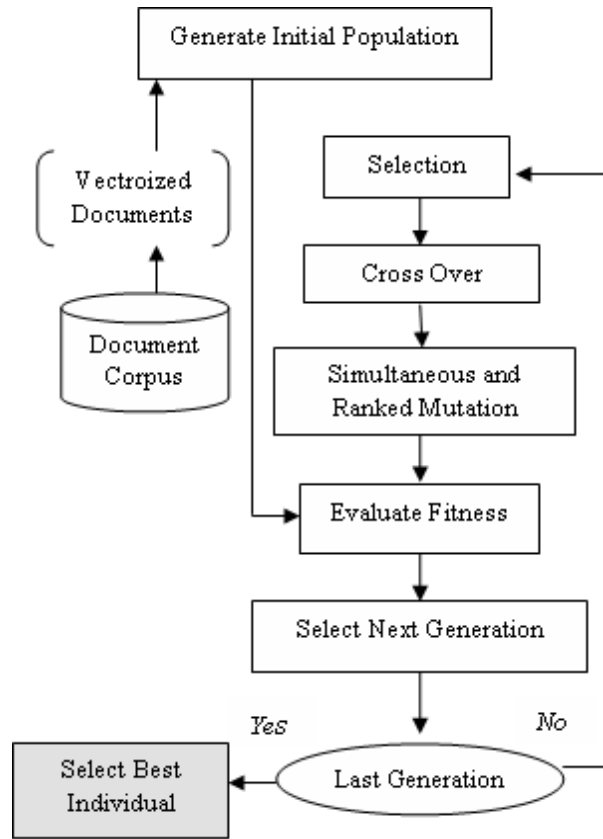


Figure 3. GA Simultaneous and Ranked Mutation for Document clustering

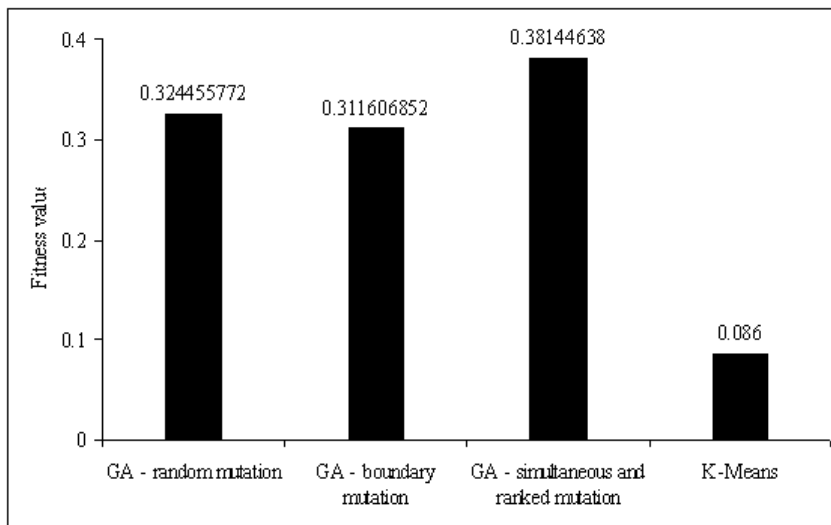


Figure 4. Fitness value obtained from various systems



Study on Cellulose-decomposed Actinomycetes in Soil in the Eastern of the Qinghai Plateau

Yan Cai

College of Resources and Environment

Northwest Sci-Tech University of Agriculture & Forestry

Yangling 712100, China

College of Resources and Environment

Sichuan Agriculture University

Yaan 625014, China

Tel: 86-835-8992-849 E-mail: caiyya@126.com

Quanhong Xue (Corresponding author)

College of Resources and Environment

Northwest Sci-Tech University of Agriculture and Forestry

Yangling 712100, China

Tel: 86-29-8709-1321 E-mail: xueqhong@public.xa.sn.cn

Zhanquan Chen & Rong Zhang

Institute of Soil and Fertilizer

Qinghai Academy of Agriculture and Forestry

Xining 810016, China

Abstract

The distribution of cellulose-decomposed actinomycetes was studied by conventional methods. Those microbes were separated in soil from the eastern part of Qinghai Plateau. The results indicated that: There were a certain amounts of cellulose-decomposed actinomycetes in soil from the eastern part of Qinghai Plateau. The number of cellulose-decomposed actinomycetes in vegetable field soil was higher than in grain field, but the strong cellulose-decomposed actinomycetes' ratio of cellulose-decomposed actinomycetes in vegetable field soil was lower than that in grain field. The strong cellulose-decomposed actinomycetes' ratio of the total cellulose-decomposed actinomycetes in natural soil had certain relevance with the soil organic matter content. In each kind of natural soil, the number of cellulose-decomposed actinomycetes in cumulated irrigated soil was the maximum, and the number of strong cellulose-decomposed actinomycete in castanozem was the most, and the strong cellulose-decomposed actinomycetes' ratio of cellulose-decomposed actinomycete in marsh soil was the highest. The results may provide scientific basis for separation and screening of the cellulose-decomposed actinomycetes.

Keywords: Quantity of actinomycete, Cellulose decomposition, Actinomycete, Qinghai Plateau

1. Introduction

Actinomycetes are an important class of microbial resources, they are important producers of antibiotics (erythromycin, rifampicin, extremadura, foreign erythromycin and so on), enzymes, vitamins and so on. Some antibiotics have been commercialized, and resulted in tremendous social value and economic value (Jiang Ch. L. and Xu L. H., 1997; Liu Zh. H., 2002; Liu Zh. H. and Jiang Ch. L., 2004). Soil is a good place for actinomycetes. It has been an open question that actinomycetes could decompose cellulose (You C. F., 1986). In fact, actinomycetes often play an important role in the latter part of cellulose decomposition (Ruan J. S., 1992). At present, research work of cellulose-decomposed actinomycetes often concentrates to find actinomycete strains having highly effective cellulase activity, their action mechanism and fermentation conditions (Qi Y. *et al.*, 2003; Song B. and Yang J., 2005; Wu X. *et al.*, 2007; B. Wu and Hu Y. Z., 2008.), and we are lack of system understanding of distribution of cellulose-decomposed actinomycetes under different ecological environment conditions, Especially ecological distribution of actinomycetes in the plateau soil. In

this paper, we had the preliminary study on the distribution of cellulose-decomposed actinomycetes under different soil use ways in the eastern of the Qinghai Plateau for the purpose of exploring resources actinomycetes distribution profile under the plateau special habitats and providing a scientific basis for actinomycete resources research, using and protection from special habitats.

2. Materials and methods

2.1 Natural Overview of Sampling areas

The eastern part of Qinghai Province mainly refers to Huangshui River Basin, whose west side is west of Qinghai Lake and east side is at the junction of Qinghai Province and Gansu Province. Its geographic coordinate is E 100°23'~102°47', N 36°16'~37°39', and its altitude is 1945~3311 meters. The Huangshui River Basin have complex and diverse ecological environment, such as farmland, pasture, salt lake, and sand and wasteland, etc., and is a microcosm of the unique ecological environment in Qinghai Province.

2.2 Sampling

We sampled 0~20cm soil samples or sampled according to different soil depths from 34 sampling plots from October 4th to 14th, 2000. Soil utilization ways of the sampling plots included grain land (dry land and irrigated land), vegetable field (open field and protected land) and natural soil, and they located at Haiyan county, Huangyuan county, Huangzhong county, Datong city, Xining city, Huzhu county, Ledu county and Pingan county Qinghai Province. Organic matter and pH of the soil samples were analyzed by conventional methods. Table 1 is the basic situation of the sampling points and the basic properties of soil samples.

<<Table 1. Basic conditions of sampling points and basic properties of soil samples>>

2.3 Separation and counting

Dilution plate spreading method was used to separate and count (Cheng L. J. and Xue Q. H., 2000). We selected microcrystalline cellulose agar as the experiment culture medium.

3. Results and discussion

The numbers of cellulose-decomposed actinomycetes in soil from the eastern of Qinghai Plateau were $8.0 \times 10^3 \sim 140.9 \times 10^4$ cfu/g, and the numbers of strong cellulose-decomposed actinomycetes were $0 \sim 55.6 \times 10^3$ cfu/g (Table 2), and whose changes were both significant. Values of $B / A \times 100$ ranged from 0 to 86.5, which noted that the strong cellulose-decomposed actinomycetes' ratios of the total cellulose-decomposed actinomycetes numbers had great difference in soil of different utilization ways.

<<Table 2. Distribution of cellulose-decomposed actinomycetes under different soil utilization ways in the eastern of Qinghai Plateau>>

3.1 Distribution of cellulose-decomposed actinomycetes under different soil utilization ways

3.1.1 Distribution of cellulose-decomposed actinomycetes in field soil

The distributions of cellulose-decomposed actinomycetes were different under different planting ways. Average number of cellulose-decomposed actinomycetes in vegetable field (79.5×10^4 cfu/g) was higher than those in grain field (52.9×10^4 cfu/g), but its $B/A \times 100$ mean value was 19.9, which was lower than grain field obviously (30.1). The reason possibly lied in grain field mainly planted wheat, rape and other grain crops, and the soil residual organic matters were senile plant remnant bodies, whose lignin content was high and which were difficult to degrade (Hu A. T. and Zhou L. X., 2003). The number and the proportion of strong cellulose-decomposed actinomycetes in grain field soil were both higher than vegetable field soil, that was the results of actinomycetes long-term adapting grain field soil environment. The many organic matters remained in vegetable field soil were new green plants bodies and easy to decompose (Hu A. T. and Zhou L. X., 2003), in addition altitudes of vegetable field were lower than grain field and its ground temperature was higher than the grain field, so microorganism activity was more active than the grain field. Therefore, although the multiple-crop index of vegetable field was higher than the grain field, but its quantity and proportion of strong cellulose-decomposed actinomycetes were lower than the grain field. We can also see from Table 2, the distributions of cellulose-decomposed actinomycetes in irrigated land soil and arid land soil had not obvious difference, which was also in protected land soil and open field soil.

3.1.2 Distribution of cellulose-decomposed actinomycetes in natural soil

From the distribution of cellulose-decomposed actinomycetes in natural soil (Table 2), We could see that the $B/A \times 100$ value and the organic matter had certain relevance. Such as the sorting of soil organic matter contents (g / kg) was 07 (21.7) <17 (35.5) <33 (39.3) <29 (54.9), and the sorting of $B / A \times 100$ values was 07(12.9) <17 (26.3) <33 (29.4) <29(65.5), which was exactly the same sequence with the previous. Organic matter contents of No. 12 and No.13 respectively were 69.8 g/kg and 116.4 g/kg, and their $B/A \times 100$ value were also high, which respectively were 54.5 and 43.0. On the same soil samples, organic matter content of the upper soil profile was generally higher than the lower, and

the number of cellulose-decomposed actinomycetes, the number of strong cellulose-decomposed actinomycetes and the $B / A \times 100$ value of the upper soil profile were all higher than those of the lower. For example (No.13 soil sample), the number of cellulose-decomposed actinomycetes of 0~7cm soil layer was 65.9×10^4 cfu/g, which was 39.6×10^4 cfu/g of 7~24cm soil layer and was 40% lower than the upper layer. The number of strong cellulose-decomposed actinomycetes of 0~7cm soil layer was 41.2×10^3 cfu/g, which was 4.1×10^3 cfu/g of 7~24cm soil layer, and the upper soil layer was 10.0 times of the lower soil layer. The $B / A \times 100$ value of 0~7cm soil layer was 62.5, which was 10.4 of 7~24cm soil layer, and the upper soil layer was 6 times of the lower layer. Several other soil samples' profile might could be seen this kind of change rule.

3.2 Distribution of cellulose-decomposed actinomycetes in different soil types

We could see from Table 3, as the parent material, topography, vegetation, and other differences between different soil types, there were clear differences of the distribution of cellulose-decomposed actinomycetes in different soil types. The number of cellulose-decomposed actinomycetes in cumulated irrigated soil was the maximum, which was 82.2×10^4 cfu/g, followed by fluvo-aquic soil (74.2×10^4 cfu/g) and serosem (73.8×10^4 cfu/g). The number of cellulose-decomposed actinomycetes in saline-alkali soil was the minimum, which was only 8.0×10^4 cfu/g and was consistent with its high salt content, sparse vegetation and low content of soil organic matter. The number of strong cellulose-decomposed actinomycetes in castanozem was the most (22.2×10^3 cfu/g), followed by alpine meadow soil (20.6×10^3 cfu/g). The number of strong cellulose-decomposed actinomycetes in forest brown soil was the least, which was only 1.1×10^3 cfu/g. The strong cellulose-decomposed actinomycetes ratio of cellulose-decomposed actinomycetes in marsh soil was the highest (54.5). Actinomycetes adopt dry environment and played an important role in decomposition of organic materials which was difficult to break down. Marsh soil was stagnant water for a long term, in which the number of cellulose-decomposed actinomycete and the number of strong cellulose-decomposed actinomycetes were both quite low, but there were a large number of organic matter hard to break down, therefore the strong cellulose-decomposed actinomycetes ratio was the highest.

<<Table 3. Distribution of the cellulose-decomposed actinomycetes in different soil types>>

4. Conclusions

There were a certain amounts of cellulose-decomposed actinomycete in soil from the eastern part of Qinghai Plateau, which were $8.0 \times 10^3 \sim 140.9 \times 10^4$ cfu/g. The number of cellulose-decomposed actinomycete in vegetable field soil was higher than in grain field, but the strong cellulose-decomposed actinomycete ratio of cellulose-decomposed actinomycete in vegetable field soil was lower than in grain field. The strong cellulose-decomposed actinomycete ratio of the total cellulose-decomposed actinomycete in natural soil had certain relevance with the soil organic matter content. In each kind of natural soil, the number of cellulose-decomposed actinomycete in cumulated irrigated soil was the maximum, which was 82.2×10^4 cfu/g. The number of strong cellulose-decomposed actinomycete in castanozem was the most, which was 22.2×10^3 cfu/g. The strong cellulose-decomposed actinomycete ratio of cellulose-decomposed actinomycetes in marsh soil was the highest, which was 54.5. The results may provide scientific basis for separation and screening of the cellulose-decomposed actinomycete. The strains separated and purified from this experiment could be used by the screening of high cellulose activity strains and even might be used for commercial production.

References

- Cheng L. J., Xue Q. H.. (2000). Microbiology experimental technique. Publisher:World Book Publishing Company, pp:80-83, 104-105. (in Chinese)
- Hu A. T., Zhou L. X. (2003). Plant nutrition science (second edition, final volume). Publisher: China Agricultural University Press, pp: 172-183,205-208. (in Chinese)
- Jiang Ch. L.,Xu L. H..(1997). Microbial Resources. Publisher:Science Press, pp:104-200. (in Chinese)
- Liu Zh. H.. (2002). Modern Microbiology. Publisher:Science Press, pp: 3-35. (in Chinese)
- Liu Zh. H.,Jiang Ch. L.. (2004). Modern Biology and Technology of Actionomycetes. Publisher: Science Press, pp: 10-50. (in Chinese)
- Qi Y., Chen F., Yuan Y. X. *et al.*. (2003). A Cellulose degrading thermophilic alkalitolerant actinomycete. *Chinese Journal of Applied and Environmental Biology*, 9(3): 322-325. (in Chinese)
- Ruan J. S.. (1992). Foundation of Actinomycete classification. Publisher:Science Press, pp:18-109. (in Chinese)
- Song B., Yang J..(2005). Screening of a cellulose-decomposing actinomycetes strain and its enzyme-producing conditions. *Journal of Microbiology*, (5): 36-39. (in Chinese)
- Wu B., Hu Y. Z..(2008). Research progress of actinomycete cellulases. *China Brewing*,(1):5-8 (in Chinese)
- Wu X., Chen Q., Xu L. H. *et al.*,(2007). Screening of a cellulose-decomposing thermoactinomycetes strain and its Enzyme-Producing Conditions. *Journal of Agro-Environment Science*, 26 (B03): 101-104. (in Chinese)

You C. F.. (1986). Actinomycete of soil microorganisms. *Soil Science Progress*, (6):1-5. (in Chinese)

Table 1. Basic conditions of sampling points and basic properties of soil samples

No	Sampling locations	Altitude (m)	Soil types	Soil utilization ways	Quarter crops or Vegetation	Front stubble crops	Organic matter (g/kg)	pH
2	Qijiacheng battalion, East area, Xining city	2300	Serosem	Open field	Spinach	Small rape	26.8	7.80
3	Chaoyang new village, East area, Xining city	2300	Serosem	Protected land	Small rape	Cucumber	17.6	7.98
5	Lejia bay, east area, Xining city	2200	Cumulated irrigated soil	Protected land	Celery	Tomato	32.5	7.88
6	unity village, east area, Xining city	2203	Alluvial soil	Irrigated land	Wheat	Rape	26.8	7.86
7	Tashan, East area, Xining city	2210	Serosem	Natural soil	<i>Achnatherum splendens</i>		21.7	8.29
8	Liujiazhai village, Pengjiazhai town, Xining city	2250	Cumulated irrigated soil	Protected land	Pepper		30.4	7.82
9	Liujiazhai village, Pengjiazhai town, Xining city	2250	Cumulated irrigated soil	Protected land	Lettuce	Tomato	28.5	7.76
10	Liujiazhai village, Pengjiazhai town, Xining city	2250	Cumulated irrigated soil	Open field	Chinese cabbage	Lettuce	27.5	8.07
11	Dabaozi village, West area, Xining city	2372	Castanozem	Irrigated land	Wheat, rape, carrot , potato		20.6	8.18
12	Gazang temple, Haiyan county	3125	Marsh soil	Natural soil	<i>Stipa capillata</i> , <i>Medicago sativa</i>		69.8	8.26
13	West mountain pass, Haiyan county	3270	Alpine meadow soil	Natural soil	<i>Kobresia pygmaea</i> , bluegrass, <i>Saussurea epilobioides</i>		116.4	8.01
14	Gahai village, Ganzi lake township, Haiyan county	3270	Mountain meadow soil	Natural soil	<i>Achnatherum splendens</i> , bluegrass		35.0	8.72
16	Ketu, Haiyan county	3311	Aeolian soil	Natural soil	<i>Achnatherum splendens</i> , <i>Agropyron</i>		4.68	8.73
17	Qinghai Lake township, Haiyan county	3081	Saline-alkali soil	Natural soil	<i>Agropyron</i> , Japanese iris		35.5	8.62
18	Dongda village, Haiyan county	3075	Castanozem	Arid land	Rape	Rape	35.5	8.38
19	Yuefeng village, Haiyan county	2910	Chernozem	Irrigated land	Rape	Wheat	23.5	8.62
20	South of Bayan township, Huangyuan county	2753	Chernozem	Irrigated land	Wheat, broad bean		18.0	8.52
21	Ajiatu village, Tawan township, Huangyuan county	2695	Castanozem	Arid land	Wheat, rape	Wheat, broad bean	15.7	8.34
22	Small Gaoling village, Heping township, Huangyuan county	2851	Alluvial soil	Arid land	Wheat	Rape	8.3	8.42
23	Opposite of Dongxia stone material factory, Huangyuan county	2604	Forest brown soil	Natural soil	Mixed forest		85.9	7.96

24 Heizhui village, Shangwuzhuang township, Huangzhong county	2380	Castanozem	Irrigated land	Wheat, rape		18.3	8.24
25 Houzi river west village, Datong county	2310	Castanozem	Irrigated land	Wheat	Rape	20.5	8.38
26 Yuejiangtai, Suobei township, Datong county	2480	Castanozem	Arid land	Wheat	Rape	24.1	8.20
28 Tree farm, Dongxia Town, Datong County	2760	Forest brown soil	Natural soil	<i>Hippophae rhamnoides</i>		143.2	6.90
29 Tree farm, Dongxia Town, Datong County	2720	Castanozem	Natural soil			54.9	7.96
30 Baiya village, Xiangbei township, Datong county	2770	Chernozem	Arid land	Wheat		29.3	8.24
31 Xindong village, Duoba town, Huangzhong county	2280	Cumulated irrigated soil	Irrigated land	Wheat, broad bean, rape, potato		20.5	8.34
32 Xiaomo village, Dacai township, Huangzhong county	2560	Chernozem	Irrigated land	Wheat		21.7	8.36
33 Xiaomo village, Dacai township, Huangzhong county	2570	Chernozem	Natural soil			39.3	8.12
34 Xujiashai village, Zongzhai township, Huangzhong county	2420	Castanozem	Irrigated land	Rape		19.0	8.30
35 Spring bay, Gaozhai township, Huzhu county	2000	Fluvo-aquic soil	Irrigated land	Wheat		14.0	8.04
37 East gate lane, Nianbo town, Ledu county	1945	Serosem	Open field	Eggplant, Cabbage, Sea cabbage		8.7	8.18
39 Small gap, Ping'an county	2080	Serosem	Irrigated land	Wheat, carrot	Sea cabbage	18.2	8.14

Table 2. Distribution of cellulose-decomposed actinomycetes under different soil utilization ways in the eastern of Qinghai Plateau

No. of soil sample	A ($\times 10^4$ cfu/g)	B ($\times 10^3$ cfu/g)	B/A $\times 100$	No. of soil sample	A ($\times 10^4$ cfug)	B ($\times 10^3$ cfu/g)	B/A $\times 100$	
Arid	53.1	12.4	23.4	Open field	85.7	24.7	28.8	
21	45.3	22.7	50.1	10	86.5	10.3	11.9	
22	51.1	12.4	24.3	37	58.5	10.3	17.6	
26	47.8	12.4	25.9	Average	76.9	15.1	19.6	
30	47.8	16.5	34.5	Protected	59.3	6.0	10.1	
Average	49.0	15.3	31.2	Vegetable field	05	84.0	41.2	49.0
Irrigated	84.9	8.2	9.7	08	140.9	6.2	4.4	
11	56.5	4.1	7.3	09	46.1	20.6	44.7	
19	68.4	10.3	15.1	36	80.3	8.2	10.2	
20	51.5	20.6	40.0	Average	82.1	16.5	20.1	
24	64.3	55.6	86.5	Average	79.5	15.8	19.9	
25	49.9	8.2	16.4	07	111.2	14.4	12.9	
31	53.6	12.4	23.1	12	26.4	14.4	54.5	
32	31.3	22.7	72.5	13	52.8	22.7	43.0	
34	35.4	16.5	46.6	14	24.7	18.5	74.9	
35	74.2	14.4	19.4	16	27.2	6.2	22.8	
39	54.4	8.2	15.1	Natural soil	17	8.0	2.1	26.3
Average	56.8	16.5	29.0	23	70.9	0	0.0	
Average	52.9	15.9	30.1	28	33.0	2.1	6.4	
13	0~7cm	65.9	41.2	62.5	29	69.2	45.3	65.5
	7~24cm	39.6	4.1	10.4	33	35.0	10.3	29.4
16	0~10cm	28.0	8.2	29.3	Average	45.8	13.6	29.7
	10~20cm	26.4	4.1	15.5				
28	0~2cm	28.0	4.1	14.6				
	2~10cm	37.9	0	0.0				

Note: A means the total number of actinomycetes measured by microcrystalline cellulose plate, which represents the number of cellulose-decomposed actinomycetes. B means the number of actinomycetes which has obvious transparent spot on the microcrystalline cellulose plate, and represents the number of strong cellulose-decomposed actinomycetes.

Table 3. Distribution of the cellulose-decomposed actinomycetes in different soil types

Soil types	A ($\times 10^4$ cfu/g)	B ($\times 10^3$ cfu/g)	B $\times 100$ /A
Fluvo-aquic soil	74.2	14.4	19.4
Aeolian soil	27.2	6.2	22.8
Alpine meadow soil	38.8	20.6	53.2
Cumulated irrigated soil	82.2	18.1	22.1
Chernozem	46.8	16.1	34.4
Serossem	73.8	12.7	17.2
Castanozem	52.7	22.2	42.0
Forest brown soil	52.0	1.1	2.0
Alluvial soil	68.0	10.3	15.1
Saline-alkali soil	8.0	2.1	26.3
Marsh soil	26.4	14.4	54.5



Illumination Compensation in Pig Skin Texture Using Local-Global Block Analysis

M Iqbal Saripan (Corresponding author), Mohd Hafrizal Azmi

Raja Syamsul Azmir Raja Abdullah & Laili Hayati Anuar

Department of Computer and Communication Systems Engineering

Faculty of Engineering, Universiti Putra Malaysia

43400 UPM Serdang, Selangor, Malaysia

Tel: 60-3-8946-4344 E-mail: iqbal@eng.upm.edu.my

Abstract

Variable illumination in a texture is a common problem occurs to a real-time image modalities. The imbalance illumination in a texture creates virtual regions within one image, hence it affects the performance of the classification methods because it introduced an artifact patterns or virtual regions to an image. This paper presents a method to overcome the variable illumination problem in a pig skin texture using the information in the local and global blocks. The focus of this paper is to provide a fast, reliable and safe method to stabilize the lighting in an image. Pig skin texture is selected because it has a special pattern characteristic that needs to be preserved. The results show that in terms of the fluctuations contrast amplitudes in an image, the local-global method give better results than the standard homomorphic filtering technique.

Keywords: Illumination Compensation, Pig Skin Texture, Local-Global Analysis

1. Introduction

An image is formed from a combination of the illumination part and the reflective part. A variable illumination condition in an image creates difficulties to further process the image, because often, different regions with different illuminations give different classification results. In this paper, we concentrate on correcting the imbalance lighting condition in an imaged texture. This is a vital pre-processing step to obtain an accurate classification result.

The problem with imbalance illumination is one of the common challenges in image processing, especially in the area of segmentation and classification like texture processing (Thai and Healey, 1998) and face recognition (Adini and Moses, 1997). To address this problem, there are many works have been done in the past using methods like wavelet transform (Du and Ward, 2005), logarithm and discrete cosine transform (Chen et al., 2004), nine points of light (Lee et al., 2001) and others. The most common method in dealing with variable illumination is probably the homomorphic filtering technique (Delac et al., 2006). This technique utilizes the physics of image creation, whereby an image is formed of an illumination component and a reflectance component. By separating these two components, one may be able to correct the imbalance lighting part without tempering with the reflectance part.

Whereby most of the previous works in the literature are concentrated on multiple objects images like digital photographic images, this work is conducted on texture images. In texture images, the non uniform illumination may lead to false classification. In addition to that, since many automatic classifications are developed based on the patterns or features analysis of the texture, variable illumination could be extracted as one of the artifact patterns in the intelligent system, thus could also creates wrong interpretation.

The type of texture that we use in this paper is a pig skin leather texture. The pig skin leather is chosen because it has a unique characteristic in the arrangement of the hair pores by having three hair pores for pig skin leather is located closely together. Figure 1 shows an example of ideal dots patterns observed from hundreds samples of pig skin.

This visible characteristic may be used to identify this type of leather. Whilst investigating different cases of illumination, these dots must be preserved in order to classify the type of texture in the latter stages, and this is the challenge taken by this project. In this work, the samples are acquired using a digital camera under different illuminations conditions, and cropped to 120×120 pixels. The illumination condition is non-linear with respect to the

area of the surface of the texture.

In this paper, we proposed a technique to repair the imbalance illumination using the information obtained in the local block, as well as in the global block for texture images with the focus on pig skin leather. Figure 2 shows the original pig skin textures that suffer from the problem of imbalance illumination. The value of the standard deviation, σ indicates the level of fluctuations of the intensity in an image. Taking (a) as an example, due to the imbalance illumination, instead of having just one uniform region, there are three regions identified in the image: top left, centre and top right of the image. As shown in the figure, the imbalance lighting area creates different partitions or regions in the image and it creates an artifact character for such texture. This false alarm affects the quality of the texture image, and it can lead to the problem of misclassification.

In the next section, we present our proposed method based on the difference of the current intensity value of a particular pixel with the mean of a local block. Then, the local normalized value is normalized again to a global block. This method is known as a local-global block analysis. Section 3 comprises of the results and discussions. The performance of the proposed method is measured objectively using the standard deviation to look at the fluctuations range, and subjectively using the visual inspections. Finally, the findings are concluded in the final section of this article.

2. Local-Global Block Analysis

Digital images are formed from a series of square pixels. For many apparent reasons, grouping a number of adjacent pixels into a block is one way of processing the image (Charalampidis, 2006). The local-global block analysis is a method developed based on the micro and macro levels analysis. The proposed method is processed in the spatial domain. Local (or micro) blocks are useful in terms of providing local information of a particular block. The assumption that we impose in developing this algorithm is, there is no or very little variation in the illumination component within the local blocks. Therefore, to make this assumption valid, the size of the blocks must be small. This is because the bigger the size of the blocks, the higher probability of the imbalance lighting within the local blocks. On the other hand, if the size of the blocks is too small, thus there will be too many local mean values that affect the local residual pixels of an image. The analysis of different sizes of blocks is included in the next section.

Figure 3 shows the difference between the local mean and the global mean, in an image. Based on the figure, we can see that the global mean covers all the area in an image, therefore, the value that will be extracted represents the mean of the total illumination component. In terms of image histogram, the global mean represents the middle value in between of the maximum and minimum bins of grey levels recorded by the image. In this case, we presume that the global mean is located exactly or about the middle within the range of the grey values. For the case of the location of the global mean in the histogram is too low or too high, the colour bit depth will be added to accommodate the global residual pixels in an image. Once the range of the bins is confirmed, it can be normalized back to the original bit depth. Next, depends on requirements, the image can be enhanced using appropriate algorithms.

If we assume that an image of $f(x, y)$ has a size of $M \times N$ and made from many blocks of $f(a, b)$ hence the local mean in the local block can be shown as

$$\mu_{local}(a, b) = \left(\sum_{x=a \times M_a}^{M_a-1} \sum_{y=b \times N_b}^{N_b-1} f(x, y) \right) / (M_a \times N_b) \quad (1)$$

where $\mu_{local}(a, b)$ is the local mean of the local blocks, (a, b) is the index number of the blocks and $M_a \times N_b$ is the size of the local blocks. For instance, a 120×120 image has 15×15 blocks of size 8×8 pixels. In this example, the search for local means is for 8×8 pixels of all 225 blocks.

In this method, the global mean value that covers all the area in an image is also calculated. The calculation can be shown as:

$$\mu_{global} = \sum_{x=0}^M \sum_{y=0}^N f(x, y) / M \times N \quad (2)$$

where μ_{global} is the global mean of an image. Notice that μ_{global} is not a function, but a constant.

Taking image in Figure 2(a) as an example, the local mean of this image when a 6×6 block is used is shown in Figure 4. The solid lines show the local means for every 6×6 block in the image, plotted across y axis. Compare that with the global mean (indicated by the straight dotted line at value 150), we can see that most of the local mean are located further from the global mean, and this imply the problem of the imbalance lighting. The difference between the local mean and the local pixel can be calculated based on the following equation:

$$\Delta(x, y) = f(x, y) - \mu_{local}(x(a), y(b)) \quad (3)$$

Finally, to obtain the illumination compensated image, the local residual pixel is normalized to the position of the global mean.

$$\hat{f}(x, y) = \Delta(x, y) + \mu_{global} \quad (4)$$

where $\hat{f}(x, y)$ in the above equation is the output image after the normalization process. In this algorithm, the normalization process is done using the adding process. There are two main purposes of choosing this process. First, it will result the positive and negative directions of the residual pixels. The positive value indicates that the particular pixel has a brighter pixel value, while the negative value implies a darker pixel value. The second purpose is to preserve the contrast between pixels in an image. By taking the original local residual pixel, the contrast within the local pixel is saved, and then it is re-located to the new value based on the global mean. By implementing this step, the local block will provide the micro level residual pixel, and the global block will provide the normalization level.

Looking at the presented steps, since the proposed method is processed in the spatial domain, hence it is actually generic and may be used for any texture images, either as the preprocessing unit or after any processes that have been imposed to the images.

3. Results and Discussion

The result obtained from the homomorphic filter is shown in Figure 5(a). The standard deviation of this image is 53.59. This image is obtained by applying the homomorphic filter to the texture in Figure 2(a). From the output image itself, we may predict that the standard deviation is large, i.e. the distribution of the intensities is wide. Although the image is getting better visually, but the problem of imbalance lighting is not cured. The image is only better to our vision because of the good contrast, but on the image segmentation aspect, the three regions are getting more separated.

Using the proposed method of local-global block processing, we must first decide the size of the local block $M_a \times N_b$. There are seven different sizes of blocks presented in this article: 2×2 , 4×4 , 6×6 , 8×8 , 10×10 , 12×12 and 24×24 . The results generated for the earlier category are given by Figure 5(b)-(h). From the initial visual inspection, we can see that in terms of the balance of the lighting, these images are better than the original image (in Figure 2(a)) or the filtered image (in Figure 5(a)).

Comparing between different sizes of blocks, we can see that the proposed method with 4×4 and 6×6 blocks, give good results. The bigger the size of the local blocks, the boundary in between of the blocks is become more visible. This is because for pixels located at the boundary of the blocks, there are cases where the intensity value is closer to the adjacent local mean instead of their local means. Therefore, the blockiness is now become a problem to be solved. Although one may use a deblocking filter like in (Sima et al., 2004), but in this article, we do not extend our work to that direction. Instead, we focus on the potential of the proposed method to directly improved the lighting distribution in a texture. Based on the subjective visual perception, the best results are given by 4×4 and 6×6 blocks. The value of the standard deviation is shown in Table 1. From the table, we can see that the larger the size of the blocks, the higher the standard deviation, i.e. the bigger fluctuation amplitudes of the intensity. However, as we have seen from Figure 5, the smallest value of the standard deviation does not also necessary indicates the most quality image. This is because, when smaller size of blocks used in this method, the averaging process wipes away the original characteristics of the texture.

4. Conclusions

In this paper, we demonstrated that using the information provided in the local block can be used to estimate the residual intensity at every individual pixels. Combining this information with the global mean of an image, we were able to show that it can be utilized for correcting the variable illumination problem in pig skin texture images. We also show that the algorithms proposed by this paper do not temper the original characteristic of an image. Pig skin texture is selected to demonstrate this feature. Comparing the proposed method with the homomorphic filtering technique shows that the illumination given by our method is more balanced than the latter method. This algorithms can be extended further by enhancing the contrast of the image and etc.

References

- Adini S. U. Y and Moses Y. (1997), Face Recognition: The Problem of Compensating for Illumination Changes *IEEE Trans. on Pattern Analysis and Machine Intelligence* 19(7), 721-732.
- Charalampidis D. (2006), Texture synthesis: textons revisited, *Proc. of IEEE International Conference on Control, Automation Robotics and Vision* 15(3), 777-787.
- Chen W., Er M. J., and Wu S.(2004), Illumination Compensation and Normalization Using Logarithm and Discrete Cosine Transform, *Proc. of IEEE Internacional Conference on Control, Automation, Robotics and Vision* 1, 380-385.
- Delac K., Grgic M., and Kos T. (2006), Sub-Image, Homomorphic Filtering Techniques for Improving Facial Identification under Difficult Illumination Conditions, *International Conference on Systems, Signals and Image Processing Budapest*, 95-98.
- Du S. and Ward R.(2005), Wavelet-Based Illumination Normalization For Face Recognition, *Proc. of IEEE*

International Conference on Image Processing 2, 954-957.

Lee K., Ho J., and Kriegman D. (2001), Nine points of light: Acquiring subspaces for face recognition under variable lighting, *Proc. of IEEE Conference on Computer Vision and Pattern Recognition 1*, 519-526.

Sima M., Zhou Y., and Zhang W. (2004), *An efficient architecture for adaptive deblocking filter of H.264/AVC video coding*, IEEE Transactions on Consumer Electronics, 50(1), 292-296.

Thai B. and Healey G. (1998), Results on deriving optimal filters for illumination-invariant color texture recognition , *Proc. of the IEEE International Conference on Systems, Man, and Cybernetic,s 5*, 4312-4317.

Table 1. The standard deviation of different sizes of blocks for image in Figure 2(a).

Size of Blocks	Standard Deviations
2 × 2	2.68
4 × 4	4.10
6 × 6	4.62
8 × 8	4.97
10 × 10	5.24
12 × 12	5.43
24 × 24	7.03

The above table shows the standard deviation of different local window size, varying from 2x2 to 24x24 pixels

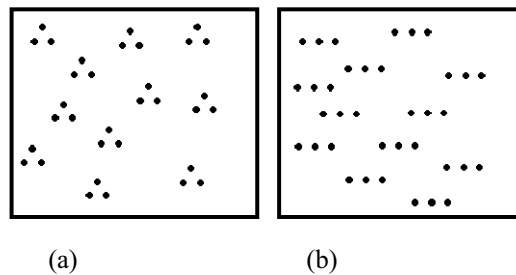


Figure 1. An ideal pattern of pig skin leather with three dots closely located together. There two different patterns of pig skin leather, either in a triangle shape (a) or a line shape (b).

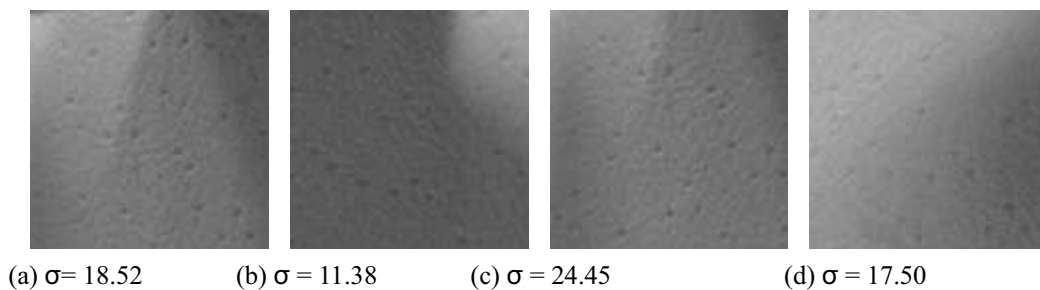


Figure 2. Examples of pig skin texture images suffer from variable illumination.

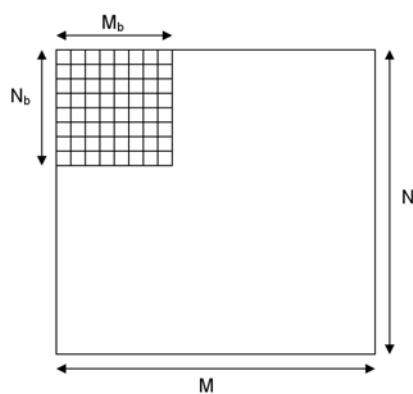


Figure 3. The difference between the local and global area in an image.

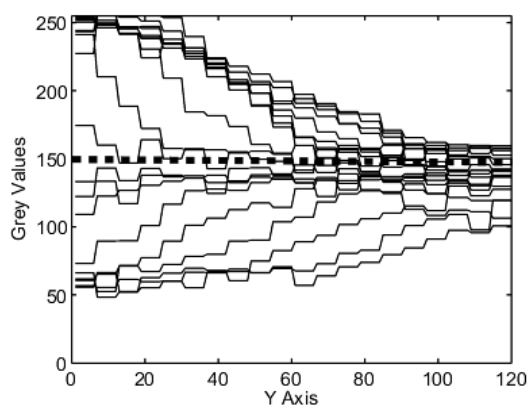


Figure 4. The local and global mean of image in Figure 2(a). The dotted thick line is the global mean while the solid lines are the local means. In this example, 6×6 blocks are used.

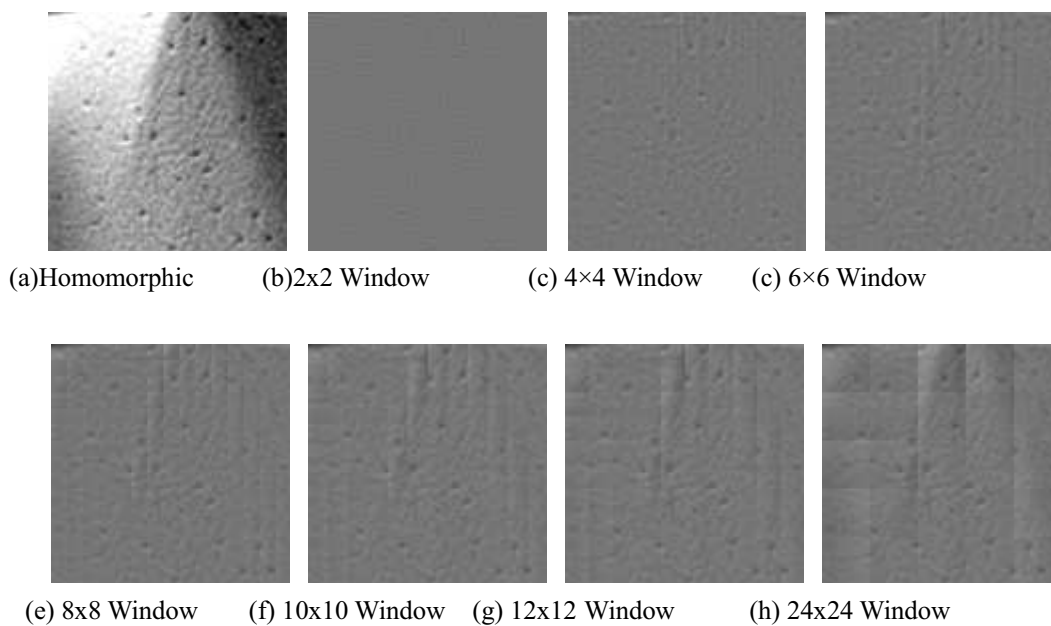


Figure 5. The output texture images.



On the PFQ-based Training Mode for the Special Force

Jianxin Yang & Min Yu

Military Preventive Medicine Department

Fourth Military Medical University

Xi'an 710032, China

Fuyong Liu

Bethune International Peace Hospital

398 West Zhongshan Road, Shijiazhuang 050082, Hebei, China

Tel: 86-311-8799-8900 E-mail: liufy1065@hotmail.com

Abstract

The purpose of the research is to construct the theoretical framework of the physical fitness quotient, the assessment system, and the PFQ-based training mode. The methodology of the research includes the PFQ-related theories, assessments, literature review and consultancy. Result shows the feasibility of the construction of the PFQ-based assessment system, in particular, of the training system for the special force. It is concluded that the PFQ-based training mode is a trend for the special force.

Keywords: Physical fitness quotient, Physical fitness training, Special force

For the extensive use of the hi-tech weapons, the ways of future wars are expected to be substantially different. This requires the special force to adapt their physical fitness to the new military battles. Therefore, a reform should be performed on the physical fitness training in relation to the contents, forms and methods. In addition, it is argued that the scientific physical fitness training is vital for the special force. Theoretical and scientific research of the methodology is compulsory for the improvement of the physical fitness. Physical fitness quotient is a new assessment, for it helps to spot the proper gifts of individuals, and helpful to launch scientific trainings.

1. An overview of the physical fitness trainings for the special force

1.1 Physical fitness

Physical fitness refers to the physical strength, a force that an individual demonstrates in making a move. It is the fundamental and primary guarantee for the human labor, living and learning. The special force is a group of special individuals demanding special physical fitness from their unusual work. Likewise, the unusual physical strength that is compulsory for special force to adapt to the warfare should include the physical movement, like running, jumping, and throwing, physical functions, like heart beats and lungs, and flexible capabilities to survive the complicated situations. The physical strength of the special force may be a significant component of the battling force, so to speak.

1.2 The features of the physical fitness trainings for the special force

It is true that the physical fitness status of an individual is greatly influenced by the hereditary factors, but it may surely be acquired by the later trainings. The approach is the especially prepared trainings aimed at the improvement of the physical fitness status of the army forces needed for the warfare. The trainings enable the army to maintain the strengthened battling force and ensure the proper performance of the warring skills. Special force forms a special community of the army, which demands an unusual status of physical fitness and warring versatility. Consequently, the courses of trainings are committed to unusual length, compact subjects and extreme tension, in addition to the purposeful missions.

1.3 The modes of the physical fitness training for the special force

The writers of the paper have reviewed the physical fitness status of the Chinese special force. The weaknesses may have impacts on the general battling force of the army. It is compulsory, therefore, the strengthening of the physical fitness and the trainings of the special force remain a realistic and urgent problem to resolve.

The physical fitness training modes applied to the Chinese special force are basically imitated from those of the US army. The trainees receive, without exception, the trainings on vigor, rapidity, agility, endurance, flexibility, balancing or steadiness, dizziness resistance, and the like to adapt to the military fighting. Concrete measures are the 5-km long race, horizontal and parallel bars (1-2), 400-meter hurdle race, grenade throwing, push-up, and barbell pushing.

All this is helpful to the trainees with the general improvement of the physical fitness, but may not take advantage of the good points of the individuals, failing to match the practical drills or emergencies. So the mode needs reforming (Ke, J. and Lin, J. 2001.)(Ren, W. and Zhang, Y. 2000.)(Lei, E. and MAO Y. 2004.).

2. The concept and classification of the physical fitness quotient

2.1 Concept

The physical fitness quotient is a standardized system to assess the physical fitness to indicate the trends of health and the status of the basic physical fitness. The higher the physical fitness quotient is, the more safe and sound the health and the physical functions are. Therefore, the PFQ-based military training of the physical fitness has become a popular tendency.

2.2 Classifications of physical fitness

Generally speaking, the physical fitness of adults may be divided into three types, the health-related physical fitness, sport-related physical fitness, and skill-related physical fitness. Likewise, the physical fitness quotient may be divided into health-related, sport-related, and skill-related physical fitness quotient.

2.2.1 The health-related physical fitness quotient

The health-related physical fitness quotient refers to the physical quotient or competence of an individual to deal with the routine of work, enjoy the leisure and recreations, and handle the potential emergencies. The detailed components are the strength of muscle, endurance of muscle, pliability, resistance of heart and lungs, and the percentage of fat.

2.2.2 The sport-related physical fitness quotient

The sport-related physical fitness quotient is closely related to the basic sport or physical competence, but includes agility, stability, balancing, speed, and response, in addition to the components for the health-related physical fitness.

2.2.3 The skill-related physical fitness quotient

The skill-related physical fitness quotient refers to the special skill-related physical fitness that is imbedded into the sport skills to a certain extent. For instance, a basket-ball player demands such sport skills as the capabilities of speedy dribbling and passing, accurate and swift shooting. Due to the immediate affects of the types of sports, the physical fitness quotient of an individual is usually justified by the combined assessments of health-related and sport-related physical fitness quotients.

As far as the physical fitness trainings for the special force are concerned, attempts should be made to spot, by the assessment of the sport-related physical fitness quotient during the training, the individual physical quotient that is the physical ability to learn the sports. In addition, a developmental strategy is applied to suitable sports in accordance with the specific sport gifts to develop the physical fitness trend of the individual(Ke, J. and Lin, J. 2001.)(Ren, W. and Zhang, Y. 2000.)(Lei, E. and MAO Y. 2004.).

3. The theoretical framework of PFQ-based physical fitness training mode for special force

3.1 Theoretical framework

The writers of the paper argue for a hypothetic structure of PFQ (Figure 1) as the theoretical framework to meet the need for the PFQ-based physical fitness training mode for the special force in which the PFQ (physical fitness quotient) is HPFQ (health-related physical fitness quotient) and SPFQ (sport-related physical fitness quotient).

Given a high rate of HPFQ of an individual, the trend of the health is observed. By the same token, the high rate of SPFQ stands for sound competence of the sports. With a high rate of both HPFQ and SPFQ, an individual possesses brilliant physical health and sport physical fitness, and is thus apt to sport achievements and sport gifts. Moreover, the individual is expected to possess special potentials for a specific sport, should his specified sport components achieve a high assessment ratio. This special training for the special force is quite different from the traditional training designed for all.

3.2 Methods of assessment

On the basis of the theoretical framework, methods of assessment are constructed of the PFQ-based training for the special force with regard to the health-related and sport-related physical fitness quotients. The assessment is carried out in two different groups. In the HPFQ group, the assessment centers on the physical buildup, pliability, muscle strength, explosive force, and functions of heart and lungs, while in the SPFQ group, the focus of the assessment includes response to rod drop, and single-leg standing with eyes closed, in order to assess the special force in relation to the

response, balancing, agility, speed, and stability (Figure 2)(Shi Y. 2002.)(Liu J. and ZHANG, J. 2002.)

4. Mode of the PFQ-based training for the special force

On the basis of the PFQ-based theory and assessment methods, the mode of the PFQ-based training is hypothesized for the special force. The flowing chart starts with the establishment of the assessment system of the physical fitness quotient, assessment in operation, designation of the specific sports for individual of the special force, and PFQ-based training in operation. Should there be problems in the course of training, they are fed back in time, so the assessment system is continually improved toward the set up of the PFQ-based training system of the special force (Figure 3)(Lin J. 2004.).

In conclusion, the PFQ-based training system of the special force is expected to greatly enhance the quality of the newly-recruited, which is helpful to the progress of the systematization, standardization, and scientific normalization. Furthermore, a timely understanding and objective assessment is achieved of the physical fitness and battling force, in particular, of the special force. The theory may serve as a guide for the PFQ-based training. Therefore, it is proposed that the PFQ-based monitoring and feedback mechanisms, centers or networks be established throughout the military zones, so that the physical tests may be regularly performed and reported to the headquarters of the military commission. The ultimate purpose of the paper is to enable the physical fitness training to be scientific and effective to provide with the theoretical and scientific basis for the physical training and improvement of the physical strength of the military force.

References

Ke, J. and Lin, J. (2001). A developmental survey of the physical fitness of the citizens and soldiers. *PLA College of Physical Education*, 20, 6-9.

Lei, E. and MAO Y. (2004). Perspectives of the comprehensive protection of the military health, *Military Medical University*,28,169-170.

Lin J. (2004). Construction of the Chinese military physical fitness, *PLA College of Physical Education*, 23,1-5.

Liu J. and ZHANG, J. (2002). A tentative study of the comprehensive assessment of physical fitness, *PLA College of Physical Education*, 21,87-90.

Ren, W. and Zhang, Y. (2000). Reflections on the physical fitness training in the military force. *PLA College of Physical Education*, 19,53-56.

Shi Y. (2002). On the new methods of assessment of the physical fitness, *First Military Medical University, Postgraduate Papers*.

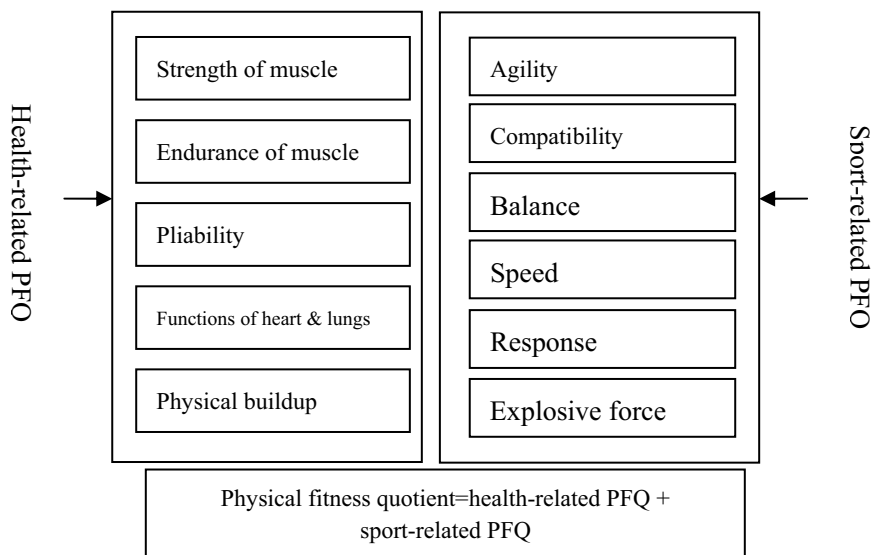


Figure 1. Diagram of the Structure of PFQ

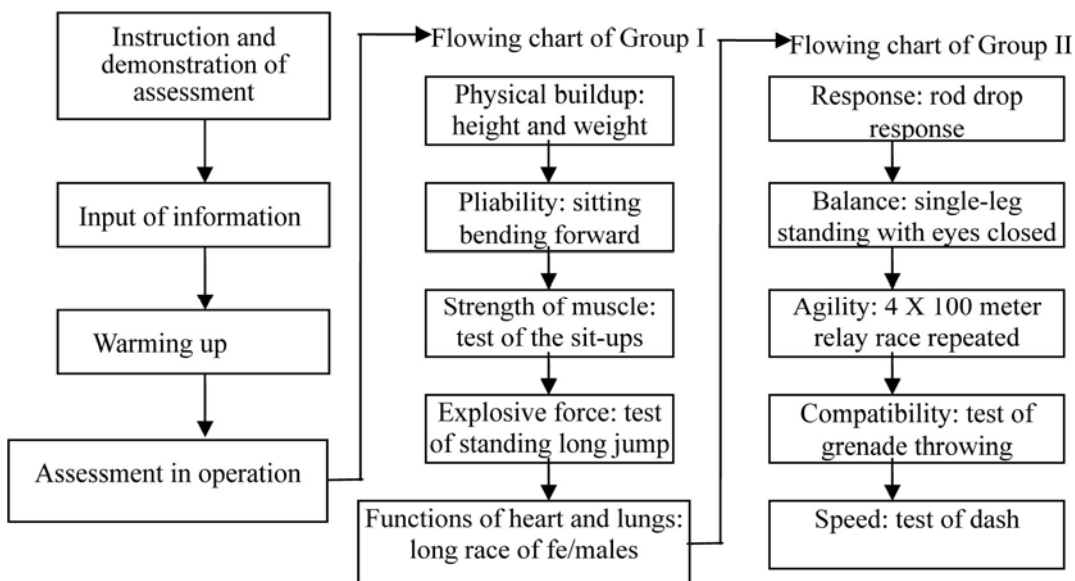


Figure 2. Methods of Assessment of the PFQ-based training for the special force

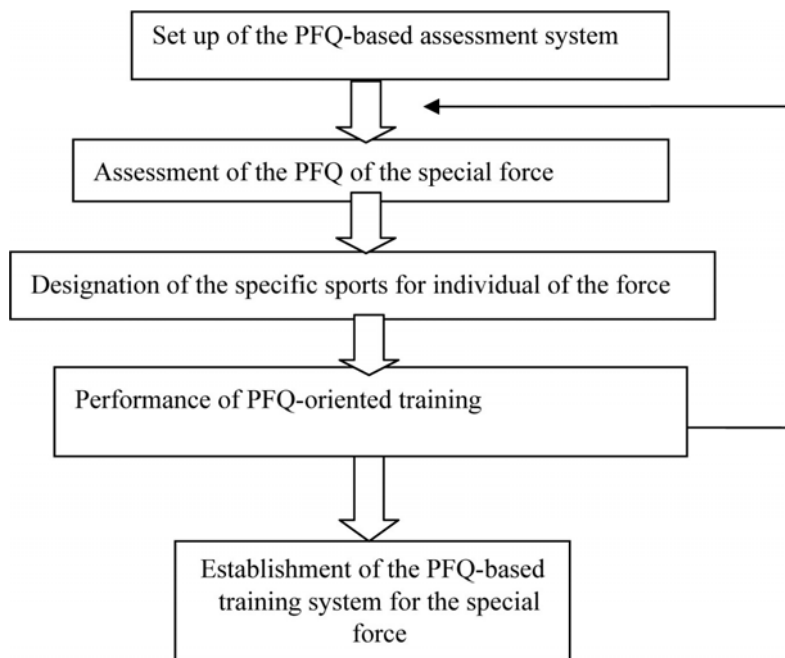


Figure 3. PFQ-based training mode for the special force



Advanced Approach in Sensitive Rule Hiding

Dr. K. Duraiswamy

K.S. R. College of Technology

Tiruchengode- 637 209, Tamil Nadu, India

E-mail: kduraiswamy@yahoo.co.in

Dr. D. Manjula

Department of Computer Science and Engineering

Anna University

Chennai, Tamil Nadu, India

E-mail: manju@annauniv.edu

N. Maheswari (Corresponding Author)

P.G. Department of Computer Science

Kongu Arts and Science College

Erode-638 107, Tamil Nadu, India

E-mail: mahii_14@yahoo.com

Abstract

Privacy preserving data mining is a novel research direction in data mining and statistical databases, which has recently been proposed in response to the concerns of preserving personal or sensible information derived from data mining algorithms. There have been two types of privacy proposed concerning data mining. The first type of privacy, called output privacy, is that the data is altered so that the mining result will preserve certain privacy. The second type of privacy, called input privacy, is that the data is manipulated so that the mining result is not affected or minimally affected. For output privacy in hiding association rules, current approaches require hidden rules or patterns to be given in advance. However, to specify hidden rules, entire data mining process needs to be executed. For some applications, only certain sensitive rules that contain sensitive items are required to hide. In this work, an algorithm ISSRH (Increase Support Sensitive Rule Hiding) is proposed, to hide the sensitive rules that contain sensitive items, so that sensitive rules containing specified sensitive items on the right hand side of the rule cannot be inferred through association rule mining. Example illustrating the proposed approach is given. The characteristics of the algorithm are discussed.

Keywords: Data Mining, Privacy Preserving, Association Rules, Sensitive Rules, Clustering, Minimum Support, Minimum confidence

1. Introduction

The concept of Privacy-Preserving has recently been proposed in response to the concerns of preserving personal or sensible information derived from data mining algorithms. Successful applications of data mining have been demonstrated in marketing, business, medical analysis, product control, engineering design, bioinformatics and scientific exploration, among others. The current status in data mining research reveals that one of the current technical challenges is the development of techniques that incorporate security and privacy issues. The main reason is that the increasingly popular use of data mining tools has triggered great opportunities in several application areas, which also requires special attention regarding privacy protection. There have been two types of privacy concerning data mining. The first type of privacy, called output privacy, is that the data is minimally altered so that the mining result will preserve certain privacy (Evmimievski, 2002, Oliveira, Zaiane, 2003 a, Oliveira, Zaiane, 2003 b). The second type of privacy, input privacy, is that the data is manipulated so that the mining result is not affected or minimally affected (Dasseni, Verykios, Elmagarmid, Bertino, 2001).

For example, through data mining, one is able to infer sensitive information, including personal information, or even patterns from non-sensitive information or unclassified data. As a motivating example of privacy issue in data mining discussed in (Yi-Hung Wu, Chia-Ming Chiang, and Arbee L.P. Chen, 2007). Consider a supermarket and two breads suppliers A and B. If the transaction database of the supermarket is released, A (or B) can mine the association rules related to his/her breads and apply the rules to the sales promotion and the goods supply. As a result, a supplier is willing to exchange a lower price of goods for the database with the supermarket. From this aspect, it is good for the supermarket to release the database. However, the conclusion can be opposite if a supplier uses the mining methods in a different way. For instance, if A finds the association rules related to B's breads, saying that most customers who buy cheese also buy B's breads, he/she can run a coupon that gives a 10 percent discount when buying A's breads together with cheese. Gradually, the amount of sales on B's breads is down and B cannot give a low price to the supermarket as before. Finally, A monopolizes the bread market and is unwilling to give a low price to the supermarket as before. From this aspect, releasing the database is bad for the supermarket. Therefore, for the supermarket, an effective way to release the database with sensitive rules hidden is required. This leads to the research of sensitive rule hiding.

In this work, the sensitive rules are given and the algorithm ISSRH is proposed to modify data in database so that sensitive rules containing specified sensitive items on the right hand side of rule cannot be inferred through association rule mining. The proposed algorithm is based on modifying or perturbing the database transactions so that the confidence of the association rules can be reduced.

The rest of the paper is organized as follows. Section 2 gives the view of the previous works. Section 3 presents the statement of the problem. Section 4 presents the framework of the approach. Section 5 presents the proposed algorithm for sensitive rule hiding. Section 6 shows the example of the proposed algorithm. Section 7 analyzes the characteristics of the algorithm. Concluding remarks and future work are described in Section 8.

2. Related Work

In output privacy, given specific rules or patterns to be hidden, many data altering techniques for hiding association, classification and clustering rules have been proposed. For association rules hiding, two basic approaches have been proposed. The first approach (Saygin , Verykios , Clifton, 2001, Verykios, Elmagarmid , Bertino , Saygin , Dasseni ,2004) hides one rule at a time. It first selects transactions that contain the items in a give rule. It then tries to modify transaction by transaction until the confidence or support of the rule fall below minimum confidence or minimum support. Either removing items from the transaction or inserting new items to the transactions does the modification of transaction. The second approach (Oliveira, Zaiane, 2002 a, Oliveira, Zaiane, 2002 b, Oliveira, Zaiane, 2003 a, Oliveira, Zaiane, 2003 b) deals with groups of restricted patterns or association rules at a time. It first selects the transactions that contain the intersecting patterns of a group of restricted patterns. Depending on the disclosure threshold given by users, it sanitizes a percentage of the selected transactions in order to hide the restricted patterns. However, both the above approaches require hidden rules or patterns been given in advance.

The work presented here differs from the related work in some aspects are as follows: First, database indexing is performed. Second, correlations among the sensitive rules are considered. Third, avoids the modification in transactions unnecessarily, if the confidence of the sensitive rule gets reduced. Fourth, alter the transactions in the cluster and finally changes can be updated in the database, which reduces the time period of database updating.

3. Problem Statement

The problem of mining association rules was introduced in (Agrawal, Imielinski, Swami, 1993). Let $I = \{i_1, i_2, \dots, i_m\}$ be a set of literals, called items. Given a set of transactions D , where each transaction T in D is a set of items such that $T \subseteq I$, an association rule is an expression $X \Rightarrow Y$ where $X \subseteq I$, $Y \subseteq I$, and $X \cap Y = \Phi$. The X and Y are called respectively the body (left hand side) and head (right hand side) of the rule. An example of such a rule is that 90% of customers buy hamburgers also buy Coke. The 90% here is called the confidence of the rule, which means that 90% of transaction that contains X (hamburgers) also contains Y (Coke). The confidence is calculated as $|X \cup Y| / |X|$, where $|X|$ is the number of transactions containing X and $|X \cup Y|$ is the number of transactions containing both X and Y . The notation \cup here is not the set union operator. The support of the rule is the percentage of transactions that contain both X and Y , which is calculated as $|X \cap Y| / N$, where N is the number of transactions in D . In other words, the confidence of a rule measures the degree of the correlation between item sets, while the support of a rule measures the significance of the item sets. A typical association rule-mining algorithm first finds all the sets of items that appear frequently enough to be considered significant and then it derives from them the association rules that are strong enough to be considered interesting. The problem of mining association rules is to find all rules that are greater than the user-specified minimum support and minimum confidence.

The objective of data mining is to extract hidden or potentially unknown but interesting rules or patterns from databases. However, the objective of privacy preserving data mining is to hide certain sensitive information so that they cannot be discovered through data mining techniques (Agrawal, Imielinski, Swami, 1993, Evfimievski, Gehrke , Srikant, 2003).

In this work, an algorithm ISSRH (Increase Support Sensitive Rule Hiding) is proposed, to hide the sensitive rules that contain sensitive items, so that sensitive rules containing specified sensitive items on the right hand side of rule cannot be inferred through association rule mining. More specifically, given a transaction database D , a minimum support, a minimum confidence and a set of sensitive items Y , the objective is to minimally modify the database D such that no sensitive rules containing sensitive items Y on the right hand side of the rule will be discovered.

4. Framework of the approach

Figure 1 shows the framework of the approach that consists of six processes. Initially, indexing is performed in the database. Then association rules are mined from the database. Sensitive items are identified to find the sensitive rules. Then the sensitive rules are generated. Clustering is performed on the sensitive rules to group the similar items. The rule hiding process is performed and the transactions are updated in the transaction table and finally it is updated in the original database. The main challenge of rule hiding is how to select the items and transactions to modify. The proposed framework hides the sensitive rules.

5. Proposed Algorithm

In order to hide an sensitive rule, $X \Rightarrow Y$, it can be either decrease its supports, $(|X|/N$ or $|X \cup Y|/N$), to be smaller than pre-specified minimum support or its confidence $(|X \cup Y|/|X|)$ to be smaller than pre-specified minimum confidence. In the transactions that do not contain both X and Y , to increase the support of X only, the left hand side of the rule, it would reduce the confidence of the rule. In order to hide sensitive rules, when considering hiding sensitive rules with 2 items, $x \Rightarrow z$, where z is a sensitive item and x is a single large one item. In theory, association rules may have more specific rules that contain more items, e.g., $xY \Rightarrow z$, where Y is a large item set. However, for such rule to exist, its confidence must be greater than the confidence of $x \Rightarrow z$, i.e., $\text{conf}(xY \Rightarrow z) > \text{conf}(x \Rightarrow z)$ or $|xY \cup z| > \text{conf}(x \Rightarrow z) * |xY|$. For higher confidence rules, such as $\text{conf}(x \Rightarrow z) = 1$, there will be no more specific rules. In addition, once the more general rule is hidden, the more specific rule might be hidden as well.

The algorithm tries to decrease the support of the right hand side of the rule.

Algorithm ISSRH

Input:

1. source database D
2. min support
3. min conf
4. sensitive items Y

Output:

a transformed database D' , where rules containing Y on RHS will be hidden.

Step 1:

Indexing the transactional database.

Step 2:

Generate the association rules.

Step 3:

Selecting the Sensitive rules with single antecedent and consequent with the sensitive item in the consequent.($x \rightarrow y$)

Step 4:

Constraint based clustering - Clustering the rules with the right hand side has the common item and indexing the rules.

Step 5:

Check all the rules in the cluster.

for cluster $i = 1$ to n

```
{
do
{
```

- 1 select the rule with high confidence
- 2 find $K = \text{mincount}$.

```

3      |Tr| = no of sensitive rules that are correlated
Such that  $k < |Tr|$ 
4      Tk = find first k transactions that do not contains the items in the correlated rules
5      sort Tk in ascending order by the number of items.
6      For i= 1 to k
      {
7          Choose the first transaction t from Tk.
8          Modify t to support x.  $count(x)=count(x) +1$ .
9          Find the confidence of every rule
10         If confidence of all the rules < min conf
      {
11         Update the transactions in the clusters
12         Exit
13         Else
14         Update the transactions in the clusters
      }
    }
15     unchecked the rules < minconf
16     }while(rules in cluster[i]==checked)
17     }

```

Step 4: update database D as transformed database D'.

The algorithm tries to generate the association rule using Agrawal, Imielinski, Swami, 1993). Then it selects the sensitive rules with the sensitive items in the right hand side. Cluster the rules with the common item in the right hand side of the rule (Han, Kamber,2001) and index the rule using (Oliveira, Zaiane, 2003 a).

The mincount= $[count(xUy/min\ conf] - count(x) +1$.

(Yi-Hung Wu, Chia-Ming Chiang, and Arbee L.P. Chen, 2007)

Therefore it would take maximum of k no of executions to hide the rule. The rules in every cluster will be hidden.

6. Example

This section shows the example to demonstrate the proposed algorithm to hide the sensitive rules.

The items in database can be represented as a bit vector 1 and 0.(Saygin Y, Verykios V, Clifton C, 2001)

TID	Items	Items
T1	ABC	111
T2	ABC	111
T3	ABC	111
T4	AB	110
T5	A	100
T6	AC	101

Frequent item sets are generated with minimum support 0.33. Association rules with minimum confidence 0.70 are generated. The rules and the corresponding confidence values are as follows:

C->B0.75, B->C0.75, C->A1.0, B->A1.0, BC->A1.0, AC->B0.75, AB->C0.75, C->AB0.75, and B-> AC0.75.

The item C is considered as sensitive item. The sensitive rule with single antecedent and consequent is B->C. The rule is clustered. In the fifth transaction the item B will be added and placed as 1.

Then the database will be updated as

TID	Items	Items
T1	ABC	011

T2	ABC	011
T3	ABC	111
T4	AB	110
T5	AB	110
T6	AC	101

After updating the database the rules $B \rightarrow C$ will have the confidence as 0.6, which is less than minimum confidence and hidden. While hiding the rule the rules $AB \rightarrow C$, $B \rightarrow AC$ are also hidden and the rule $A \rightarrow B$ is generated as side effect.

7. Analysis

This section analyses some of the characteristics of the proposed algorithm. The first characteristic is the database indexing. The indexing helps in reducing the number of scanning of the database. The second characteristic is the time effect. The time taken to scan the database to search the sensitive rules in the database is reduced because of clustering the sensitive rules. The third characteristic is the database effect. The minimum numbers of transactions are modified because of correlation among the sensitive rules. The fourth characteristic is the efficiency of the algorithm. The database is updated after all the rules are hidden that saves the updating time. The fifth characteristic is the transaction effect. The alteration in the transactions are stopped when the confidence of the sensitive rules are reduced than the minimum confidence.

8. Conclusion

In this work, the database privacy problems caused by data mining technology are discussed and the algorithm for hiding sensitive rules is presented. The proposed algorithm here can automatically hide sensitive rule sets. The previous works does not consider the characteristics that are discussed here. Example illustrating the proposed algorithm is given and the characteristics of the algorithm are analyzed. Further the efficiency of the algorithm will be analyzed and improved by reducing the side effects.

References

- Agrawal R, Imielinski T, Swami A (1993) Mining association rules between sets of items in large databases. *In: Proceedings of ACM SIGMOD International Conference on Management of Data*, Washington DC
- Dasseni E, Verykios V, Elmagarmid A, Bertino E (2001) Hiding association rules by using confidence and support. *In: Proceedings of 4th Information Hiding Workshop*, Pittsburgh, PA, pp 369–383
- Evfimievski A (2002) Randomization in privacy preserving data mining. *SIGKDD Explorations* 4(2), Issue 2:43–48
- Evfimievski A, Gehrke J, Srikant R (2003) Limiting Privacy Breaches in Privacy Preserving Data Mining. *PODS 2003*, San Diego, CA
- Evfimievski A, Srikant R, Agrawal R, Gehrke J (2002) Privacy preserving mining of association rules. *In: Proceedings of the 8th ACM SIGKDD Int'l Conference on Knowledge Discovery and Data Mining*, Edmonton, Canada
- Han, J., Kamber, M, (2001) *Data Mining : Concepts and Techniques.*, Morgan Kaufmann Publishers.
- Oliveira S, Zaiane O (2002 a) Privacy preserving frequent item set mining. *In: Proceedings of IEEE International Conference on Data Mining*, November 2002, pp 43–54.
- Oliveira S, Zaiane O (2002 b) A framework for enforcing privacy in mining frequent patterns. *Technical report, TR02-13*, Computer Science Department, University of Alberta, Canada
- Oliveira S, Zaiane O (2003 a) Algorithms for balancing privacy and knowledge discovery in association rule mining. *In: Proceedings of 7th International Database Engineering and Applications Symposium (IDEAS03)*, Hong Kong
- Oliveira S, Zaiane O (2003 b) Protecting sensitive knowledge by data sanitization. *In: Proceedings of IEEE International Conference on Data Mining*
- Saygin Y, Verykios V, Clifton C (2001) Using unknowns to prevent discovery of association rules. *SIGMOND Record* 30(4):45–54
- Verykios V, Elmagarmid A, Bertino E, Saygin Y, Dasseni E (2004) Association Rules Hiding. *IEEE Trans Knowledge and Data Eng* 16(4):434–447
- Yi-Hung Wu, Chia-Ming Chiang, and Arbee L.P. Chen, (2007), Hiding Sensitive Association Rules with Limited Side Effects, *IEEE Trans Knowledge and Data Eng*, Vol. 19, No. 1.

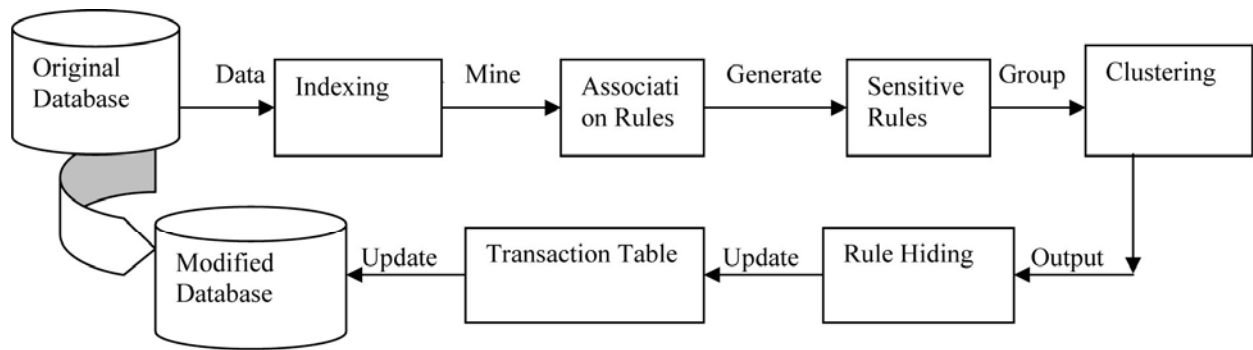


Figure 1. Framework of the approach
The framework describes the proposed approach of rule hiding.



Boundedness of Commutators on Generalized Morrey Spaces

Yuze Cai

Shazhou Polytechnical Institute Of Technology
Jiangsu 215600 China

Hao Zhang

Wuxi Institute of Technology
Jiangsu 214121, China

Abstract

In this paper, we establish the boundedness of strongly singular integrals operators T and commutators T_b on generalized Morrey spaces, where T_b are generated by $BMO(R^n)$ functions b and the strongly singular integrals operators T .

Keywords: Strongly singular integrals, Generalized Morrey spaces, Commutators, BMO functions

Let $\nu \in C_c^\infty(R^n)$, $\text{supp } \nu \subset \{x \in R^n : |x| \leq 2\}$. We define strongly singular integrals kernels $K(x) = \frac{e^{i|x|^{-s'}}}{|x|^n} \nu(x)$,

where $0 < s < 1, s' = \frac{s}{1-s}$, and the corresponding strongly singular integrals

$$Tf(x) = p.v. \int_{R^n} K(x-y)f(y)dy.$$

Let $b \in BMO(R^n)$. We define the commutators T_b generated by functions b and operators T as the following:

$$T_b f(x) = p.v. \int_{R^n} (b(x) - b(y)) K(x-y)f(y)dy.$$

Wainger S.etc (Wainger, S. 1965.) had studied the boundedness of the operators T on $L^q(R^n)$. Chanillo (Chanillo, S. 1984.) developed weighted $L^q(R^n)$ theory by virtue of a basal lemma which will be mentioned later. Garcia-Cuerva J. etc (Garcia-Cuerva, J. , Harboure, E. , Segovia, C. and Torrea, J. L.) obtained the boundedness of higher-order commutators on weighted $L^q(R^n)$. Morrey (Morrey, C. B. 1938.) proposed the classical Morrey spaces when he studied the properties of local solutions of second order elliptic equations. In Ref. (Mizuhara T.. 1991.) Mizuhara introduced the following generalized Morrey spaces.

Let Φ be positive increasing functions on $(0, \infty)$ satisfying $\Phi(2r) \leq D\Phi(r)$ for any $r > 0$, where $D \geq 1$ is a constant independent of r .

Definition 1 (Mizuhara T. 1991.) For $1 \leq p < \infty$, we define the generalized Morrey spaces as the following

$$L^{p,\Phi}(R^n) = \left\{ f \in L^p_{loc} : \|f\|_{L^{p,\Phi}} < \infty \right\},$$

Where $\|f\|_{L^{p,\Phi}}^p = \sup_{t \in R^n, r > 0} \frac{1}{\Phi(r)} \int_{B(t,r)} |f(x)|^p dx$, $B(t,r)$ is a sphere r in radius whose center is at point t .

We know that when $\Phi(r) = r^\lambda$, $(0 < \lambda < n)$, $L^{p,\Phi}$ are the classical Morrey spaces.

In this paper we will show the boundedness of strongly singular integrals operators T on generalized Morrey spaces by weighted inequations. Furthermore, we will show the boundedness of the commutators generalized by BMO functions b of operators T by virtue of sharp estimate.

1. Boundedness of strongly singular integrals operators T on generalized Morry spaces

We fix the following notations in Lemma 1 and Theorem 1:

For $\forall x_0 \in R^n, r > 0, f(y) = f\chi_{B(x_0, 2r)}(y) + \sum_{k=1}^{\infty} f\chi_{B(x_0, 2^{k+1}r) \setminus B(x_0, 2^k r)}(y) \equiv \sum_{k=0}^{\infty} f_k(y)$.

Lemma 1 For $1 \leq D(\Phi) < 2^n, 1 < p < \infty, f \in L^{p, \Phi}$, if T are strongly singular integrals then for $\forall k, (k > 0)$ we have:

$$\int_{B(x_0, r)} |T(f_k)(x)|^p dx \leq C \left(\frac{D}{2^{\theta n}} \right)^k \|f\|_{L^{p, \Phi}}^p \Phi(r),$$

Where $\theta \in \left(\frac{\ln D}{\ln 2^n}, 1 \right)$.

Proof: By the weighted property of A_p , for any $\alpha \in (0, 1), \forall k > 0, (M\chi_{B(x_0, r)})^\alpha \in A_1 \subset A_p, (1 < p \leq \infty)$, we have

$$\begin{aligned} \int_{B(x_0, r)} |T(f_k)(x)|^p dx &\leq C \int_{B(x_0, r)} \left| \int_{B(x_0, 2^{k+1}r)} \frac{|f_k(y)|}{|x-y|^n} dy \right|^p dx \\ &\leq C \int_{B(x_0, r)} |M(|f_k|)(x)|^p dx \\ &\leq C \int_{R^n} |M(|f_k|)(x)|^p (M\chi_{B(x_0, r)})^\theta dx \\ &\leq C \int_{R^n} |f_k(x)|^p (M\chi_{B(x_0, r)})^\theta dx \\ &\leq C \frac{1}{(2^{k-1})^{n\theta}} \int_{B(x_0, 2^{k+1}r)} |f_k(x)|^p dx \\ &\leq C \frac{1}{(2^{k-1})^{n\theta}} \|f\|_{L^{p, \Phi}}^p \Phi(2^{k+1}r) \\ &\leq C \left(\frac{D}{2^{\theta n}} \right)^k \|f\|_{L^{p, \Phi}}^p \Phi(r). \end{aligned}$$

Theorem 1 For $1 \leq D(\Phi) < 2^n, 1 < p < \infty$, and T are strongly singular integrals then T are bounded on $L^{p, \Phi}(R^n)$.

Proof: $\forall x_0 \in R^n, r > 0$, by the boundedness of T on $L^p(p > 1)$ (Wainger, S. 1965.), we get

$$\int_{B(x_0, r)} |T(f_0)(x)|^p dx \leq C \int_{B(x_0, 2r)} |f(x)|^p dx \leq C \|f\|_{L^{p, \Phi}}^p \Phi(r).$$

And by Lemma 1 we have

$$\begin{aligned} \left[\int_{B(x_0, r)} |T(f)(x)|^p dx \right]^{\frac{1}{p}} &\leq \sum_{k=0}^{\infty} \left[\int_{B(x_0, r)} |T(f_k)(x)|^p dx \right]^{\frac{1}{p}} \\ &\leq C \left[1 + \sum_{k=1}^{\infty} \left(\frac{D}{2^{n\theta}} \right)^{\frac{k}{p}} \right] \|f\|_{L^{p, \Phi}} \Phi^{\frac{1}{p}}(r) \\ &\leq C \|f\|_{L^{p, \Phi}} \Phi^{\frac{1}{p}}(r). \end{aligned}$$

We used $\theta \in \left(\frac{\ln D}{\ln 2^n}, 1 \right)$ in the last inequation.

2. Boundedness of the commutators on generalized Morrey spaces

Lemma 2 (Mizuhara T. 1991.) For $1 \leq D(\Phi) < 2^n, 1 \leq q < p < \infty$, then $M_q f(x) = \left(M|f|^q(x) \right)^{\frac{1}{q}}$ are bounded on $L^{p, \Phi}(R^n)$, where M are H-L maximum operators.

Lemma 3 (Ding, Y. 1997.) For $1 \leq D(\Phi) < 2^n, 1 < p < \infty$, then for $\forall f \in L^{p,\Phi}(R^n)$ we have

$$\|Mf\|_{L^{p,\Phi}} \leq C \|f^\#\|_{L^{p,\Phi}},$$

where $f^\#(x) = \sup_{x \in Q} \frac{1}{|Q|} \int_Q |f(y) - f_Q| dy$.

Lemma 4 If T are strongly singular integrals, $1 < r, s < \infty, b \in BMO(R^n)$, then for $a.e. x \in R^n, \forall f \in L^{p,\Phi}(R^n), (1 < p < \infty)$ there exists a constant C independent of b, f so that the following inequations hold

$$(T_b f)^\#(x) \leq C \|b\|_* \left\{ \left(M|Tf|^{r'} \right)^{\frac{1}{r}}(x) + \left(M|f|^{r'} \right)^{\frac{1}{r}}(x) \right\}.$$

Proof: We only need to show for any $x_0 \in R^n$ the following inequations hold

$$(T_b f)^\#(x_0) \leq C \|b\|_* \left\{ \left(M|Tf|^{r'} \right)^{\frac{1}{r}}(x_0) + \left(M|f|^{r'} \right)^{\frac{1}{r}}(x_0) \right\}.$$

We choose a cube Q with side length $\delta, s.t. x_0 \in Q$. Let $4\delta_0 = \delta_0^{\frac{1}{1+s}}$ and we know δ_0 is a constant less than 1.

Case 1: $\delta < \delta_0$.

Suppose cube \tilde{Q} with side length $\delta^{\frac{1}{1+s}}$ has the same center as Q . We have

$$f = f\chi_{4Q} + f\chi_{\tilde{Q} \setminus 4Q} + f\chi_{R^n \setminus \tilde{Q}} \equiv f_1 + f_2 + f_3.$$

$$T_b f(x) = \int_{R^n} (b_Q - b(y))k(x-y)f(y)dy - (b_Q - b(x)) \int_{R^n} k(x-y)f(y)dy.$$

Let $C_Q = \frac{1}{|Q|} \int_Q \int_{R^n} (b_Q - b(y))k(z-y)f_3(y)dydz$. It is obvious that C_Q is a constant. So

$$\begin{aligned} & \frac{1}{|Q|} \int_Q |T_b(f)(x) - C_Q| dx \\ & \leq \frac{1}{|Q|} \int_Q |(b_Q - b(x))Tf(x)| dx + \frac{1}{|Q|} \int_Q \left| \int_{R^n} (b_Q - b(y))k(x-y)f_1(y)dy \right| dx \\ & + \frac{1}{|Q|} \int_Q \left| \int_{R^n} (b_Q - b(y))k(x-y)f_2(y)dy \right| dx \\ & + \frac{1}{|Q|} \int_Q \left(\frac{1}{|Q|} \int_Q \int_{R^n} (b_Q - b(y))(k(x-y) - k(z-y))f_3(y)dydz \right) dx \\ & = A_1 + A_2 + A_3 + A_4. \end{aligned}$$

As for A_1 , we have

$$\begin{aligned} A_1 & \leq C \left(\frac{1}{|Q|} \int_Q |b_Q - b(x)|^{r'} dx \right)^{\frac{1}{r}} \left(\frac{1}{|Q|} \int_Q |Tf(x)|^r dx \right)^{\frac{1}{r}} \\ & \leq \|b\|_* \left(M(|Tf|)^r \right)^{\frac{1}{r}}(x_0). \end{aligned}$$

As for A_2 , for $1 < q < t, u > 1$ so that $qu = t$, by Hölder inequation we have

$$A_2 \leq C \left\{ \frac{1}{|Q|} \int_Q |T((b_Q - b)f_1)(x)|^q dx \right\}^{\frac{1}{q}}$$

$$\begin{aligned} &\leq C \left\{ \frac{1}{|Q|} \int_Q |(b_Q - b)f(x)|^q dx \right\}^{\frac{1}{q}} \\ &\leq C \left\{ \frac{1}{|Q|} \int_Q |(b_Q - b(x))|^{qu'} dx \right\}^{\frac{1}{qu'}} \left\{ \frac{1}{|Q|} \int_Q |f(x)|^{qu} dx \right\}^{\frac{1}{qu}} \\ &\leq C \|b\|_* \left(M|f|^{t'} \right)^{\frac{1}{t}}(x_0). \end{aligned}$$

As for A_4 , by noting $x \in Q, z \in Q, y \notin \tilde{Q}$, and mean value theorem, we have

$$|k(x - y) - k(z - y)| \leq \frac{C\delta}{|y - z|^{n+s'+1}}.$$

$$\begin{aligned} A_4 &\leq C \frac{1}{|Q|} \int_Q \left(\delta \int_{|y-x_0| > \frac{1}{2}\delta^{1+s'}} |b_Q - b(y)| |y - z|^{-(n+s'+1)} |f(y)| dy \right) dz \\ &\leq C \frac{1}{|Q|} \int_Q \left(\sum_{k=0}^{\infty} 2^{-k} (2^k \delta)^{\frac{-n}{1+s'}} \int_{|y-z| < 2(2^k \delta)^{\frac{1}{1+s'}}} |b_Q - b(y)| |f(y)| dy \right) dz \\ &\leq C \frac{1}{|Q|} \int_Q dz \sum_{k=0}^{\infty} 2^{-k} \left\{ (2^k \delta)^{\frac{-n}{1+s'}} \int_{|y-z| < 2(2^k \delta)^{\frac{1}{1+s'}}} |b_Q - b(y)|^{t'} dy \right\}^{\frac{1}{t'}} \left\{ (2^k \delta)^{\frac{-n}{1+s'}} \int_{|y-z| < 2(2^k \delta)^{\frac{1}{1+s'}}} |f(y)|^t dy \right\}^{\frac{1}{t}} \\ &\leq C \|b\|_* \left(M|f|^{t'} \right)^{\frac{1}{t}}(x_0). \end{aligned}$$

As for A_3 , we use the similar ways in Chanillo (Chanillo, S. 1984.). Let $l > 1, m > 1$ satisfying $2 + s' < l', lm = t$, then

$$\begin{aligned} &\int_{R^n} (b_Q - b(y))k(x - y)f_2(y)dy \\ &= \int_{R^n} \frac{e^{i|x-y|^{-s'}} \nu(x - y)}{|x - y|^{\frac{n(2+s')}{l'}}} \left(\frac{1}{|x - y|^{n(1-\frac{2+s'}{l'})}} - \frac{1}{|x_0 - y|^{n(1-\frac{2+s'}{l'})}} \right) (b_Q - b(y))f_2(y)dy \\ &+ \int_{R^n} \frac{e^{i|x-y|^{-s'}} \nu(x - y)}{|x - y|^{\frac{n(2+s')}{l'}}} \frac{(b_Q - b(y))f_2(y)}{|x_0 - y|^{n(1-\frac{2+s'}{l'})}} dy \\ &= B_1 + B_2. \end{aligned}$$

As for B_1 , by the mean value theorem, we get

$$\begin{aligned} B_1 &\leq C \sum_{k=0}^{\infty} 2^{-k} (2^k \delta)^{-n} \int_{|y-x_0| < 2^{k+1}\delta} |b_Q - b(y)| |f(y)| dy \\ &\leq C \|b\|_* \left(M|f|^{t'} \right)^{\frac{1}{t}}(x_0). \end{aligned}$$

As for the estimate of B_2 , we need the following lemma.

Lemma 5 (Chanillo, S.) For $0 < s < 1, s' = \frac{s}{1-s}, t > 1, \frac{s'+2}{t} < 1$ $\tilde{K}_{s',t} \equiv \frac{e^{i|x|^{-s'}}}{|x|^{\frac{n(s'+2)}{t}}}$, we have $\forall f \in L^t(R^n)$,

$$\|\tilde{K}_{s',t} * f\|_{L^t(R^n)} \leq C \|f\|_{L^t(R^n)}.$$

By Lemma 5 and using the similar ways in Chanillo (Chanillo, S. 1984.), we get

$$\frac{1}{|Q|} \int_Q |B_2(x)| dx \leq C |Q|^{-\frac{1}{l'}} \left(\int_{R^n} \frac{|b_Q - b(y)|^l |f_2(y)|^l}{|x_0 - y|^{n l (1 - \frac{2+s'}{l'})}} dy \right)^{\frac{1}{l'}}$$

And $\frac{1}{|Q|} \int_Q |B_2(x)| dx$

$$\leq C |Q|^{-\frac{1}{l'}} \left\{ \sum_{k=0}^{k_0} (2^k \delta)^{(l-1)(1+s')n} (2^k \delta)^{-n} \int_{|y-x_0| < 2^{k+1} \delta} |b_Q - b(y)|^l |f(y)|^l dy \right\}^{\frac{1}{l'}}$$

Where k_0 satisfies $2^{k_0} \delta < \delta^{\frac{1}{1+s'}} < 2^{k_0+1} \delta$.

$$\begin{aligned} &\leq C |Q|^{-\frac{1}{l'}} \sum_{k=0}^{k_0} (2^k \delta)^{\frac{(l-1)(1+s')n}{l}} \left\{ (2^k \delta)^{-n} \int_{|y-x_0| < 2^{k+1} \delta} |b_Q - b(y)|^{lm'} dy \right\}^{\frac{1}{lm'}} \\ &\times \left\{ (2^k \delta)^{-n} \int_{|y-x_0| < 2^{k+1} \delta} |f(y)|^{lm} dy \right\}^{\frac{1}{lm}} \\ &\leq C \|b\|_* \left(M|f|^l \right)^{\frac{1}{l}}(x_0). \end{aligned}$$

Case 2: $\delta \geq \delta_0$.

Let $\gamma = 5\delta_0^{-1}$, $f = f\chi_{\gamma Q} + f\chi_{R^n \setminus \gamma Q}$.

$$\begin{aligned} \frac{1}{|Q|} \int_Q |T_b(f)(x)| dx &\leq \frac{1}{|Q|} \int_Q |(b_Q - b(x))Tf(x)| dx \\ &+ \frac{1}{|Q|} \int_Q \left| \int_Q (b_Q - b(y))k(x-y)f(y) dy \right| dx \\ &+ \frac{1}{|Q|} \int_Q \left| \int_{R^n \setminus \gamma Q} (b_Q - b(y))k(x-y)f(y) dy \right| dx \\ &= D_1 + D_2 + D_3. \end{aligned}$$

And the discussion of D_1 is similar with A_1 , D_2 is similar with A_2 , so we omit the proof here..

We note that when $x \in Q, y \notin \gamma Q, |x - y| > 2, k(x - y)$ is equal to 0.

So we get the lemma.

Theorem 2: For $1 \leq D(\Phi) < 2^n, 1 < p < \infty$, if T are strongly singular integrals, then T_b are bounded on $L^{p,\Phi}(R^n)$.

Proof: By Lemma 2,3,4 and Theorem 1, we get

$$\|T_b f\|_{L^{p,\Phi}} \leq \|M(T_b f)\|_{L^{p,\Phi}} \leq C \|(T_b f)^\# \|_{L^{p,\Phi}} \leq C \|b\|_* \left\| \left(M(|Tf|^r) \right)^{\frac{1}{r}} + \left(M(|f|^s) \right)^{\frac{1}{s}} \right\|_{L^{p,\Phi}},$$

where $\left\| \left(M(|Tf|^r) \right)^{\frac{1}{r}} \right\|_{L^{p,\Phi}} \leq \|Tf\|_{L^{p,\Phi}} \leq \|f\|_{L^{p,\Phi}}$, and we can choose $r < p$ by Lemma 4. So

$$\left\| \left(M(|f|^s) \right)^{\frac{1}{s}} \right\|_{L^{p,\Phi}} \leq \|f\|_{L^{p,\Phi}}.$$

We get the theorem.

References

- Chanillo, S. , Weighted norm inequalities for strongly singular convolution operators, *Trans. Amer. Math. Soc.* 218 (1984), 77-107.
- Ding, Y. , A characterization of BMO via commutations, *Northeast. Math. J.* 13(4) (1997), 422-432.
- Garcia-Cuerva, J. , Harboure, E. , Segovia, C. and Torrea, J. L. , Weighted norm inequalities for commutators of strongly singular integrals, *Indiana Univ. Math. J.* 40 (1991), 1397-1420.
- Garcia-Cuerva, J., Rubio de Francia, J. L., Weighted norm inequalities and related topics, North-Holland, Amsterdam, 1985.
- Liu, Z. G. , Boundedness of commutators of strongly singular convolution operators on Herz-type spaces, *Studia Math.* 157(1) (2003) 33-46.
- Lu, S. Z. , Yang, D.C. , Zhou, Z. S. , Sublinear operators with rough kernel on generalized Morry spaces, *Hokkaido Math J.*,27 (1998), 219-232.
- Mizuhara T., Boundedness of some classical operators on generalized Morrey spaces. *In Harmonic Analysis, ICM-90 Conference Proceedings* (ED. S. Igari), Springer-verlag, Tokyo, (1991), 183-189.
- Morrey, C. B. , On the solutions of quasi linear elliptic partial equations , *Trans. Amer. Math. Soc.*, 43 (1938), 126-166.
- Wainger, S. , Special trigonometric series in k-dimensions, *Mem. Amer. Math. Soc.* 59 (1965).



Investigation on Dielectric Constant of Zinc Oxide

Khalid Omar

School of Physics

Universiti Sains Malaysia

11800 Penang, Malaysia

E-mail: khalhadithi@yahoo.com

M. D. Johan Ooi & M. M. Hassin

School of Physics

Universiti Sains Malaysia

11800 Penang, Malaysia

Abstract

The studies of the behavior of zinc oxide and its dielectric constant at different temperature ranging from 700 °C (975K) up to 1000 °C (1275K) have been done, as well as the fabrication of pellet. The pellets were sintered at 700 °C, 800 °C, 900 °C and 1000 °C, in a Nabertherm Controller Furnace and the heating rate is 6 °C/min. The capacitance and dissipation factor ($\tan \delta$) were taken and calculated the relative permittivity, ϵ_r and dielectric loss, ϵ_i which are indicated the behavior and dielectric constant of zinc oxide that depend on different temperatures of sintered pellet and frequency of the applied LCR meter.

Keywords: Semiconductor, Zinc oxide, Dielectric constant

1. Introduction

Zinc oxide was the material of choice for this observation because it by far is the most common material used in the commercial manufacture and research due to its low cost and wide availability. It is valuable both for direct application or preparation of other compounds. Zinc oxide has been produced commercially for considerably more than century, originally for use as a pigment in paints and also for rubber, glass, porcelain enamels and pharmaceuticals. More recently, Zinc oxide has found new applications in semiconductors, luminescence, and photoconductivity. Under certain conditions, atoms of zinc in stoichiometric excess can lodge in these lacunae and this hypothesis is often useful in explaining certain specific properties of the oxide such as its semiconductivity, photoconductivity, luminescence, catalytic properties and solid state chemistry. It possess thermochromic which change color from white to yellow when heated, and back again to white color when cooled down due to various types of crystal lattice defects. It remains white when exposed to hydrogen sulfide or ultraviolet light. The larger red atoms are zinc atoms while the smaller purple atoms are oxygen atoms. In wurtzite, the tetrahedral are stacked in hexagonal close packed array with the tetrahedral edges of alternate layers rotated through 180° about the c-axis. ZnO is almost insoluble in water but soluble in acids or alkalis. Its solubility is "0.005 g/l" at 25°C in water while in aqueous ammonia its solubility is "0.28 g/l" in 1% ammonia at 25°C. Its solubility is increased by the presence of ammonium salts [M. Farnsworth and C. H. Kline, (1973)]. Zinc oxide may be reduced by heating in hydrogen or carbon monoxide but it does not react with dry carbon dioxide. It is gradually changed to zinc oxycarbonate in humid air. It also does not react with oxygen to form peroxide. The band gap of ZnO can be tuned via divalent substitution on the action to produce heterostructures. Cadmium, (Cd) doping can decrease the band gap to as low as ~ 3.0 eV, whereas Magnesium (Mg) doping can increase the band gap to as high as ~ 4.0 eV [http://en.wikipedia.org/wiki/Zinc_oxide]. Electron doping in nominally undoped ZnO has been attributed to Zinc interstitials, oxygen vacancies, or hydrogen. The intrinsic defect levels lead to n-type doping lay approximately 0.01 - 0.05 eV below the conduction band. Electrical properties of ZnO depend on the concentration of intentional impurities, called dopants. The dopants determine whether the current is carried by electrons or holes. In semiconducting oxides, it is generally possible to achieve one or other of these types, but not both. The dopants are also called shallow level impurities because they introduce energy levels close to one of the allowed energy bands in the

material and are easily ionized as a result. There may also be unintentional impurities introduced during the growth of ZnO that have a deleterious effect on the properties of the material. These are called deep level defects or impurities and may be either elemental impurities arising from contamination of the growth environment or structural defects in the ZnO crystal lattice. These structural defects can be vacancies in the crystal structure or interstitials, i.e. atoms sitting in the open regions around lattice sites. In both cases, they may introduce energy levels deep within the forbidden band gap of ZnO and act as traps for carriers in the material. These uncontrolled defects make it very difficult to obtain reproducible device performance and reliability. For ZnO, n-type conductivity is relatively easy to realize via excess Zinc or with Aluminum (Al), Gallium (Ga), or Indium (In) doping, but p-type doping has only recently been achieved. This is a fairly common occurrence in wide band gap semiconductors, where difficulty in achieving bipolar “n-type and p-type” doping is not unusual. This doping difficulty in wide band gap semiconductors can be explained by compensation by native point defects or dopant atoms that locate on interstitial sites. The defect compensates for the substitution impurity level through the formation of a deep level trap. In some cases, strong lattice relaxations can drive the dopant energy level deeper within the gap. In other systems, one may simply have a low solubility for the chosen dopant, which limits the accessible extrinsic carrier density. In ZnO, most candidate p-type dopants introduce deep acceptor levels. The most promising dopants for p-type material are the group V elements [D. P. Norton, et al (2004)]. Conductivity of ZnO is decreases when heated in oxygen under pressure and when heated in vacuum, its conductivity increases. Conductivity in the lower temperature range is believed to be caused by the ionization of interstitial zinc atom pairs whose ionization energy is 2×10^{-2} V or less. The change in conductivity of Zinc oxide can also be caused by the addition of varying amounts of monovalent oxides decreases the conductivity whereas addition of trivalent oxides such as Aluminum (Al) or Chromium (Cr) increases the conductivity. Zinc oxide is transparent to visible light to a relatively high and uniform degree so that it exhibits a pure white of high brilliance. It is opaque to ultra – violet radiation below 3655\AA [M. Farnsworth et al (1973)]. Meanwhile the optical properties of ZnO, studied by using photoluminescence, photoconductivity, and absorption reflect the intrinsic direct band gap, a strongly bound exciton state, and gap states arising from point defects. A strong room temperature, near-band-edge ultraviolet (UV) photoluminescence peak at ~ 3.2 eV is attributed to an exciton state, as the exciton binding energy is on the order of 60 meV. The high exciton binding energy is more resistant to radiation, and is multifunctional with uses in the areas as a piezoelectric [<http://www.physorg.com/Zinc Oxide Nanostructures: Growth, Properties and Applications>]. Zinc oxide is considered a better material than Gallium nitride (GaN) for making blue LED devices because, it naturally emits and absorbs at 368nm more efficiently and it is also cheap and abundant. The new LEDs will deliver 10 times the light-emitting efficiency. These LEDs are used as light sources in applications requiring high luminance, long service life and high efficiency, such as large outdoor displays, traffic signals, liquid-crystal display backlighting and illuminations [<http://www.spectrum.ieee.org>]. Zinc oxide continues as an essential ingredient in the "soft" type of ferromagnetic materials for television, radio, and telecommunication applications. In these fields ferrites based on Magnetite, Nickel oxide and Zinc oxide are used as elements in many types of electronic devices [<http://www.navbharat.co.in>]. The latest research about ZnO is that a team from Northwestern University had found that when they pumped disordered Zinc oxide powders with a conventional laser at low power, the materials gave off light with a broad band of wavelengths which the light in fact is a laser emission. The lasing wavelength is 380 nm and the devices operate at room temperature. If the lasing powder can be mass produced, they would be cheaper and more efficient than the LEDs now used as laser sources in cell phones, calculators and other devices with luminescent displays.

2. Correlation between diffusion coefficient, mobility and conductivity

Zinc oxide possesses a semiconductor behavior which it can be a dielectric at low temperature and being a conductor at high temperature. It is due to decreasing of energy band gap as temperature of the material increase but for this experiment, the factor that determines the behavior of ZnO is related to diffusion of atom during sintering process.

Zinc oxide contains a large number of grain boundaries, which represent a high- energy area because of the inefficient packing of the atoms. A lower overall energy is obtained in the material if the amount of grain boundary area is reduced by grain growth. Grain growth involves the movement of grain boundaries, permitting larger grains to grow at the expense of smaller grains. For grain growth in materials, diffusion of atoms across the grain boundary is required. In order to move to a new location, the atom must overcome an energy barrier which is the activation energy Q , and for that a thermal energy is required to exceed this barrier. The kinetics of process of diffusion is strongly dependent on temperature [D. R. Askeland et al (2005)]. The diffusion coefficient D is related to temperature by an Arrhenius- type equation,

$$D = D_0 \exp\left(\frac{-Q}{RT}\right) \quad (1)$$

where Q is the activation energy (cal/mol), T is the absolute temperature (K), D_0 is Einstein diffusion constant and R is gas constant which is 8.314 (J/K.mol).

According “Equation 1”, when the temperature of material increases, the diffusion coefficient D increases and thermal energy supplied to the diffusing atoms permits the atoms to overcome the activation energy barrier and more easily move to another grain. High temperature increase diffusion coefficient. Existence of impurities also increases the electrical conductivity because it can diffuse and help carry the current. Therefore, at low temperature, the diffusion is slow, thus decreasing mobility and conductivity of the material [D. R. Askeland et al (2005)].

2.1 Dielectric in term polarization and electric field

ZnO crystal could possess a dielectric behavior when its energy barrier is large and its diffusion coefficient is low. Besides, the utmost important of ZnO is that it has built in polarization. Thus, it is important to know the basic of dielectric in term of polarization and electric field. In dielectric, all charges are attached to specific atoms or molecules and all they can do is move a bit within it. Their microscopic displacement, affects the characteristics behavior of dielectric materials. In any substance, including ZnO crystal, the atom is electrically neutral because there is a positively charged core “nucleus” and a negatively charged electron cloud surrounding it. These two regions of charge within the atom are influenced by the electric field. The nucleus is pushed in the direction of the field, and the electrons are pushed in the opposite ways. In principle, if the electric field is large enough, it can pull the atom apart completely, “ionizing” it. Thus, the substance then becomes a conductor. With less extreme electric fields, however, equilibrium is soon established. If the center of the electron cloud does not coincide with the nucleus, these positive and negative charges attract one another, and this holds the atoms together. The two opposing forces, electric field, E pulling the electrons and nucleus apart, their mutual attraction drawing them together reach a balance, leaving the atom polarized, with plus charge shifted slightly one way and minus the other. In other words, dielectric polarization arises due to the existence of atomic and molecular forces, appears whenever charges in a material are displaced with respect to one another under the influence of an electric field [David J. Griffiths].

3. Fabrication of Zinc oxide pellets

The process involve in making ZnO pellets are the same with fabricating a ceramic. The involved procedures are Pulverization, Pressing and Sintering. The pulverization process is to reduce the particle size with the action of mechanical force. This is to provide a homogeneously mixture and has a sufficiently small particle size. The pressing is important in order to affect the sample in increasing the mechanical strength in order to make it more compact and Reducing void between particles. There are two techniques in this pressing process which are Isostatic Press and Hydraulic Press. Sintering is the critical process in fabricating ZnO pellets. It is commonly refers to processes involved in the heat treatment of powder compacts below its melting point until its particles adhere to each other where porosity is usually reduced and the grain size increases significantly through mass transport [R.M. German (1991)]. The sintering process is illustrated in the “Figure 1”.

4. Calculation of dielectric constant

The dielectric constant, ϵ is consists of real permittivity or relative dielectric constant which is generally called dielectric constant of the test material, ϵ_r and imaginary permittivity or dielectric loss ϵ_i . Dielectric constant of the test material, ϵ_r is calculated from the measurement of capacitance value which can be obtained using the following equation,

$$\epsilon_r = \frac{t \times C_p}{A \times \epsilon_o} = \frac{t \times C_p}{\pi \left(\frac{d}{2}\right)^2 \times \epsilon_o} \quad (2)$$

where,

t = Thickness of the pellet

C_p = Equivalent parallel capacitance which obtained from the data of measurement

ϵ_o = permittivity of vacuum = 8.854×10^{-12} (F/m)

d = Diameter of guard electrode = 5×10^{-3} (m)

Thus, the above equation becomes,

$$\epsilon_r = \frac{t \times C_p}{6.25 \times 10^{-6} \times \pi \times \epsilon_o} = \frac{t \times C_p}{1.74 \times 10^{-16}} \quad (3)$$

Whereas, the imaginary permittivity or dielectric loss, ϵ_i , is obtain from the value of dissipation factor, D .

Where, dissipation factor, D ,

$$D = \frac{\varepsilon_i}{\varepsilon_r} \quad (4)$$

$$\varepsilon_i = D \times \varepsilon_r \quad (5)$$

With dissipation factor, D , is directly obtain from data of our measurement and ε_r is obtained from "Equation 3". Meanwhile, the dielectric dissipation factor, $\tan \delta$ or loss tangent of test material D_r , can be obtained directly by measuring the dissipation factor from the "Equation 4".

5. Results and discussion

All figures are shown the behavior of Zinc oxide pellets that were sintered at different temperature and its behavior will determine dielectric constant of the pellets.

The relative permittivity ε_r of the pellets versus frequency of the applied LCR meter ranging from 1 kHz until 5 MHz with temperature as the function is shown in "Figure 2". Based on this, the relative permittivity ε_r of the pellets is decrease with increasing of frequency. The figure of sintered pellet at 800°C and 900°C are said to be in sequential order denotes, they possess the same behavior whereas as the temperature increase to 1000°C, the behavior of the pellets seems to have changed. For pellet that was sintered at 700°C, the figure shows that the sample has some defect.

For pellets sintered at 1000°C, its ε_r is smaller than the pellets that are sintered at 900°C and 800°C due to increasing conductivity of the pellets. This is because, when those pellets were subjected to a sintering process at 1000°C, volume of pore space between the particle is reduce. Thus, there are larger grain grows at the expense of smaller grains. Therefore, the energy barrier is reduced and rapidly increases the diffusion of atoms to another grain which means the diffusion coefficient is increase. Hence, the conductivity is increase with increasing of mobility, indicates the pellets sintered at 1000°C possess a conductor behavior.

For pellets that were sintered at 800°C and 900°C, the relative permittivity of the pellets, ε_r are bigger than the other two pellets sintered at 700°C and 1000°C because at low temperature, therefore, the diffusion of atom is very slow due to an increasing of energy barrier. The diffusion coefficient is reduced which means the mobility and conductivity were decreased. Thus, the pellets can absorb and stored electrical potential, which indicate it possess dielectric behavior. Whereas for pellet subjected to 700°C, it obtains ε_r lower than pellets sintered at 1000°C. Based on theory, the pellets should obtain high ε_r . This failure could be due to the existence of impurities during the preparation of the pellets. These impurities can diffuse and help carry the current and thus increasing the conductivity resulting small value relative permittivity of the pellets, ε_r .

The imaginary part of permittivity or dielectric loss ε_i versus frequency of the applied field ranging from 1 kHz until 5MHz with the temperature as the function is shown in "Figure 3". The pellet's dielectric loss, ε_i are decreasing with increasing frequency. Pellets that were sintered at 700°C, 800°C and 900°C have small dielectric loss comparable to ε_i of sintered pellet at 1000°C. This indicates that they can store more energy due to small loss. Hence, they possess dielectric behavior. Meanwhile, ε_i for sintered pellets at 1000°C is high, indicates there are increasing of dielectric loss. Thus, it cannot store energy, therefore it possess conductor behavior.

The relative permittivity ε_r of the pellets versus temperature of the sintered pellets with the frequency of applied LCR meter as the function is shown in "Figure 4". This figure shows that relative permittivity of the pellets ε_r , decreases with increased of frequency. This is because mechanisms of polarization have varying time response capability to an applied field frequency. For the frequency range between 1 kHz and 1 MHz, the total contribution of polarization is arises from electronic displacement, ionic displacement, dipole orientation and space charge displacement. As the frequency increase at 1 MHz, the polarization of the molecule begins to lag the field reversals increasing the dielectric loss ε_i , and decreasing relative permittivity ε_r . Meanwhile, as the frequency decrease at 1 kHz, generates little loss, as the polarization mechanism is much slower than the field reversals.

The imaginary part of permittivity or dielectric loss ε_i , versus temperature of the sintered pellets with the frequency of applied LCR meter as the function is shown in "Figure 5". With decreasing of frequency at 1 kHz and 10 kHz, the molecules have large relaxation time with delayed polarization processes. Hence, the dielectric loss is small. Whereas, with increasing frequency at 1 MHz and 100 kHz, the molecules are instantaneously polarized, thus the dielectric loss is high.

6. Conclusion

There are larger grain grows at the expense of smaller grains. The diffusion coefficient is increase due to the reduction of energy barrier and rapidly increases the diffusion of atoms to another grain. The diffusion coefficient is reduced when the mobility and conductivity were decreased. The pellets can absorb and stored electrical potential. The relative permittivity of the pellets ε_r , decreases on term of increased of frequency due to the polarization, the molecules have large relaxation time when decreasing of frequency. It can be stored more energy because the dielectric loss is small.

References

Askeland D. R. and Fulay P. P (2005) The Science and Engineering of Materials, Thomson-Engineering, Fifth Edition p.p. 156-694.

Griffiths D. J., Introduction to Electrodynamics 3rd Ed (1999). Prentice Hall of India, p.p.160-192.

http://en.wikipedia.org/wiki/Zinc_oxide, available.

<http://www.navbharat.co.in>, (available 2008).

<http://www.physorg.com>, (available 2008).

<http://www.spectrum.ieee.org>, (Apr. 2008).

Marie Farnsworth and Charles H Kline, Zinc chemicals (1973) VG- Ex-lib (corporate) p.p. 36- 57.

Norton D. P., Heo Y. W., Ivill M. P., Ip K., Pearton S. J., Chisholm M. F., and Steiner T., (June 2004) ZnO growth, doping and processing, Material Today, p.p. 35- 36.

R.M. German, "Fundamentals of Sintering", Engineering Materials Handbook, volume 4, (1991). Ceramics and Glasses, ASM International.

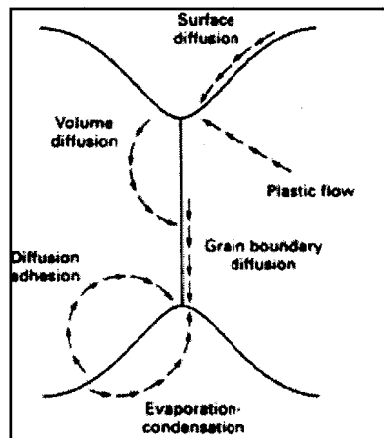


Figure 1. Mass flow paths in the neck region of two particles during sintering

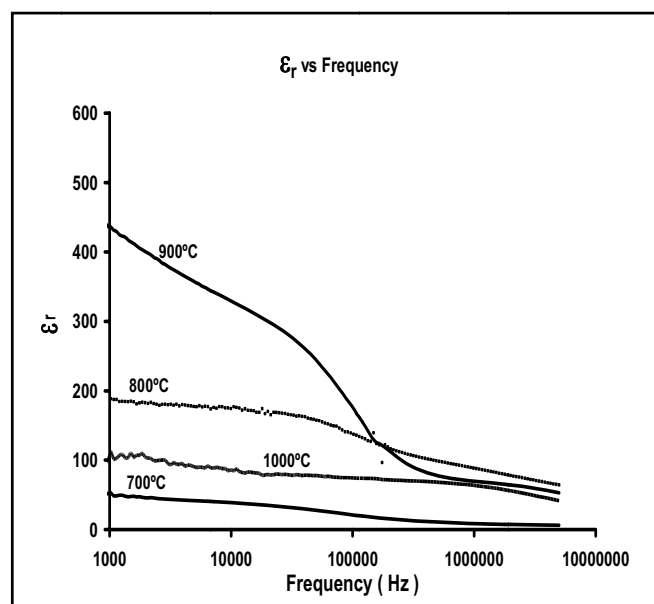


Figure 2. ϵ_r versus frequency (Hz)

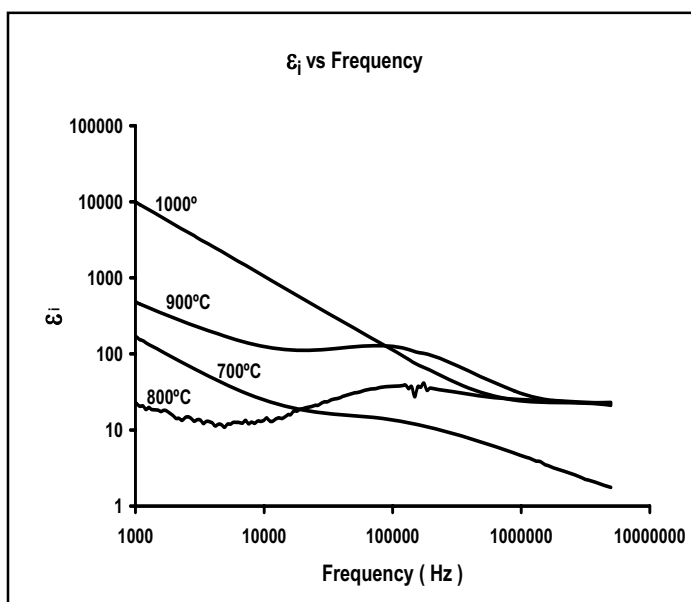


Figure 3. ϵ_i versus frequency (Hz)

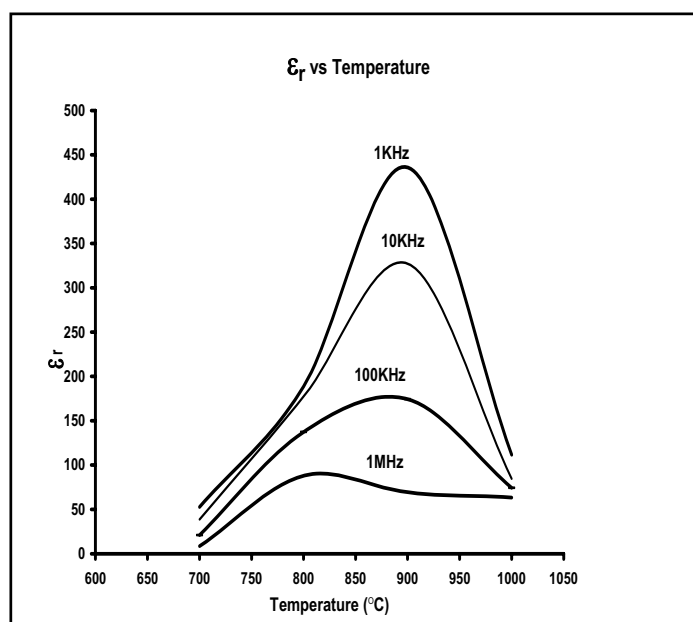


Figure 4. ϵ_r versus Temperature

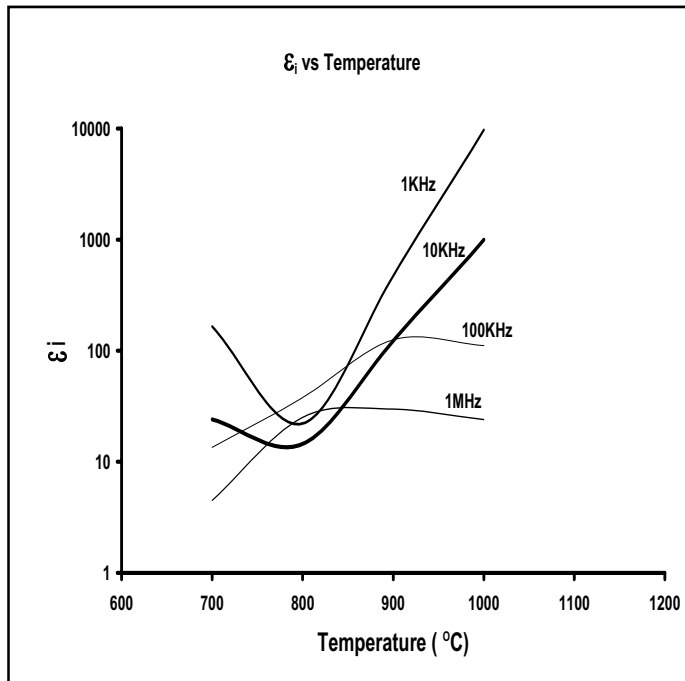


Figure 5. ϵ_i versus Temperature



Aerodynamics Simulation of Hypersonic Waverider Vehicle

Dingyi Wu & Hong Xiao

School of Power and Energy

Northwestern Polytechnical University

PO box 185, Xian, Shaanxi, China

Tel: 86-29-8849-4394 E-mail: xhong@nwpu.edu.cn

The research is financed by China Aerospace Scientific and Technological Innovation Foundation & Northwestern Polytechnical University Scientific and Technological Innovation Foundation.

Abstract

The purpose of this paper is to examine the aerodynamic characteristics of three hypersonic configurations. Three hypersonic forebodies were designed. For the purpose to integrate with ramjet or scramjet, all forebodies were designed integrated with hypersonic inlet.

To better understand the forebody performance, three dimensional flow field calculations of these hypersonic forebodies integrated with hypersonic inlet were conducted in the design and off design conditions. Computational result show that waverider offer an aerodynamic performance advantage in the terms of high lift-drag ratios over the other two configurations. Liftbody offer good aerodynamic performance in subsonic region. The aerodynamic performance of the liftbody integrated with waverider configuration is not comparable to that of pure waverider in the terms of lift-drag ratios and is not comparable to that of pure liftbody in subsonic. But the liftbody integrated with waverider configuration exhibit good lateral-directional and longitudinal-directional stability characteristics. Both pure waverider and liftbody integrated with waverider configuration can provide relatively uniform flow for the inlet and offer good aerodynamic characteristics in the terms of recovery coefficient of total pressure and uniformity coefficient.

Keywords: Waverider, Liftbody, Inlet, Hypersonic, Forebody

1. Introduction

Hypersonic waveriders are promising shapes for the forebodies of propulsion-integrated hypersonic vehicles. The aerodynamic advantage of the waverider is that high pressure behind the shock wave under the vehicle does not “leak” around the leading edge to the top surface, so that the lift-to-drag ratio (L/D) for the waverider is considerably higher than that for the conventional aerodynamic vehicle. Furthermore, because they are designed with an inverse methodology, the flow field is first selected, then the appropriate generating shape is determined, the resulting shapes provide relatively uniform inlet conditions, corresponding to the flow conditions of the original generating flow(Charles E.Cockrell.J NASA-Technical-Paper-1996-3559).

Liftbody configuration is a promising shape for aero plane. It can offer good aerodynamic performance in subsonic region (Liu Wei(AIAA-2005-5250)).

The purpose of current research work is to integrate waverider with liftbody and examine the aerodynamic characteristics of three hypersonic configurations including pure liftbody configuration, pure waverider configuration and liftbody integrated with waverider configuration.

2. Hypersonic forebody and inlet design

In the derivation of forebody, the first step is to select design Mach number and then select the forebody shock wave's number and angle according to the inlet requirement(Xiao.Hong AIAA-2006-8090).

In this paper, we defined the design Mach number as 6.0, and the first shock wave angle was defined as $13.0(\beta_1)$.

According to equation of flow past the shock wave,

$$Ma_1^2 = \frac{Ma^2 + \frac{2}{\gamma - 1}}{\frac{2\gamma}{\gamma - 1} Ma^2 \cdot \sin^2 \beta - 1} + \frac{\frac{2}{\gamma - 1} Ma^2 \cos^2 \beta}{Ma^2 \cdot \sin^2 \beta + \frac{2}{\gamma - 1}}$$

The Ma_1 , which is Mach number after the first shock wave, can be calculated. According to Ma_1 and the second shock wave angle β_2 , the Mach number Ma_2 after the second shock wave can be calculated.

The angle of shock wave can be defined by equal shock wave strength method, as

$$Ma \sin \beta_1 = Ma_1 \sin \beta_2 = Ma_2 \sin \beta_3$$

The angle of shock wave can also be defined by equal shock wave angle method, as

$$\beta_1 = \beta_2 = \beta_3$$

In this paper, we used equal shock wave angle method.

According to the Mach number before shock wave and angle, equation of angle of shock wave (β) and angle of flow swerve (α), the three angle of flow swerve $\alpha_1, \alpha_2, \alpha_3$ can be calculated.

$$\tan \alpha = \frac{Ma^2 \sin^2 \beta - 1}{\left[Ma^2 \left(\frac{\gamma + 1}{2} - \sin^2 \beta \right) + 1 \right]} \cdot \tan \beta$$

β_4 can also be calculated by flow swerve angle $\alpha_4 = \alpha_1 + \alpha_2 + \alpha_3$.

The forebody and inlet parameters are showed in Fig.1.

3. Pure waverider design

The design objective of waverider is that all three shock waves are closed in the design flight condition. As showed in Fig 2, in the design condition, the shock wave created by O_1 communicate to B, and the shock waves created by O_2, O_3 also communicate to B (O_1, O_2, O_3 are located in the same longitudinal profile).

Waverider design steps are described in the flowing:

- (1) Select one point O at the top inlet curve willfully, and then find O_3 along negative X axial. The angle of O_3 O and X axial is $\alpha_1 + \alpha_2 + \alpha_3$ and the angle of O_3 B and X axial is $\beta_3 + \alpha_1 + \alpha_2$.
- (2) O_3 as the start point, then find O_2 along negative X axial. The angle of O_2 O_3 and X axial is $\alpha_1 + \alpha_2$ and the angle of O_2 B and X axial is $\beta_2 + \alpha_1$.
- (3) O_2 as the start point, then find O_1 along negative X axial. The angle of O_1 O_2 and X axial is α_1 and the angle of O_1 B and X axial is β_1 .
- (4) Repeat the step (1) (2) (3) along the top inlet curve. Join all the O_1 , and then get the first leading edge. Join all the O_2 , and then get the second leading edge. Join all the O_3 , and then get the third leading edge.
- (5) Form the first compress surface by the first leading edge and the second leading edge. Form the second compress surface by the second leading edge and the third leading edge. Form the third compress surface by the third leading edge and the top inlet curve. All three compress surfaces form the waverider bottom compress surface.
- (6) Move the first leading edge along flow direction (X axial) to get the top surface of waverider.

We define the design Mach number $Ma = 6.0$ and the angle of shock wave $\beta_1 = \beta_2 = \beta_3 = 13^\circ$. The inlet height is 30mm and inlet width is 150mm.

4. Liftbody design

The liftbody design steps (Saltzman and Edwin J AIAA-1999-0383) are described in the flowing:

- (1) Define top view curve of liftbody.
- (2) Define top surface curve.
- (3) Define compress surface.
- (4) Define forebody bottom surface.

5. Liftbody integrated with waverider configuration design

In this configuration design, the bottom surface is same to the waverider design steps and the top surface is same to liftbody design steps (Zhenxia Liu and Xiao Hong AIAA-2007-5413).

Three hypersonic inlets are designed by same parameters.

Three hypersonic models are given in Fig.5-7.

6. Simulation

To better understand the forebody performance, three dimensional flow field calculations of these hypersonic forebodies integrated with hypersonic inlet were conducted in the design and off design conditions.

We have used our developed-in-home CFD code to simulate the flow around the forebody with the flow in the inlet. We used the Roe's flux differencing scheme with the min-mod flux limiter to achieve second-order spatial accuracy. This Navier-Stokes code uses Sutherland's viscosity model and the ideal gas law to compute the gas density. The ratio of the specific heats was assumed to be 1.4. We used 1132300 grid cells in the computation. Aerodynamic characteristics of each of configurations are examined over the Mach number range from 0.5 to 8.0 and the attack angle range from -6 to 10, and the performance of these configurations are compared to that of the pure waverider configuration. Effects of attach angle on aerodynamic performance of hypersonic configuration at Ma=6.0 are shown in Fig.8. The maximum lift-drag ratio for each configuration also occurs near 2 angle of attack at Mach 6.0. The angle of attack for maximum lift-drag ratio increases as Mach number decreases. A direct comparison of three configurations is shown in Fig.8. The pure waverider configuration produces higher values of lift-drag ratio than the other two configurations at each Mach number.

The pitching-moment characteristics of three configurations are shown in figure 9. This figure shows the pitching-moment coefficient versus angle of attack at each Mach number 6.0. The moment reference center location here is an arbitrarily selected location at the approximate location of the center of gravity of the model. The liftbody integrated with waverider configuration was expected to provide improved directional stability.

To compare the performance of the waverider in this paper with the two others, We define the performance parameter as flowing:

(1) Flow coefficient

$$\alpha = \frac{A_\infty}{A_1} = \frac{\rho u}{(\rho u)_\infty}$$

A_∞ The free flow tube area A_1 The inlet area

(2) Recovery coefficient of total pressure

$$\eta = \frac{P_2}{P_0}$$

P_2 Average total pressure in the inlet exit profile P_0 Total pressure of free flow

(3) Uniformity coefficient

$$\varepsilon = \frac{\sum_{I=1}^N \sqrt{(M_I - \bar{M})^2}}{N \times \bar{M}}$$

\bar{M} Average Mach number in the inlet out profile

M_I Mach number in the I node

N Node number

Compared with two comparative reference models, the liftbody integrated waverider configuration show better performance with the flow coefficient increased by 5.96%, 14.8%; the recovery coefficient of total pressure increased by 5%, 10.5%, respectively; the uniformity coefficient of inlet outlet is increased by 2.1%, 6.3%.

7. Conclusion

The purpose of this paper is to examine the aerodynamic characteristics of three hypersonic configuration ns including pure liftbody configuration, pure waverider configuration and liftbody integrated with waverider configuration.

Hypersonic forbodies were designed based on these configurations. For the purpose to integrate with ramjet or scramjet, all the forebodies were designed integrated with hypersonic inlet.

To better understand the forebody performance, three dimensional flow field calculations of these hypersonic forebodies integrated with hypersonic inlet were conducted in the design and off design conditions. Computational results show that waverider offers an aerodynamic performance advantage in the terms of higher lift-drag ratios over the other two configuration ns. Liftbody offer good aerodynamic performance in subsonic region. The aerodynamic performance of the liftbody integrated with waverider configuration is not comparable to that of pure waverider in the terms of lift-drag ratios and is not comparable to that of pure lift body in subsonic. But the liftbody integrated with waverider

configuration exhibit good lateral-directional and longitudinal-directional stability characteristics. Both pure waverider and liftbody integrated with wave rider configuration can provide relatively uniform flow for the inlet and offer good aerodynamic characteristics in the terms of recovery coefficient of total pressure and uniformity coefficient.

References

Charles E.Cockrell,J, ect. (1996). Aerodynamics Characteristics of Two Waverider-Derived Hypersoni-c Cruise Configurations. NASA-Technical-Paper-3559. 1996.

Liu Wei ect. (2005). High-order WNND Scheme and Its Application in Topological Structure Analysis of Hypersonic Flow around Liftbody. AIAA-2005-5250.

Xiao Hong ect. (2006). Simulation and Experiment of Hypersonic Waverider Forebody Integrated with Inlet. AIAA-2006-8090.

Saltzman, Edwin J ect. (1999). Flight-determined subsonic lift and drag characteristics of seven Lifting-body and wing-body reentry vehicle configurations with truncated bases.AIAA-1999-0383.

Zhenxia Liu, Xiao Hong, ect. (2007). Aerodynamic performance of waverider forebody Integrated with Inlet and Isolator. AIAA-2007-5413.

Table 1. Performance comparison of forebody integrated with inlet

Model	Pure Waverider	Liftbody	Liftbody integrated with waverider
Mass flow rate	3.02	2.786	3.2
Total pressure recovery coefficient	0.40	0.38	0.42
Average Mach in the inlet exit profile	2.0	2.3	2.05
Uniformity coefficient	0.193	0.201	0.189

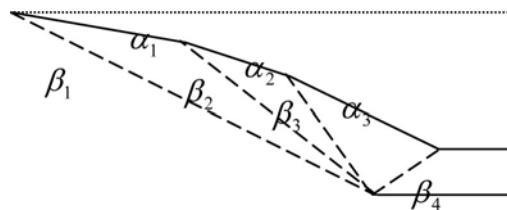


Figure 1. Forebody and inlet parameters

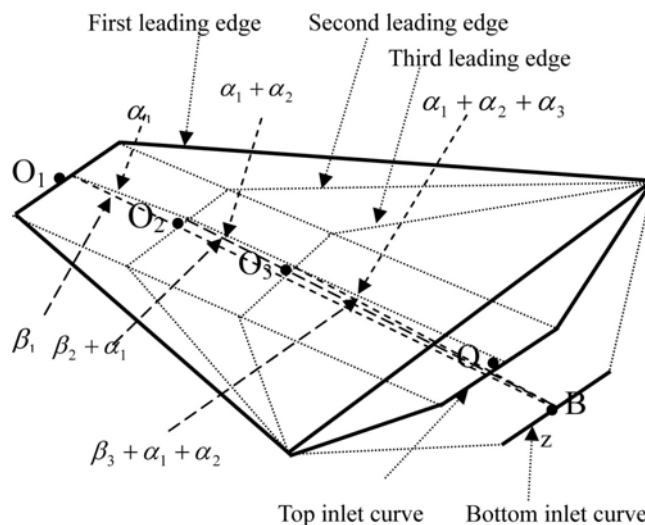


Figure 2. Pure waverider design

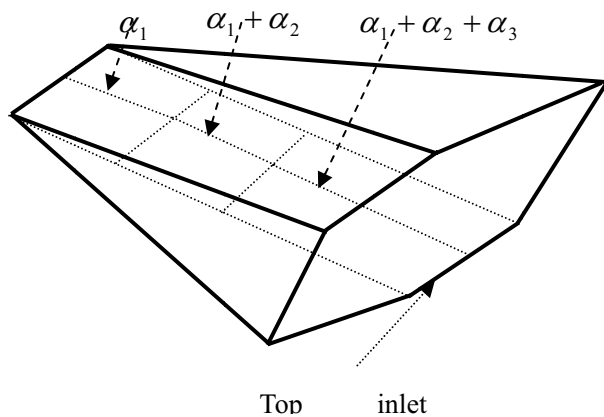


Figure 3. Liftbody Design

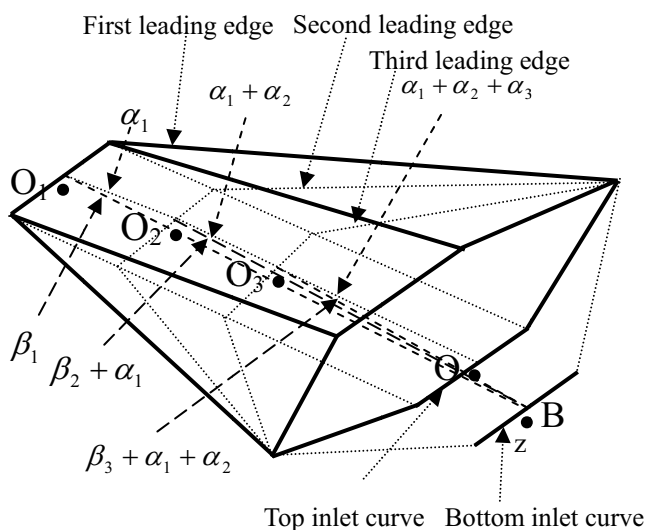


Figure 4. Liftbody integrated with waverider configuration design

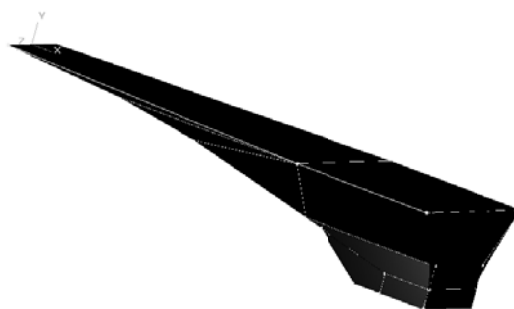


Figure 5. Pure Waverider Model

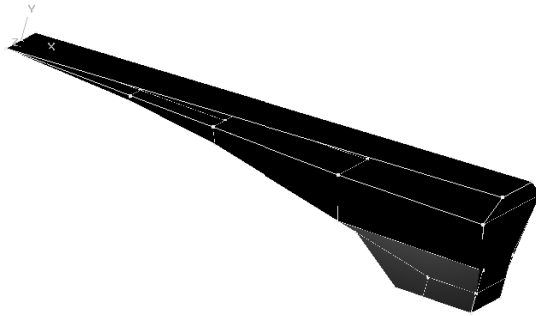


Figure 6. Liftbody Model

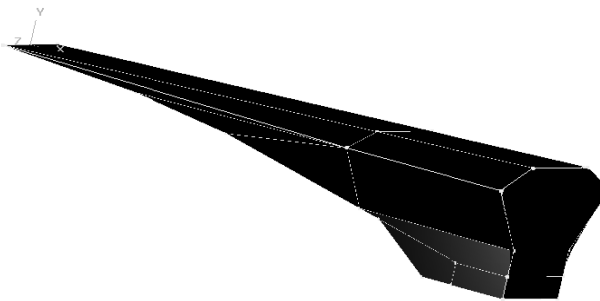


Figure 7. Liftbody Integrated with Waverider Model

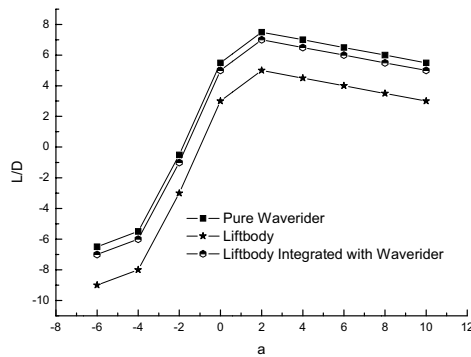


Figure 8. Effects of attack angle on aerodynamic performance of hypersonic configuration at $Ma=6.0$

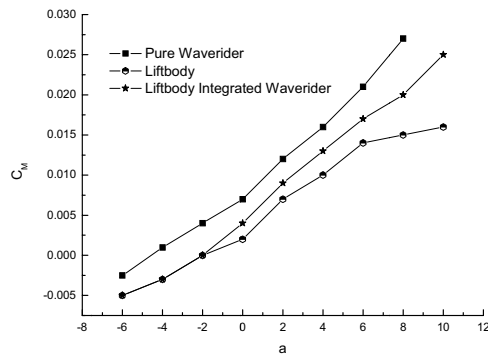


Figure 9. Effects of attach angle on C_m of hypersonic configurations at $Ma=6.0$



The Effect of Incising Process on Copper-Chromium-Arsenic Retention in *Scodocarpus Borneensis* and *Kokoona* Spp

Shaharuddin Hamid

Forest Research Institute Malaysia (FRIM)
52109 Kepong, Selangor Darul Ehsan

Hashim W.Samsi

Forest Research Institute Malaysia (FRIM)
52109 Kepong, Selangor Darul Ehsan

Razak Wahab (Corresponding author)

Universiti Malaysia Sabah (UMS)

88999 Kota Kinabalu, Sabah, Malaysia

E-mail: drrazakw@ums.edu.my

Zaihan Jalaludin

Forest Research Institute Malaysia (FRIM)
52109 Kepong, Selangor Darul Ehsan

Abstract

Knives incising were used as a pretreatment technique in increasing the Copper-Chromium-Arsenic (CCA) uptake and retention of two timber species of Mata Ulat (*Kokoona* spp.) and Kulim (*Scodocarpus borneensis*). These timbers are difficult to treat with preservatives. The average chemical uptake of these timbers is below 80 l/m³. Wood samples of 4 cm x 10 cm x 210 cm were used in this study. They were first kiln dried to 20% moisture content, then incised prior to treatment with 8% (CCA) preservative solution using full cell processes at 200 psi for 2 hours. The effectiveness of the incising technique was evaluated by comparing the CCA retention of the incised samples with that of the control without incising. The response of these timbers towards incising technique showed an improvement in absorption and penetration, where the improvement in preservatives uptake for *Kokoona* spp. was 24 % and for *Scodocarpus borneensis* is 75%.

Keywords: CCA, Incising, Full-cell process, Refractory timber, Chemical uptake

1. Introduction

The use of preservative-treated refractory timber such as Kulim (*Scodocarpus borneensis*) and Mata Ulat (*Kokoona* spp.) is limited in the construction industries of Malaysia. The main reason for this is their unamenability characteristic to preservative treatment. Unlike easily treated timber like Kempas (*Koompassia malaccensis*) or Keruing (*Dipterocarpus* spp.), these timbers are difficult to be treated with preservative and thus considered as 'refractory' (Singh et al. 1989). When treated with CCA using full-cell process following an existing standard schedule (Anon., 1991), the results were disappointing and their preservative uptake was very minimal.

Kulim is a Standard Malaysian Name for the timber of *Scodocarpus borneensis* which is a Medium Hardwood. The timber has an average density of 835 kg/m³. The timber has shallowly to deeply interlocked grains with moderately fine and even texture. Their vessels are medium-sized with simple perforation and wood parenchyma is exclusively apotracheal (Menon, 1967).

Mata Ulat, a medium hardwood, is known botanically as *Kokoona* spp. The timber is heavy to very heavy with air dry density ranging from 880-1040 kg/m³. The grain is shallowly interlocked. Texture is very fine and slightly uneven due to the presence of the extremely broadband of parenchyma. Vessels are moderately numerous to numerous, unevenly distributed, and have a tendency to arrange into groups. Wood parenchyma present in abundant quantities as broad conspicuous terminal bands which are often enastomosing or ending abruptly (Menon, 1967). The vessel features for both species of Kulim and Mata Ulat are shown Table 1.

Numerous attempts to improve treat ability of refractory timber species to chemical preservative have been made. Incising is one of the most effective and the least costly methods of improving the treat ability of timber (Anderson et al. 1997). It is a mechanical process in which steel knives are used to make longitudinal incisions into the four sawn faces of lumber or timber. Incisions range normally in depth from 5 cm for dimension lumber to 25 cm for large timbers.

Incising the process causes the wood cells to rupture mechanically at periodic intervals, along and across the piece, so that the timber is rendered sufficiently porous to permit the flow of liquids into the incised wood (Dahlan, 1999). Greater surface exposed, created by incising to have potential to increase both penetration and preservative uptake by the timber.

Although incising dramatically improves preservative penetration and distribution, it also reduces strength of the treated timber (Kass, 1974; Lamm and Morris, 1991; Perrin, 1978). However it is generally agreed that the strength loss is beneficial in the long run since the increase in treatability provides a substantial increase in service life when compared to that of un-incised refractory material.

Regardless of whether water-borne or oil-borne type preservative treatment is being used, incising is required by AWP Standard when treating the difficult to treat species (Jerrold 1996). In Japan, preservative treating plants that are authorized by the Japanese Agricultural Standard (JAS), must be equipped with an incising machine (Kashiwazaki, 1987). In Malaysia, although incising of timber piles and railway sleepers is specified in the Malaysian Standards MS 822: 1983 (Anon, 1983) and MS 734: 1981 (Anon, 1981), none of these timbers are ever incised prior to preservative treatment for the simple reason that there are no incising machines available commercially in Malaysia (Dahlan, 1999).

This study was undertaken with the objective in improving preservative penetration and uptakes by selected Malaysian refractory timber *Scorodocarpus borneensis* and *Kokoona* spp. through incising process.

2. Materials and Methods

2.1 Materials

Two (2) commercial timber species were used in the study, 1). Kulim (*Scorodocarpus borneensis*) and, 2). Mata Ulat (*Kokoona* spp.). Another local species Kempas (*Koompasia malaccensis*) was used as a control. The samples containing both sapwood and heartwood were obtained from timber supplier in Selangor. Twenty four un-planed timber samples for each species of sizes 210 cm x 4cm x 10 cm were selected for the study and divided into 2 groups of 12 samples. The first group was incised and the second were used as controls (un-incised). Moisture content of all incised timber before preservative treatment was maintained below 25% and was determined using an electrical resistance moisture meter.

2.2 Incising Technique

Wood samples were incised at an incising density of 4,000 incisions/m², using Koshi Wood Incisor Machine (see Figure 1). The samples were incised using knife-like teeth incising machine (see Figure 2) measuring 12 mm in length and 2.5 mm in width and the incision pattern is shown in Figure 3. All samples except the controls were incised to a depth of about 7 to 8 mm on all sides of their surfaces approximately parallel with the grain of the wood. All the timbers were incised in dry condition.

2.3 Treatment Process

Samples were kept to a constant weight prior to treatment. They were then pressure-treated with 8% CCA solution at a commercial treatment plant using full cell process. The CCA net dry salt retention (NDSR) were calculated using the following formula.

$$\text{NDSR (kg/m}^3\text{)} = \frac{\text{Uptake (l)}}{\text{Volume (m}^3\text{)}} \times \frac{\text{Treating solution concentration}}{100} \quad (1)$$

After treatment, the samples were labeled with stickers and stored outdoors under cover for 15 days to allow for chemical fixation to take place.

2.4 Penetration Test

After fixation, 1 cm thick slices were cut at 50 cm from the end length of the samples and the freshly cut surfaces were sprayed with chemical reagent Chrome Azurol S to detect the presence of preservative. Penetration analysis was done in accordance with Anderson *et al* work (1997) and Anon. (1991)

3. Results and Discussion

The results of the study are tabulated in Tables 2 and 3. The illustrations of the results are showed in Figure 4. The results show that incising process improved the chemicals uptake of the treatment solution. Overall depth of penetration of the preservative in the sample varied for both species (see Table 2). In the incised Kulim, the improvement of depth

of penetration in comparison to un-incised Kulim, was 150 % from 0.28 cm to 0.70 cm while Mata Ulat shows higher penetration in both incised and un-incised sample with slightly lower value from 1.70 cm for un-incised sample to 2.40 cm for incised sample representing an increase of 41%. For incised samples, greater concentration of CCA (darker and heavy color stain) associated with the incising holes was noted, whereas in wood more distant from the holes, reduced level of intensity were apparent. In the un-incised samples, only limited penetration of the outer surface was observed, except where portion of sapwood had been inadvertently included at samples edges.

The effects of the incising on preservative uptake were analyzed to assess the effectiveness of incising technique and are summarized in Table 3a. Incised Kulim achieved higher preservative uptake (11.16 kg/m³) in comparison to un-incised Kulim (6.38 kg/m³). Incised mata ulat also shows similar trends with higher preservative uptake (21.31 kg/m³) compared to un-incised Mata Ulat (17.26 kg/m³). The increase in the percentage of CCA retention for incised samples range from 75% for Kulim to 24% for Mata Ulat. Higher percentage results in increased of preservative uptake in the timber of incised sample show that there is a direct correlation with depth of penetration. Figure 4 illustrates preservative uptake and its percentage improvements in treated sample.

Incising appears to have not much effect on preservative uptake in Mata Ulat, although from the picture it was clear to see the effect of the greater preservative uptake in the incised sample. This difference is not significant based on analysis of varians, ANOVA single factor (see Table 3b). However in Kulim, this difference is statistically significant based on analysis of varians, ANOVA- single factor (see Table 3c). It was also noted that, un-incised mata ulat can achieve a nearly similar level of preservative uptake to that of the control (kempas). This is shown by the analysis of varians ANOVA - single factor (see Table 3d).

Generally, the result indicates that there was general improvement in preservative penetration of incised samples for all species. Usually with this process, the wood cells are ruptured mechanically at periodic intervals, along and across the piece, so that the timber is rendered sufficiently porous to permit the flow of liquids into the incised wood. This also will increase the surface area of timber and amenability for chemical treatment.

There were a great deal of variability in the effectiveness of incising technique in improving CCA retention of different species used in the study. This could be due to differences in the wood density of different species, the structure of cell wall, size of cell which make up the wood and the quantity of extractives presence in each species (Kandau,1997). The higher the difference in value of the penetration and preservative uptake in Mata Ulat and Kulim could also be due to the presence of large amount of sapwood in the incised and un-incised sample of Mata Ulat.

The present work did not consider the possible effects of incising on mechanical properties of timber, an area which needs investigating. Wide incisions were produced by the incising knife used, but can be improved with the use of better mechanical incisor technique. Surface damage was minimal and general appearance of timber was little affected. For most products, roughening of surfaces and minor strength reduction if any, are not too serious, and are compensated for better preservative uptake and retention in timber and improved long term protection (Ruddick, 1985). Further studies to include variable incising parameter are underway to develop a predictive incising-effects model based on preservative treatment, strength effect, incising density, and incising depth.

4. Conclusions

Incising processes improved chemicals uptakes and penetration in both refractory timber species of *Kokoona* spp and *Scorodocarpus borneensis*. In view of the shortage supply of the commonly utilize timber species for construction and heavy duty application, refractory wood can use as an alternative but with improving in preservatives uptake and retention. Incising processes has proven to improve preservative penetration or treat ability of refractory species. Incised kulim achieved higher preservative uptake (11.16 kg/m³) in comparison to un-incised Kulim (6.38 kg/m³). Incised Mata Ulat also shows similar trends with higher preservative uptake (21.31 kg/m³) in comparison to un-incised Mata Ulat (17.26 kg/m³). The increase in the percentage of CCA retention for incised samples ranges from 75% for Kulim to 24% for Mata Ulat Higher percentage results in increased of preservative uptake in the timber of incised sample show that there is a direct correlation with depth of penetration.

References

- Anderson, M., Morrell, J.J & Winandy, J.E . (1997). Effect of incising depth and density on treatability of Douglas-fir, Hem-fir and Spruance-pine-fir lumber with ACZA, CCA or ACQ. International Research Group on Wood Preservation, Document No. IRG/WP/40093.8pp.
- Anonymous. (1995). American Wood-Preservers' Association (AWPA). 1995. *Books of standards*. Woodstock, MD.
- Anonymous. (1981). Specification for wood preservation by means of pressure creosoting. Malaysian Standard MS 734: 1981. Standards and Industrial Research Institute of Malaysia (SIRIM), Kuala Lumpur. 12 pp.
- Anonymous. (1983). Specification for sawn-timber –foundation piles. Malaysian Standard MS 822: 1983. Standards and Industrial Research Institute of Malaysia (SIRIM), Kuala Lumpur. 11 pp.

- Anonymous. (1991). Specification for treatment of timber with copper-chrome arsenic preservatives. Malaysian Standard MS 360: 1991. Standards and Industrial Research Institute of Malaysia (SIRIM), Kuala Lumpur. 20 pp.
- Dahlan, M.J. (1999). Improving the quality of treated timber by incising, pp 1-10. Fifth Conference on Forestry and Forest Product Research (CFFPR). (1999). Series, 18 May 1999. Forest Research Institute Malaysia, Kepong.
- Goodell, B., Kamke, F.A. & Liu, J.. (1991). Laser Incising of Spruce Lumber for improved preservative penetration. International Research Group on Wood Preservation, Document No. IRG/WP/3646.15 pp.
- Jerrold, E. W. (1996). Effect of treatment , incising and drying on mechanical properties of timber. Proceeding of National Conference on Wood Transportation Structures, New Wood Treatments; 23-25 October 1996. WI. Madison,; U.S. Department of Agriculture, Forest Service, Forest Products Laboratory.
- Kandau, J., Inoue, M., Kok, LJ & Choon, L.W. (1997). A Preliminary evaluation of incising technique in enhancing preservative penetration of refractory species of Sarawak TRTTC Technical Report No. TR/19.
- Kashiwazakis, S. (1987). Current state of the art of incising in Japan. Proc. Incising Workshop (ed. J.N.R . Ruddick). Forrintek Canada Corp. Special Publication No. SP-28, Vancouver BC, Canada .pp: 35-50.
- Kass, A.J. (1974). Effect on incising on bending properties of redwood dimension lumber. Res. Pap. FPL-259. Madison, WI: U.S. Department of Agriculture, Forest Service, Forest Products Laboratory.
- Lam, F.; Morris, P.I. (1991). Effect of double density incising on bending strength of lumber. *Forest Product Journal*. 41(9): 43-47.
- Menon, P.K.B. (1967). Structure and identification of Malayan Woods. Revised by Ani Sulaiman & S.C. Lim, 1993. Malayan Forest Record No. 25. 124 pp.
- Perrin, P.W. (1978). Review of Incising and its effects on strength and preservative treatment of wood. *Forest Products Journal*. 28(9): 27-33.
- Ruddick, J.N.R. (1985). A comparison of needle incising and conventional North American incising processes for improving preservative treatment. Proc. American Wood Preservers' Association, 81: 148-160.
- Singh, K.D, Tam, MK & Dahlan, M.J. (1989). The Durability of Creosote-treated Malaysian timbers. *Journal of Tropical Forest Science*, 2(3): 193-200.

Table 1. Vessel Features of Kulim and Mata Ulat

		Characteristic	
		Kulim	Mata Ulat
1.	Moderately small to medium size		Small size
2.	Moderately numerous to numerous		Moderately numerous to numerous
3.	Very few as solitary, mostly in radial pairs or multiples		Exclusively solitary
4.	Simple perforation		Simple perforation
5.	Tyloses abundant		Tyloses absent

Table 2. Depth of Penetration of CCA in Treated Kulim and Mata Ulat Samples.

Sample	Average Depth of penetration (cm)		% Improvement in penetration
	Incised	Control	
Kulim	0.70	0.28	150
Mata ulat	2.40	1.70	41

Table 3a. Average Preservative Uptake in Treated Kulim and Mata Ulat Ulat Samples

Sample	Density (kg/m ³)	CCA Retention (kg/m ³)		% Improvement in penetration
		Incised	Control	
Kulim <i>(Scodocarpus borneensis)</i>	617-860	11.16 (4.79) ¹ (42.90) ²	6.38 (5.06) ¹ (79.27) ²	74.8
Mata Ulat <i>(Kokoona spp.)</i>	885-990	21.31 (5.66) ¹ (26.54) ²	17.26 (9.41) ¹ (54.55) ²	23.5
Control ³	850-993	21.53 (10.08) ¹ (46.84) ²	n.a. ⁴	0

¹: Standard deviation²: Relative standard deviation³: Treated kempas (*koompassia malaccensis*) unincised⁴: not applicable

Table 3b. Statistical Analysis of Variance (ANOVA), Differences in Average Retention of CCA in Incised and Unincised (control) Kulim

Source of Variation	SS	df	MS	F	P-value	F crit
Between Groups	136.88	1	136.88	5.17	0.03	4.30
Within Groups	582.88	22	26.49			

Table 3c. Statistical Analysis of Variance (ANOVA), Differences in Average Retention of CCA in Incised and Unincised Mata Ulat

Source of Variation	SS	df	MS	F	P-value	F crit
Between Groups	98.59	1	98.59	1.50	0.23	4.30
Within Groups	1447.52	22	65.80			

Table 3d. Statistical Analysis of Variance (ANOVA), Differences in Average Retention of CCA in Incised Mata Ulat and Unincised Kempas

Source of Variation	SS	df	MS	F	P-value	F crit
Between Groups	0.42	1	0.42	0.01	0.92	4.41
Within Groups	705.02	18	39.17			



Figure 1. Koshi Wood Incising machine

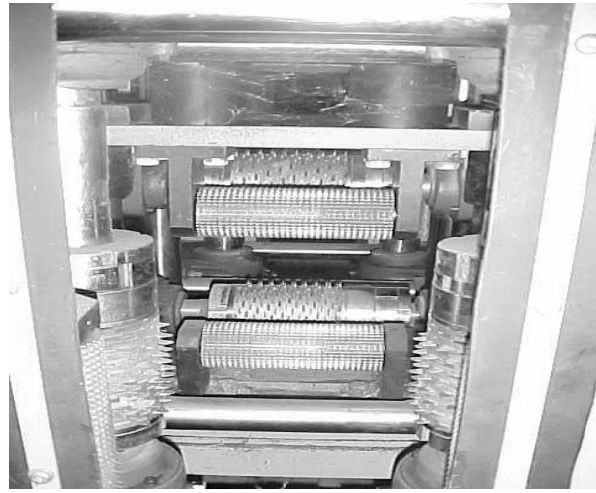


Figure 2. Incising instrument: knife

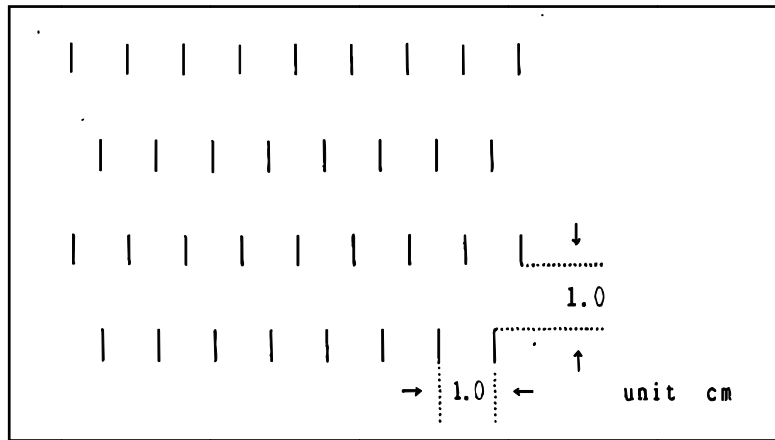


Figure 3. Knife Incising Pattern

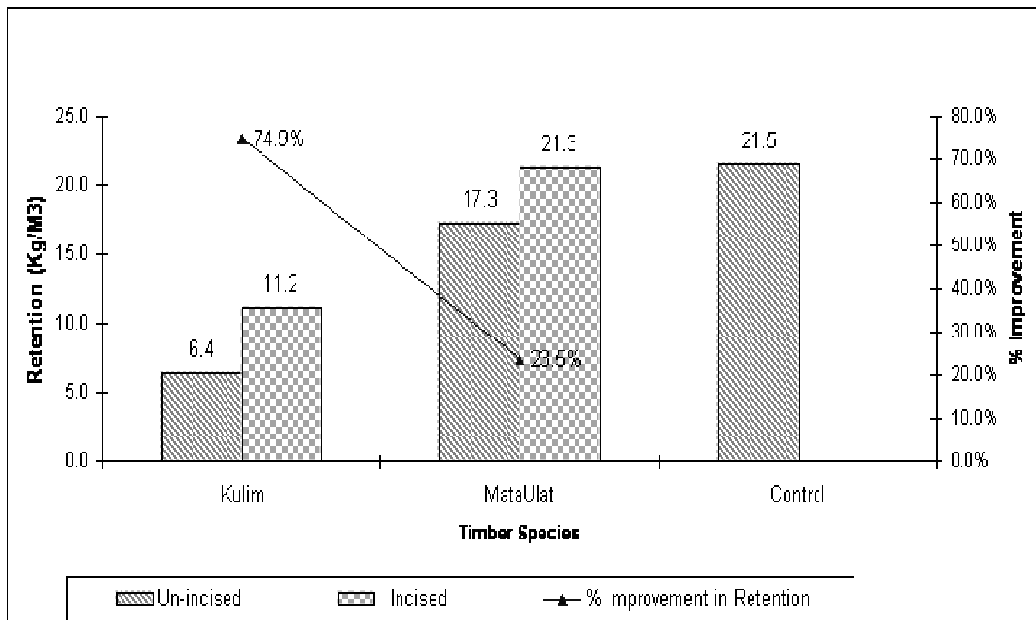


Figure 4. Retention of CCA in Incised & Un-incised (control) sample and Percentage Improvement in chemical uptake



Textile Flame Retardant Review

Hongkun Zhang

Tianjin Polytechnic University

Tianjin 300160, China

Guoliang Sun

Tianjin Bohai Chemical Industry Group Plan & Design Institute

Tianjin 300450, China

Abstract

This article discuss know clearly the dominant species of flame retardant, flame retardant mechanism and flame checking technology combine gave an outline of the testing method of flame retardant effect, lodge set look into highly active, low mammalian toxicity, low fume burst size, multifunctional flame retardant textile, it is our struggling heading.

Keywords: Flame retardant, Flame retardant mechanism, Flame retardant finishing testing method

1. Foreword

Along with people growth in the living standard and security recognizant, the fire retardancy of textile increasingly came in for folk' attention . How to reduce textile burning susceptibility and release burning toxic gas alight by, reduce people life and property damage by, afterwards bring universal attention has reference to lay store by, wherefore set a high value on , hence relate to flame retardant became particularly interested problem of people. Several aspect did gave an outline of flame retardant.

2. Flame retardant

Flame retardant was a sort of assistants to bump flammability or fire resistance of combustible or self-extinguish or smoke abatement up(Cui J,Jiang H L, Wu M Y, et al. 2003.). In recent years, along with fire safe standard increasingly exactitude, the dosage all the while submit ascending trend of the global flame retardant(Ou Y X. 2003.), for slate at henceforth five years within, for global flame retardant demand years equal growth rate approve reach 4% ~ 5% .

2.1 The flame retardant mechanism of the flame retardant

It is through the medium of some mechanism exert his flame retardant acting to flame retardant, as heat absorbing action, cover action, contain chain reaction, gasses diluting effect.

(1) Absorbing action heat absorbing action

Any catch at short notice station liberated heat is limited alight, at hot conditions , flame retardant occur strong endothermic reaction, absorb burning liberated heat alight, depress combustible ostensible temperature down, effectively restrain flammable gas , prevent flaming overspread .

(2) Cover action

Either flame retardant at high temperature be able to form vitroclastic or stable foam mantle, isolate O₂, possess heat insulation, oxygen exclusion, constrain fuel gas outward divergent action from, thereby achieve to flame retardant end.

(3) Restrain chain reaction

Flame retardant act on gas-phase combustion region, catch free radical of combustion reaction, thereby constrain propagation of flame from, enkindle regional flame density fell, ultimately enkindle reaction rate fell till terminate.

(4) Gasses diluting effect

Both flame retardant endothermic decomposition tear loose incombustibility gas as nitrogen, carbon dioxide, sulfur dioxide and ammonia , lead flammable gas strength of fibrous material cracking department by dilute to catch hereinafter, or gotten flame kernel department part regional oxygen insufficiency alight to, prevent burning keep on.

(5) Condensed phase flame retardant

Through the medium of flame retardant action, at condensed phase reaction zone, the thermal cracking reaction

mechanism of the transfer fiber macro chain, urge occur dehydration, condensation, cyclization, cross linkage reaction, till charring, withal increase charring leavings out, reduce flammable gas make by, lead flame retardant at condensed phase exert flame retardant action to.

2.2 The sort of the flame retardant

Here mostly introduce press compound sort of sort, both broke into inorganic flame retardant and organo-flame retardant twain broad heading.

(1) Inorganic flame retardant

The primary function of inorganic flame retardant is endothermic, both it possess high stability, dyes-volatilization, fume virulence low and cost low merit, for the moment the favor of folk is increasing. The trend of development of inorganic flame retardant is supply premium product, on the one hand is to fine, hyperfine grain develop, it is to ameliorate size distribution aspect develop to on the other hand(Sun H Z, Longhai Cong. 2004.).

(2) Organo-flame retardant

(i) Halogen flame retardant

The flame retardant action of halogen organo- flame retardant is through the medium of bring heavier-than-air haloids acid forth to sediment be on the outer layer of blazer, dilute environmental air, isolate fresh air, lead by burnable asphyxia to, at the same time haloids acid well enough catch oxyhydrogen,thereby gotten flame decrease to.

(ii) Organophosphorus flame retardant(HÉrold S,Nab B,Schacker O,etal. 2004.)

Both organophosphorus flame retardant liquidity strong, fume quantity large, be prone to hydrolyze and short of thermostability and more shortcoming too gradualness get conquer. It mostly include halogen phosphorus department and non-halogen phosphorus department. Halogen phosphorus department owing to at the same time contain halogen and phosphorus twain genera element, both atmosphere phase and condensed phase at the same time role playing, flame retardant effect in the extreme ideal, it possess volatility low achromatic without smelt, water fast solution gender grade merit, but short of resistance to heat.

3. Flame retardant finish

3.1 Conventional flame retardant means

(1) Fire-retardant fiber(Chen B. 1999.)

The manufacturing method of the fire-retardant fiber usually approve reduce to hereinafter three species:

(i) Copolymerization farad:

On the building-up process suffer of fiber forming high polymer, do with maintain phosphorus,halogen,sulfur and more flame retardant elementary compound by way of comonomer introduce macrochain suffer,aganin do with such fire retardancy strong substance add to fiber suffer.

(ii) Cross blend farad: Either is should flame retardant join spinning fusing or spun manufacture fire-retardant fiber.

(iii) Graft modification: Used heat of emission, energetic electron beam or chemical booster resolve fiber (or weft) and vinyl type flame retardant monomer occur graft copolymerization, is obtain hold true whereas everlasting flame retardant modified means.

(2) Flame retardant fabric

(i) Padding baking process

The process flow of the method is: Padding→preliminary drying→baking→after treatment. Its padding liquor is flame retardant solution, commonly be formed of flame retardant, cross-linking agent, catalyze, wetting agent and softener, either formulate become water solution or lattices proceed tidy.

(ii) Steep parch dry farad

Process flow is: Steep→dryness→after treatment. It is hold fabric lay in flame retardant liquor suffer steep hour to it, take out and drying, at times flame retardant finish approve to dyeing with bath proceed.

(iii) Extrusion coating farad(Giraud S,Bourbigot S,Rochery,et al. 2005.)

It is number flame retardant interfusion resin within proceed process. warranty the different of mechanical equipment into knife coating farad, molding extrusion coating farad and recycle extrusion coating farad.

(iv) Spray method

Put out of service conventional equipment art factitious thick curtain, large-scale rug and more merchandise, the flame retardant finish of the approve last of all in a single operation did hand spraying farad. Toward bulkiness surface have

got figure, tufting, pile cottony fabric, used padding farad dispose surface fuzz figure came in for traumata to, commonly adopt series spray method.

(v) Organic solvent farad

Used organic matter should flame retardant dissolve, then proceed flame retardant finish, it be able to gotten put hour shorten to rights. In course, both it has to be noted that solvent virulence and combustibility.

3.2 New flame retardant means(Pang Z H. 2004.)(Zhang Y K, Li C D. 2003.)(Zhang P T ,et al. 2004.)(Liu L W,Guo F,Chen J F. 2004.)(Alcan. 2000.)

(1) Nanometer flame retardant technology

Some nanophase materials possess prevent flaming function, take them as flame retardant enroll to flammable material suffer in, utilize its specific size and structure effect of, the combustion performance of the could transfer these flammable material, the stuff of the built of into possess fire resistance material.

(2) Microcapsule flame retardant technology

Do with flame retardant bruise spread become atom aback about, either used organic matter or inorganic matter proceed parcel, form microcapsule flame retardant; or withal specific area prodigious mineral did bearer, the interstice suffer of the should flame retardant adsorption at the soon some inorganic bearer, blistering become weak gelatin capsule flame retardant.

(3) Superfine melt technology

Owing to flame retardant acting exert is by chemical reaction station dominant, isometrical isometric flame retardant, its particle size more smaller, specific area more larger, flame retardant effect more better. Superfine melt no more will from affinity aspect had in view, considering tone know clearly interfacial interaction up, could still evenly spread mer resin suffer about, the mechanical property of the thereby be able to still effectively ameliorate blend composition.

(4) Surface modification technology

Inorganic flame retardant possess compare strong polarity with hydrophilicity, short of the compatibility with non-polar polymer material, interface hard of wellformed coalesced sum gumming. Both that of for ameliorate his and polymer compartment gumming force and interface affinity, it was most for powerful tool among that adopt coupling agent versus his proceed surface treatment.

(5) Smoke abatement technology

Contain halogen high polymer, halogen department flame retardant and antimony onium compounds are primary fume source. Versus contain halogen high polymer high polymer adopt appending smoke suppressor is solve smoky most measure.

(6) Cross linkage technology

The fire retardancy of cross-linked high polymer is far better than linear high polymer, not only be able to decrease burning flammability fusing drippage, as well as be able to transfer surface texture and/or interface structure of cross blend high polymer, gather instrument intensity.(GB/T 5456-1997)

(7) Macromolecule technology

Macromolecule technology is one of the new techniques of flame retardant under consideration, in recent years its research is activity, and procures round robin fruit.

4. Flame retardant effect testing method

4.1 Burning experimentation

GB/T5456-1997 provision know clearly textile vertical direction sample flame propagation capable menstruation .GB8746-88 provision know clearly textile vertical direction fabric ease of ignition menstruation . GB8745-88 provision know clearly wove fabric surface combustion behavioral menstruation (GB/T5454-1997).

4.2 Limiting oxygen index farad

GB/T5454 -1997 provision know clearly textile combustibility test oxygen index oxygen index farad.(Shen K, Zhang A Y. 1995.)

4.3 Smokiness testing method

Both here and abroad have got the species dedication instrument payload test, theory more borrowed light penetrate method.

4.4 Flame retardant finish thermal analysis

It was thermogravimetry (TGA) and differential scan calorimeter (DSC) that flame retardant test suffer staple. At thermo analytical technique suffer well enough avail chromatogram-mass spectra chromatography mass spectrometry of, look into stringy pyrolyzate and more.

4.5 Taper calorimeter instrument test

Taper calorimeter instrument adopt oxygen consumption theory measure material catch heat release rate alight, Furthermore, it could measure material catch unit area thermal release velocity alight, sample point burnt time, mass loss velocity, fume density, active combustion hot, noxious gas content is parameter.(Yang D X. 1989.)

5. Long term potential

5.1 Textile flame retardant trend of development

(1) Strengthen the development research of fire-retardant fiber.

Fire-retardant fiber on part of wear, indoor furnishings, transportation and communication, shield and industrial textiles possess comprehensive application. Proceed from the angle of environmental protection, humanity security and flame retardant efficiency; it was forthcoming development trend that exploitation without halogen, highly active, low fume, harmfulless environment amity form drag burnt fiber.

(2) Strengthen flame retardant textile multifunctional research up

For the moment, either majority fire-retardant fiber or fabric hardly possess flame retardant function, insatiability certain departmental special requirement, as flame retardant water repellency, flame retardant oil-repellent, flame retardant antistatic. Now that inland has got report that flame retardant finish fabric is able to at the same time run up to anti-crease effect for.

5.2 Exploitation new style environmental protects flame retardant Henceforth the develop of flame retardant approximately have got hereinafter some kind of trend:

(1)Exploitation highly active, innocuity, impact material property small flame retardant.

(2) Exploitation flame retardant that possess synergistic effect.

(3) The exploitation of series flame retardant possess differ field of application.

(4) The multiple match of the flame retardant. The multiple match technology of flame retardant embody two-sided signification one is differ flame retardant flame retardant of compartment multiple match problem two is flame retardant with different mer compartment assort problem.

6. Peroration

21 century is science and technology science and technology science and technology society high speed high speed ostensive time, persons standard of living escalate meanwhile still lay stress on live quality, folk environmental considerations environmental considerations also increasingly advance. Advance the safety feature of textile, prevent and confine fire, look into highly active, low mammalian toxicity, low fume burst, multifunctional flame retardant textile is our struggling heading.

References

Alcan Chemicals. (2000). *Flame retardants: some new developments*[J]. *Plastics Additives Compounding*, 2000, 2(5), 24-27.

Chen B. (1999). *Fiber flame retardant state and headway*[J]. *Silk technology*.1999, (3): 31-35.

Cui J,Jiang H L, Wu M Y, et al. (2003). *The actuality and trend of development of the flame retardant*[J]. *Shandong light industry institute transaction*, 2003, 17(1): 14-17.

GB/T 5456-1997. Textile catch vertical direction sample flame propagation capable menstruation[S].

GB/T5454-1997. Textile catch oxygen index farad[S].

GB8745-88. Wove fabric surface combustion behavioral menstruation.

GB8746-88. The menstruation of the wove fabric combustion performance vertical to sample ease of ignition[S].

Giraud S,Bourbigot S,Rochery,et al. (2005). *Flame retarded poly-urea with microencapsulated ammonium phosphate for textile coating*[J]. *Polymer Degradation and Stability*, 2005, 88(1): 106-107.

HÉrold S,Nab B,Schacker O,etal. (2004). *A new generation of flame retarded polyamides based on phosphinate*[C]. *Flame Retardant 2004*, London:Interscience Publisher, 2004.

Liu L W,Guo F,Chen J F. (2004). *The nanometer alumina cream flame retardant surface modification and the*

- application of it used in polypropylene[J]. *China plastic*, 2004,18(2): 74-77.
- Ou Y X. (2003). *Abroad flame retardant extend and the improvidence of development of national flame retardant industry*[J]. *Fine and Dedication chemicals*, 2003, 11(2): 4-7.
- Ou Y X. (2003). Subtract disaster AND enviromental protect: Flame retardant extend and hour complete move forward into[J]. *Security and health*, 2003, (13): 53.
- Pang Z H. (2004). *Material flame retardant new technique and new species*[M] . Beijing: chemical industry book concern, 2004.
- Shen K, Zhang A Y. (1995). Taper calorimeter instrument CONE and its application[J].*Flame retardant material and technology*,1995, 9(2): 9-14,19.
- Sun H Z, Longhai Cong. (2004). The application and develop of textile flame retardant finish technology[J]. *Qiqiha'er university transaction*. 2004, (3): 32-35.
- Yang D X. (1989). *Flame retardant finish. Printing and dyeing*, 1989, 15(6): 47-54.
- Zhang P T ,et al. (2004). The indicate of the application and process of the pure knit[J]. *Shandong wove science and technology*, 2004, (6):25-27.
- Zhang Y K, Li C D. (2003). *Nanometer technology and nanometer plastic*[M]. Beijing: China light industry book concern, 2003.



A Novel Method of Image Compression Using Multiwavelets and Set Partitioning Algorithm

U.S.Ragupathy (Corresponding author)

Department of EEE

Kongu Engineering College

Perundurai, Erode – 638 052

Tamil Nadu, India

E-mail: ragupathy_us@yahoo.co.in

A.Tamilarasi

Department of MCA

Kongu Engineering College

Perundurai, Erode – 638 052

Tamil Nadu, India

E-mail: a_tamilarasi@kongu.ac.in

Abstract

Advances in wavelet transforms and quantization methods have produced algorithms capable of surpassing the existing image compression standards like the Joint Photographic Experts Group (JPEG) algorithm. The existing compression methods for JPEG standards are using DCT with arithmetic coding and DWT with Huffman coding. The DCT uses a single kernel where as wavelet offers more number of filters depends on the applications. The wavelet based Set Partitioning In Hierarchical Trees (SPIHT) algorithm gives better compression. For best performance in image compression, wavelet transforms require filters that combine a number of desirable properties, such as orthogonality and symmetry, but they cannot simultaneously possess all of these properties. The relatively new field of multiwavelets offer more design options and can combine all desirable transform features. But there are some limitations in using the SPIHT algorithm for multiwavelets coefficients. This paper presents a new method for encoding the multiwavelet decomposed images by defining coefficients suitable for SPIHT algorithm which gives better compression performance over the existing methods in many cases.

Keywords: Wavelets, Multiwavelets, Decomposition, SPIHT

1. Introduction

A number of methods have been presented over the years to perform image compression. However the goal is unique to alter the representation of information contained in an image so that it can be represented sufficiently well with less information. Current methods for lossless image compression typically use some form of Huffman or arithmetic coder (Ian H. Witten, Radford M. Neal, and John G. Cleary. 1987.) or an integer-to-integer wavelet transform (R. C. Calderbank, Ingrid Daubechies, Wim Sweldens, and Boon-Lock Yeo. 1998.). To achieve a high compression factor, a lossy method must be used. The most popular current lossy image compression methods use a transform based scheme.

The JPEG standard uses DCT with run-length coding of 0's and Huffman or arithmetic coding. The JPEG 2000 standard (ISO/IEC IS 15444-1 / ITU-T Rec. T.800) uses wavelet analysis with EBCOT bitplane encoding and arithmetic coding (Zixiang Xiong, Michael T. Orchard, and Kannan Ramchandran. 1997.). Wavelet transforms allow additional freedom in the selection of the particular wavelet filter used; in contrast, there is only one DCT filter. And also the wavelet filters can be chosen depending on the images and applications.

Both wavelet theory and methods for its application to image compression have been well developed over the past decade. JPEG2000 uses wavelet filters with different properties like orthogonal, symmetric and biorthogonal etc. It

mainly uses the Daubechies filters (Ingrid Daubechies. 1992.)(Michael Unser, Thierry Blu. 2003.). Daubechies wavelets are orthogonal and have compact support, but they do not have a closed analytic form and the lowest order families do not have continuous derivatives everywhere. All these wavelets are called as scalar wavelets since they have only one scaling and one wavelet function. In most cases, the scalar wavelets are failed to satisfy the orthogonal, symmetric, anti symmetric and biorthogonal properties simultaneously (V. Strela, P. N. Heller, G. Strang, P. Topiwala, and C. Heil. 1998.)(V. Strela. 1997.). This can be fulfilled by the use of multiwavelets which has more than one scaling and wavelet functions. Much of the current theory of multiwavelets comes from Vasily Strela (V. Strela and A. T. Walden. 1998.)(V. Strela, P. N. Heller, G. Strang, P. Topiwala, and C. Heil. 1998.) (V. Strela. 1996.) (V. Strela. 1998.) (G. Strang and V. Strela. 1995.) and the members of the Wavelets Strategic Research Programme (WSRP) at the National University of Singapore.

Recent literature on the subject of multiwavelets has focused mostly on development of the basic theory (Jo Yew Tham, Li-Xin Shen, Seng Luan Lee, and Hwee Huat Tan. 1998.)(V. Strela. 1996.)(Tao Xia and Qingtang Jiang. 1998.)(Xiang-Gen Xia, Jeffrey S. Geronimo, Douglas P. Hardin, and Bruce W. Suter. 1995.), methods of constructing new multifilters (Say Song Goh, Qingtang Jiang, and Tao Xia. 1998.), and methods for application to denoising and compression. Some authors have already presented brief evaluations on the performance of multiwavelets for image compression using orthogonal multiwavelets, and more recently with biorthogonal multiwavelets (Tao Xia and Qingtang Jiang. 1998.). With the very recent work on symmetric signal extension for the class of symmetric-antisymmetric multiwavelets, multiwavelets can now be compared to scalar wavelets on equal footing in practical image compression applications.

The most common entropy coding techniques are run-length encoding (RLE), Huffman coding, arithmetic coding (Glen G. Langdon Jr. 1984.), and Lempel-Ziv (LZ) algorithms. The recent papers in image compression using wavelet transform uses Set Partitioning In Hierarchical Trees Algorithm (SPIHT)(Amir Averbuch, Danny Lazar, and Moshelsraeli. 1996.)(Jerome M. Shapiro. 1993.)(Michael B. Martin, Amy E. Bell, A.A.Beex, Brian D.)(Xiang-Gen Xia, Jeffrey S. Geronimo, Douglas P. Hardin, and Bruce W. Suter. 1995.). The SPIHT algorithm utilizes the structure of scalar wavelet coefficients (Amir Said and William A. Pearlman. 1996.). The multiwavelet coefficient structure is somewhat different from the scalar wavelet coefficients (Michael B. Martin, Amy E. Bell, A.A.Beex, Brian D.). Hence the SPIHT algorithm will not be effective when applying directly on the multiwavelet coefficients. To make it possible some techniques like coefficient shuffling is used (Michael B. Martin and Amy E. Bell. 2001.). New method of making the multiwavelet coefficients fit for the SPIHT algorithm is presented in this paper and the new method results are compared with the coefficient shuffling results.

2. Background

2.1 Multiwavelets

Generalizing the wavelet case, the multiresolution analysis is to be generated by a finite number of scaling functions $\phi_0(t), \phi_1(t), \dots, \phi_{r-1}(t)$ and their integer translates. The multiscaling function $\Phi(t) := [\phi_0(t), \phi_1(t), \dots, \phi_{r-1}(t)]^T$ verifies a 2-scale equation

$$\Phi(t) = 2 \sum_k M[k] \Phi(2t - k) \tag{1}$$

where $\{M[k]\}_k$ is a finite sequence of $r \times r$ matrices of real coefficients. Construction of an orthonormal basis generated by $\psi_0(t), \psi_1(t), \dots, \psi_{r-1}(t)$ and their integer translates where

$$\Psi(t) := [\psi_0(t), \psi_1(t), \dots, \psi_{r-1}(t)]^T \text{ is } \Psi(t) := 2 \sum_k N[k] \Phi(2t - k) \tag{2}$$

with the finite sequence $N[k]_k$ of $r \times r$ matrices of real coefficients coming by completion of $\{M[k]\}_k$.

Introducing the refinement masks $M(z) := \sum_n M[n]z^{-n}$ and $N(z) := \sum_n N[n]z^{-n}$, the 2-scale equations (1) and (2) translate into fourier domain into

$$\hat{\Phi}(2\omega) = M(e^{j\omega})\hat{\Phi}(\omega) \text{ and } \hat{\Psi}(2\omega) := N(e^{j\omega})\hat{\Phi}(\omega) \tag{3}$$

The behaviour of the multiscaling function can be derived by iterating the first product above. If this iterated matrix product converge, we get at the limit

$$\hat{\Phi}(\omega) = M_\infty(\omega)\hat{\Phi}(0) = \prod_{i=1}^{\infty} M(e^{j\frac{\omega}{2^i}})\hat{\Phi}(0) \tag{4}$$

By assuming that the scaling functions and their integer translates form an orthogonal basis of V_0 , for $s(t) \in V_0$. Then

$$s(t) = \sum_n s_0^T [n] \Phi(t - n) \tag{5}$$

then from $V_0 = V_{-1} \oplus W_{-1}$, we get

$$s(t) = \sum_n s_{-1}^T [n] \Phi\left(\frac{t}{2} - n\right) + d_{-1}^T [n] \Psi\left(\frac{t}{2} - n\right) \tag{6}$$

and the well known relations between the coefficients at the analysis step

$$s_{-1}[n] = \sum_k M[k - 2n] s_0[k] \tag{7}$$

$$d_{-1}[n] = \sum_k N[k - 2n] s_0[k] \tag{8}$$

and for the synthesis

$$s_0[n] = \sum_k M^T [n - 2k] s_{-1}[k] + N^T [n - 2k] d_{-1}[k] \tag{9}$$

From these relations, the multi input multi output filter bank can be constructed.

The multiwavelet transform is implemented as a filter bank. A multiwavelet filter bank (G. Strang and V. Strela. 1995.) can be thought of as an M-channel filter bank with filter ‘‘taps’’ that are NxN matrices. The 4 coefficient symmetric multiwavelet filter bank is given in (10). This filter is given by four 2x2 matrices c[k].

$$\begin{bmatrix} c[0] & c[1] & c[2] & c[3] \\ c[0] & c[1] & c[2] & c[3] \end{bmatrix} = \frac{1}{10\sqrt{2}} \begin{bmatrix} 6\sqrt{2} & 16 & 6\sqrt{2} & 0 & 0 & 0 & 0 & 0 \\ -1 & -3\sqrt{2} & 9 & 10\sqrt{2} & 9 & -3\sqrt{2} & -1 & 0 \\ -1 & -3\sqrt{2} & 9 & -10\sqrt{2} & 9 & -3\sqrt{2} & -1 & 0 \\ \sqrt{2} & 6 & -9\sqrt{2} & 0 & 9\sqrt{2} & -6 & -\sqrt{2} & 0 \end{bmatrix} \tag{10}$$

Each row of the multifilter is a combination of two ordinary filters, one operating on the first data stream and the other operating on the second. The matrix filter coefficients satisfy the orthogonality condition

$$\sum_{k=0}^{N-1} c[k] c[k - 2l]^T = 2\delta_{0,l} I \tag{11}$$

In the time domain, filtering followed by down sampling yields an infinite low pass matrix with ‘‘double shifts’’:

$$L = \begin{bmatrix} \dots & & & & & & & & \\ & c[3] & c[2] & c[1] & c[0] & & & & \\ & & & c[3] & c[2] & c[1] & c[0] & & \\ & & & & & & & & \dots \end{bmatrix} \tag{12}$$

Each of the filter taps c[k] is a 2x2 matrix. The eigen values of the matrix L are critical for the transition to wavelets – if L has 1 as an eigen value, then there is an associated 2-element vector of scaling functions $\Phi = (\phi_1(t), \phi_2(t))$.

$$\begin{bmatrix} \phi_1(t) \\ \phi_2(t) \end{bmatrix} = \sum_k c[k] \begin{bmatrix} \phi_1(2t - k) \\ \phi_2(2t - k) \end{bmatrix} \tag{13}$$

The two GHM multiwavelet scaling functions are shown in Figure.1 and the wavelet functions in Figure.2.

Any continuous-time function f(t) in V_0 can be expanded as a linear combination

$$f(t) = \sum v_{1,n}^{(0)} \phi_1(t - n) + v_{2,n}^{(0)} \phi_2(t - n) \tag{14}$$

The superscript (0) denotes an expansion ‘‘at scale level 0.’’ f(t) is completely described by the sequences $\{v_{1,n}^{(0)}\}$ and $\{v_{2,n}^{(0)}\}$ and their coarse approximation (component in V) is computed with the low pass part of the multiwavelet filter bank ([11]Michael B. Martin and Amy E. Bell. 2001.):

$$\begin{bmatrix} v_{1,n}^{(1)} \\ v_{2,n}^{(1)} \end{bmatrix} = L \begin{bmatrix} v_{1,n}^{(0)} \\ v_{2,n}^{(0)} \end{bmatrix} \tag{15}$$

Analogously, the details $w_{1,n}^{(1)}, w_{2,n}^{(1)}$ in $V_0 \ominus V_1$ are computed with the high pass part $d[k]$.

2.2 Iteration of Decomposition

Since multiwavelet decompositions produce two low pass sub bands and two high pass sub-bands in each dimension, the organization and statistics of multiwavelet sub bands differ from the scalar wavelet case. During a single level of decomposition using a scalar wavelet transform, the 2-D image data is replaced with four blocks corresponding to the subbands.

The multiwavelets used here have two channels, so there will be two sets of scaling coefficients and two sets of wavelet coefficients. Since multiple iterations over the low pass data are desired, the scaling coefficients for the two channels are stored together. Likewise, the wavelet coefficients for the two channels are also stored together. The single level of decomposition for both scalar and multiwavelets are shown in Figure. 3.

Scalar wavelet transforms give a single quarter-sized low pass subband from the original larger subband. The multiwavelet decompositions iterate on the low pass coefficients from the previous decomposition which is shown in Figure.4. In the case of scalar wavelets, the low pass quarter image is a single subband.

But when the multiwavelet transform is used, the quarter images of low pass coefficients is actually a 2×2 block of subbands. Due to the nature of the preprocessing and symmetric extension method, data in these different subbands becomes intermixed during iteration of the multiwavelet transform (V. Strela, P. N. Heller, G. Strang, P. Topiwala, and C. Heil. 1998.).

2.3 SPIHT Algorithm

The SPIHT algorithm was designed and introduced by Said and Pearlman (Amir Said and William A. Pearlman. 1996.). SPIHT exploit the spatial dependence by partitioning the pixel values into parent-descendent groups.

The coder starts with a threshold value that is the largest integer power of two that does not exceed the largest pixel value. Pixels are evaluated in turn to see if they are larger than the threshold; if not, these pixels are considered insignificant. If a parent and all of its descendents are insignificant, then the coder merely records the parent's coordinates. Since the children's coordinates can be inferred from those of the parent, those coordinates are not recorded, resulting in a potentially great savings in the output bit stream. The parent – child relationship in this scheme is shown in Figure 5.

There are three lists maintained in SPIHT encoding. List of significant pixels (LSP), List of insignificant pixels (LIP), and List of insignificant sets (LIS). The descendents of a node include children and grand children. Set of coordinates of all descendents of node (i, j) is denoted as $D(i, j)$. Set of coordinates of four direct offspring of node (i, j) is denoted as $O(i, j)$. Set of coordinates of all grandchildren of node (i, j) is denoted as $L(i, j)$. After locating and recording all the significant pixels for the given threshold, the threshold is reduced by a factor of two and the process repeats. By the end of each stage, all coefficients that have been found to be significant will have their most significant bits recorded.

3. SPIHT for Multiwavelets

The assumptions that the SPIHT quantizer makes about spatial relations between subbands hold well for scalar wavelets, but they do not hold for multiwavelets. More specifically, the three largest highpass subbands in a scalar wavelet transform are each split into a 2×2 block of smaller subbands by the multiwavelet transform, destroying the parent-child relationship that SPIHT presumes. To work around this limitation, there is a method in the thesis of Michael B. Martin (Michael B. Martin and Amy E. Bell. 2001.), referred as coefficient shuffling which presents a new quantization method that allows multiwavelet decompositions to receive most of the benefits of using a quantizer like SPIHT.

3.1 Coefficient Shuffling

The basic idea is to try to restore the spatial features that SPIHT requires for optimal performance. Examination of the coefficients in a single-level multiwavelet transform reveals that there generally exists a large amount of similarity in each of the 2×2 blocks that compose the $L_i H_j, H_i L_j$ and $H_i H_j$ subbands, where $i=1, 2$ and $j=1, 2$.

The coefficient shuffling explains the method of rearranging the 2×2 block so that the coefficients corresponding to the same spatial locations are placed together. A clearer picture of this is given in Figure. 6. The remaining coefficient data has the same structure as that of 4-level scalar wavelet decomposition. Solid lines denote new subband boundaries and dashed lines show subband boundaries that are removed by coefficient shuffling.

In this method of coefficient shuffling, the multiwavelet decomposed structure has been altered for implementing SPIHT algorithm. After this process, the spatial relationship of scalar wavelet decomposition is gained in multiwavelet also. Hence, the SPIHT algorithm can be applied for this structure with the usual parent – child relationship. The experimental results using this coefficient shuffling method are giving some better performance over the scalar wavelet

based compression (Michael B. Martin and Amy E. Bell, 2001.). Still it has the performance lack in some type of low frequency images in terms of blocking artifacts.

3.2 Proposed Method

In the coefficient shuffling method, some of the bandpass properties of the coefficients are shuffled with the highpass and lowpass coefficients.

Hence, visual artifacts can be noted in the reconstructed images. In this paper, we propose a new method for making the multiwavelet structure, applicable for SPIHT algorithm without mingling the bandpass coefficients with the highpass coefficients. This process utilizes the conventional multiwavelet decomposition along with the coefficient shuffling.

The horizontal and vertical detail coefficients have their own importance in the reconstruction with same filters used for decomposition. In this method, the decomposition using multiwavelet is done on the entire 2x2 block coefficients of the lowpass filters L_1 and L_2 . i.e. the four subbands L_1L_1, L_1L_2, L_2L_1 and L_2L_2 are considered as approximate coefficients. These four subband coefficients are rearranged and then processed for the second level of decomposition.

The multiwavelet used here is GHM multiwavelet with two scaling and two wavelet functions. There are two lowpass and two highpass filters for decomposition and reconstruction. In each decomposition level, there are four main subbands with their own four subbands as the output of the combination of the filters. Though the coefficient shuffling make the multiwavelet decomposition structure as like the scalar wavelet structure, the combined output of the inner subband coefficients of multiwavelet structure are scattered in the SPIHT encoding. Hence there is large number of blocking artifacts in the reconstructed images, and it is more in natural images (Michael B. Martin and Amy E. Bell, 2001.).

To minimize the artifacts, the shuffling part is avoided for the detailed coefficients in the multiwavelet decomposition. The iteration of decomposition is done until we get the 4x4 matrix as the approximate coefficients. Hence the horizontal, vertical and diagonal details also have the order of 4x4.

At this point, in the approximate 4x4 matrix, the lowest subband element from the filter combination L_1L_1 is considered as the root value without any descendants. Even though the other three coefficients in the same subbands are approximate coefficients, they are considered as detail coefficients for satisfying the SPIHT structure. Then the other three lowest detail subbands are assigned as the children of these three coefficients as like scalar wavelet structure. This is shown in the Figure.8. The dotted lines denote the outputs of the four combinations of the two filters.

In Figure.8, the four coefficients marked by a circle and squares are approximate coefficients of the final level of the decomposition. In this method only one coefficient which is having the highest coefficient value marked by the circle is considered as approximate coefficient and the other three coefficients having the values just less than the highest approximate coefficient are considered as detail coefficients. Here, the actual detail coefficients are assigned as the children of the assumed detail coefficients. Hence the parent child relationship is converted exactly like the scalar wavelet structure. Here the same SPIHT code is applied with these considerations and the results are compared.

4. Experimental Results

Image compression experiments using GHM multiwavelet were conducted in both the coefficient shuffling method and the new method. The results of GHM multiwavelet with coefficient shuffling is denoted by GHM(CS) and the new proposed method is denoted as GHM(N).

Objective results are given in the form of tables of peak signal-to-noise ratio (PSNR) values. Since all tests here are performed on 8-bit grayscale images, the peak signal value is 255. Hence the PSNR values in dB for an $M \times N$ image signal x and its reconstruction \hat{x} are calculated via

$$PSNR = 10 \log_{10} \left(\frac{255^2}{MSE} \right) \quad (16)$$

where the mean squared error (MSE) is defined as

$$MSE = \frac{1}{MN} \sum_{m=0}^{M-1} \sum_{n=0}^{N-1} |x(m,n) - \hat{x}(m,n)|^2 \quad (17)$$

For each image, three scalar wavelets, a multiwavelet with coefficient shuffling and the new method are tested and the results are compared at different compression ratios. The compression results of different images with different filters are given in the table. The first column gives the image and the second gives wavelet type. The third column gives the PSNR values in dB for that particular image at various compression/bit rates. The bit rates used here correspond to 8-bit grayscale images, so the number of bits per pixel (bpp) is 8 divided by the compression factor. The test results are given for 1.0bpp (8:1), 0.5 bpp (16:1), 0.25 bpp (32:1), or 0.125 bpp (64:1).

The PSNR results for the natural images are given in the Table 1. The natural images contains more low and medium frequency components and also have different type of image structures like straight, curves and surface planes etc. From the results, the new proposed method with GHM multiwavelet outperforms the multiwavelet with coefficient shuffling method in all the cases. It also gives better compression over the scalar wavelets in most of the cases.

The PSNR results for Synthetic images in Table 2 show that the multiwavelets are not that much efficient as the scalar wavelets. Here, for these high frequency components the scalar wavelets are showing very good performance over the multiwavelet methods. Even in some cases, the scalar wavelets are giving lossless compression. Also for the synthetic images for the compression rates considered, the GHM multiwavelet with the new method again giving much better performance than the GHM multiwavelet with the coefficient shuffling method.

5. Conclusion

The performance of multiwavelets in general depends greatly on the image characteristics. For the natural test images, the new method of multiwavelet decomposition and coefficient definition introduced in this paper gives a better performance in many compression rates over the scalar wavelets and the multiwavelet with coefficient shuffling method of encoding. The synthetic images are having more high frequency components. For these types of high frequency images the multiwavelet methods are failed to make over the scalar wavelets. While the shuffling method and the new method present here help standard multiwavelet decompositions work better with zerotree-based quantizers for natural images and synthetic image results are still at a disadvantage. A design of a new multiwavelet with various required mathematical properties could come with a great performance both in natural and synthetic image cases.

References

- Amir Averbuch, Danny Lazar, and MosheIsraeli. (Jan 1996). Image Compression Using Wavelet Transform and Multiresolution Decomposition , *IEEE transactions on Image processing*, Vol. 5, No. 1.
- Amir Said and William A. Pearlman. (June 1996). A new, fast, and efficient image codec based on set partitioning in hierarchical trees. *IEEE Trans. on Circ. and Syst. For VideoTech.*, 6(3): 243–250.
- G. Strang and V. Strela, (1995). Short wavelets and matrix dilation equations, *IEEE Trans. SP*.
- Glen G. Langdon Jr. (March 1984). An introduction to arithmetic coding. *IBM J. Res. Develop.*, 28(2):135–149.
- Ian H. Witten, Radford M. Neal, and John G. Cleary. (June 1987). Arithmetic coding or data compression. *Communications of the ACM*, 30(6): 520–540.
- Ingrid Daubechies. (1992). Ten Lectures on Wavelets, SIAM, Philadelphia PA, first edition.
- ISO/IEC IS 15444-1 / ITU-T Rec. T.800, JPEG 2000 image coding system.
- Jerome M. Shapiro. (December 1993). Embedded image coding using zerotrees of wavelet coefficients. *IEEE Trans. on Image Proc.*, 41(12):3445–3462.
- Jo Yew Tham, Li-Xin Shen, Seng Luan Lee, and Hwee Huat Tan. (1998). A general approach for analysis and application of discrete multiwavelet transforms. Preprint.
- Michael B. Martin and Amy E. Bell. (April 2001). New image compression techniques using multiwavelets and multiwavelet packets. *IEEE Transactions onImage Processing*, Vol.10, No. 4.
- Michael B. Martin, Amy E. Bell, A.A.Beex, Brian D., Applications of multiwavelets to image compression. PG thesis, Blacksburg, Virginia.
- Michael Unser, Thierry Blu. (September 2003). Mathematical Proprieties of the JPEG2000 Wavelet Filters, *IEEE transactions on Image Processing*, Vol. 12, No. 9.
- R. C. Calderbank, Ingrid Daubechies, Wim Sweldens, and Boon-Lock Yeo. (1998). Wavelet transforms that map integers to integers. *Applied and Computational Harmonic Analysis*, 5(3): 332–369.
- R. R. Coifman, Y. Meyer, and M. V. Wickerhauser. (1992). Wavelet analysis and signal processing. In *Wavelets and their Applications*, pages 153–178. Jones and Bartlett, Boston MA.
- Say Song Goh, Qingtang Jiang, and Tao Xia. Construction of biorthogonal multiwavelets using the lifting scheme. preprint, 1998.
- Tao Xia and Qingtang Jiang. Optimal multifilter banks. (1998). Design, related symmetric extension transform and application to image compression. Preprint.
- V. Strela. (1996). Multiwavelets: Theory and Applications. PhD thesis, Massachusetts Institute of Technology.
- V. Strela. (1998). A note on construction of biorthogonal multi-scaling functions. *Contemporary Mathematics*, 216:149–157.

V. Strela and A. T. Walden. (1998). Orthogonal and biorthogonal multiwavelets for signal denoising and image compression. Proc. SPIE, 3391:96–107.

V. Strela, P. N. Heller, G. Strang, P. Topiwala, and C. Heil. (1998). The application of multiwavelet filter banks to image processing. preprint.

Xiang-Gen Xia, Jeffrey S. Geronimo, Douglas P. Hardin, and Bruce W. Suter. (1995). On computations of multiwavelet transforms. Proc. SPIE, 2569:27–38.

Zixiang Xiong, Michael T. Orchard, and Kannan Ramchandran. (1997). A comparative study of DCT and wavelet based coding. Proc. SPIE, 3164: 271 278.

Table 1. PSNR Results for Natural Test Images

Image	wavelet	1.000 bpp	0.500 bpp	0.250 bpp	0.125 bpp
Mandrill	Haar	31.733	30.603	29.980	29.724
	Db4	32.430	30.852	30.069	29.774
	Bior 3.7	31.890	30.513	29.940	29.593
	GHM(N)	42.668	37.223	35.942	31.517
	GHM(CS)	20.419	17.647	16.905	16.460
Boat	Haar	39.211	35.421	33.666	32.565
	Db4	40.902	36.566	34.039	32.481
	Bior 3.7	40.159	36.026	33.850	32.393
	GHM(N)	42.969	37.057	36.625	31.326
	GHM(CS)	21.943	18.334	17.282	16.936
Camera man	Haar	38.176	34.554	33.392	32.759
	Db4	38.145	34.355	32.798	32.073
	Bior 3.7	37.147	34.117	32.685	31.524
	GHM(N)	42.724	37.331	31.264	30.987
	GHM(CS)	21.961	18.557	17.621	17.198
Texture	Haar	29.221	28.320	27.856	27.680
	Db4	30.339	29.220	28.413	27.995
	Bior 3.7	30.348	29.170	28.512	28.054
	GHM(N)	36.728	30.794	25.553	24.374
	GHM(CS)	15.825	13.741	12.574	10.800
Lena	Haar	40.526	36.762	34.715	33.295
	Db4	42.474	39.088	36.202	34.252
	Bior 3.7	41.448	38.554	35.903	34.070
	GHM(N)	42.782	37.073	36.836	31.483
	GHM(CS)	22.790	19.613	18.234	17.822

Table 2. PSNR Results for Synthetic Test Images

Image	wavelet	1.000 bpp	0.500 bpp	0.250 bpp	0.125 bpp
Gray21	Haar	∞	∞	∞	72.108
	Db4	∞	79.961	55.588	47.986
	Bior 3.7	∞	99.306	58.167	47.245
	GHM(N)	48.032	37.096	36.691	31.374
	GHM(CS)	25.448	20.471	18.501	17.752
Testpat	Haar	34.788	32.505	31.409	29.718
	Db4	34.299	31.677	30.426	29.532
	Bior 3.7	34.962	32.046	30.507	29.520
	GHM(N)	37.076	31.183	25.652	25.431
	GHM(CS)	15.960	13.634	12.853	11.913
Ruler	Haar	36.072	31.703	29.547	27.762
	Db4	30.317	28.788	28.713	27.673
	Bior 3.7	31.251	31.321	29.170	27.099
	GHM(N)	30.805	29.697	25.668	25.393
	GHM(CS)	13.074	10.733	8.738	8.074
Barchart	Haar	44.156	36.925	33.134	31.700
	Db4	37.887	33.239	31.473	30.401
	Bior 3.7	38.201	33.317	31.374	29.930
	GHM(N)	36.890	31.182	29.806	25.186
	GHM(CS)	15.342	13.094	12.458	12.045
MRI	Haar	41.108	36.618	34.915	34.103
	Db4	41.779	37.205	35.373	33.991
	Bior 3.7	39.939	36.562	35.139	34.280
	GHM(N)	44.601	39.253	33.964	32.757
	GHM(CS)	35.013	28.963	26.391	25.222

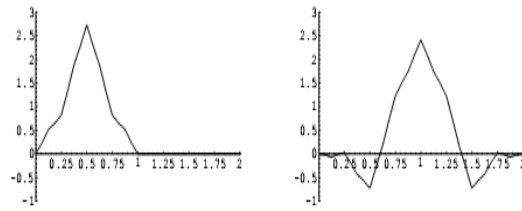


Figure 1. Geronimo-Hardin-Massopust pair of scaling functions

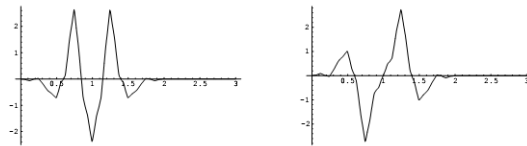


Figure 2. Symmetric GHM pair of wavelet functions

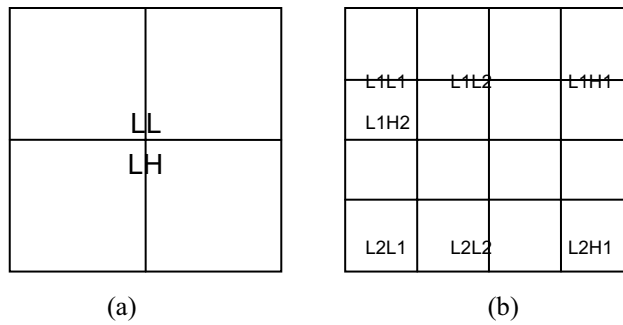


Figure 3. Single level decomposition structure for (a) scalar wavelets and (b) multiwavelets

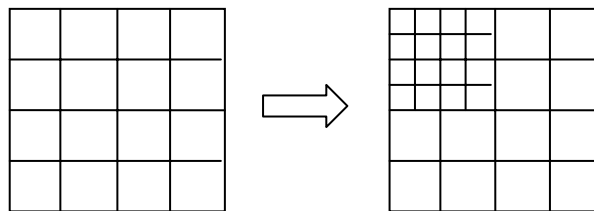


Figure 4. Iteration of multiwavelet decomposition.

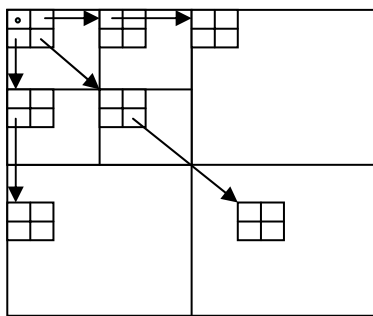


Figure 5. Illustration of parent-child relationship

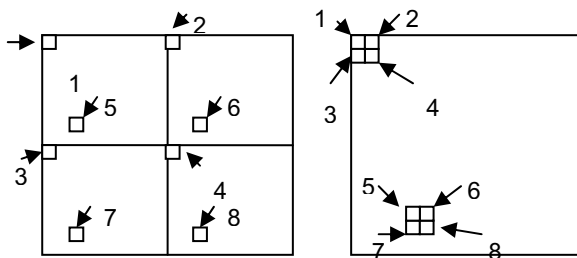


Figure 6. Illustration of coefficient shuffling

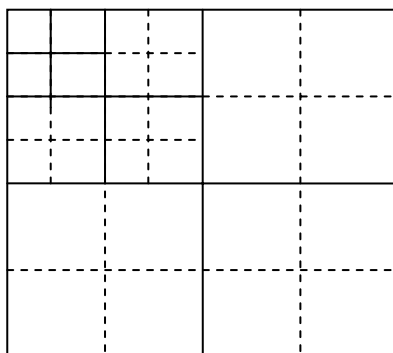


Figure 7. Subbands in 2-level multiwavelet decomposition after coefficient shuffling

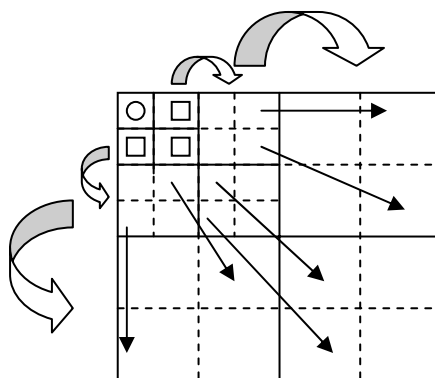


Figure 8. Parent-child relationship of multiwavelet decomposed structure



Polymorphism of Lactoferrin Gene with PCR - RFLP and its Association with Subclinical Mastitis in Dairy Cows

Changhong Zhao, Gaoming He (Corresponding author), Yanliang Wang, Zhaoxia Zhang

College of Animal Science & Technology

Shihezi University

Shihezi 832000, China

Abstract

Incidence of mastitis was checked by the California Mastitis Test (CMT). 120 cows were screened and classified into 2 groups, 60 each group, namely control group (healthy) and experimental group (subclinical mastitis). Polymorphism of cow lactoferrin gene promoter was determined by polymerase chain reaction-restriction fragment length polymorphism (PCR-RFLP). The results showed that lactoferrin gene promoter was polymorphic among different groups, which indicated that its polymorphism was related to mastitis infection.

Keywords: Lactoferrin Gene, RFLP-PCR, Subclinical Mastitis

1. Introduction

Lactoferrin in cow milk belongs to the serum transferrin gene family, and is nonhemachrome iron-binding glycoprotein synthesized by glandular epithelial cells and neutrophils (Plaffl, 2003, PP.538-545). Some researches reported (Barkema, 1998, PP.411-419, Hirvoen, 1999, PP.35-46) that Lf concentration in milk and serum would change during the infection of mastitis, which indicated that there was some association between Lf and mastitis. Therefore, observation on polymorphism of Lf gene by PCR-RFLP, and association between Lf and mastitis could give some novel insight into theory and practice. In the present paper, polymorphism of Lf gene promoter was investigated by PCR-RFLP, and association between Lf and mastitis was also observed.

2. Materials and methods

2.1 Sampling

Milk samples collected from a farm in Shihezi, Xinjiang, were detected with CMT reagent, and was primarily classified into two groups, namely control group (healthy) and experimental group (subclinical mastitis), 60 dairy cows each group. Aseptic sampling procedures were undertaken before the start of the project. 10 ml blood samples were collected from the jugular vein of each cow with anticoagulant acid citrate dextrose (ACD) solution, and serum was separated and kept frozen at -20°C for later determinations.

2.2 DNA extraction

Genomic DNA was extracted by a sodium dodecyl sulphate method and dissolved in distilled water. The concentration and purity were determined by the optical density method using an Eppendorf

spectrophotometer at 260 and 280 nm. DNA samples were diluted to 50 ng/μl and kept frozen at -20°C until further use.

2.3 Primer design

The primers were designed on the basis of DNA sequence of Lf gene promoter accepted by the Genebank (Accession: AY319306) using the oligonucleotide design tool Primer 5.0 software. Forward and reverse primer was 5'-CACATTACAAGCAGGATCTTTTGCTG-3' and 5'-CTGGCCAATGAGCCCTATATGTGT-3', respectively (Shenggong CO.Ltd, Shanghai, China).

2.4 PCR amplification

PCR reactions were performed in a 25 μl mixture containing 0.7μl forward primers, 0.7μl reverse primer, 1.5μl of 2.5mM dNTP (deoxyribonucleotide triphosphate), 2.5 μl 10 × reaction buffer, 1.5μl of 2.5mM MgCl₂, 2μl 1 unit of Taq-DNA polymerase, and 2.5μl of 50 ng/μl genomic DNA as template. The PCR was performed under the following conditions: 94°C for 4 min, followed by 35 cycles of denaturing at 94°C for 30 s, annealing at 61°C for 45 s, extension at 72°C for 45s; a final extension at 72°C for 10 min. PCR products were electrophoretically separated on 0.7% agarose gel at a constant 75 V, stained with ethidium bromide and excised for sequencing.

2.5 Digestion by Hinf I

Digestion was performed in a 10 μ l mixture containing 5 μ l PCR products, 0.2 μ l Hinf I, 1 μ l Buffer, 3.8 μ l aseptic double-distilled water. The reaction system was performed under the conditions of 37°C for 3h, and resulting fragments were separated on 8.0% polyacrylamide gels at a constant 150 V and detected by silver staining.

2.6 Data analysis

Allelic and genotypic frequencies of products after digestion by Hinf I were calculated.

3. Results and discussion

3.1 Amplification of PCR

Amplification products resulted in a 1143 bp fragment with differences detected by 8.0% PAGE (polyacrylamide gel electrophoresis) and subsequent silver staining in Lf gene promoter examined in our study (Figure 1).

3.2 PCR-RFLP results

Different fragments were separated by PCR products in Lf gene promoter using Hinf I. Among 120 dairy cows detected in this study, 2 allele genes and 3 genotypes were revealed in each group. Allele gene (638bp) was defined as A, whilst allele gene (462bp) as B. Other related genotypes were defined as A/A, A/B and B/B, respectively (Figure 2).

After digestion, allelic and genotypic frequencies were listed in Table 1. As seen in Table 1, Among healthy dairy cows (control group), A/A genotypic frequency was obviously higher than in experimental group. Through χ^2 -Test, there was great significance between them ($P < 0.01$); On the contrary, among dairy cows of subclinical mastitis (experimental group), B/B genotypic frequency was obviously higher than control group. Through χ^2 -Test, there was great significance between them ($P < 0.01$); As for A/B genotypic frequency, there was no significance ($P < 0.05$). In addition, B allele frequency in experimental group was obviously higher than in control group ($P < 0.01$) whilst A allele frequency in control group was obviously higher than in experimental group ($P < 0.01$).

4. Conclusions

Different fragments were obtained in this paper which indicated that there was substitution site mutation in the region of Lf gene promoter. However, in order to confirm effects of such mutation on the expression Lf gene and its association with subclinical mastitis, expression level of Lf gene mRNA and concentration dynamics of Lf in the tissues of dairy cows with subclinical mastitis should still need further investigation.

References

- Barkema, H.W. (1998). Incidence of clinical mastitis in dairy herds grouped in three categories by bulk milk somatic cell counts. *J Dairy Sci*, 81 (2): 411-419
- Plaffl, M.W., Wittmann, S.L., & Meyerh, H.D., et al. (2003). Gene expression of immunologically important factors in blood cells, milk cells and mammary tissue of cows. *J Dairy Sci*, 86 (3) : 538-545
- Hirvoen, J., Eklund, K., & Teppo, A.M., et al. (1999). Acute phase response in dairy cows with experimentally induced mastitis. *Acta Vet Scand*, 40: 35-46

Table 1. Allelic and genotypic frequencies of Lf gene promoter by RFLP

Group	Sample number	Allelic frequency			Genotypic frequency	
		A /A	A /B	B /B	A	B
Control group	60	0.5**	0.4	0.1	0.78**	0.22**
Experimental group	60	0.15	0.23	0.62**	0.17	0.83

Note: **, $P < 0.01$, great significance

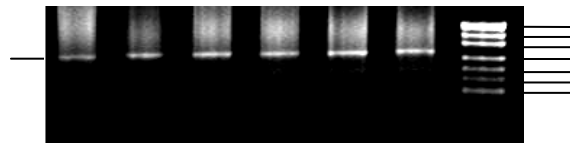


Figure 1. Amplification of PCR products

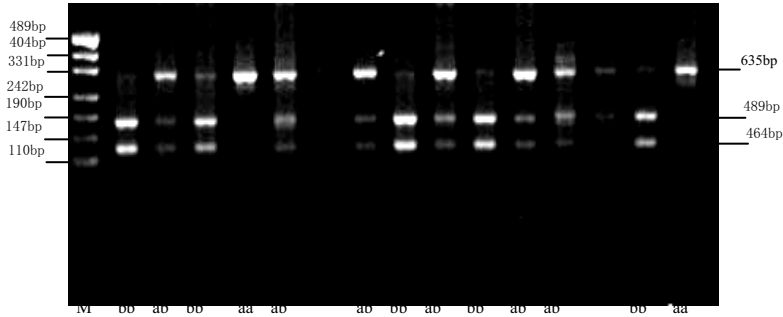


Figure 2. Electrophoresis of digestion with Hinf I in Lf gene promoter



Studies on the Performance of Quarry Waste in Flowable Fly Ash-Gypsum Slurry

Revathi .V.

K.S.R. College of Engineering

Tiruchengode, Tamilnadu - 637 215, India

Tel: 98-6544-2862 E-mail: revthiru2002@yahoo.com

Dr. Narasimha. V. L.

Pondicherry Engineering College

Pondicherry-605 014, India

Tel: 94-4353-7995 E-mail: narasimhavl@yahoo.com

Dr. Jayanthi. S.

Government College of Technology

Coimbatore, Tamilnadu-641 013, India

Tel: 98-9405-5758 E-mail: jaigct@yahoo.co.in

Abstract

Mining the sand, from riverbed is hazardous to environment. The deep pits dig in the riverbed for sand mining effects on ground water level and erode the nearby land. Most of the provincial Governments in India have imposed ban on mining sand from riverbeds. In such a situation the quarry waste can be an alternative to river sand. The present paper deals with the experimental investigation on the performance of quarry waste in fly ash gypsum slurry. The flow ranges selected for the study are 500 ± 25 mm, 425 ± 25 mm, 375 ± 25 mm, 300 ± 50 mm, & 150 ± 50 mm. The content of the quarry waste in the mix was increased from 0% to 50% for each of the above flows. Twenty mixes were proportioned and used in the study. These mixes were evaluated for flowability and compressive strength. Results indicate that quarry waste in fly ash gypsum slurry showed satisfying performance and suitable for a wide range of applications.

Keywords: Quarry waste, Fly ash, Gypsum, flowable slurry, CLSM, Activation

1. Introduction

Increased sand mining not only affects the aquifer of the river bed but also causes environmental problems. Digging of sand from river bed reduces percolation of rain water and interrupts the recharge of ground water table. The rain water as it passes through sand bed gets filtered and pure water will reach the water table. Uncontrolled mining of sand expose the natural soil to the running water. This will alter the river dynamics. River starts to scour the exposed soil and make banks unstable. In the backdrop of the above many provincial Governments have imposed ban on sand mining from river beds. In such a situation quarry waste from crushers are being used as an alternative to river sand.

Crushed stone is a prosaic but nearly indispensable construction material. About 3 billion tones are produced worldwide from a great variety of rock type. Residue form stone crusher called as quarry waste, a by-product in the production of crushed coarse aggregate. This residue generally represents less than 1% of aggregate production.

This quarry waste is dumped in forest areas, destroying the natural vegetation and ecology of the area and adversely affecting the fertility of the soil, contaminating water sources and contributing to drainage problems. It is possible to use the quarry waste as fine aggregate in construction industry in replacement of natural river sand. This will reduce not only the demand for natural sand but also the environmental burden. (Nagaraj.et.al, 1996, Narasimhan.et.al, 1999)

However, the literature on use of quarry waste is in the budding stage. This paper focuses on the use of quarry waste in flowable slurry.

Flowable slurry is a self compacting, cementitious material used primarily as a backfill material in place of compacted fill. Flowable slurry has a specified compressive strength of 8.3MPa or less at the age of 28-days. If future excavation is desired the compressive strength should be less than 2.1MPa. It is also referred as controlled low strength material (CLSM), flowable fill, controlled low density fill etc. In recent decades flowable slurry has gained momentum due to its wide variety of applications and several advantages. The applications include filling utility trenches, building

excavations, underground storage tanks, abandoned sewers and utility lines, underground mine shafts and pavement sub-bases/bases. Flowable slurry provides an excellent opportunity to make use of industrial waste materials. (ACI Commimittee 229R, 1994).

High fly ash slurry consists of fly ash, 4 to 5% cement and enough quantity of water to produce the flowability required for particular application. High fly ash slurry was successfully used in filling underground structures. (William C.Krell,1989, Tarun Naik et.al,1990& Bruce.et.al, 1994)

Low fly ash mixes normally consists of high percentage of filler material/fine aggregate, a low percentage of fly ash and cement and enough water to obtain the desired flowability. The amount of cement, fly ash, fine aggregate and water is in the range of 3%, 8%, 72% and 17% by weight of total mix respectively (W.E.Brewer, 1994). The successive case histories such as protecting ground water form contamination, protecting ground river banks, culverts, drainage ditches and bridges from damaging effects of moving water has been documented on use of low fly ash flowable slurry. (Ronald L.Larsen, 1990, Zhongjie Zhang, 2007)

Waste foundry sand, a by-product of the metal casting industries was used as a fine aggregate in flowable slurry. The excavatability slurry was developed with desirable properties using foundry sand as a replacement for fly ash up to 85%. The permeability values ranged from 10^{-5} to 7×10^{-6} cm/sec (Bhat.et.al, 1996, Tarun Naik.et.al 1997, Paul.J.Tikalashy et.al, 1998 & 2000)

Phospho gypsum, a by-product in the production of phosphoric acid in the manufacture of fertilizers was used along with class C fly ash. S.Gandham, 1996 was suggested that it provided adequate flowability, strength and stability characteristics. In order to reduce long term liability associated with ash disposal site, pond ash was used in flowable slurry formulation in place of fly ash. The pond ash slurry was not recommended for structural fill (Christine A.Langton.et.al, 1998).

The use of flue gas desulphurization (FGD) ash was used as a replacement for conventional fly ash in flowable slurry. The properties were comparable with normal flowable slurry in terms of place ability, compressive strength and excavatability. FGD flowable fill with addition of additives and admixtures compared favorable with the characteristics of conventional quick-set flowable fill (Butalia.et.al, 2001).

The potential use of cement kiln dust (CKD) which is a fine powdery by-product of Portland cement manufacturing was used in flowable slurry. It is reported that CKD could be beneficially added to produce a very low strength material that offered comparable strength to soils used for conventional fills and many other low strength applications. (Pierce.et.al, 2003, M.Lacheme.et.al, 2008)

The potential use of scrap tire rubber could be utilized as light weight aggregate in flowable fill in the construction of bridge abutment fills, trench fills and foundation fills. C.E.Pierce& M.C. Blackwell, 2003)

The feasibility of using bottom ash as flowable slurry was investigated. Results showed that blending bottom ash with fly ash was a suitable method for developing acceptable flowable slurry. (J.P.Won.et.al, 2004)

Amnon Katz and Kovel, 2004 investigated the use of industrial by-products for the production of flowable slurry. Five different by-products such as cement kiln dust, dust from asphalt plants, coal fly ash, coal bottom ash and quarry waste were used. The results indicated that flowable slurry with good properties could be made with significant amounts of cement kiln dust (25 to 50% by weight).

Ata.G.Doven and Ayse Pekrioglu, 2005 developed structural fill using high volume fly ash with cement, lime, silica fume, high range water reducer and water. The experimental results showed that this composite material could be effectively used as a structural fill.

The effects of prolonged mixing and retempering (remixing) on flowable slurry were investigated by Sarah.I.et.al, 2001. They found that prolonged mixing did not change flowability or bleeding but time of setting was increased. Retempering did not significantly impact the material in the fluid state and 28-day strength.

Effect of curing condition on strength development of flowable slurry was investigated by Kevin.J.Folliard.et.al, 2003. They found that flowable slurry mix containing class C fly ash exhibited a significant increase in strength when cured under the highest temperature of 38°C.

The effect of water quality on the strength of flowable fill mixes was evaluated by Al.Harthy.et.al, 2005. Water samples were obtained from four major oil fields in Oman. The results indicated that use of non-fresh water produced low compressive strength in comparison with potable water. David Trejo.et.al, 2005 evaluated the corrosion performance of iron pipes and galvanized pipes completely embedded in flowable slurry. The results indicated that corrosion activity was less than pipes embedded in sand/soil/clay.

Being a pozzolanic material fly ash is normally activated by ordinary Portland cement. Many investigations showed that OPC might be replaced by alkalies and sulphates (industrial by-product/ reagent grade) to obtain a binder with similar

properties. Hence studies on the fly ash activated by industrial by-product chemicals and its use as a binder in CLSM will boost the large-scale utilization of fly ash and industrial wastes. (AmitavaRoy.et.al, 1992, C.S.Poonet.al, 2001, Narasimha,V.L et.al 1995, Revathi. V.et.al, 2005)

In the present study flowable fly ash gypsum slurry along with quarry waste was developed to propose for various applications. This paper focuses the influence of quarry waste in flowable fly ash gypsum slurry.

2. Experimental Program

2.1 Materials and Mix Proportions

This study included high calcium fly ash, gypsum and quarry waste. The fly ash was obtained from Neyveli Lignite Corporation (NLC). The gypsum used in this study was obtained from TANFAC Cuddalore, Tamil Nadu, India. Quarry waste with dust fraction passing through 4.75mm sieve and retained on 300 μ m sieve was used for this present study.

For the experimental investigation five different flow series flowable fly ash gypsum slurry mixes were considered. The mixes were proportioned for flow of 500 \pm 25mm, 425 \pm 25mm, 375 \pm 25mm, 300 \pm 50mm, & 150 \pm 50mm. A total of twenty different fly ash gypsum slurry mixes were proportioned. Of these, five were the control mixes without quarry waste and the remaining had three different quarry waste content (10, 30 %and 50% by weight of binder, fly ash + gypsum). The gypsum content in the binder was 10% by weight of fly ash. The details of mixes are presented in table.1

2.2 Determination of flowability

Mixing of materials for both dry and wet mixes, were done mechanically. The prepared slurry was filled in an open ended cylinder 75mmdia x 150mm long (3"φ x 6"). The cylinder was slowly lifted and the slurry was allowed to spread. Spread of the slurry was measured using a metallic scale in two different directions.

2.3 Determination of compressive strength of F-G slurry

Immediately after measuring the spread the slurry was remixed and casted into 50mm cubical moulds. Cubes were de-mould after 24 hours and humid cured until testing. Twelve specimens were prepared, cured and tested for each mix.

3. Results and Discussions

3.1 Flow test

Flow tests were conducted for all the mixes with W/B ratios 0.30 to 0.82. The results obtained shown in figure 1. From the results obtained the following are noted.

The flow behaviour of F-G slurry is a very important property. Therefore it is essential to understand how different ingredients of the slurry affect this behaviour. Water is the main responsible for flow. The amount of water required to produce flow depends primarily on the proportions of fly ash, gypsum and quarry waste in the mix. The effect on flow of increasing quarry waste content is understood from the flow figure.1.

Water content for 'A' series mixes varied from 0.65 to 0.82 to obtain the flow of 500 \pm 25 mm. Water content for 'B' series mixes was found as 0.60 and remained same for all quarry waste content to obtain a flow of 425 \pm 25 mm. Water content for 'C' series was found as 0.50 for 0% and 10% quarry waste content, for 30% it was found as 0.55 and for 50% it was found as 0.57 to obtain a flow of 375 \pm 25 mm. Water content for 'D' series mixes varied from 0.40 to 0.50 to obtain a flow of 300 \pm 50 mm flow. Water content for 'E' series mixes varied from 0.30 to 0.45 to obtain a flow of 150 \pm 50 mm flow.

During flow test it was found that 150 \pm 50 mm flow was not readily flowable as other flow ranges. Water content for all flow ranges were found to increase with quarry waste content except 'B' series mixes. As the binder content increased the water demand decreased to obtain the desired flow.

3.2 Compressive Strength

Table.2 summarizes the test results of this study. As expected the compressive strength increased with age. The compressive strength for all flow range mixes with and without quarry waste ranged from 0.356 to 4.04 MPa at the age of 3-day, 1.41 to 6.20 MPa at the age of 7-day, 1.70 to 7.60 MPa at the age of 28-day and 2.72 to 7.61 at the age of 56-day. The strength obtained for all the mixes were below 8.3 MPa as specified by ACI 229 R. Therefore the strength requirement of flowable slurry was satisfied. All the mixes may be used as structural fills (Strength between 0.69 to 8.3MPa).

Figures.2 shows the effect of quarry waste on the relative compressive strength of F-G slurry at 28 days. It was clearly shown that there was optimum quarry waste for the compressive strength at 28-day. All flow ranges indicate that 10% quarry waste content as the optimum mix composition. At the optimum composition 300mm flow mix showed the higher improvement in compressive strength at the age of 28-day compared to other flow mixes.

The compressive strength of F-G slurry depended on the flowability of different mixes. Mixes at the normal flowability indicated high strength when compared with high flowable mixes. Beyond 425mm flow series mixes caused significant

reduction in strength. However there was a significant increase in strength up to 3-day when compared with 425mm flow series mixes. Most of the mixes showed significant strength gain within 7-day. However, no significant strength improvement was observed for the period from 28-day to 56-day.

4. Conclusion

Industrial waste materials such as fly ash, gypsum and quarry waste were used in the preparation of flowable slurry. From the results obtained the following is concluded.

F-G slurry satisfies the requirements of the ACI Committee 229R as a CLSM. FG slurry can be an economic viable material to conventional compacted fill. The experimental results indicated that the quarry waste can be effectively used in fly ash gypsum slurry. Increase in quarry waste content increases the water requirement except 425±25mm flow mixes. Mixes with 50% quarry waste content for corresponding 500±25mm flow and mix without quarry waste corresponding to 425±25mm flow can be excavated using any mechanical equipment. All the mixes can be used as structural fill except 30% and 50% quarry waste content mixes corresponding to 500±25mm flow. The flowable fly ash gypsum slurry with quarry waste is environment friendly as it uses only industrial by-products.

References

- ACI Committee 229R, (1994). Controlled Low Strength Materials (CLSM). *ACI Concrete International*. (July) 16(7), 55-64.
- Al-Harthy, A.S., Taha, R., Abu-Ashour, J., Al-Jabri, K., & Al-Ojami, S. (2005). Effect of water Quality on the Strength of Flowable Fill Mixtures. *Cement & Concrete Composites*, 27, 33-39.
- Amitava Roy., Paul Schilling., Harvill C., Eaton., & Roger, K. Seals. (1992). Alkali activation of Class C flyash. *Proc. Utilization of Waste materials in Civil Engineering Construction, ASCE National Convention, New York*, (Sep) 13-17, 104-115.
- Amnon Katz., &Konstantin Kovler. (2004). Utilization of Industrial by products for the production of Controlled Low Strength Materials (CLSM). *Waste Management*, 24, 501-521.
- Ata.G.doven., & Ayse Pekrioglu. (2005). Material Properties of High Volume Fly ash Cement Paste Structural Fill. *Journal of Materials in Civil Engineering*, (Dec) 17(6), 686-693.
- Bhat, S.T., & Lovell, C.W. (1997). Mix Design for Flowable Fill. *Transportation Research Record*, 1589, 26-28.
- Brewer, W.E. (1994). Durability Factors Affecting CLSM. *SP 150-3, American Concrete Institute, Detroit, MI, USA*, 39 – 51.
- Bruce, W.Ramme., Tarun, R.Naik., & Henry, J.Kolbeck. (1990). Use of fly ash slurry for underground facility construction. *Construction and Building Materials*, 8, (1), 63-67.
- Butalia, T.S., Wolfe, W.E., Lee,J.W. (2001). Evaluation of a dry FGD material as a flowable Fill . *Fuel*, 80, 845-850.
- Ceki Halmen., David Trejo., Kevin, J.Folliard & Lianxiang Du. (2005). Corrosion of Metallic Materials in Controlled Low-Strength Materials-Part 3. *ACI Materials Journal* (Nov-Dec) 102(6), 429-437.
- Charles, E.Pierce., Himanshu Tripathi., & Travis, W.Brown. (2003). Cement Kiln Dust in Controlled Low-Strength Materials. *ACI Materials Journal*, (Nov-Dec) 100(6), 455-462.
- Christine, A.Langton., Rajendran, N., & Stanley, E.Smith. (1998). Use of Pond Ash in CLSM. *ACI Concrete International*,(Dec), 58-62.
- David Trejo, Ceki Halmen, Kevin J.Folliard and Lianxiang Du, (2005). Corrosion of Metallic Materials in Controlled Low-Strength Materials-Part 4. *ACI Materials Journal*, (Jan-Feb) 103(3), 53-59.
- David Trejo., Ceki Halmen., Kevin, J.Folliard., & Lianxiang Du. (2005). Corrosion of Metallic Pipe in Controlled Low-Strength Materials-Part 1 and Part 2. *ACI Materials Journal*, (May-June), 192-201.
- Gandham, S., Seals, R.K., and Paul, T.Foxworthy. (1996). Phosphogypsum as a Component of Flowable Fill. *Transportation Research Record*, 1546, 79-87.
- Kevin, J.Folliard., Lianxiang, Du., & David Trejo. (2003). Effects of Curing Conditions on Strength Development of Controlled Low Strength Material. *ACI Materials Journal*, (Jan-Feb), 100(1), 79-86.
- Lachemi, M., Hossain, K.M.A., Shehata, M., & Thaha,W. (2008). Controlled low strength materials incorporating cement kiln dust from various sources. *Cement & Concrete Composites*, 30, 381-392.
- Nagaraj, T.S., & Zahida Banu. (1996). Efficient Utilization of Rock dust and Pebbles in Portland cement concrete. *Indian Concrete Journal*, 70(1), 53-56.
- Narasimha,V.L., Sundararajan,T., & Ramalingam, C. (1995). Mix proportioning of FaL G Concrete Using Different

- Quality Limes. *Proc of the Intl. Conference on Fly ash Disposal and Utilization, New Delhi*, 21 -22, III-25 to III-30.
- Narasimhan,C., Patil, B.T., & Sannai,H. (1999). Performance of Concrete with Quarry dust as fine aggregate- An Experimental Study. *Civil Engineering and Construction Review*, 19-24.
- Paul Tikalsky., Mike Gaffney., & Ray Regan. (2000). Properties of Controlled Low Strength material Containing Foundry Sand, *ACI Materials Journal* (Nov-Dec) 97(6), 698-702.
- Paul,J. Tikalsky., earl Smith., & Raymond Regan, W. (1998). Proportioning Spent Casting Sand in Controlled Low Strength materials. *ACI Materials Journal*, (Nov-Dec) 95(6), 740-746.
- Pierce, C.E., & Blackwell, M.C. (2003). Potential of Scrap Tire Rubber as Lightweight Aggregate in Flowable Fill. *Waste Management*, 123(3), 197-208.
- Poon, C.S., Kou, S.C., Lam, L., & Lin, Z.S.. (2001). Activation of fly ash/cement systems using calcium sulfate anhydrite CaSO_4 . *Cement and Concrete Research*, 31,873-881.
- Revathi, V., & Narasimha.V.L. (2005). Development and Characterization of Flowable High –Calcium Fly ash-Gypsum Slurry. *Indian Concrete Journal*, (Jan), 49-53.
- Ronald, L.Larsen. (1990). Sound Uses of CLSMs in the Environment. *ACI Concrete International* (July) 12(7), 1-7.
- Sarah, L.Gassman., & Charles, E.Pierce., & Aaron, J.Schroeder. (2001). Effects of Prolonged Mixing and Retempering on Properties of Controlled Low Strength Material (CLSM). *ACI Materials Journal*, (Mar-April), 98(2), 194-199.
- Tarun, R.Naik., & Shiw, S.Singh.(1997). Flowable Slurry Containing Foundry Sands. *Journal of Materials in Civil Engineering*, (May), 93-102.
- Tarun, R.Naik., Bruce, W.Ramme., & Henry, J.Kolbeck. (1990). Filling Abandoned Underground Facilities with CLSM Fly ash Slurry. *ACI Concrete International*. (July) 12 (7), 1-7.
- William, C. Krell.(1989). Flowable Fly ash. *ACI Concrete International*. (November) 11(11), 54-58.
- Won, J.P. Lee, Y.S. Park, C.G. & Park, H.G. (2004). Durability Characteristics of Controlled Low Strength Materials containing Recycled bottom ash. *Magazine of Concrete Research*, (Sep) 64 (7)), 429-436.
- Zhongjie Zhang., & Mingjiang Tao. (2007). Flowable Fill as Geotechnical Material in Highway Cross-Drain Trenches. *Geotechnical Testing Journal*, 30(1), 1-6.

Table 1. Mix Proportions of Fly ash Gypsum slurry with quarry waste

Sl.No	Flow range	Mix Identity	Mix Ingredients						Flow/ Spread (mm)
			Fly ash (Kg/m ³)	Gypsum (Kg/m ³)	Quarry waste (Kg/m ³)	Water (Kg/m ³)	W/ (FA+ G)	Quarry waste (%)	
1	500 ± 25 mm flow	A ₁	898.05	89.8	--	642.00	0.65	0	481.0
2		A ₂	825.54	82.55	90.8	635.66	0.70	10	503.0
3		A ₃	742.85	74.28	245.13	612.84	0.75	30	490.4
4		A ₄	677.34	67.73	372053	610.95	0.82	50	491.0
5	425 ± 25 mm flow	B ₁	941.26	94.126	--	621.23	0.60	0	420.0
6		B ₂	907.88	90.78	99.86	599.08	0.60	10	405.0
7		B ₃	845.93	84.59	279.15	558.31	0.60	30	404.0
8		B ₄	791.42	79.14	435.28	522.33	0.60	50	405.0
9	375 ± 25 mm flow	C ₁	1053.43	105.34	--	579.38	0.50	0	391.0
10		C ₂	1008.82	100.88	110.97	554.85	0.50	10	387.0
11		C ₃	889.31	88.93	293.47	538.03	0.55	30	397.0
12		C ₄	809.44	80.94	445.19	507.51	0.57	50	380.0
13	flow	D ₁	1188.19	118.81	--	522.8	0.40	0	274.0

14	150 ± 50 mm flow	D ₂	1100.39	110.03	121.04	514.43	0.43	10	262.0
15		D ₃	932.89	93.28	307.85	513.08	0.50	30	294.0
16		D ₄	829.03	82.9	455.96	501.56	0.55	50	280.0
17		E ₁	1366.57	136.65	--	450.96	0.30	0	185.0
18		E ₂	1212.38	121.23	133.36	466.76	0.35	10	133.0
19		E ₃	983.83	98.383	324.66	486.99	0.45	30	185.0
20		E ₄	867.61	86.76	477.18	477.18	0.50	50	183.0

Table 2. Compressive strength of various F-G slurry mixes

Sl. No	Flow range	Mix Identity	Quarry waste (% by weight)	Compressive Strength at various ages (MPa)			
				3 days	7 days	28 days	56 days
1	500±25mm flow	A ₁	0	1.43	2.01	2.36	2.72
2		A ₂	10	1.12	2.34	2.74	2.82
3		A ₃	30	1.12	1.73	2.77	2.82
4		A ₄	50	1.03	1.52	2.09	2.33
5	425±25mm flow	B ₁	0	0.36	1.41	1.70	3.10
6		B ₂	10	0.45	2.10	2.85	3.47
7		B ₃	30	0.86	2.61	2.79	3.34
8		B ₄	50	0.88	2.62	2.80	3.50
9	375 ± 25 mm flow	C ₁	0	2.62	3.72	5.00	5.70
10		C ₂	10	2.67	4.58	5.20	5.80
11		C ₃	30	2.68	5.00	5.10	5.20
12		C ₄	50	2.84	2.97	3.50	3.60
13	300 ± 50 mm flow	D ₁	0	2.96	4.19	5.41	5.90
14		D ₂	10	3.01	4.40	7.60	7.61
15		D ₃	30	3.06	5.02	5.64	6.07
16		D ₄	50	3.63	5.20	5.82	5.83
17	150 ± 50 mm flow	E ₁	0	3.20	5.60	5.61	6.50
18		E ₂	10	3.47	6.20	6.80	6.91
19		E ₃	30	4.04	5.02	5.30	5.80
20		E ₄	50	3.02	4.81	4.91	6.10

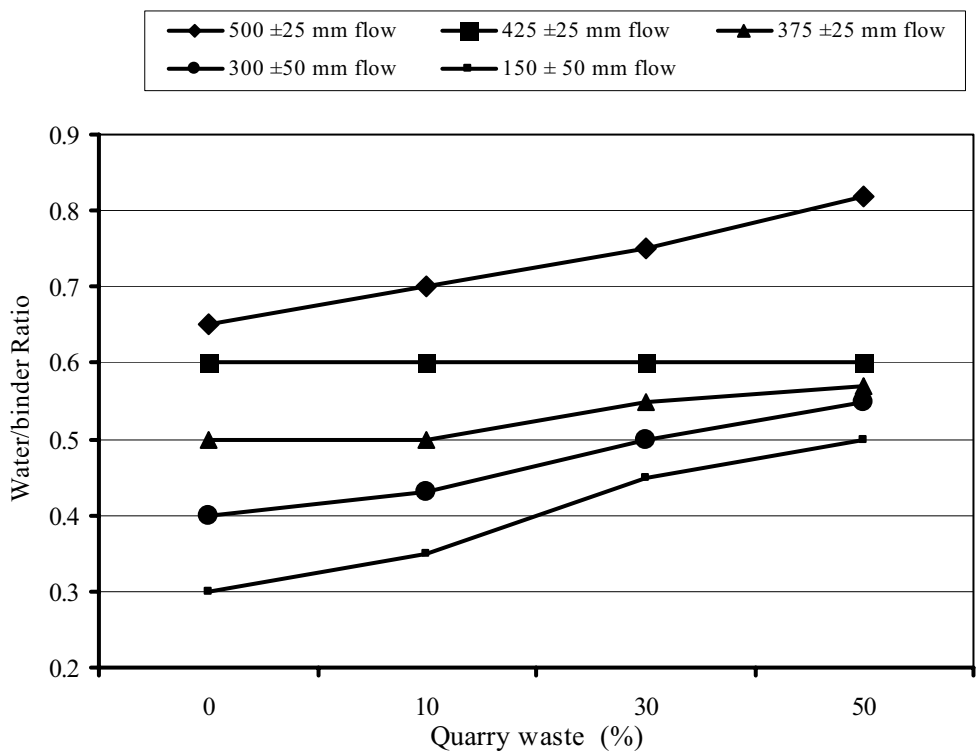


Figure 1. Water requirement for various Quarry waste Content

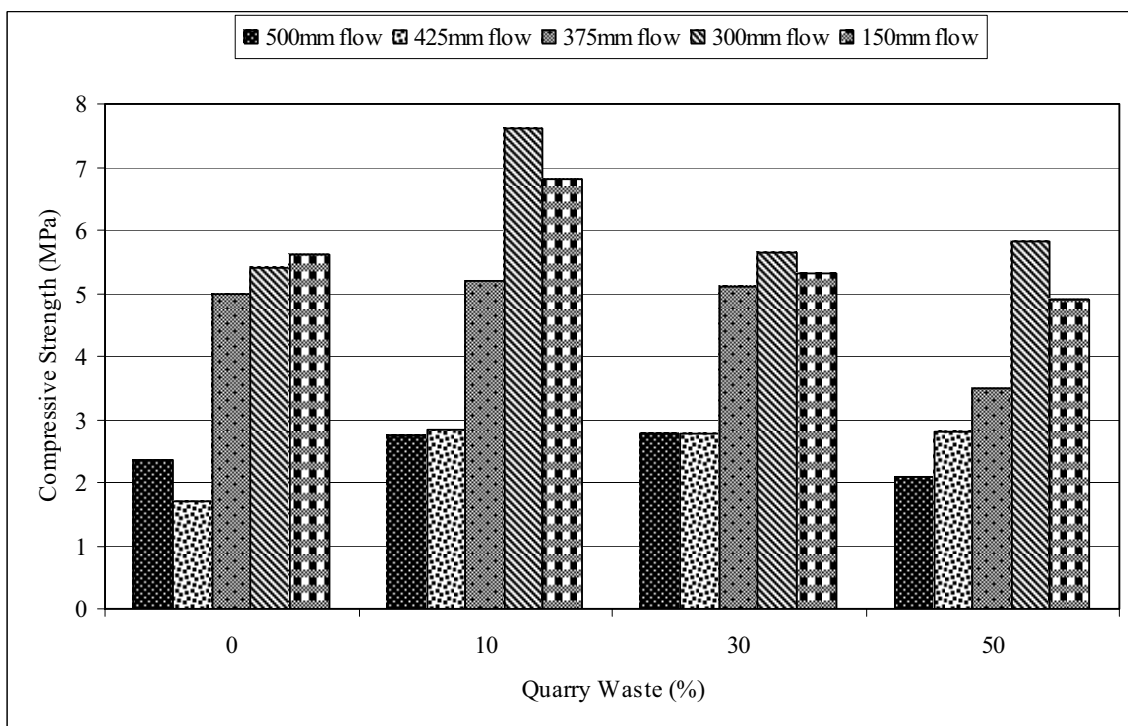


Figure 2. Effect of quarry waste on F-G slurry at 28 days Compressive Strength



Nanotechnology in Textiles Finishment

Dongxue Liu & Weiguo Dong

College of Textile

Tianjin Polytechnic University

Tianjin 300160, China

E-mail:snow_1314@sina.com

Abstract

The ways of using the nanometer material to give the textile fabric some function is listed and compared in this article. In the early research, first the nanometer material preparation is alone carries on. And then using this to make the finishing agent. Finally put the agent on the fabric by finishment. At present, people combine the preparation of nanometer material and finishing agent together, and then cover this on fabric through the normal finishment. Recently research the trend is to compact the three steps to one step, completing the nanometer material preparation, the finishment agent production and the finishing process at the time. Various examples are given in this article. At the end, some reserches about cotton fiber hole structure are listed, which has implicated a new way to take advantage of nanometer merterial and a bright future about a new type cotton fiber.

Keywords: Nanotechnology, Textiles, Finishment, Nano- tex

1. Introduction

Fiber-based materials in technical applications are an increasing worldwide market and cover a wide area. Numerous textile materials are integrated in automotive systems being responsible there for many functions within important fields like safety, comfort or light weight.

The inorganic nanometer material dispersion will fix on the textile, enable the textile to have each kind of function, will be the various countries material study and textile industry's expert continuously in diligently with the attention and hot spot.

2. Domestic and foreign research progress

In the early research, the nanometer material preparation is alone carries on, then a nanometer granule will disperse to the spinning fluid in uses altogether mixes the spinning preparation chemical fiber, or the nanometer material granule will disperse to the finishing agent, through soak rolls and the nanometer coating is attaching to the textile fiber product on, the implants also is used to implant a nanometer material into the textile fiber.

Altogether mixes the spinning method development the function textile fiber mainly to have: The antibacterial chemical fiber, the far infrared linear chemical fiber, the fire-resisitant textile fiber, the regeneration adjusts the warm textile fiber, shines the textile fiber, the electric conduction textile fiber and so on. With altogether will mix the nanometer granule to join in the textile fiber, the existence question mainly will be its easy reunion. The inorganic nanometer particle reunion not only has affected the nanometer material function display, moreover becomes the important restriction factor, which the influence spinning smoothly carries on. In order to solve this problem, generally is disperses a nanometer granule into the mother granule, again uses the mother granule altogether to mix the system with the textile fiber spinning fluid to produce a high polymer/nanometer granule the complex fiber.

At present, generally uses the fabric finishment for natural. The main method includes: soak rolls and the nanometer coating . Nanometer addictive The soak rolls with nanometer addictive is suitable for putting on the soft fabric to the request. The nanometer coating is joins right amount nanometer in the coating, after drying and the essential heat treatment, forms a thin film in the fabric surface. The coating law adapts broadly to the textile fiber type, processing cost low, but the fastness of wash-resistant and the handles of fabric are bad.

The Xia men China Hua Pu high-tech industry limited company studies one kind of one's own appropriation technology, (Yinqing Wu, 2000) called for implants, the nanometer ceramic powder body implants in the textile fiber, and fixed effectivly, this method may use in the natural fiber also to be allowed to use in the chemical fiber. The Yongli Chen and other person has studied the feasibility of implanting several kind of nanometer granules into the PET chemical fiber,

the findings indicated that, In the sol the nanometer granule of carbon black, Fe (OH) 3 and natural ore powder at 130 °C can enter the PET amorphous region, at the low temperature can permanent solidify. During implants, the size of implanted the nanometer granule particle is limited by the fibrous material aperture size, the nanometer granule reunion question also need to solve during the implanting process.

3. The present research tendency

The home position production during spinning or finishing will solve the nanometer material dispersible problem.

The home position polymerization during spinning, by nanometer material and the high polymer, the preparation nanometer material/polymer compound material, through the spinning preparation nanometer function textile fiber, this method truly will realize a nanometer pellet to be dispersible in high polymer nanometer level, not only enhanced the spinning efficiency, moreover enable the material mechanics, the heat studies performance to obtain a bigger enhancement. But only can apply on the chemical fiber textile, cannot apply to the natural fiber textile. This aspect research includes:

Shanghai University of communication (Kulpinski, 2005) the scientific researcher completes a nanometer titanium oxide (TiO₂) the anti-ultraviolet ray textile fiber uses a nanometer titanium oxide and the polyester home position polymerization method, owning the independent intellectual property rights, the preparation nanometer TiO₂/polyester complex fiber.

The Chinese Yi Zheng petrochemical industry the chemical fiber limited liability company. Through joins the chemical additive in the polyester building-up reactions raw material, the hydrogen which in the use polyester esterify process produces, causes titanium alkoxide, titanium inorganic salt, ethylsilicate to have the hydrolytic reaction, the home position forms the nanometer level titanium dioxide or the silicon dioxide inorganic granule, these inorganic granules evenly disperse around the polymer macro-molecule, improved the polyester crystallization and the orientation performance, thus then produces the high strength polyester industry silk using the convention technical process and the equipment.

Chronakis, Ioannis S of IFP Research, (Chronakis, 2005) Swedish Institute for Fiber and Polymer Research, Sweden, covers the active research area of producing ceramic and composite nanofibers with various compositions and properties by means of the electrospinning process. Current critical issues are discussed, such as carbon nanofibers made from electrospun precursor polymer nanofibers, encapsulation and alignment of carbon nanotubes within nanofibers to construct unique functional composite nanostructures, and organic-inorganic nanofibers (hybrids).

Arnim, Volkmar V; Dauner, Martin; Scherrieble, Andreas; Stegmaier, Thomas; Planck, Heinrich of Institute for Textile Research and Process Engineering (ITV), (Arnim, 2005) Denkendorf, Germany, offer a great chance to gain novel physical and chemical properties of the fiber-based materials. ITV Denkendorf focuses on nano structures and nano particles in textile development and processing by finishing systems as well as electro spinning and bi-component technologies. One subject of current interest is the generation of nano scaled textiles by spinning of nanofibers using electro spinning to meet the increasing request for filter media with high filter efficiency in the sub-micrometer range. The demand is based on the need for the filtration of airborne aerosols and nanoparticles as well as on the request for an effective barrier effects against bacteria (less than or equal 0.3 μm), viruses and other microorganisms. The filtration efficiency can be increased by fiber diameter reduction. Fibers in the nanometer scale were produced among others using solutions of polyacrylonitrile PAN and polyimide. At ITV Denkendorf provisions to increase the productivity in electro spinning are under investigation.

The home position polymerization during finishing. A nanometer granule in the reorganization process the home position production during medicinal preparation, will be allowed to cause a nanometer granule to be effective in the reorganization medicinal preparation is dispersed, this aspect research will include:

Wang qing, Chu Yanyan, Cui Shizhong of Area south of Yellow River engineering institute, take titanate acid butyl ester and the zinc acetate as the forerunner, the glacial acetic acid for the catalyst and peptizator, the absolute ethyl alcohol for the titanate acid butyl ester solvent, after the hydrolysis, the condensation responded the preparation titanium dioxide and the dioxide zinc and mix the silverion nanometer sol reorganization medicinal preparation.

The Shanxi scientific and technical university, Ma Jianzhong, under the alkali catalysis condition take the tetraethoxy silane as a raw material, uses sol-gel method preparation nanometer SiO₂, uses in leather finishing. Daoud, Walid A. xin.john.h of nano technology center, Textile and Garment college, Hong Kong university of science and technology, studied the surface characterization of low-temperature processed titania coatings produced on cotton fabrics by the sol-gel method.

Mahlting, B of GMBU e.V., Arbeitsgruppe Funktionelle Schichten German, used the sol-gel method to prepare nano zinc oxide (ZnO) and titanium oxide on the fabric meanwhile produce the biocidal coatings based on silica nanosols.

The department of materials applied science in engineering college of Osaka University, used the polyethylene and the tetraethoxy silane by the sol-gel method to prepare the fluorizate finishing agent used on nylon fabric. By this way the fabric can acquire highly wear and oil repellency characteristic, and anti-wear characteristic.

Yadav, A.; Prasad, Virendra; Kathe, A.A.; Raj, Sheela; Yadav, Deepti; Sundaramoorthy, C.; Vigneshwaran, N of Nanotechnology Research Group, Central Institute for Research on Cotton Technology. In the present work, zinc oxide nanoparticles were prepared by wet chemical method using zinc nitrate and sodium hydroxide as precursors and soluble starch as stabilizing agent. These nanoparticles, which have an average size of 40 nm, were coated on the bleached cotton fabrics (plain weave, 30 s count) using acrylic binder and functional properties of coated fabrics were studied. On an average of 75%, UV blocking was recorded for the cotton fabrics treated with 2% ZnO nanoparticles. Air permeability of the nano-ZnO coated fabrics was significantly higher than the control, hence the increased breathability. In case of nano-ZnO coated fabric, due to its nano-size and uniform distribution, friction was significantly lower than the bulk-ZnO coated fabric as studied by Instron [registered trademark] Automated Materials Testing System.

Using the hole structure of textile fiber. Lies between the hole structure using the textile fiber, carries the nanometer material production and on the textile fiber load the research report which step completes quite to be few.

Dong Weiguo of Tianjin polytechnic university, (Weiguo Dong,2006)assembles the barium phosphate and the barium hydrogen phosphate granule using high-pressure autoclave into the cotton textile fibres, the temperature control in 150 °C below, washes after the standard 12 above time, rate of live weight growth maintains above 6%, its cotton fibres fabric anti- burns the index to be allowed to reach 21.5%, the textile fibres force drops is smaller than 30%.

The Zhejiang technical University's patent, picks hydro-thermal method,in textile home position production nanometer titanium oxide. The reaction temperature is 145 °C~200 °C.

Take the natural fiber material as the pattern plate, the preparation nanometer material research include:

Li, Nan; Li, Xiaotian; Wang, Wei; Qiu, Shilun of Jilin University, used human hair as template for the synthesis of mesoporous silica tubes. This was accomplished by immersing the human hair in the precursor solution of mesoporous silica then calcining in air. Products showed not only tubular morphology at micron scale but also mesophase at nanometer scale.

Huang, J.; Matsunaga, N.; Shimano, K.; Yamazoe, N.; Kunitake, T of Topochemical Design Laboratory, Frontier Research System, Institute of Physical and Chemical Research (RIKEN), Japan. SnO₂ nanotubular materials were prepared by using a natural cellulosic substance as template, and their morphologies were determined by scanning electron microscopy (SEM) and transmission electron microscopy (TEM). The sizes of the nanoparticle obtained by calcination at 300 and 900°C were 2.0 and 9.2 nm, respectively, in fair agreement with TEM observation.

4. The cotton fiber hole structure research

South China University of Science and Technology paper making and pulping project, country key laboratory, Tang Aimin, Zhang Hongwei, Chen Gang, Liu Yingyao, studied the cellulose textile fiber to be possible and the porous performance attribute, used the N₂ adsorption law, the dye adsorption law, the water retention value determination and so on to token the porosity of the cellulose textile fiber of different raw material. They also studied the change of the cellulose textile fiber relative surface accumulated, the amount of porosity, the aperture and the absorbability to the liquid after mercerization and the ultrasonic wave pretreatment. The result indicated that mercerization and ultrasonic wave processing can further enhance the water retention value and attainability surface area of the cellulose textile fiber.

A Yang, Zhou Xiang, Huang Wenhao, used the opposition gel permeation chromatography to test the relations between volume and diameter of differential coefficient attainability aperture in cotton fiber and the accumulation surface area of the aperture in the cotton fiber.

Dong Weiguo of Tianjin polytechnic university,has studied the structure of aperture inside of the cotton fiber used the nitrogen adsorption method. Through the analysis adsorption uniform temperature line and the DFT analysis to token the structure of aperture of cotton fiber (aperture volume, aperture diameter distribution). The result indicated that the interior of cotton fiber existence open hole. The aperture with 2.2 nm diameters, its volume density of distribution is the biggest. the apertures with diameter between 2.0 and 4.0nm,their volumes account for the total hole volume68·16%, the diameter of the aperture over 5.0 nm, their volumes account for the bulk volume 18·49%.

As is shown before, a new research about taking advantage of cotton fiber hole structure is possible.

5. Conclusion and Future

Liking Dr. Tushar Ghosh said that Nanotechnology ushering in a new phase of the textile industry with a bright future. Nanotechnology will not only help the marketing of fabric and fashion because of its unique and incompatible

properties but it is also a revolution for human beings just like the internet wave.

References

- Arnim, Volkmar V, Dauner, Martin, Scherrieble, Andreas, Stegmaier, Thomas, Planck, Heinrich. (2005). *Nano structured textiles*, VDI Berichte, n 1920, 2005, p 97-101.
- Chronakis, Ioannis S. (2005). Novel nanocomposites and nanoceramics based on polymer nanofibers using electrospinning process - A review, *Journal of Materials Processing Technology*, v167, n2-3, p 283-293.
- Daoud, Walid A. xin, john. h. (2005). Surface characterization of low-temperature processed titania coatings produced on cotton fabrics. *Eramic Transactions, v 158, Surfaces, Interfaces, and the Science of Cearmic Joining - Proceedings of the 106th Annual Meeting of the American Ceramic Society*, 2005, p 47-52.
- Kulpinski, Piotr, (2005). Cellulose nanofibers prepared by the N-methylmorpholine-N-oxide method. *Journal of Applied Polymer Science*, 2005, v98. Nov.15: 1855-1859.
- Weiguo Dong, Junpeng Huang, Development of inflaming new cotton fiber. *Textile Science Progress*, 2006, 6P47, 48.
- Wu, Yinqing, Lv, Junfeng, Wang Shuiju. (2000). The research and development of the application of Silver plating, Far IR, and new nanophase ceramics on cotton fabric. *Knitting*, 2000, (5), 30-32.



Equilibrium Adsorption Isotherms of Anionic, Nonionic Surfactants and Their Mixtures to Shale and Sandstone

Mazen Ahmed Muherei (Corresponding author)

Department of Petroleum Engineering

FKKKSA, UTM

81310 Skudai, Johor, Malaysia

Tel: 60-17-768-3487 E-mail: mazen_moherrey@yahoo.com

Radzuan Junin

Department of Petroleum Engineering

FKKKSA, UTM

81310 Skudai, Johor, Malaysia

Tel: 60-19-789-9703 E-mail: radzuan@fkkksa.utm.my

Abstract

In this paper, the adsorptive behaviour of two surfactants (Triton X100 and SDS) and their mixtures (1:2; 1:1; 2:1 SDS:TX100 by wt) with two local adsorbents, sandstone and shale was examined. Adsorption of surfactants was assessed using a surface tension technique for aqueous phase surfactant concentrations less than critical micelle concentration (CMC). SDS (anionic surfactant) adsorption was not detected to any of the adsorbent samples. In contrast Triton X100, an ethoxylated nonionic surfactant, adsorbed to both adsorbents. Surfactant adsorbed/Kg adsorbent was lower for TX100-SDS mixtures in comparison to TX100 alone particularly for shale. Adsorption data for sub-micelle concentrations were found to fit successfully both Freundlich and Langmuir isotherms. Freundlich models pretty much represent the data than the Langmuir model. Because of their ability to minimize their amounts adsorbed to different adsorbents, mixed anionic-nonionic surfactant particularly TX100-SDS may show potential advantages in surfactant enhanced aquifer remediation (SEAR) and surfactant enhanced oil recovery (EOR) applications.

Keywords: Surfactant, CMC, Surface tension, Mixed Surfactants, Adsorption, Adsorption Isotherms

1. Introduction

The adsorption of surfactants on rock/soil/sediment solid matrix may result in the loss and reduction of their concentration, which may render them less efficient or ineffective in practical treatment. Adsorption of surfactants from aqueous solutions in porous media is very important in enhanced oil recovery (EOR) of oil reservoirs because surfactant loss due to adsorption on the reservoir rocks impairs the effectiveness of the chemical solution injected to reduce the oil-water interfacial tension (IFT) and renders the process economically unfeasible (Curbelo et al., 2007). Furthermore, the adsorption of surfactants by soils can result in much surfactant being unavailable for the micellar solubilisation of hydrophobic organic compounds (HOCs), thereby decreasing its efficiency for desorption. Nevertheless, the presence of adsorbed or immobilised surfactants in soils gives rise to the partition or adsorption of HOCs in the soil-water system, which exacerbate desorption of organic compounds (Edwards et al., 1994; Sun et al., 1995). In this sense, comparable to the selection of a surfactant to solubilise the contaminant or reduce the oil IFT is its minor tendencies to be adsorbed by the soil/sediment/reservoir rock under consideration.

Surfactant adsorption to solid-liquid interfaces is a process where transfer of surfactant molecules from bulk solution phase to the solid-liquid interface takes place. It can be considered as a partitioning of the adsorbate species between the interface and the bulk, and can occur if the interface is energetically favoured by the surfactant in comparison to the bulk solution (Paria and Khilar, 2004; Zhang and Somasundaran, 2006). In presence of soil or sediment, adsorption of surfactant as monomers may occur at low aqueous surfactant concentrations. With an increase in surfactant

concentrations, surfactant monomers adsorbed to a solid surface begin to aggregate and form micelle-like structures called admicelles or hemimicelles, depending on whether the aggregates have one or two surfactant layers. Once these structures form on a solid surface, adsorption of additional surfactant may rapidly increase until a complete bilayers of surfactant covers the solid surface. These surface aggregates form beyond a critical concentration below the CMC, and is known as critical hemimicellar concentration (HMC); hemimicellization was first hypothesized by Gaudin and Fuerstenau (Gaudin and Fuerstenau, 1955).

Kinetics and equilibrium adsorption of surfactants at the solid-liquid interface depend on the nature of surfactants and the nature of the solid surface (Zhang and Somasundaran, 2006). Three types of interactions are generally involved in the adsorption of a surfactant at solid/liquid interface. The attractive or repulsive interaction between the hydrophilic group and the surface, the attractive interaction between the hydrophobic group and the surface and the lateral interactions that occur between adsorbed surfactants. For surfactants, the most important interactions between the hydrophilic group and the surface are the electrostatic and hydrogen bonding (Paria and Khilar, 2004; Zhang and Somasundaran, 2006). Electrostatic interactions are most important for ionic surfactants. If the surfactant and the adsorbent are oppositely charged, the rate of adsorption is very fast and the equilibrium time is less. In the other hand, if surfactant and the adsorbent are similarly charged, repulsion forces take place and minor adsorption is resulted.

The adsorption isotherm of an ionic surfactant on an oppositely charged solid usually follows "Somasundaran–Fuerstenau" type. Somasundaran–Fuerstenau adsorption isotherm is a typical isotherm of a surfactant on a solid surface that can be subdivided into four regions (Somasundaran and Fuerstenau, 1966). In region I, adsorption obeys Henry's law, that is, adsorption increases linearly with concentration. Region II shows a sudden increase in adsorption, while region III shows a slower rate of increase in adsorption than region II. Region IV is the plateau region above the CMC. The explanations for the nature of adsorption curve in the first three regimes are well accepted. The sudden rise in adsorption in region II is due to formation of surface aggregate of the surfactant molecules on the solid surface. In Region III, the solid surface is electrically neutralized by the adsorbed surfactant ions, the electrostatic attraction is no longer operative and adsorption takes place due to lateral attraction alone with a reduced slope. However, in Region IV, the surfactant concentration reaches critical micelle concentration, the surfactant monomer activity becomes constant and any further increase in concentration contributes only to the micellization in solution and it does not change the adsorption density.

Although the adsorption of single surfactants at pure solid-liquid interface has been investigated intensively, there have been only a few studies of mixed systems, in spite of their great importance. Nevertheless, adsorption of surfactant mixtures to natural soils is even scarce. From the application point of view, adsorption from surfactant mixtures is of particular interest, since in most applications surfactants are used in combination with other surfactants. The obvious reason for this is that producing monodisperse surfactants is often too expensive, but in addition to this, many surfactants show synergistic behaviour together with other surfactants, making the use of multi-component systems favourable.

In many applications, surfactant mixtures in particular anionic-nonionic mixtures often give rise to enhanced overall performance over single component systems. For example, anionic-nonionic surfactant mixtures might show advantageous solubilisation behaviour, exhibiting cloud points higher than those of the single nonionic surfactant, along with Krafft points lower than those of the single anionic surfactant. Mixed surfactants could be employed over a wide range of temperature, salinity, and hardness conditions than the individual surfactants (Gu and Galera-Gomez, 1995; Al Ghamdi and Nasr-El-Din, 1997; Goell, 1999). Therefore, surfactant mixtures with superior properties are always required in a wide variety of practical applications. Consequently, one of the main challenges in adsorption studies is to extend the knowledge from fundamental studies on single surfactant systems to multi-component systems, thereby approaching the applied systems.

Recently, the adsorption of anionic-nonionic surfactant mixtures on natural soils was studied by Zhou and co-workers (Yu et al., 2007; Zhou and Zhu, 2007a&b). The study showed that the adsorption isotherm of TX100 from single surfactant solution was nonlinear and typical S-shape curves, reaching a plateau in adsorption amount at surfactant equilibrium concentration around the CMC. The addition of 10 mol% SDS to TX100 resulted in a 25% decrease in the maximum adsorption amount for TX100. Thus, the higher the mole fraction of SDS in mixed surfactant solutions, the greater the decrease in the maximum adsorption amount for TX100. These results showed that, when SDS was mixed together with TX100, the sorption of nonionic surfactant onto soil was severely restricted and a higher mole fraction of SDS in surfactant solution meant that a lower plateau adsorption can be reached with a smaller TX100 concentration in surfactant solution.

Zhou and co-workers findings provided the incentive for the present investigation, in which the role of mixing anionic surfactant with nonionic surfactants on adsorption is considered for local adsorbents. As the adsorption of surfactants onto different adsorbents diminishes their active concentration, it becomes economically important to reduce surfactant

adsorption. This is particularly vital to improve surfactant-facilitated transport of organic contaminants in SEAR operations as well as surfactant EOR for mature oil fields.

Generally, the most common method for the determination of the adsorption is the depletion method, where the change in surfactant concentration (depletion) after contact with adsorbents is measured and assumed to be adsorbed. The results from the adsorption experiment are generally expressed in the form of adsorption isotherms, where the amount adsorbed is plotted as a function of equilibrium concentrations. Adsorption isotherms are measured by keeping solution environment conditions, such as temperature, pH and ionic strength constant. In this study, the adsorption of TX100, SDS, and their mixtures by shale and sandstone substrates is investigated. The experimental results are fitted to Langmuir and Freundlich isotherms and the characteristic parameter of each model are obtained.

2. Materials

2.1 Surfactants

Polyethylene glycol tert-octylphenyl ether-Triton X100 (TX100) was supplied by Scharlau Chemie, Spain. It is a nonionic surfactant ($C_8H_{17}C_6H_4[OCH_2CH_2]_xOH$) with a CMC which spans between 0.13-0.2 g/L (0.2-0.31 mmol/L) (Zhou and Zhu, 2004; Zhou and Zhu, 2007a&b; Zhu and Feng, 2003; Rodriguez-Cruz et al., 2005; Zhao and Zhu, 2006). It has an average of 9.5 ethylene oxide units per molecule with an average molecular weight of 646.37g/mol. Sodium Dodecylsulfate-SDS ($C_{12}H_{24}NaSO_4$) is an anionic surfactant with a CMC which spans between 1-2.4 g/L (3.32-8.4 mmol/L) (Zhou and Zhu, 2004; Zhu and Feng, 2003; Rodriguez-Cruz et al., 2005). SDS molecular weight is 288.4 g/mol and was supplied by Merck with a high grade of purity (99%). All chemicals were used as received without further purification.

2.2 Adsorbents

Shale Samples were collected from an outcrop of a local shale formation (Batu Arang, Selangor, Malaysia). Sandstone Samples were collected from an outcrop of a local sandstone formation (Bukit Bangkong, Kuala Rompin, Pahang). Samples were disintegrated into small pieces by jaw crusher and then ground using rock pulveriser (Fritsch, Germany). Samples were air dried for 24hrs followed by oven drying at 105°C for 24hrs. Dried rock samples were sieved to obtain particles less than 2mm and larger than 1mm in all experiments.

3. Methods

3.1 Preparation of Surfactant Solutions

The surfactant solutions were prepared in a standard 1000mL volumetric flasks, surfactants were weighed on mass basis and emptied into the volumetric flask and then double distilled water was used to complete the solution to the final weight (1Kg). After the preparation of the stock solution, it was diluted to obtain desired concentration. TX100 and SDS solutions were prepared at concentrations ranged from 0.0025wt% to 1wt% corresponding to molar concentrations of 0.039-15.47mM for TX100 and 0.0867-34.68mM for SDS. Mixed surfactant solutions were prepared by mixing SDS and TX100 solutions of the same weight concentrations with different mass ratios of 2:1, 1:1, and 1:2 SDS:TX100. This results in a mole fraction of SDS in the total mixtures of 0.82, 0.69 and 0.53, respectively. Mixed surfactant solutions were allowed to equilibrate for at least 5hrs before any measurements were made.

3.2 Surface Tension Measurements

The surface tension technique was applied to determine the CMC in various combinations of shale/sandstone and/or surfactant systems. The surface tension measurements were carried out with Krüss tensiometer (Krüss GmbH, Hamburg, Instrument Nr, K6) using a platinum-iridium ring at constant temperature ($25\pm 1^\circ C$).

3.3 CMC Measurements

The CMC values were obtained through a conventional plot of the surface tension versus the surfactant concentration. The CMC concentration corresponds to the point where the surfactant first shows the lowest surface tension. The surface tension remains relatively constant after this point.

3.4 Adsorption Experiments

Adsorption isotherms were determined by batch equilibrium adsorption procedures. 10g of shale/sandstone are added to a set of 60mL surfactant solutions (surfactant initial concentrations spans from 0.0025wt% to 1wt%) in a 100mL glass vials and allowed to equilibrate at $25\pm 1^\circ C$. Preliminary experiments indicated that within the first 16hrs- almost all adsorption takes place. 24hrs contact time at rest was long enough for equilibrium and complete separation to be obtained. Surfactant sample aliquots are taken for surfactant concentration determination before and after adsorption. All experiments were conducted with 3 replicates at $25\pm 1^\circ C$. To determine the maximum sorption of surfactants into shale/sandstone, a surface tension method was used. The amount of surfactant adsorbed and/or abstracted was computed from the difference of surface tension values before and after adsorption, and means of three replicates were used. The amount of solute adsorbed, Γ , is expressed in g/Kg and was determined as:

$$\Gamma = (C_i - C_e) \frac{V}{W} \quad [1]$$

Where C_i and C_e are the initial and equilibrium liquid phase concentrations of surfactant solutions (g/L), respectively; V is the volume of the surfactant solution (L); and W is the mass of the dry adsorbents (Kg).

3.5 Adsorption Models

An adsorption model is required to predict the loading on the adsorption matrix at a certain concentration of the component. The two general adsorption isotherms that can be used to describe the equilibrium adsorption relation are the well-known monolayer Langmuir and empirical Freundlich model.

3.5.1 Langmuir Isotherm

The Langmuir adsorption isotherm has been widely applied to many adsorption processes. It has produced good agreement with a wide variety of experimental data for adsorption of a solute from a liquid solution. A basic assumption of the Langmuir theory is that the sorption takes place at specific homogeneous sites in the adsorbent. Moreover, when a site is occupied by a solute, no further adsorption can take place at that site.

The rate of adsorption to the surface should be proportional to a driving force and area. The driving force is the concentration in the solution, and the area is the amount of bare surface. The Langmuir equation relates solid-phase adsorbate concentration Γ , the uptake, to the equilibrium liquid concentration at a fixed temperature. The equation was developed by Irving Langmuir in 1916 (Langmuir, 1916). The Langmuir equation is expressed as:

$$\Gamma = \frac{\Gamma_{\max} K_L C_e}{1 + K_L C_e} \quad [2]$$

Where Γ = amount adsorbed (g/Kg); Γ_{\max} = maximum amount adsorbed (g/Kg); K_L = Langmuir equilibrium constant (L/g); C_e = equilibrium aqueous concentration (g/L).

Equation [2] can be rewritten in the well known linearized expression of the Langmuir model as follows:

$$\frac{1}{\Gamma} = \frac{1}{C_e K_L \Gamma_{\max}} + \frac{1}{\Gamma_{\max}} \quad [3]$$

A plot of $1/\Gamma$ versus $1/C_e$ yields a slope = $1/(\Gamma_{\max} K_L)$ and an intercept = $1/\Gamma_{\max}$.

3.5.2 Freundlich Isotherm

Freundlich (Freundlich, 1906) developed an empirical equation to describe the adsorption process. His development was based on the assumption that the adsorbent has a heterogeneous surface composed of different classes of adsorption sites. Freundlich demonstrated that the ratio of the amount of solute adsorbed onto a given mass of an adsorbent to the concentration of the solute in the solution was not constant at different solution concentrations. This isotherm does not predict any saturation of the adsorbent by the adsorbate; thus, infinite surface coverage is predicted mathematically, indicating multilayer sorption of the surface (Rawajfih and Nsour, 2006). The Freundlich isotherm assumes that if the concentration of the solute in the solution at equilibrium, C_e , is raised to the power $1/n$, the amount of solute adsorbed being Γ , the $C_e^{1/n}/\Gamma$ is constant at a given temperature:

$$\Gamma = K_F C_e^{1/n} \quad [4]$$

Where Γ = amount adsorbed (g/Kg); K_F = Freundlich equilibrium constant (L/g); C_e = equilibrium aqueous concentration (g/L); n =Freundlich constant.

Freundlich isotherm has been derived by assuming an exponentially decaying sorption site energy distribution. This equation can be rearranged in the linear form by taking the logarithm of both sides as:

$$\log \Gamma = \log K_F + \frac{1}{n} \log C_e \quad [5]$$

K_F and $1/n$ are the Freundlich constants related to sorption capacity and sorption intensity, respectively. The intercept and the slope of the linear plot of $\log \Gamma$ versus $\log C_e$ at a given experimental conditions provide the values of K_F and $1/n$, respectively.

4. Results and Discussion

4.1 Surfactant Aqueous Solutions

The CMC of pure surfactants and mixtures were obtained from surface tensions vs. concentration plot (Figure 1). The CMC of SDS is obtained at 0.1wt% (3.468 mM/L or 1g/L) while the CMC value of TX100 achieved is about 0.02

wt%, much lower than that obtained for SDS. These values are comparable well with values reported in previous published studies (Zhou and Zhu, 2004; Zhou and Zhu, 2007a&b; Zhu and Feng, 2003).

As seen in Figure 1, the CMC values for the mixtures were not lower than that obtained by TX100. This is in agreement with previous studies (Janczuk et al., 1995; Paria et al., 2003; Mata, 2006). The CMCs of mixed surfactants are lower than that of sole SDS and very close to that of pure TX100. In this respect, our experimental results for fresh solutions agrees with those observed by Mata (2006) who found a decrease in the CMC of mixtures with increase in mole fraction of TX100, however, the CMC of the mixed system at any composition could not be reduced than that of pure TX100.

4.2 Adsorption to Shale

Adsorption of surfactants onto shale at a particular surfactant dose can be determined by comparing surface tension measurements in aqueous and in shale/aqueous systems. As illustrated in Figure 2, Surface tensions for SDS have not been changed before and after equilibration with shale. However, surface tensions for TX100 were increased significantly after equilibration with shale. This is a result of less surfactant concentrations in solutions after equilibration with shale. This significant loss of TX100 monomers is attributed to their adsorption to organic matter/clay minerals in shale.

For instance, in a shale/aqueous system consisting of 10g of shale, 60mL of surfactant aqueous solution, the minimum amount of TX100 required for the aqueous-phase CMC to be attained is 1.5wt%. However, TX100 attain CMC in aqueous phase at much lower concentrations, i.e., 0.02wt%. Thus, the mass of TX100 that must be added before the aqueous-phase CMC is attained in a shale/aqueous system is much greater than that in an aqueous system without shale.

Generally, micelles do not appear to adsorb onto soil, and the amount of surfactant that is adsorbed thus plateaus at a maximum value at the aqueous-phase CMC. At the CMC values, the concentration of the bulk solutions will be saturated with surfactant monomers. As the fresh surfactant solution monomer reaches the CMC, it is assumed that surfactant/shale supernatant would reach the CMC at the same monomers indicating the same surface tension at both CMCs. Hence, the amount of surfactant adsorbed to shale can be calculated from difference between CMC obtained after equilibration with shale and the original CMC. The difference in CMCs as determined from surface tension curves was found to be 0.13 wt% (0.15-0.02). This concentration can be normalized to shale mass to yield g-TX100 to Kg-shale, i.e., 7.8g-TX100/Kg-shale. Similar values have been reported in literature for natural soil (Zhou and Zhu, 2007a; Zheng and Obbard, 2002).

It is obvious from Figure 2 that SDS-TX100 mixtures at all SDS molar fractions do improve behaviour of the nonionic surfactant. All CMCs of SDS-TX100 are similar to that of pure SDS at 0.1wt% and lower than that of pure TX100 (0.15wt%). Hence, the maximum adsorption for mixtures ($\Delta\text{CMC} = 0.1 - 0.02 = 0.08\text{wt}\%$) are lower than that of pure TX100 ($\Delta\text{CMC} = 0.15 - 0.02 = 0.13\text{wt}\%$), approximately around 39% less. Accordingly, it can be said that the presence of SDS (at molar ratios used in this work) did reduce adsorption of TX100 to shale. This is in agreement with the observation made by other researchers (Yu et al., 2007; Zhou and Zhu, 2007a).

4.3 Adsorption to Sandstone

Surface tension trend for TX100 was also increased after equilibration with sandstone (Figure 3). However, TX100 sorption to sandstone was much lower than in case of shale. The difference in CMCs obtained for sandstone case is 0.03 wt% (0.05-0.02) which is much lower than 0.13wt% obtained in case of shale. This concentration when normalized to sandstone mass yield a value of 1.8g-TX100 to Kg-sandstone. TX100-SDS mixtures at all SDS molar fractions have similar adsorption capacities as pure TX100 (Figure 3).

4.4 Sub-CMC Adsorption Isotherms

The amount of surfactant adsorbed at sub-CMC doses can be estimated from the difference in dose necessary to attain a specified value of surface tension. Data were fitted to Langmuir and Freundlich models and applicability of the isotherm equations was compared by judging the correlation coefficients, R^2 . The best-fitted parameters together with regression coefficients for the four-surfactant systems and both adsorbents are given in Tables 1-4. Tables 1 and 2 show Freundlich-fitted equations, constants, and correlation coefficients (R^2) for the four-surfactant systems adsorbed to shale and sandstone, respectively. Similarly, Tables 3 and 4 provide the Langmuir-fitted equations, constants and correlation coefficients (R^2) for the four-surfactant systems adsorbed to shale and sandstone, respectively.

The data obtained from the adsorption of the four surfactant systems were fitted to the Freundlich model by plotting $\log \Gamma$ versus $\log C_e$. The linear plot obtained has a slope that has the value of $1/n$ and y intercept that is $\log K_F$. K_F is a constant in the Freundlich model which is related to the bonding energy. K_F can be defined as an adsorption or distribution coefficient and represents the quantity of adsorbate adsorbed onto adsorbents for a unit equilibrium concentration. As seen in Tables 1 and 2, the K_F values of TX100 on both shale and sandstone are the highest, while the

TX100-SDS mixtures are more or less identical. Furthermore, K_F values are higher for the four-surfactant systems in case of shale as compared to sandstone. This result expressed the high adsorption capacity of shale for the surfactant systems in comparison to sandstone.

The slope $1/n$, ranging between (0.33-1.18), is a measure for the adsorption intensity or surface heterogeneity, becoming more heterogeneous as its value gets closer to zero. A value for $1/n$ below one indicates a normal Freundlich/Langmuir isotherm while $1/n$ above one is indicative of cooperative adsorption. Furthermore, a relatively slight slope (and hence a high value of n) indicates that the adsorption is good over the entire range of concentrations studied, while a steep slope (and hence small n) means that adsorption is good at high concentration but is much poorer at lower concentrations. Accordingly, the result in Tables 1 and 2 allow to conclude that TX100 adsorption to shale involves cooperative adsorption ($1/n=1.18$).

Adsorption data fitting to Langmuir isotherm was achieved by plotting $1/\Gamma$ versus $1/C_e$ which yields a slope = $1/(\Gamma_{\max}K_L)$ and an intercept = $1/\Gamma_{\max}$. Langmuir isotherm allows determining the adsorption grade by means of its K_L and Γ_{\max} parameters. K_L is homologous to K_F in Freundlich isotherm and indicates the adsorption capacity of the adsorbent to the respective solutes: the greater the K_F/K_L the greater the Γ value. Similar to the Freundlich model, K_L values of TX100 on both adsorbents are by far higher than those of the binary mixtures of SDS-TX100 and again they are higher for the four surfactant systems in case of shale as compared to sandstone (Tables 3 and 4). The relation of greater to lower K_F/K_L value is: shale > sandstone and TX100 > TX100-SDS mixtures.

Langmuir constant, Γ_{\max} , represents the maximum amount of the surfactant adsorbed. As seen from Table 3 and 4, Γ_{\max} values are higher for the shale than for the sandstone indicating higher capacities of shale to different surfactant systems. However, as it is the case with 'n' values of the Freundlich model, the Γ_{\max} values of the four systems are more or less identical.

According to the values of the correlation coefficients, R^2 , it can be concluded that the Freundlich model represents the adsorption data reasonably well. Correlation coefficients range between 0.978-0.997 for Freundlich-fitting while they range between 0.910-0.997 for the Langmuir-fitting. However, a better criterion for the assessment of experimental isotherm data is a parameter known as normalized percent deviation (Ayranci and Duman, 2007) which is defined by the following equation:

$$P = \frac{100}{N} \sum_{i=1}^N \frac{|\Gamma_{(pred)} - \Gamma_{(exp)}|}{\Gamma_{(exp)}} \quad [6]$$

Where $\Gamma_{(exp)}$ is the experimental Γ at any C_e and $\Gamma_{(pred)}$ the corresponding predicted Γ according to the equation under study with the best-fitted parameters and N is the number of observations. It is clear from this equation that the lower the P value, the fit is considered to be excellent (Ayranci and Duman, 2007). The calculated P values for the Freundlich model are seen to be much lower than those for Langmuir model (Table 5). Therefore, it can be concluded that the Freundlich model represents the experimental isotherm data of surfactants at 25 °C better than the Langmuir model.

In light of the results obtained with shale and sandstone, it seems that adsorption of TX100 in a natural system depend largely on the adsorbent properties including chemical (mineralogical and organic) composition. The low affinity of SDS to both adsorbents is attributed mainly to repulsion forces between adsorbents and surfactants. This is because soils in aqueous solutions often obtain negative charges on the surface thus; maintain repulsion with anionic surfactants.

Adsorption of a nonionic surfactant such as TX100 is commonly thought to involve hydrogen bonding. Hydrogen bonding (also known as hydrophobic bonding) is weaker than electrostatic interactions. Hydrophobic bonding can also be important for adsorption on solids that possess a fully or partially hydrophobic surface. In this case, surfactant molecules can adsorb flat on the hydrophobic sites on the solid.

Another probably influential factor is the clay minerals and organic matter which are abundant in shale compared to sandstone. Surfactant adsorption by soils/sediments depends on the type of surfactant and the soil properties. In this sense, the results of different studies addressing the adsorption of anionic and nonionic surfactants by soils/sediments with different compositions have revealed the relative importance of soil/sediment organic matter and clay minerals on the adsorption of anionic and nonionic surfactants. Furthermore, Nonionic surfactants were found to adsorb extensively to pure clay minerals, however, adsorbed amounts of anionic surfactant were significantly lower (Rodriguez-Cruz et al., 2005).

More importantly, surfactant adsorption is related to the chemical potential of the surfactant molecules (monomers) in solution. Under mixed micellization conditions, the chemical potential of monomers will be lower than that for the single surfactant system and this in turn can reduce adsorption at the solid-liquid interface. Beyond the CMC, the aqueous monomer concentration will not increase with any further addition of surfactant since the additional surfactant

will form micelles. Adsorption of TX100 surfactant as well as SDS-TX100 mixtures to shale/sandstone is limited by their CMCs and reaches a plateau at their CMCs. The CMC-limited adsorption of surfactants reflects the significant effects in reducing the CMC of surfactant systems; in other words, a reduction in their CMCs reduces their adsorption.

5. Conclusion

The adsorption of surfactant onto shale/sandstone results in the dose to achieve micellization being much greater than that for an aqueous system without shale/sandstone. From this study, it can be concluded that nonionic surfactants tended to be strongly adsorbed to shale compared to sandstone. The possible sorption mechanism for nonionic surfactant is the adsorption by hydrogen bonding and it strongly seems to show correlation with clay minerals. Anionic surfactant, SDS, on the other hand showed minor adsorption capacities to both shale and sandstone. It has been shown that the maximum adsorption amounts of SDS on both shale and sandstone were lower compared with that of TX100. This was attributed to repulsion forces between the negatively charged SDS and the negatively charged shale/sandstone.

The results emphasise that for adsorption from surfactant mixtures, it is necessary to take into account the changes in the CMC with changes in composition. For adsorption from mixtures of surfactants with similar properties, i.e., CMC is same as ideal mixing; the adsorbed amount from the mixtures will fall between that of the individual surfactants. In contrast, adsorption from mixtures of surfactants that exhibit synergism in CMC (CMC is lower than ideal mixing) may show even lower adsorption tendencies. This is related to the lower chemical potential of the surfactant monomers in solution.

References

- Al-Ghamdi, A.M., & Nasr-El-Din, H.A. (1997). Effect of Oilfield Chemicals on the Cloud Point of Nonionic Surfactants. *Colloids Surf. A*, 125, 5-18.
- Ayranci, E., & Duman, O. (2007). Removal of Anionic Surfactants from Aqueous Solutions by Adsorption onto High Area Activated Carbon Cloth Studied by In Situ UV Spectroscopy. *J. Hazard. Mater.*, 148, 75–82.
- Curbelo, F.D.S., Santanna, V.C., Barros Neto, E.L., Dutra Jr., T.V., Castro Dantas, T.N., Dantas Neto, A.A., & Garnica, A.I.C. (2007). Adsorption of Nonionic Surfactants in Sandstones. *Colloids Surf. A*, 293, 1–4.
- Edwards, D.A., Adeel, Z., & Luthy, R.G. (1994). Distribution of Nonionic Surfactant and Phenanthrene in Sediment/Aqueous System. *Environ. Sci. Technol.*, 28, 1550-1560.
- Freundlich, H.M.F. (1906). Über die adsorption in lösungen. *Z. Phys. Chem.*, 57 A, 385–470.
- Gaudin, A.M., & Fuerstenau, D.W. (1955). Quartz Flotation with Cationic Collectors. *Trans. AIME*, 202, 958 – 962.
- Goell, S.K. (1999). Critical Phenomena in the Clouding Behavior of Nonionic Surfactants Induced by Additives. *J. Colloid Interface Sci.*, 212, 604-606.
- Gu, T., & Galera-Gomez, P.A. (1995). Clouding of Triton X-114: The Effect of Added Electrolytes on the Cloud Point of Triton X-114 in the Presence of Ionic Surfactants. *Colloids Surf. A*, 104, 307-312.
- Janczuk, B., Bruque, J.M., Gonzalez-Martin, M.L., & Doradu-Calasanz, C. (1995). The Properties of Mixtures of Inoic and Nonionic Surfactants in Water at the Water/Air Interface. *Colloids Surf.*, A, 104, 157-163.
- Langmuir, I. (1916). The Constitution & Fundamental Properties of Solids & Liquids. *J. Am. Chem. Soci.*, 38(11), 2221-2295.
- Mata, J.P. (2006). Hydrodynamic and Clouding Behaviour of Triton X-100 + SDS Mixed Micellar Systems in the Presence of Sodium Chloride. *J. Dispersion Sci. Technol.*, 27, 49-54.
- Paria, S., & Khilar, K.C. (2004). A review on Experimental Studies of Surfactant Adsorption at the Hydrophilic Solid-Water Interface. *Adv. Colloid Interface Sci.*, 110, 75-95.
- Paria, S., Manohar, C., & Khilar, K.C. (2003). Experimental Studies on Adsorption of Surfactants onto Cellulosic Surface and Its Relevance to Detergency. *J. Instit. Eng., Singapore*, 43(2), 34-44.
- Rawajfih, Z., & Nsour, N. (2006). Characteristics of Phenol and Chlorinated Phenols Sorption onto Surfactant-Modified Bentonite. *J. Colloid Interface Sci.*, 298, 39–49.
- Rodriguez-Cruz, M.S., Sanchez-Martin, M.J., & Sanchez-Camazano, M. (2005). A Comparative Study of Adsorption of an Anionic and a Nonionic Surfactant by Soils Based on Physicochemical and Mineralogical Properties of Soils. *Chemosphere*, 61, 56-64.
- Somasundaran, P., & Fuerstenau, D.W. (1966). Mechanisms of Alkyl Sulfonate Adsorption at the Alumina-Water Interface. *J. Phy. Chem.* 70, 90 – 96.
- Sun, S., Inskeep, W.P., & Boyd, S.A. (1995). Sorption of Nonionic Organic Compounds in Soil-Water Systems Containing a Micelle-Forming Surfactant. *Environ. Sci. Technol.*, 29, 903–913.

Yu, H., L. Zhu, & Zhou, W. (2007). Enhanced Desorption and Biodegradation of Phenanthrene in Soil-Water Systems with the Presence of Anionic/Nonionic Mixed Surfactant. *J. Hazard. Mater.*, 142, 354-361.

Zhang, R., & Somasundaran, P. (2006). Advances in Adsorption of Surfactant and their Mixtures at Solid/Solution interfaces. *Adv. Colloid Interface Sci.*, 123-126, 213-229.

Zhao, B., & Zhu, L. (2006). Solubilization of DNAPLs by Mixed Surfactant, Synergism and Solubilization Capacity. *J. Hazard. Mater.*, B136, 513-519.

Zheng, Z., & Obbard, J.P. (2002). Evaluation of an Elevated Nonionic Surfactant Critical Micelle Concentration in a Soil/Aqueous System. *Water Res.*, 36, 2667-2672.

Zhou, W., & Zhu, L. (2007b). Efficiency of Surfactant-Enhanced Desorption for Contaminated Soils Depending on the Component Characteristic of Soil-Surfactant-PAHs System. *Environ. Pollut.*, 147, 66-73.

Zhou, W., & Zhu, L. (2004). Solubilization of Pyrene by Anionic-Nonionic Mixed Surfactants. *J. Hazard. Mater.*, B109, 213-220.

Zhou, W., & Zhu, L. (2007a). Enhanced Desorption of Phenanthrene from Contaminated Soil Using Anionic/Nonionic Mixed Surfactant. *Environ. Pollut.*, 147, 350-357.

Zhu, L., & Feng, S. (2003). Synergistic Solubilization of Polycyclic Aromatic Hydrocarbons by Mixed Anionic-Nonionic Surfactants. *Chemosphere*, 53, 459-467.

Table 1. Parameters of Freundlich models fitted to shale data

Shale	Surfactant	Fitted Freundlich Equation	R_F^2	n	K_F [L/Kg]
	TX100	$\text{Log}[\Gamma]=0.3969 \times \text{Log } C_e + 1.1758$	0.9966	2.52	14.99
	SDS-TX100 [1:2 by wt]	$\text{Log}[\Gamma]=0.3839 \times \text{Log } C_e + 0.7703$	0.9878	2.60	5.89
	SDS-TX100 [1:1 by wt]	$\text{Log}[\Gamma]=0.5496 \times \text{Log } C_e + 0.9909$	0.9934	1.82	9.79
	SDS-TX100 [2:1 by wt]	$\text{Log}[\Gamma]=0.4132 \times \text{Log } C_e + 0.8641$	0.9972	2.42	7.31

Table 2. Parameters for Freundlich model fitted to sandstone data

Sandstone	Surfactant	Fitted Freundlich Equation	R_F^2	n	K_F [L/Kg]
	TX100	$\text{Log}[\Gamma]=0.6682 \times \text{Log } C_e + 0.7285$	0.9901	1.50	5.35
	SDS-TX100 [1:2 by wt]	$\text{Log}[\Gamma]=0.7465 \times \text{Log } C_e + 0.4325$	0.9899	1.34	2.71
	SDS-TX100 [1:1 by wt]	$\text{Log}[\Gamma]=0.7369 \times \text{Log } C_e + 0.3476$	0.9777	1.36	2.23
	SDS-TX100 [2:1 by wt]	$\text{Log}[\Gamma]=0.6953 \times \text{Log } C_e + 0.3301$	0.9921	1.44	2.14

Table 3. Parameters for Langmuir model fitted to shale data

Shale	Surfactant	Fitted Langmuir Equation	R_L^2	Γ_{\max} [g/Kg]	K_L [L/g]
	TX100	$1/\Gamma=0.0009 \times 1/C_e + 0.2762$	0.9102	3.62	306.89
	SDS-TX100 [1:2 by wt]	$1/\Gamma=0.0051 \times 1/C_e + 0.4225$	0.9652	2.37	82.84
	SDS-TX100 [1:1 by wt]	$1/\Gamma=0.0086 \times 1/C_e + 0.356$	0.9559	2.81	41.40
	SDS-TX100 [2:1 by wt]	$1/\Gamma=0.0042 \times 1/C_e + 0.3983$	0.9498	2.51	94.83

Table 4. Parameters for Langmuir model fitted to sandstone data

Sandstone	Surfactant	Fitted Langmuir Equation	R_L^2	Γ_{\max} [g/Kg]	K_L [L/g]
	TX100	$1/\Gamma=0.0186 \times 1/C_e + 1.8183$	0.9727	0.55	97.76
	SDS-TX100 [1:2 by wt]	$1/\Gamma=0.1002 \times 1/C_e + 1.2657$	0.9904	0.79	12.63
	SDS-TX100 [1:1 by wt]	$1/\Gamma=0.1151 \times 1/C_e + 1.7052$	0.9803	0.59	14.81
	SDS-TX100 [2:1 by wt]	$1/\Gamma=0.0887 \times 1/C_e + 1.8708$	0.996	0.53	21.09

Table 5. Estimated 'P' Values

Surfactant	Estimated 'P' Values			
	Freundlich		Langmuir	
	Shale	Sandstone	Shale	Sandstone
TX100	3	7	19	23
SDS-TX100 [1:2 by wt]	4	8	9	9
SDS-TX100 [1:1 by wt]	4	9	13	13
SDS-TX100 [2:1 by wt]	2	6	13	9

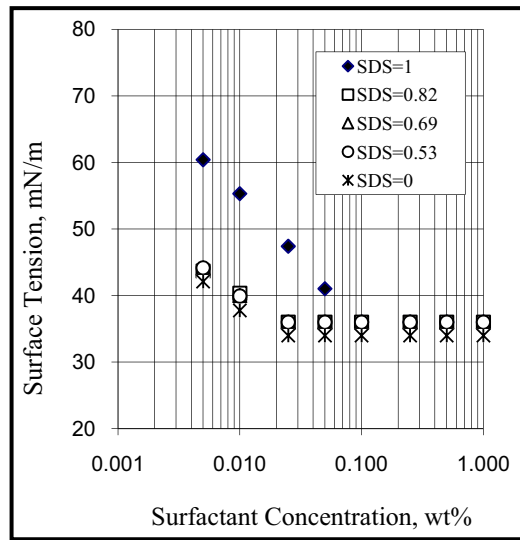


Figure 1. CMCs of surfactants systems in Aqueous Solutions

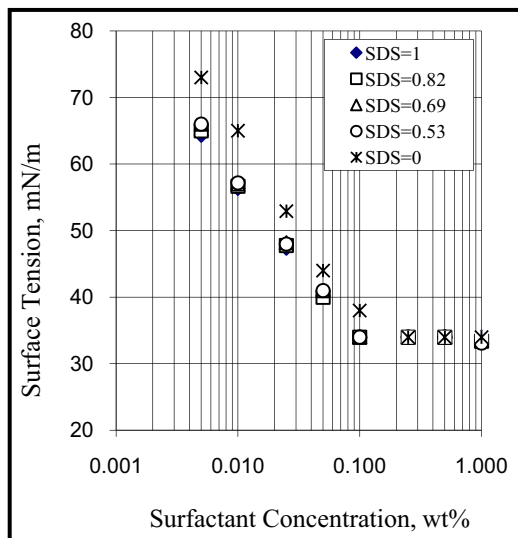


Figure 2. CMCs of surfactant systems after equilibration with shale

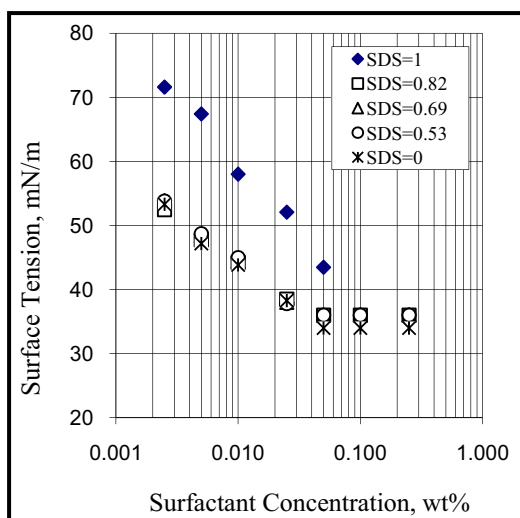


Figure 3. CMCs of surfactant systems after equilibration with sandstone



Effect of Truncation on the Performance of Busemann Inlet

Zhi Zhao & Wenyan Song
School of Power and Energy
Northwestern Polytechnical University
Xi'an 710072, China
E-mail: zhaozhinwpu@gmail.com

Abstract

The aerodynamic design of hypersonic inlets is a critical issue for the overall performance of an air-breathing propulsion system. The design procedure of basic Busemann inlet is presented. Five truncated Busemann inlets with a contraction ratio of 9 are designed for Mach 6. These inlets have different truncation angles range from 0° to 6°. Numerical simulations have been performed to investigate the effects of truncation on inlet performance. The results of numerical simulations confirmed the good performance of the Busemann inlet. The truncation angle of 4° is preferred.

Keywords: Hypersonic inlet, Truncation, Busemann inlet, Contraction ratio

1. Introduction

The aerodynamic design of hypersonic inlets is a critical issue for the overall performance of an air-breathing propulsion system. The inlet of a scramjet engine serves to capture and compress the engine air flow. The inlet must compress the flow with minimal skin friction, heat transfer, and shock loss, while providing uniform flow to the combustor. During the past, many types of hypersonic inlets, such as two-dimensional inlets, axisymmetric inlets and sidewall-compression inlets, have been evaluated (Billig, F. S., 2003).

Recently there has been a renaissance of the inward turning inlets for hypersonic air-breathing propulsion (Adam Siebenhaar, 2006; Bulman, M.J., 2006). The two-dimensional inlets compress the flow only in one direction, while the inward turning inlets have three-dimensional compression surface. Inward turning inlets derived from efficient compression flowfield offer unique performance. The potential benefits include improved flowpath performance, greater structural efficiency, and great flexibility in vehicle configuration development. Due to the highly integrated nature of hypersonic vehicles, the flowpath configuration strongly influences the overall vehicle configuration.

Previous work has shown that axisymmetric Busemann and streamtraced Busemann inlets are good candidates for hypersonic air-breathing vehicles. Billig (Billig, F. S., 1995) described the scramjet missile concept at APL/JHU between 1962 and 1978, which was based on tracing streamlines through a Busemann flowfield. Van Wie (Van Wie, D M, 1992) and Billig (Billig, F. S., 1999) presented the sample Busemann inlet design.

2. Busemann Inlet Design Procedure

As showed in Figure 1, the Busemann inlet is an axisymmetric, internal contraction inlet which has very low inviscid losses as well as a small ratio of flow cross-section area to wetted surface area. The Busemann inlet flowfield is an inviscid inward turning axisymmetric flowfield that terminates in a conical shock wave. At the design Mach number, the compression upstream of the conical shock wave is isentropic and the flow down-stream is uniform. The conical shock wave is the only entropy producing feature of inviscid design. The resulting inviscid compression efficiency is remarkably higher than other classes of inlets. This type of flowfield is well suited for scramjet engine inlets.

The flowfield of the Busemann inlet between the freestream and the conical shock wave is conical symmetric and irrotational. So the Taylor-Maccoll equation for the external flowfield past a cone can be used here. In spherical coordinate system, the Taylor-Maccoll equation for a calorically perfect gas can be written as follows:

$$v_{\theta} \left(v_r \frac{dv_r}{d\theta} + v_{\theta} \frac{dv_{\theta}}{d\theta} \right) - a^2 \left(\frac{dv_{\theta}}{d\theta} + 2v_r + v_{\theta} \cot \theta \right) = 0 \quad (1)$$

$$v_{\theta} - \frac{dv_r}{d\theta} = 0 \quad (2)$$

The solution of equation (1) and (2) is started from the downstream shock, because of a singularity at the upstream Mach wave. In the numerical solution, the post shock Mach number M_3 and the shock angle θ_s are specified. The parameters upstream the conical shock wave can be solved from relations across oblique shock wave. Then the flowfield inside the inlet can be calculated. The Taylor-Maccoll equation is then numerically integrated using the Runge-Kutta algorithms. Numerical integration is then performed in the upstream direction until the freestream condition is reached. Also, the streamline integration can be terminated at some angle, formed by the freestream vector and the velocity vector, which is called truncation angle.

3. Effects of Truncation Angle

The relative large length and corresponding heavy weight of the basic Busemann inlets prevent it from realistic application. An efficient approach is truncation of the leading edge (Billig, F. S., 1999). Therefore in this study, the effects of truncation angle on inlet performance were examined. Numerical simulations have been performed to evaluate the performance of these inlets. The effect of the truncation angle on kinetic energy efficiency, compressive efficiency and Mach number are analyzed. The viscous effects and the heat loss through the wall are taken into account.

Computational simulations for the axisymmetric inlets for both inviscid and viscous analysis were performed. The Reynolds averaged Navier-Stokes Equations were solved using the CFD code. This code utilizes finite volume methods. The Roe's second order flux difference splitting algorithm was used. The k- ϵ turbulence model with wall function was adopted. The structured grids had 600 grids axially, 200 points radially and were clustered near the wall to fulfill $y^+ \approx 10$. The freestream conditions correspond to flight Mach number 6, altitude of 25km. A wall temperature of 1000K was set for the isothermal cases.

A more equitable comparison should be to examine truncated inlets with same contraction ratio. Five truncated Busemann inlets with a contraction ratio of 9 are designed for Mach 6. Figure 2 shows geometry profiles of these inlets, and Mach number contours of inviscid flowfields. Because of symmetry, only half of the flowfield is displayed. These inlets have different truncation angles that range from 0° to 6° . Each inlet was generated in an iterative manner by holding the freestream Mach number and capture height constant while varying the throat Mach number, until a specified contraction ratio was obtained. For example, the Busemann inlet of with a contraction ratio of 10.6 at Mach 6 was truncated at 4° , resulting the CR=6, to reduce the size and weight of the inlet.

Figure 2 also shows that the conical shock wave are nearly perfectly cancelled at the shoulder for truncation angle less than 4° .

Figure 3 shows the length of inlet with different truncation angles, the length are normalized by the exit radius. As the truncation angle increases, the length of inlet decreases rapidly, by as much as 35% for the 4° truncation and 45% for the 6° truncation.

The effect of the truncation angle on exit pressure and Mach number is shown in figure 4. For inviscid case the exit pressure increases with the truncation angle. As the truncation angle is increased, an oblique shock is formed at the sharp leading edge. When viscous effects are included, the exit pressure is in the range of 85~90kPa, and the lowest exit pressure is reached at 3° inlet. The inviscid exit Mach number decrease slightly with the increasing truncation angle. For viscous cases, the Mach number is near 2.8.

Figure 5 shows the effect of the truncation angle on compression efficiency and kinetic energy efficiency. The highest kinetic energy efficiency is reached by the 0° inlet. This near perfect efficiency is a result of the inviscid flowfield having an ideal isentropic compression followed by a single conical shock. As the truncation angle is increased, the shock wave from the leading edge introduces a second source of total pressure loss, and drives down the kinetic energy efficiency. When viscous effects are included, the adiabatic kinetic energy efficiency shows a decrease of approximately 1.8% for all truncation angles. An additional 1.0% decrease occurs when heat loss to the wall ($T_w = 1000K$) is taken into account.

For the compression efficiency, it can be seen that the inviscid 0° inlet performs perfectly, while the larger truncation angles show a substantial loss in efficiency. When viscous effects are included, the compressive efficiencies remain constant near 96% for less than 4° .

Based on the trends shown in Fig. 3, 4, and 5, we have concluded that a truncation angle between 2° and 4° gives a good balance of inlet performance. The 2° inlet and 4° inlet are approximately 25% and 35% shorter than the 0° inlet. The truncation angle of 4° is preferred.

4. Conclusions

The results of numerical simulations confirmed the high performance of these inlets. As the truncation angle is increased, an oblique shock is formed at the sharp leading edge. And that shock distorts the flowfield, reduces the total pressure, and decreases the inlet's efficiency. The results show that the best truncation angle is 4° . Compared with basic Busemann inlet, the length of the 4° truncated inlet decrease about 35%, while performance still relative good.

References

- Adam Siebenhaar, Bogar T.J. (2006). The Impact of Round Combustors on TBCC Propulsion and Hypersonic Cruise Vehicles, AIAA 2006-7986.
- Billig, F. S. (1995). Supersonic Combustion Ramjet Missile, *Journal of Propulsion and Power*, 11, pp: 1139-1146.
- Billig, F. S., Baurle, R., and Tam, C. (1999). Design and Analysis of Streamline Traced Hypersonic Inlets, AIAA 99-4974.
- Billig, F. S., Jacobsen, L. (2003). Comparison of Planar and Axisymmetric Flowpaths for Hydrogen Fueled Space Access Vehicles, AIAA 2003-4407.
- Bulman, M.J., Adam Siebenhaar (2006). The Rebirth of Round Hypersonic Propulsion, AIAA 2006-5035.
- Van Wie, D M, Molder, S. (1992). Application of Busemann Inlet Designs for Flight at Hypersonic Speeds, AIAA 92-1210.

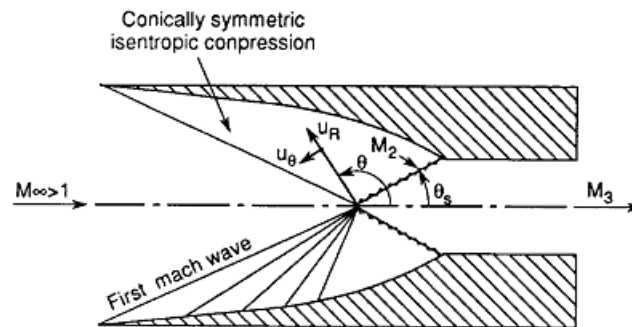


Figure 1. Flowfield of the Busemann Inlet (Van Wie, D M,1992)

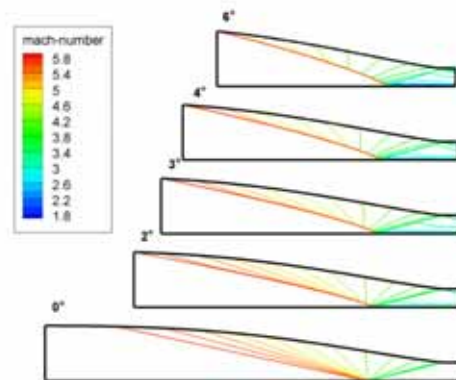


Figure 2. Busemann Inlet flowfield with Different Truncation Angles

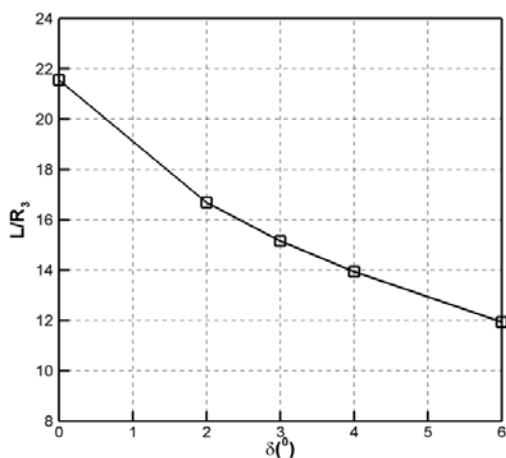


Figure 3. Length of Inlet with Different Truncate Angles

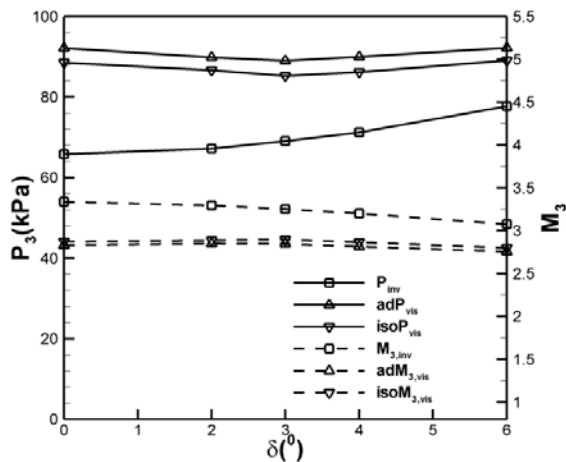


Figure 4. Effect of Truncation angle on pressure and Mach Number

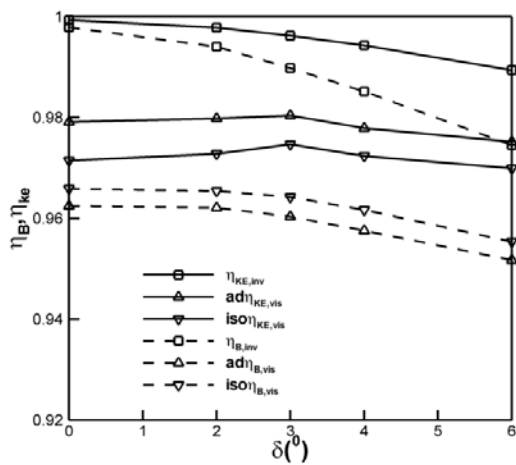


Figure 5. Effect of Truncation angle on compression efficiency and kinetic energy efficiency



The Structure and Optical Performance of InGaN/GaN Multiple Quantum Wells Grown on C-plane Sapphire

Xiaolei Peng, Pingjuan Niu, Xiaoyun Li, Ke Ding & Caifeng Wang

School of Information and Communication Engineering

Tianjin Polytechnic University

Tianjin 300160, China

Abstract

In this article, we study the structure and optical performance of penetration dislocation to the epitaxial GaN-base quantum well on C-plane sapphire. On the one hand, the penetration dislocation will make the interface of quantum wells disperse and largely fluctuate, and accordingly increase the localization effect of quantum wells. On the other hand, as the nonradiative recombination center, the penetration dislocation makes the radiation intensity of quantum wells to be reduced. The influence of penetration dislocation to the optical performance of InGaN/GaN multiple quantum wells decides the competition between both. In addition, the localization effect intensity of InGaN quantum wells possesses linear relation with the content of In in definite range of wavelength.

Keywords: Multiple quantum wells, Metal organic chemical vapor deposition, X ray, AFM

1. Introduction

In this article, we widely and deeply study the growth condition, structure character and radiation performance of InGaN/GaN structure. But because the crystal lattice mismatch of InN and GaN is big, the solid solubility is small and the epitaxial growth condition is very rigorous, so the quality of crystal is low. In the process of growth, the alloy of InGaN will produce the phenomenon of mutual separation, form the enrichment zone of In similar with quantum point, and bring the localization effect to the carrier (Yukio Narukawa, 1997, P. 1938 & P. 981). And the dislocation density on the epitaxial layer is high (10^8 - $10^{12}/\text{cm}^2$), and the GaN-base LED grows along the direction of [0001], and the spontaneous polarization effect and the piezoelectricity polarization effect exist in the nitride from this direction, and these factors are integrated together, which makes the problem more complex. So for the InGaN/GaN quantum wells, there are many problems to be further studied.

Differing with the epitaxies of other compound semiconductor system, III-V nitride can only be extended on other underlay with big mismatch and heterogeneity. The crystal lattice mismatch of GaN and sapphire is 14%, and the big mismatch inevitably induces two basic problems in the epitaxial films, the deficiency with high density and the large plane stress. We can adopt the two-step growth method, and the penetration dislocation density is 10^8 - $10^{12}/\text{cm}^2$, but surprisingly, though such high dislocation density exists, the exterior quantum efficiency of GaN-base LED has achieved 30% at present, and the life has achieved tens thousands hours, which is unimaginable in arsenide semiconductor and phosphide semiconductor and arouses human large interests, and people have deeply researched the dislocation character in the GaN epitaxial material.

2. Experiment

In the experiment, we select the common C-plane sapphire (0001) as the underlay, utilize the low-pressure MOCVD system to grow the LED structure with multiple quantum wells, and get the epitaxial films with different penetration dislocation densities through the change of growth condition. And we utilize temperature-change fluorescence, AFM, high resolution X ray diffraction and other measures to study the influences of penetration dislocation to the structure and optical performance of InGaN/GaN multiple quantum wells.

Before the epitaxial material grows, in hydrogen, the sapphire underlay is heated to 1050°C in ten minutes to eliminate the impurities on the surface of the underlay. The epitaxial growth adopts the two-step growth method, and first grow the GaN low temperature buffer layer with the depth of 30nm in 500 - 600°C , through 1000°C high temperature anneal, grow the LED structure under high temperature. The structure includes $4\mu\text{m}$ GaN:Si under 1050°C , InGaN/GaN multiple quantum wells with 5 periods grown under 800°C , and the p area grown on 1000°C . The GaN barrier of quantum wells is mixed into Si, and the adulteration concentration is $3 \times 10^{18} \text{ cm}^{-3}$, and InGaN is not adulterated. The structures of sample A and sample B are same in the experiment, and the difference is that both samples adopt different V/III ratio (the V/III ratio of sample A is 1280 and the V/III ratio of sample B is 640) to grow ten minutes in the initial

growth stage of high temperature GaN, then both samples adopt the V/III ratio of 1280 to complete the growth of high temperature GaN layer. In the growth process, we adopt the method of optical measure to implement original position supervision, and the detection light wavelength is 600nm to optimize the growth conditions.

In the measure of fluorescence, the blaze lamp-house adopts 7mW He-Cd laser with 325nm, the system adopts 0.5m homochromy meter and GaAs photoelectrical multiple increase detector, and the temperature range of temperature change measurement is 10K-300K. The spectrum curve eliminates the influence of F-B interference through Lorenz fitting, and we can get exact fluorescence peak value and integral intensity. High resolution X ray diffraction is measured by the Bede D1 system, and the wavelength of X ray is $\lambda=0.1541\text{nm}$. After measuring the fluorescence character of epitaxial structure, we utilize the method of plasma etch to eliminate the p area and multiple quantum wells area, and then put the samples in the phosphoric acid of 160°C to erode in 6 minutes, then study the dislocation density and character of epitaxial films, and the disposal detail is in P. Visconti's article (P. Visconti, 2002, P.229).

3. Result and discussion

The dislocation density of the etched sample is confirmed by AFM measurement. The measure range of AFM is $3\mu\text{m}\times 3\mu\text{m}$, and the image is seen in Figure 1. The maculas in the image are sunken holes eroded by the phosphors acid when the penetration dislocation is terminated on the surface of films (D. Kapolnek, 1995, P.1541). Through the measure of the density of maculas, we can calculate the penetration dislocation density of epitaxial material. From the Figure, we can see that the dislocation densities of etched sample A and sample B (they are signed as BLA and BLB respectively) are respectively $1.6\times 10^9\text{cm}^{-2}$ and $7\times 10^7\text{cm}^{-2}$, and comparing with BLA, the dislocation density of BLB is lower.

Because the dislocation density of BLA is high, so the etched surface is coarser than BLB. In the GaN epitaxial process of two-step growth method, though the quality of low temperature buffer layer crystal is bad, but it reduces the interface energy between GaN and sapphire, and offers an easy core-formation surface for the growth of high temperature GaN. The high temperature GaN first forms the GaN island on the buffer layer, and in the initial growth term, the GaN island continually grows up till encounter, and forms continual epitaxial films, and the growth is translated into the step-flow mode, and the GaN films are transformed into smooth films which surfaces have many steps. Strictly speaking, the epitaxial films of GaN is a sort of structure similar with mosaic, here, the penetration dislocation is composed by two parts, and the small part is in the middle of the island, and the big part is at the boundary encountered by islands. So the growth condition of high temperature GaN in the initial growth stage has decisive influences to the crystal quality of the whole epitaxial films. In this stage, most part dresses are released, and with the encounter and mature of islands, the dislocation produces at the boundary of islands. And the researches indicate the V/III ratio can effectively influence the size of island in the initial growth period of epitaxial material, and change the dislocation density in the materials (T. Yang, 2000, P.45 & S. Figge, 2000, P.262), and the experiment result approves that. Because the V/III ratio in the initial growth period of high temperature GaN is reasonable selected, the dislocation density of sample B reduces over one quantity level.

The swing curve (ω scan) of X ray diffraction includes symmetry scan and asymmetry scan, and it is a sort of method which is extensively used to study the deficiency of epitaxial films, and the peak width at half height of swing curve can reflect the density and character of dislocation. Figure 2 displays the X ray ω scan symmetry (002) and asymmetry (105) curves of BLA and BLB, and the fitting results of experiment data show that the half peak widths of symmetry (002) and asymmetry (105) scan of BLA are respectively 331.8arcsec and 356.3arcsec, and corresponding fitting data of BLB respectively are 244.8arcsec and 252.1arcsec. We can see that the swing curve of asymmetry scan is more obvious than the symmetry scan. According to B. Heying's researches (B. Heying, 1996, P.643), for the symmetry scan mode, only the whorl dislocation and mixed dislocation in the epitaxial layer would produce the expanding width with peak shape, and the pure edge dislocation has no influence to the expanding width with the peak shape, and for the asymmetry scan mode, all types of dislocation will produce the expanding width with peak shape. In addition, according to the researches of the fitting to the GaN (002) diffraction peak, we found its linearity was close to pure Gauss linearity, which indicates that the epitaxial films possess the structure of mosaic, and the expanding width of diffraction peak is mainly aroused by mutual function of crystal epitaxial warp, transverse size effect, and epitaxial films location press field. From the half peak widths of two samples, the half peak width of BLB is small, and it presents better crystal quality, which accords with the result of AFM measure.

In conclusion, the measures of AFM and X ray swing curve all prove the optimization of the V/III ratio in the initial high temperature GaN growth period can effectively reduce the dislocation density of epitaxial material and enhance the crystal quality and optical performance of material. Based on GaN epitaxial materials with different dislocation densities, we studied the influences of penetration dislocation to the structure and optical performance of InGaN quantum wells.

Generally speaking, the measure of X ray macle diffraction to the epitaxial single crystal film usually adopts two sorts of scan mode, i.e. the θ -2 θ scan mode that the sample circumrotates θ angle and the detector circumrotates 2 θ angle,

and the ω scan mode that the detector is fixed on the position of double diffraction angle and the sample only circumrotates about the diffraction angle, i.e. the swing curve. Simply speaking, the θ - 2θ scan is sensitive to the crystal lattice aberration of crystal at the vertical direction on the surface, and the ω scan is sensitive to the aberration of crystal at the parallel direction on the surface.

To further reveal the influence of penetration dislocation to the optical performance of multiple quantum wells, we utilize the temperature-change fluorescence to study two samples, and the temperature range of measure is 10k-300k.

Some researches indicate that GaN-based LED possess thus high radiation efficiency because the phenomenon of mutual separation will occur in InGaN alloy and the enrichment zone of In similar to quantum points forms, which will produce the localization effect to carriers and be propitious to the compound radiation of electron and cavity. So the radiation of InGaN quantum wells shows the localization characteristics. Because large numbers of enrichment In areas exists in quantum wells and the components of In in different enrichment In areas are different, so to electron and cavity, different potential energy minimums exist, which is seen in Figure 3. Under very low temperature, the heat excitation energy is small, and the radiation carrier can only be randomly distributed at different potential energy minimum values and form localization exciton, and the nonradiative compound and heat effect can be ignored.

Figure 3 shows fluorescence spectrums of sample A and B quantum wells under 10k of low temperature in the radiation area, and the radiation peak values displayed on two spectrum lines are about 2.68eV (463nm). On the spectral side with low energy, the extension of sample A is little higher than the extension of sample B, and the linearity forms of two spectrum lines are consistent. But on the side with high energy, the extension of sample A is much higher than sample B. InGaN quantum wells under low temperature is localization exciton compound radiation, the high energy end and the low energy end of spectrum line respectively reflect the compounds of radiated carriers on the weak localization energy level and on the strong localization energy, which indicates the penetration dislocation induces shallow localization energy level, and influences little the deep localization energy level. The localization effect of InGaN quantum wells mainly roots in two aspects, i.e. the mutual separation of InGaN alloy and the width fluctuation of quantum wells formed by the interface fluctuation of quantum wells. According the analysis of HRXRD, the quantum wells interface fluctuation of sample A is bigger than sample B, so we can think that the shallow localization energy level roots from the fluctuation of quantum wells interface.

With the further increase of temperature, the heat energy inspires the carriers from the localization energy level, and more and more carriers are seized by the nonradiative compound center, and the nonradiative compound process begins to increase until it occupies the leading status. Because the penetration dislocation density of sample A is higher than sample B, and the attenuation of sample A is more notable than sample B in this temperature area, which can prove that the penetration dislocation certainly is effective nonradiative compound center in InGaN quantum wells.

The differences of light intensity and peak form with different radiation wavelengths for the quantum wells are produced by the differences of the crystal quality and In content of InGaN alloy, and the differences of growth temperature and In component for the quantum wells will produce the localization differences of quantum wells. Figure 4 shows the relationship between the radiation wavelength and In component of quantum wells and the localization energy, and with that the radiation wavelength of quantum wells increase from 365nm and 460nm to 516nm, the In content in the InGaN alloy presents ascending trend which increase from 3.1% and 9.6% to 17.6%, and the localization energy of quantum wells also present ascending trend, and both aspects possess linear relationship. It is obvious that the In component and localization energy of quantum wells have same change trend in this radiation wave band, which proves that the localization effect of quantum wells is mainly produced by the participation of In atoms.

From above experiment results, we can see that the influences of penetration dislocation to the structure of optical performance of quantum wells include flowing aspects, and the first one is that the penetration dislocation will deteriorate the interface quality of quantum wells and introduce the localization effect in InGaN quantum wells, and the second one is that the penetration dislocation is the nonradiative compound center in the quantum wells and makes the radiation intensity of InGaN quantum wells reduced.

4. Conclusions

In this article, we study the influences of penetration dislocation to the structure and optical performance of epitaxial GaN quantum wells on C-plane sapphire. And the research found that on the one hand, the penetration would disperse the interface of quantum wells, and increase the fluctuation, and accordingly increase the localization effect of quantum wells, and on the other hand, as the nonradiative compound center, the penetration dislocation would reduce the radiation intensity of quantum wells. The influences of penetration dislocation to the optical performance of InGaN/GaN multiple quantum wells are decided by both competition.

The localization effect intensity of InGaN quantum wells possesses linear relationship with In content in certain wavelength range. The In content has important influence to the light intensity with the attenuation of temperature, but high In content will weaken the crystal quality of quantum wells, and comparing with purple light and green light, the

blue light radiation possesses better optical performance, which is the balanced result between two aspects.

References

B. Heying, X. H. Wu, S. Keller, Y. Li, D. Kapolnek, B. P. Keller, S. P. DenBaars, and J. S. Speck. (1996). Role of Threading Dislocation Structure on the x-ray Diffraction Peak Widths in Epitaxial GaN Films. *Appl. Phys. Lett.* 68. P.643.

D. Kapolnek, X. H. Wu, B. Heying, S. Keller, B. P. Keller, U. K. Mishra, S. P. DenBaars, and J. S. Speck. (1995). Structural Evolution in Epitaxial Metalorganic Chemical Vapor Deposition Grown GaN Films on Sapphire, *Appl. Phys. Lett.* 67. P.1541.

P. Visconti, D. Huang, M.A. Reshchikov, F. Yun, R. Cingolani, D.J. Smith, J. Jasinski, W. Swider, Z. Liliental-Weber, H. Morkoc, Mater. (2002). *Sci. Eng. B.* 93. P.229.

S. Figge, T. Bottcher, S. Einfeldt & D. Hommel. (2000). In Situ and Ex Situ Evaluation of the Film Coalescence for GaN Growth on GaN Nucleation Layers. *J. Crystal Growth* 221. P.262.

T. Yang, K. Uchida, T. Mishima, J. Kasai & J. Gotoh. (2000). Control of Initial Nucleation by Reducing the V/III Ratio During the Early Stages of GaN Growth. *Phys. Stat. Sol. (a)* 180. P.45.

Yukio Narukawa, Yoichi Kawakami, Mitsuru Funato, Shizuo Fujita, Shigeo Fujita and Shuji Nakamura. (1997). Role of Self-formed InGaN Quantum Dots for Exciton Localization in the Purple Laser Diode Emitting at 420 nm. *Appl. Phys. Lett.* 70. P. 981.

Yukio Narukawa, Yoichi Kawakami, Shizuo Fujita, Shigeo Fujita and Shuji Nakamura. (1997). Recombination Dynamics of Localized Excitons in In_{0.20}Ga_{0.80}N-In_{0.05}Ga_{0.95}N Multiple Quantum Wells. *Phys. Rev. B* 55. P.1938.

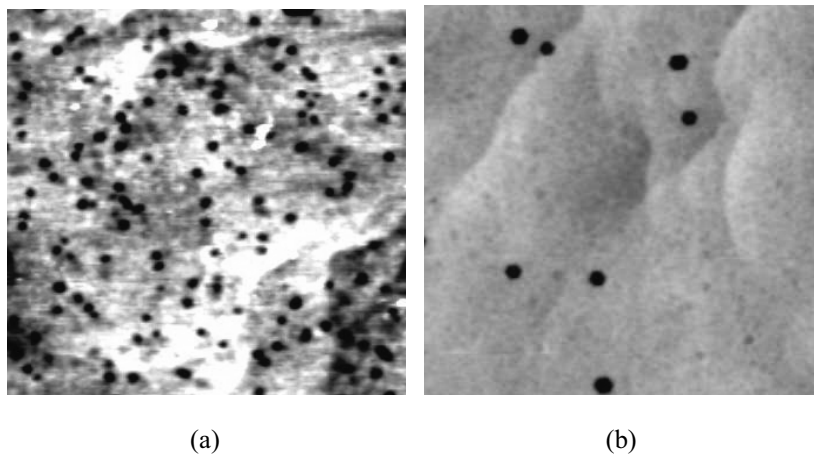


Figure 1. AFM Images of Sample (a) and Sample (b) after Etching (The Measure Area is 3µm×3µm)

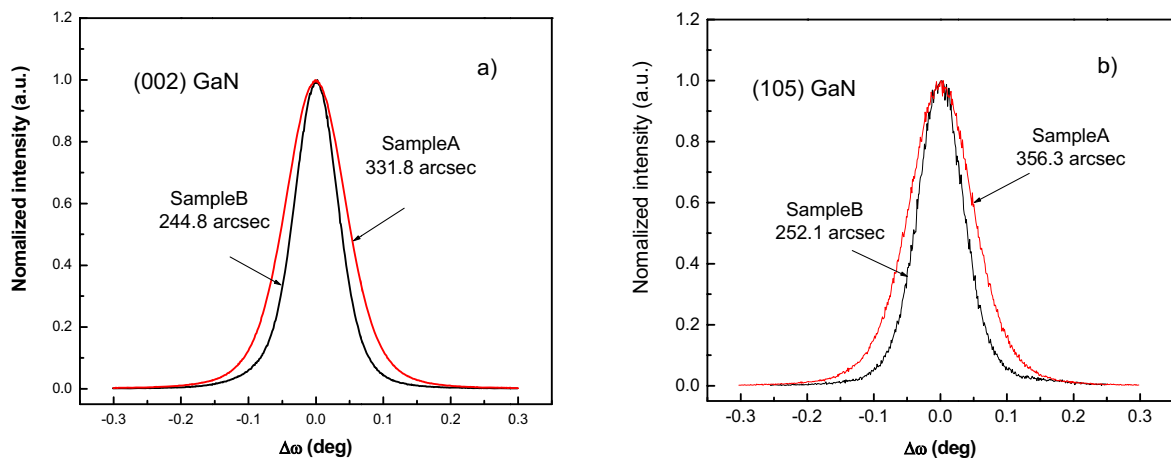


Figure 2. X-ray ω Scan Curves of Sample Symmetry (002) and Asymmetry (105)

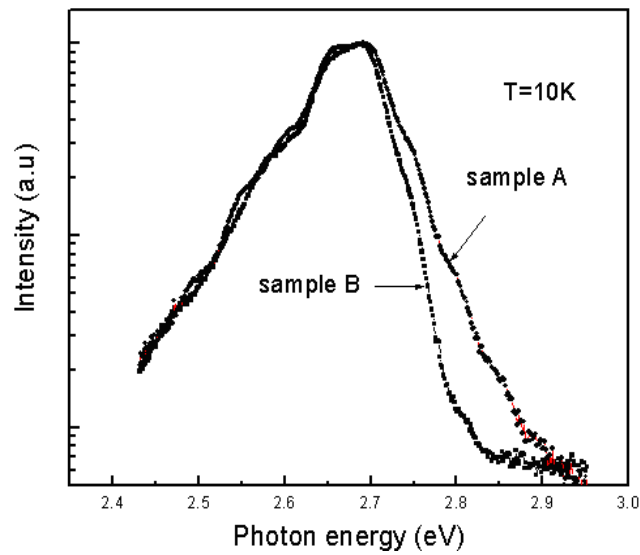


Figure 3. Quantum Wells Low Temperature PL Spectrum of Sample A and B

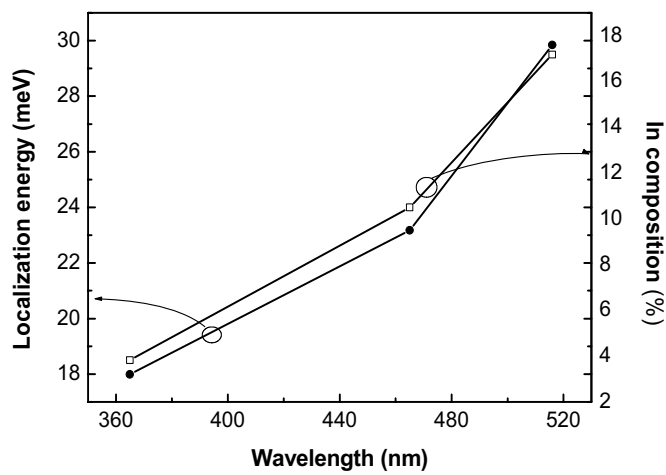


Figure 4. The Relationship of Quantum Wells Radiation Wavelength and In Component with Localization Energy



Effect of Corner Radius and Friction Parameters on the Optimization of the Cold Forging Die Design

A. R. Ab-Kadir

School of Mechanical Engineering

Universiti Sains Malaysia

Engineering Campus, 14300, Nibong Tebal, Pulau Pinang, Malaysia

E-mail: ahmad_razlee@yahoo.com

A. R. Othman

School of Mechanical Engineering

Universiti Sains Malaysia

Engineering Campus, 14300, Nibong Tebal, Pulau Pinang, Malaysia

Z. Samad

School of Mechanical Engineering

Universiti Sains Malaysia

Engineering Campus, 14300, Nibong Tebal, Pulau Pinang, Malaysia

Khaleed Hussain. M. T.

School of Mechanical Engineering

Universiti Sains Malaysia

Engineering Campus, 14300, Nibong Tebal, Pulau Pinang, Malaysia

A. B. Abdullah

School of Mechanical Engineering

Universiti Sains Malaysia

Engineering Campus, 14300, Nibong Tebal, Pulau Pinang, Malaysia

Abstract

Finite element (FE) method is extensively employed in solving linear and non-linear problems and widely used particularly in analyzing a forming process. It enables the analysis on internal properties such as stress effective, forming load, metal flow and deformation to be performed, in which results in an increase on the performance of forging process. Heading process which is often performed in conjunction with other cold forging process has been simulated by FE-code DEFORMTM F3 v6.0. The numerical results were analyzed to evaluate the effect of the fillet size and the friction value on the cold heading process. It was found that the heading process provided good precision and productivity as the size of fillet was increased; due to intensification of the metal flow to infuse the die cavity. On the other hand, the friction value also played an important role in governing the reaction force between workpiece and punch in the process.

Keywords: Finite element method, Cold forging, Forming load, Friction coefficient, DEFORM

1. Introduction

1.1 Forging Process

Cold forging is an essential process and widely used in a typical manufacturing production. In the process, the metal is continuously pressed under high pressure into high strength parts and as a result, the material experienced extensive plastic deformation during the progression. Normally, it is used to produce mass production of mechanical components such as connecting rods, bolts, screw, nut, universal joint and many others. In comparison to another processes such as

casting and machining, cold forging has many advantages. One of them is maximizing the material properties in the finished part. In the process, the grain structure of the material is rearranged to follow the contour of the component and hence, increases the strength of the component. On the other hand, cutting process would cause damages to the grain structure and therefore, the properties of the part become inferior to the initial workpiece from which it was. In addition, the extrusion operation could also cause the metal to flow only along the axis of the workpiece, hence reduces the mechanical performance in the transverse direction. Besides, cold forging has a high performance on the production rate and repeatability. The parts with cold forging process are largely produced at high rate compare to those achieved by the machining processes as the parts are immediately ready for use after the forging; the process is conducted by automated production lines that directly converts the workpiece to the finished parts. The repeatability of the process becomes excellent with optimal die design, low temperature and optimal lubrication (Ngaile, G., Saiki, H., Ruan, L. and Marumo, Y. 2007.). Another important advantage of cold forging process is the amount of waste material for finished part is very insignificant. The process is a “chipless machining”, in which sometimes requires less or no cutting process as well as eliminates secondary grinding.

1.2 Computer-Aided Engineering Technology

In general, it has been concluded that the major variables involved in forging process includes workpieces properties and geometry, tools properties and geometry, interface condition between tool and workpiece, environmental conditions, forging machining (force, velocity and direction of tool movement), and mechanics of the deformation zone (Ko, D. C., Kim, D. H. and Kim, B. M. 1999.)(Altan, T., Ngaile, G. and Shen, G. 2005.). However, these critical issues are very difficult to address during the real-time forging process. Computer-aided engineering (CAE) code is perhaps, the best tool in order to generate, validate, verify and optimize the design solutions before they are implemented in the process (Kobayashi, S., Oh, S. I. and Altan T. 1989.). The CAE enables the analysis of the design of forming process, material selection, tooling structure, properties configuration and quality of the product to be performed. CAE codes with finite element method permits simulation of the system in solving linear and non-linear problems and is widely used in manufacturing including the forging process. Furthermore, it is also able to evaluate the internal properties such as stress effectiveness, forming load, strain distribution, deformation and temperature distribution.

Santos et al (Santos, A. D., Duarte, J. F., Reis, A., Rocha, B., Neto, R. and Paiva, R. 2001.) utilized the FE method to determine the size of initial material of workpieces and the forces that to be implemented. The authors have been discussed that the numerical simulation could in fact assist modification and hence reduce trial and error stage in preparing the tools for forming process. FE method may also provide an important answer in predicting the process and defects. Jun et al (Jun, B. Y., Kang, S. M., Lee, M. C., Park, R. H. and Joun, M. S. 2007.) presented a powerful approach in estimating the geometry of cold forging part by using FE codes by analyzing the die structure and springback characteristics of the workpiece. Lee et al (Jun, B. Y., Kang, S. M., Lee, M. C., Park, R. H. and Joun, M. S. 2002.) have performed a study to evaluate the dimensional differences between forged components and forging die by using FE method as well as experimental data. In numerical simulation with a commercial FE code of DEFORM-2D™, two different approaches have been discussed comprehensively for comparison with the measured elastic strains. On the other hand, Chen et al (Chen, X., Balendra R. and Qin, Y. 2004.) presented the least square approach in order to minimize the component mistake with regards to the die-elasticity, springback, secondary yielding and temperature variations. In order to clearly illustrate the approach, an axisymmetric closed-die forging has been employed. Also, Wu and Hsu (Wu, C. Y. and Hsu, Y. C. 2002.) have analyzed the influence of die shapes with different fillet radii and draft angles on the extrusion process. In addition, they performed comparisons between the prediction of finite element method and experimental results of the respective deformation mode in reference to the parameters of flow condition, the flange width, the boss height, as well as load and strain distributions.

Proper lubrication is extremely important to the completion of heading process of stainless steels, high temperature alloys or other specialty metals. It was found that a basic knowledge of lubrications could prevent subsequent fabrication difficulties like tooling failure, galling, wear or die seizing (Schey, J. A. 1983.). As the heading processes, which include upsetting and forming or a combination of operation, require high pressure application that generates high temperature elevations due to tremendous external and internal friction, lubricant helps to reduce friction in heading operation by providing a film that prevents metal-to-metal contact. Subsequently, friction is an undesired factor which has to be reduced in order to have low forming load, low stress and deformation distribution on die as well as better product quality. In addition, combination lubrications are essential for heading process as greater pressure produces higher heat and friction, hence results in rapid breakdown of the coating.

On the other hand, in cold forging process, die design parameters such as size of fillet corner, draft angel, flash geometry and die surface contact area may influence die wear and hence, the fatigue life. Corner and fillet radii are vital in die design in order to allow preclusion of defects in the product as well as to prolong the die life. For an instance, results of an analysis provide stress concentration and deformation data on die that are depended on the geometry of the die, in which the stresses are redistributed over an area. Commonly, early failure occurs due to excessive stresses which

are concentrated in a sharp corner of the die. In addition, it was anticipated that the size of radii will greatly affect the die filling state as well as the forming load taking into account the quality of forged part.

In this paper, an approach to evaluate an optimal size of corner fillet in cold forging die design as well as an optimal combination of lubrications to employ in cold heading process are presented. Die stress and deformation analyses are carried out to analyze the effect of different sizes of fillet and different friction coefficient values. The optimal size of fillet and friction coefficient is assessed with the value of die stress and forming load, respectively. The CAD models are incorporated in CAE simulation by using FE codes in order to identify the stress and deformation distributions on punch as well as to determine the respective forming load.

2. Methodology

The diagram shown in Figure 1 represents a methodology framework of CAE simulation for forging process and tool analysis. It showed that the CAD models for process simulation were created in different platforms and subsequently were transferred into FE codes via data exchange platforms such as STEP, IGES or STL. In the present study, the workpiece, punch, bottom die and die assembly components were constructed in the CAD models before the commercial FEM-code DEFORMTM F3 v6.0 was implemented via CAE platforms to establish the simulation. In the CAE platform, a number of parameters were specified including the process control and constraints, re-meshing control and criteria, boundary condition, and the loading step before conducting the die stress and deformation analysis.

During FE simulation, there are possibilities for the computational error to take place due to large displacement and deformation. Since, the relative movement between the deforming materials and die surface is very significant, computation with a Lagrangian mesh is difficult in accommodating the changes in deformation of one mesh system as well as the complexity in combining the die boundary profile into FE mesh with increasing relative deformation. In order to overcome these problems, it is necessary periodically to apply remeshing algorithm into the system. The remeshing involved two procedures; first, was the integration of new mesh into the workpiece, and second, was the relocation of information from old to the new mesh. A commercially available mesh generator was utilized in order to generate the new mesh scheme that was essentially the same as the initial mesh generation.

On the other hand, the boundary surface, S can be written in three distinct parts as the following.

$$S = S_u + S_F + S_c$$

Where S_c is the boundary condition along the workpiece-tool interface, S_u is the velocity boundary condition and S_F is the traction boundary condition. In the algorithm, S_u enforced the velocity condition only at nodes, in which velocities of elements and nodes shape function were determined along the element-side. With respect to the node velocity component, the first derivative of π_{SF} is recalled and hence, the imposition of the traction boundary condition on S_F would be straightforward. Subsequently, the traction boundary condition was imposed in the form of nodal-point forces. On the surface S_u , the velocity was prescribed in the normal direction to the interface and on the other hand, the traction was prescribed in the tangential direction.

In addition, the process parameters such as friction coefficient value, movement of die, workpiece and die temperature and the positioning the object between workpiece and die have also to be defined. The simulation results, which included forming forces, stress and deformation distributions as well as metal flow, were considered in order to analyze the effect of the corner radius and the friction value on forging process. Therefore, the optimal size of fillet and the friction coefficient value were configured in order to enhance the performance of forging process.

2.1 Computational Simulation of Cold Forging Process

Fastener manufacturing process is one of the cold forging processes and is also known as cold heading. The process involves applying a force through a punch to the end of a workpiece contained in a die. In order for the workpiece to experience a plastic flow, the applied force should exceed the elastic limit of the metal. Typically, the heading process is often performed in conjunction with other cold forging process, in which consists of two or three different operations; i.e. one or two performing method and one finishing process. The principal stages of the cold heading process of fastener, simulated by FEM-code DEFORMTM F3 v6.0, are shown in Figure 2. The operation consisted of a performing process followed by the head compression. Extensive study for die stress analyses was performed in the area of the latter stage to determine the stresses and deformations on the punch. Figure 3 shows the final geometry of workpiece obtained in the simulation, in which was similar to actual fastener geometry.

Table 1 lists the mechanical and physical properties of the model. On the other hand, two different analyses were implemented for the FE study and were specified in Table 2. In the study to determine the optimal friction coefficients for the process, four different types of lubricants were utilized on the die punch. Lub 1 contained the metal soap (calcium and sodium) and chemically combined with chlorine and fluorine. On the other hand, Lub 2 and Lub 3 were restricted to only a metal soap (calcium and sodium) but the percentage of calcium in the latter was more than the former. The final parameter, Lub 4 was a combination of zinc phosphate coating and metal soap that is commonly used

for cold forging and its friction coefficient was 0.1. Note that, the friction coefficient value for Lub 1, Lub 2 and Lub 3 were specified as 0.4, 0.12 and 0.14, respectively.

The geometric dimension of the punch is highlighted in Figure 4 and R_p denotes the fillet location which presumably would affect the forming load and die filling. The computational model provided the material flow of the cold heading process, in which exhibited an informative grid distortion pattern. Therefore, Figure 5 highlights the grid pattern obtained from process modeling output at 30%, 60% and 95% of material reductions. It demonstrated the significance of the metallurgical properties in the process of cold heading in achieving superior finished part. It was found that along the axis of the blank of the metal flow, the grain structure was rearranged during the operation to the contour of the part and this new grain structure apparently supported the parts and added the strength to bolt head. This unique property provided an advantage to the cold forging; the grain flow lines established by the various cold forming process remain uninterrupted in the finished part and the grain structures were appeared finer than in hot-forged parts.

3. Results and Discussion

3.1 FE results of different sizes of fillet

Results of the FE analyses for different sizes of fillet were comprehensively discussed. Figure 6 denotes the final filling state of the punch for various fillets. It was found that the material was unable to fill in the punch cavity for the case of $R_p = 1.0$ mm and 1.5 mm, whilst the punch-filling state was attained when R_p equal or more than 2.0 mm. If the size of fillet was too small (< 2.0 mm), it prevented the material to effectively switch to the side wards of die cavity due to the centrifugal flow which was attributed to compression of the cylindrical workpiece. As a result, the unfilled area was simultaneously trapped at the die corner. Therefore, the precision and productivity of forging process were very much depending on the geometry of the die; it was found that the size of die corner affected the metal flow of the workpiece. The forging process provided good precision and productivity when the size of fillet increases, as the metal was able to flow easily to fill in the die cavity.

It was observed that the fillet of 1.0 mm produced a very low precision of the final product and unfilled state. Figure 7 shows that the maximum forming load increased with the size of fillet as the punch progressed for the full die-filling state. The values of the maximum load exhibited by 1.0 mm, 1.5 mm, 2.0 mm, and 2.5 mm fillets were 457 kN, 440 kN, 427 kN and 400 kN, respectively. This was attributed to the continuously increasing load in the final forming operation in order to fill the die corners. Accordingly, the largest size of fillet only required the lowest forming load rather than those of the smaller sizes.

According to Figure 8, it certified that the permanent displacement was not proportional to the size of fillet, but increased as the size of fillet decreased. The highest and lowest values for the permanent displacement were attained as 0.0702 mm and 0.0662 mm when R_p were 0.1 mm and 2.5 mm, respectively. In addition, by referring to Figure 9, it shows that the highest value for maximum stress was 1600 MPa when R_p was at 0.1 mm and the lowest value for maximum stress was 1450 MPa as R_p approached 2.5 mm. significantly, the maximum stresses were observed at the corner of the punch, but not at the top surface. It was observed that the metal flow was mainly influenced by the tool geometry, in which provided the effects to the force constraints of the process, stress concentration and permanent displacement on the tool. Furthermore, it was observed that the geometry of the tool influenced the deformation of the workpieces, given that the fillet corner increased, die wear would decrease and hence the fatigue life increased, since a small corner would introduce high stress concentration and permanent displacement. Subsequently, it was suggested from this study that the optimal size of the corner radius for the punch design should equal or more than 2.0 mm in order to achieve superior quality of finished parts.

3.2 FE results of different types of lubricant

By referring to Figure 10; it indicates that the total forming load was increased with the values of friction coefficient. The highest maximum forming load was produced when Lub 1, which has the highest friction coefficient value, was employed. On the other hand, the lowest maximum forming load was generated as Lub 4 was applied on the punch. It was found that the forming load values exhibited by Lub 1, Lub 2, Lub 3, and Lub 4 were 675 kN, 510 kN, 542 kN and 489 kN, respectively. It has been evaluated from the FE results that the forming load was found to be proportional to the friction coefficients, as the friction values increased, the die life decreased as higher friction coefficients required higher load to fill the die cavity. On the other hand, it was observed that for the minimum value of friction coefficient, the workpiece deformed almost uniformly, but when the maximum value of friction was present, the deformation of the workpiece was found inconsistent. Based on the analyses, the friction utilized in the die design to a great extent influenced the metal flow as well as the reaction force between the workpiece and the punch in the forging process. It was noticed that the metal flow was unable to effectively fill the die cavity as those of the friction value has increased.

In addition, it was indicated in Figure 11 that the permanent displacement also increased with friction coefficients. The lowest permanent displacement was 0.0771 mm with the friction coefficient approached 0.1 for Lub 4. Also, from Figure 12, it shows that the stress value has increased as the friction coefficient intensified, in which an increase in die

wear was evaluated and hence, the fatigue life would be reduced. From the analysis, the highest maximum stress was found as 1550 MPa with friction coefficient of 0.4 for Lub 1, whilst the lowest value of maximum stress on the punch was 1390 MPa with friction coefficient value of 0.1 for Lub 4. Note that, Lub 4 was a high lubricity material that was capable to reduce considerably the sliding friction between the punch and the workpiece. Therefore, the workpiece would deform with ease in order to fill the die cavity and hence decreasing the permanent displacement at punch. Subsequently, the stress concentration at punch would be decreased, in which the die wear was reduced accordingly with the fatigue life increased. In addition, the erosion of the punch surface would be reduced as Lub 4 has the high characteristic of non-abrasive. In summary, it was suggested that the optimal value of friction coefficient in cold forging operation was 0.1, in which the lubricant consisted of zinc phosphate coating and metal soap combination (calcium + sodium).

4. Conclusions

Computer-aided engineering (CAE) simulation is a useful tool to optimize, validate, verify and hence, generate the design solutions before they are implemented. The results can be utilized to analyze the tool design and forming processes during the designing stage as well as in the trouble shooting stage. In the current study, the effects of corner radius and friction coefficients were studied on the optimization of the cold forging die design. Workpiece and die assembly components were constructed in the CAD models before the commercial FEM-code DEFORMTM F3 v6.0 was implemented via CAE platforms in order to establish the cold heading process of fastener.

It was found that the precision and productivity of forging process were very much depending on the geometry of the die; the size of die corner affected the metal flow of the workpiece. It was observed that the geometry of the tool influenced the deformation of the workpieces, given that the fillet corner increased, die wear would decrease and hence the fatigue life increased, since a small corner would introduce high stress concentration and permanent displacement. In addition, it was concluded that the forging process provided good precision and productivity when the size of fillet increases, as the metal was able to flow easily to fill in the die cavity. Subsequently, it was suggested that the optimal size of the corner radius for the punch design should be equal or more than 2.0 mm in order to achieve superior quality of the finished parts.

It has been evaluated from the FE results that the forming load was found to be proportional to the friction coefficients, as the friction values increased, the die life decreased as higher friction coefficients required higher load to fill the die cavity. On the other hand, it was observed that for the minimum value of friction coefficient, the workpiece deformed almost uniformly, but when the maximum value of friction was present, the deformation of the workpiece was found inconsistent. Based on the analyses, it was concluded that the optimal value of friction coefficient in cold forging operation is 0.1, in which the lubricant consisted of zinc phosphate coating and metal soap combination (calcium + sodium).

References

- Altan, T., Ngaile, G. and Shen, G. (2005). 'Cold and hot forging fundamentals and applications'; ASM International the Materials Information Society;
- Chen, X., Balendra R. and Qin, Y. (2004). 'A new approach for the optimization of the shrink-fitting of cold-forging dies', *J. Mater. Process. Technol.* 145, 215-223.
- Jun, B. Y., Kang, S. M. Lee, M. C. Park, R. H. and Joun, M. S. (2007). 'Prediction of geometric dimensions for cold forgings using the finite element method', *J. Mater. Process. Technol.* 189, 459-463.
- Ko, D. C., Kim, D. H. and Kim, B. M(1999). 'Application of artificial neural network and Taguchi method to perform design in metal forming considering workability'; *Int. J. Mach. Tools Manufact.* Volume 39, Issue 5, 771-785.
- Kobayashi, S., Oh, S. I. and Altan T. (1989). 'Metal forming and the finite element method'. New York: Oxford University Press.
- Lee, Y., Lee, J. and Ishikawa, T. (2002). 'Analysis of the elastic characteristic at forging die for the cold forged dimensional accuracy', *J. Mater. Process. Technol.* 130, 532-539.
- Ngaile, G., Saiki, H., Ruan, L. and Marumo, Y. (2007). 'A tribo-testing method for high performance cold forging lubrications'; *WEAR*, 262, 684-692.
- Santos, A. D., Duarte, J. F., Reis, A.; Rocha, B., Neto, R. and Paiva, R. (2001). 'The use of finite element simulation for optimization of metal forming and tool design', *J. Mater. Process. Technol.* 119, 152-157.
- Schey, J. A. (1983). 'Tribology in Metalworking, Friction, Lubrication and Wear', American Society for Metals.
- Wu, C. Y. and Hsu, Y. C. (2002). 'The influence of die shape on the flow deformation of extrusion forging', *J. Mater. Process. Technol.* 124, 67-76.

Table 1. Mechanical and physical properties employed in the analysis

Items	Forging Conditions
Die material	AISI-D2
Poisson ratio, ν	0.3
Model of die	Plastic
Friction coefficient, μ	0.12
Workpiece material	SS 302
Model of workpiece	Plastic
Initial temperature of workpiece	25°C
Initial temperature of die	25°C
Number of mesh	50000
Simulation mode	isothermal

Table 2. Two different analyses implemented for the FE simulation

Different fillet size at second punch, R_p	1.0mm, 1.5mm, 2.0mm, 2.5mm
Lubricant types	
Lub 1	Calcium, sodium, chlorine, fluorine ($\mu = 0.40$)
Lub 2	Calcium and sodium soap ($\mu = 0.12$)
Lub 3	Calcium and sodium soap (higher Ca% than Lub 2, $\mu = 0.14$)
Lub 4	Zinc phosphate coating + metal soap (calcium + sodium, $\mu = 0.10$)

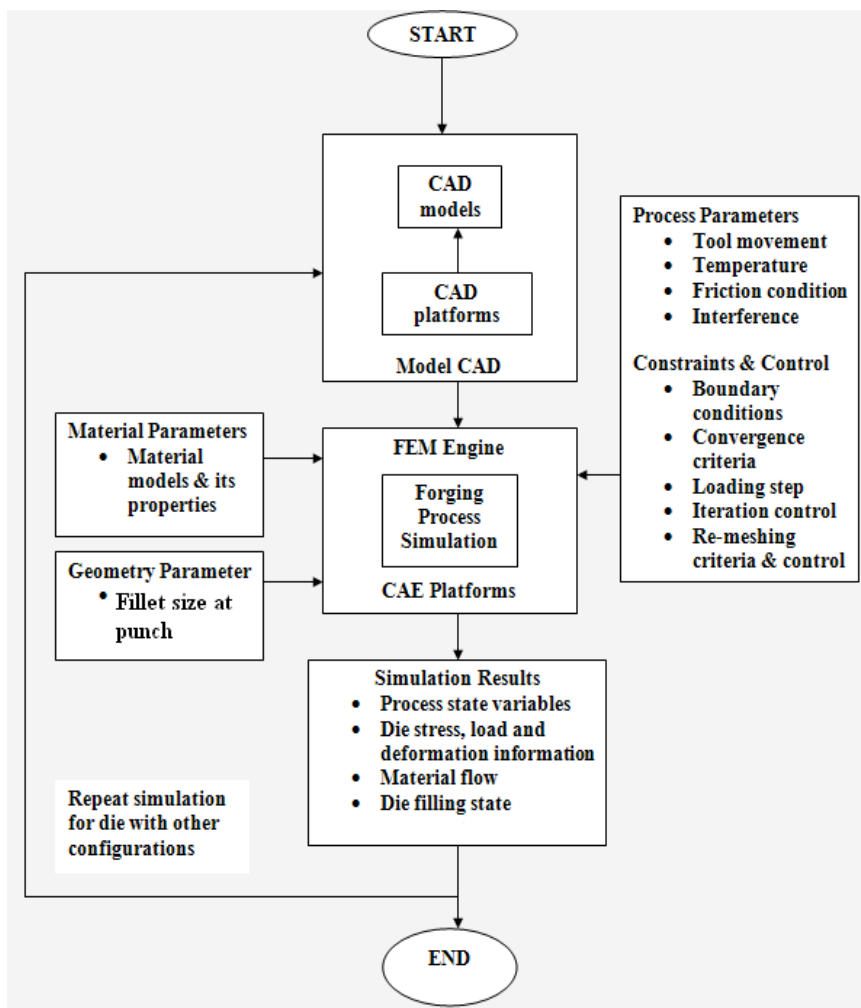
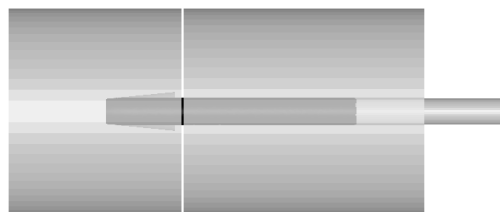


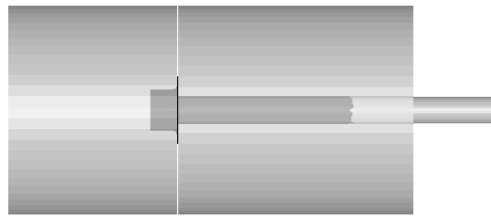
Figure 1. Methodology framework



a) The position of punch prior to the cold forging process



b) Pre-forming operation (First stroke)



c) Heading compression (Final stroke)

Figure 2. The forming stages of cold heading process of fastener

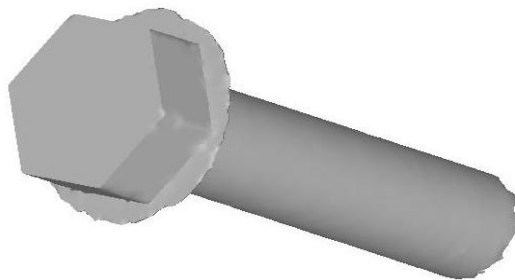


Figure 3. Isometric view of fully deformed workpiece

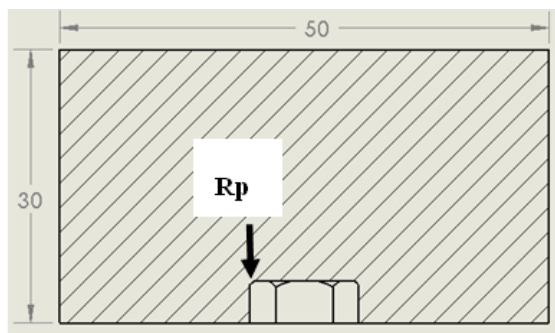


Figure 4. Geometric dimension of the second punch and R_p denotes the fillet at corner of punch

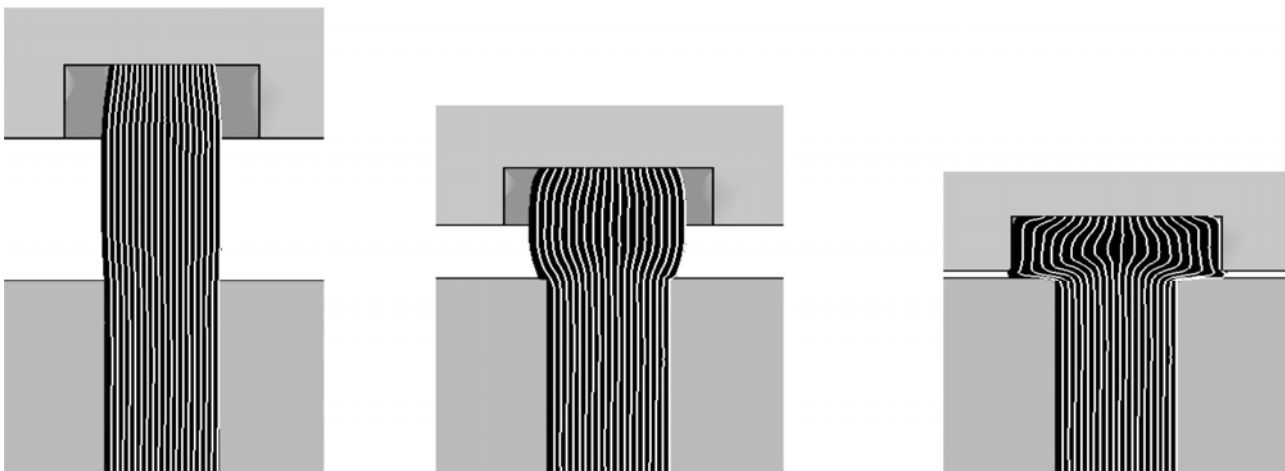


Figure 5. Computational simulation of material flow in heading at 30% reduction, 60% reduction and 95% reduction.

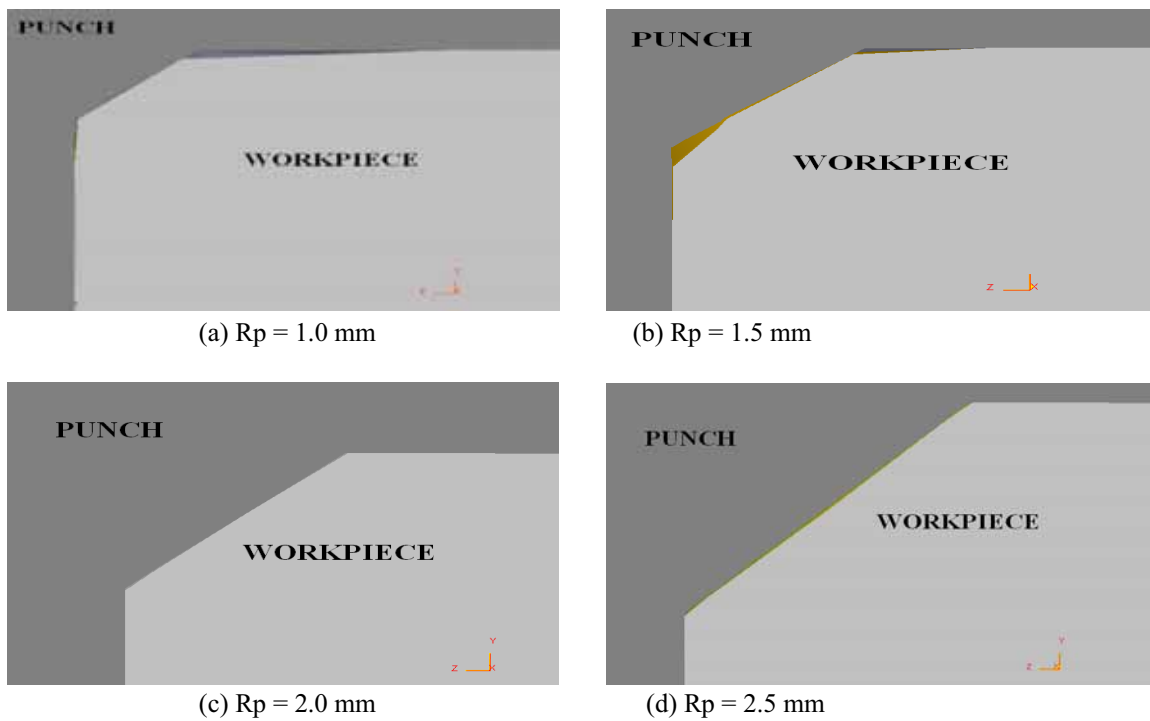


Figure 6. The final filling states of the punch for various fillet sizes

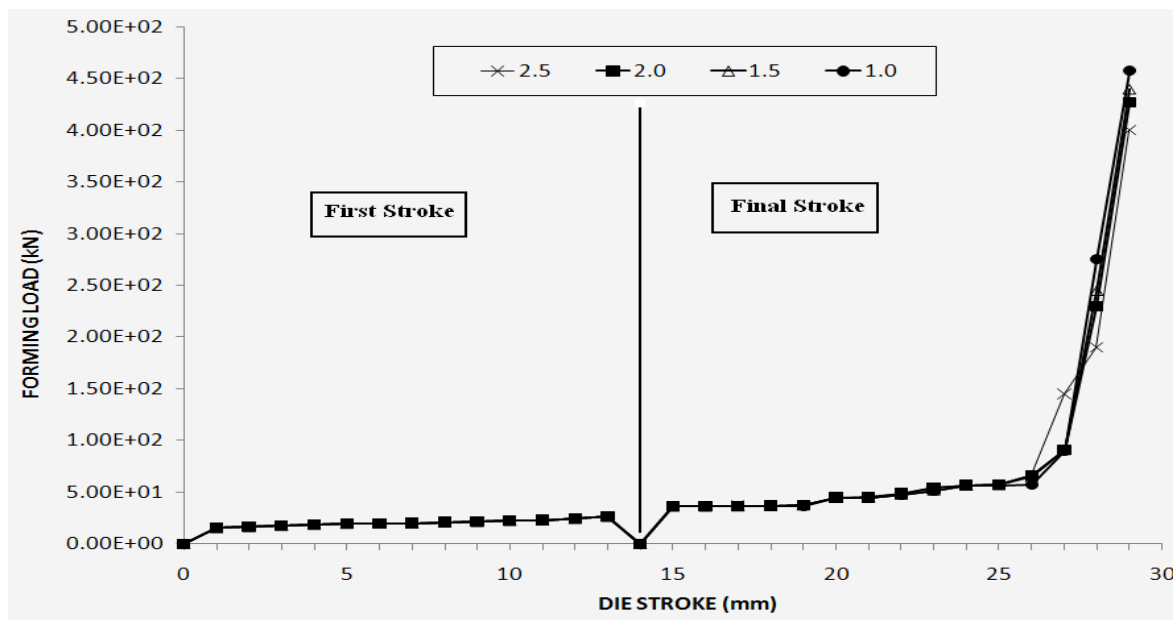


Figure 7. Forming load vs. die stroke curves for various R_p

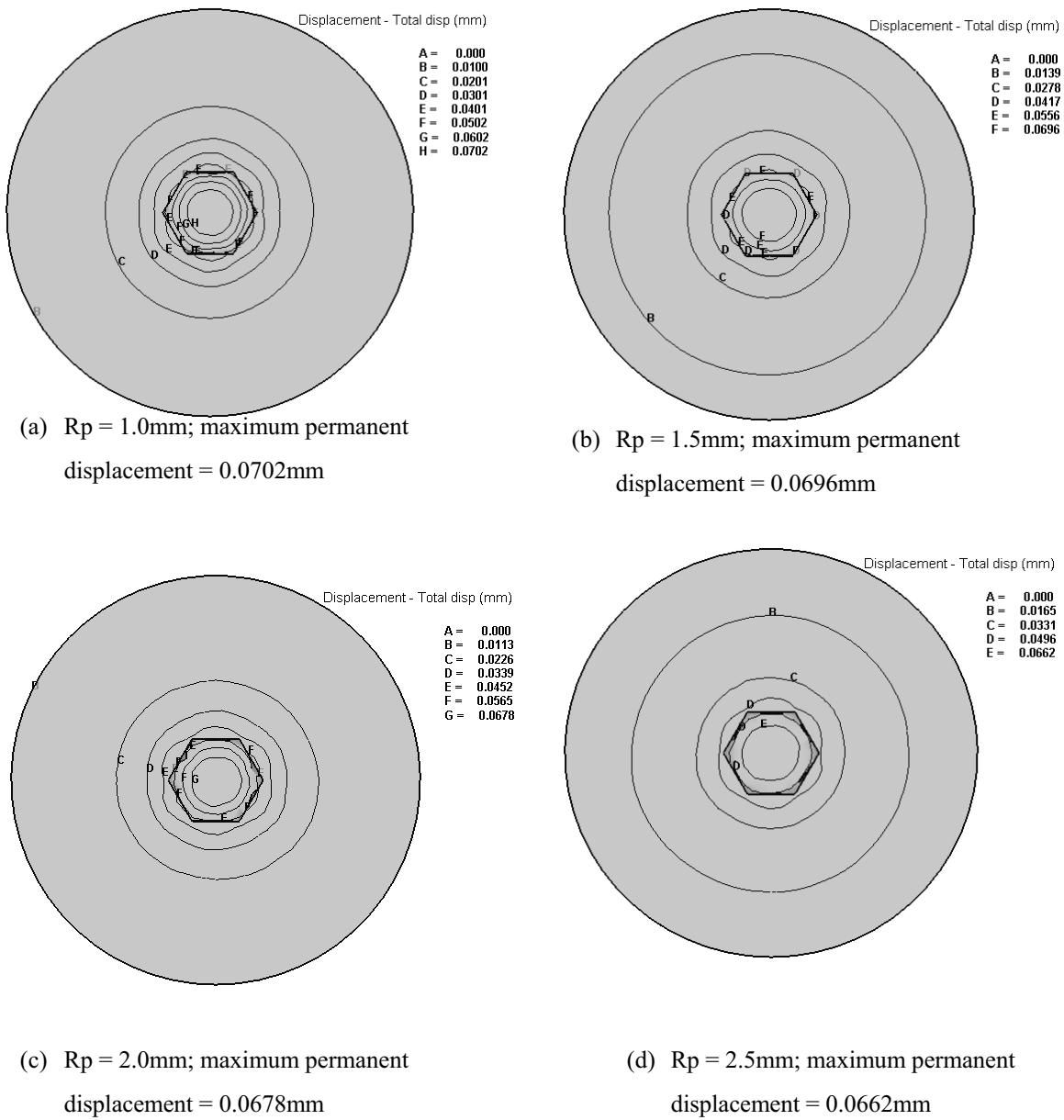
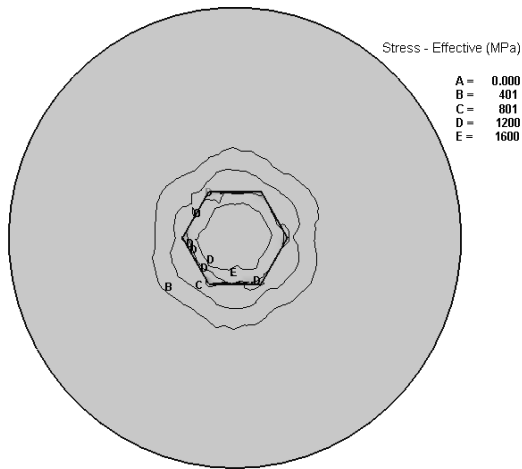
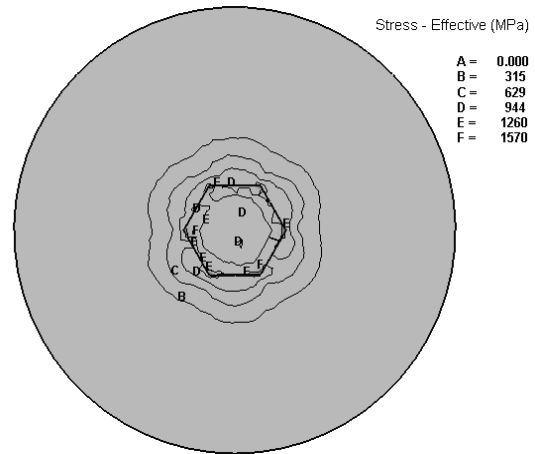


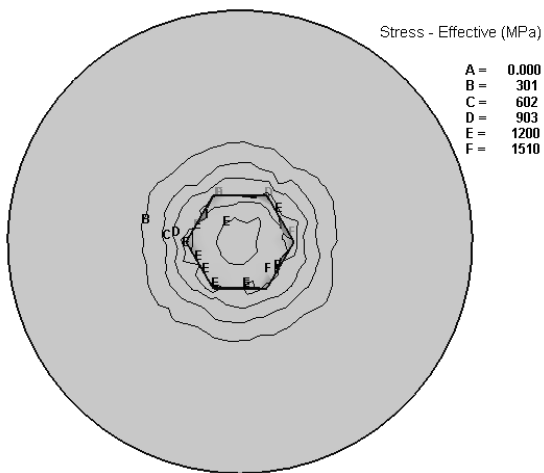
Figure 8. Tool permanent displacement at second punch evaluated by finite element method for different sizes of corner fillet.



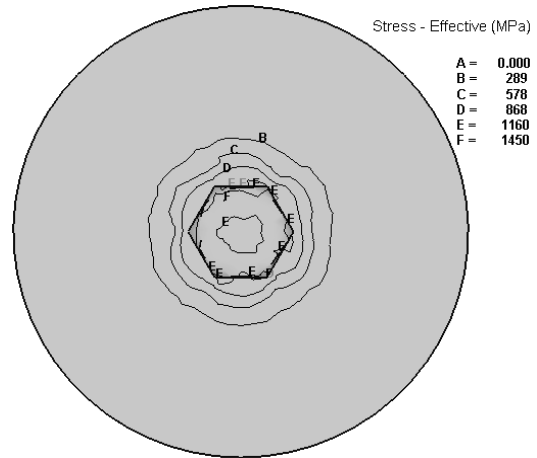
(a) $R_p = 1.0\text{mm}$;
maximum stress = 1600MPa



(b) $R_p = 1.5\text{mm}$;
maximum stress = 1570MPa



(c) $R_p = 2.0\text{mm}$;
maximum stress = 1510MPa



(d) $R_p = 2.5\text{mm}$;
maximum stress = 1450MPa

Figure 9. Tool stress contour at second punch evaluated by finite element method for different sizes of corner fillet.

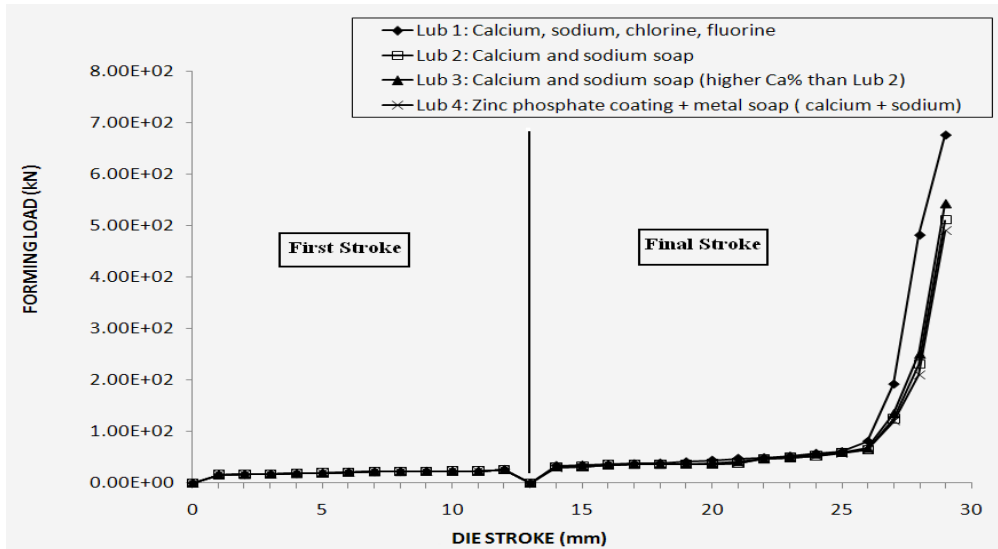


Figure 10. Forming load vs. die stroke curves for different types of lubricant.

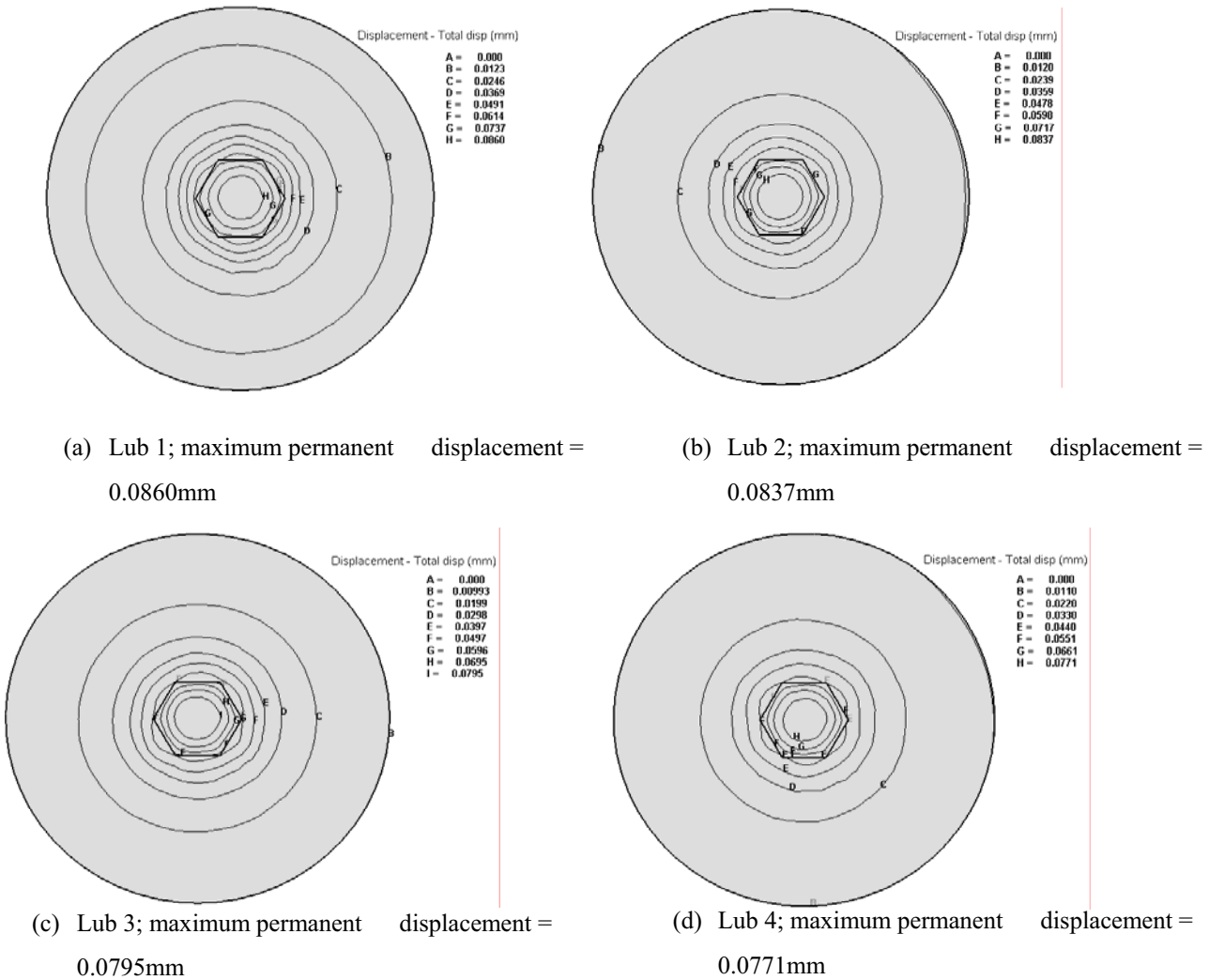
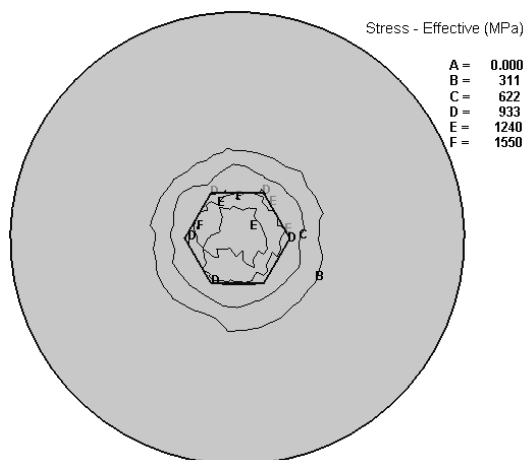
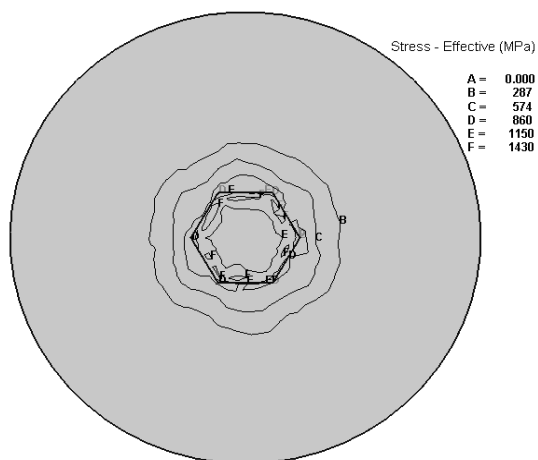


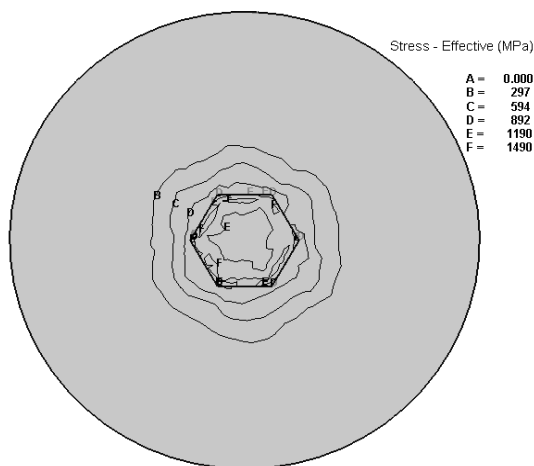
Figure 11. Tool permanent displacement at second punch evaluated by finite element method for different types of lubricant.



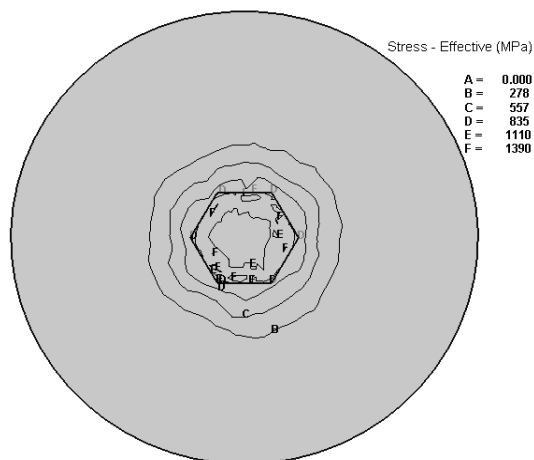
(a) Lub 1; maximum stress = 1550MPa



(b) Lub 2; maximum stress = 1430MPa



(c) Lub 3; maximum stress = 1490MPa



(d) Lub 4; maximum stress = 1390MPa

Figure 12. Tool stress contour at second punch evaluated by finite element method for different types of lubricant.



Analysis of the Flow Pipe Arrangement in RTM Process

Jinliang Liu & Xiaoping Wu

Key Laboratory for Advanced Textile Composite of Ministry of Education

Tianjin Polytechnic University

Tianjin 300160, China

E-mail: wuxiaoping@tjpu.edu.cn

Tianjin Municipal Science and Technology Commission (NO. 06YFJMJC03100, 08JCZDJC24500)

Abstract

In RTM process, the condition which the flow of resin in the pipeline according with the Darcy's law is the movement of laminar fluid and the Reynolds number less than 1. This paper simulated the flow of the resin in the pipeline by changing the length and diameter of the passageway of pipeline with finite element analytical method. In the result, the relationship of the fluid speed on the exit in pipeline and Reynolds number, also the scope of flow rate of the resin in the pipes can be gained. The test result shows that: exit velocity had little to do with the length, but the ratio of pipeline diameter. When the diameter of entrance assume value of 6 mm, 10mm, 16mm and 20mm and the diameter of exit 6 mm, 10mm and 16 mm respectively, the maximum speed should be 694.442 mm per second, 416.667 mm per second and 260.414 mm per second accordingly.

Keywords: RTM, Reynolds number, Flowing speed of resin, Numerical simulation

1. Introduction

RTM (Resin transfer molding) is a composite closed molding technology, which has the advantage of low-cost, high-quality production of composite material (Rudd, C.D., 2004, p1-8) applied to volume production of the small and medium-size components. There are mainly design and manufacture of molding, production and laying of preform, injection, compaction and molding of resin, and its stripping and post-processing etc (Rudd, C.D., 1997, p. 254-292) in RTM process. The basic method is design and manufacture mold based on product needed, making preform of fiber reinforced materials based on the shape of product needed, and then adding it into mold cavity. After injecting liquid resin into the mold cavity and making preform fully impregnated and cured, and then opens ultimate composite material components. RTM is a semi-mechanized composite molding process, which is suitable for an overall shape, and without secondary shear adhesive (Deng, jie, 2005, p. 50-52). Compare to the traditional process of pressing tank molding or Pultrusion, it saves a lot of tooling equipment, which make the production more efficient, relatively low cost. Through using low-viscosity resin and heating curing process, composite materials are created by the high-quality, low scrap rate, and its production process less depends on the operator's skill level.

RTM process falls under the combined effect of a variety of factors, such as the structure and shape of mold, the material properties of the fibers (permeability (Fan, Xiaoqin, 2006, p. 44-49), interface status), the choice of resin type, and molding process parameters, which molding process is the most important. There are many variables in the mold filling, such as injection pressure, temperature and vacuum injection mouth and the mouth of location, number. It is easy to produce dry patches and molding incomplete phenomenon in the experiment (Wang, Yongxiang, 2005). A computer simulation of the molding process plays a very good role in guiding, thereby it can saves money and shortens the cycle. Due to the importance of RTM process in the industrial application, a good simulation technology develops and the development of several commercial simulation software (Simacek, P., 2004, p. 355-367; Brusckhe, M. V., 1990, p. 398-405; Liu, Ningsheng, 2005, p. 40-42; Lu, Mingkun, 2005, p. 31-35), a lot of people simulated and studied mold filling process (Phelan, F. R. Jr., 1992, p. 90-102; Van, Melick, H. G. H, 1998, p. 17-22; Dai, Fuhong, 2004, p. 161-167; Li, Haichen, 2003, p. 58-61; Dai, Fuhong, 2004, p. 335-340; Shojaei, 2006, p. 1434-1450; Wang, Baichen, 2006, p. 297-300). In early studies Martin and son (Martin, G. Q., 1986, p. 149-157) simulated the mold filling process, and used the computer software (POLYFLOW) to simulate resin flow. Zhong, Cai (Zhong, Cai, 1992, p. 1310-1338) studied the calculation process of the simplifying RTM resin flow. In view of some simple model, the resin flow of various boundary conditions in entrance can calculate. However, the above-mentioned research work focuses on the totality of the molding resin flow and pressure and speed control, there is no pipeline in the process of the RTM resin flow problems for research. In RTM Process, in a resin preform mold cavity to streamline the flow of fluids in porous media

flows, and these flows must be consistent with Darcy's law. Before the resin flowing in the pipeline, resin into the mold cavity must also be consistent with Darcy's law, and in order to meet the resin into the mold cavity with Darcy's law, the flow must be laminar flow. This paper uses the finite element method to simulate the resin flow by designing the different length and the diameter rate of the pipeline. With the Darcy's law and the Reynolds number is less than 1, the general law of the resin flow in the pipeline can be obtained.

2. Theory

In the RTM process, the resin in the pipeline must be the laminar flow, and the Reynolds number has played a very important role. Reynolds number must be less than 1 which can meet the technical requirement. In order to calculate the flow of resin in the pipeline, the Reynolds number equation as follows:

$$\text{Re} = \frac{\rho v D_h}{\mu} \quad (1)$$

Where ρ is the fluid density of resin, μ is the fluid viscosity, v is the fluid velocity and D_h is pipe diameter.

In the two-dimensional model, the inside diameter is twice the height of the import. Reynolds number in the calculation of fluid flow is an important role, and by the inertial force and the ratio of viscosity to determine whether the flow is the laminar or turbulent.

In RTM Process, on the assumption that pre-shop preform in the cavity is rigid and the resin is the incompressible Newtonian fluid, and the surface tension is neglected. The interstice of mat is much smaller than the pore size of the cavity, so the resin flow in the closed cavity can be described by the Newtonian fluid flow through porous media. Darcy's law can be expressed as:

$$v = \frac{K}{\mu} \nabla P \quad (2)$$

Where v is the resin flow velocity, μ is the resin viscosity, K is the fiber permeability tensor, and ∇P is the pressure gradient.

3. Calculation

3.1 Piping Design

In the RTM process, the pipeline connects the mold and the resin tank, then resin flows through the pipeline mold cavity. In order to study the impact of pipeline to the process, the design of the pipeline form as shown in Figure 1.

According to different shapes of the pipeline as shown in Figure 2, the import will be divided into length of 50 mm, 100mm, 150mm, 200mm, radius of 5 mm, 8mm, 10mm, 12mm, and transition of the 20 mm; the export will be divided into length of 20 mm, 60mm, radius of 3mm, 5mm, 8mm. Import and export pipeline length and radius of a free portfolio, there are a total of 96 combinations.

3.2 Calculation of simulation process

In order to better demonstrate the calculation process, the example in view of Fig1 is calculated. The import length of the pipeline is 50 mm with a radius of 5 mm, transition of the 20 mm, and the length of export is 20 mm, with a radius of 3 mm. the flow of resin in the pipeline can be considered as a two-dimensional interface shown in Figure 2.

In order to study the speed of the export pipeline and pipeline diameter and length how to impact the Reynolds number, assuming that the density and viscosity of the resin is known.

$$\rho = 1.2E - 3g / mm^3 \quad (3)$$

$$\mu = 0.5g / mm \cdot s \quad (4)$$

Simulation of the process usually consists of three phases: preconditioning, resolution and post-processing. After founding the model shown in Fig2, and separating grid, and setting parameters, ultimately the relationship of the diameter of export pipeline and the speed can be got in Fig3. From the corresponding relations in Fig3 can be seen that in the location of 1.5000 mm, the maximum speed is by 41.939 mm / s. In the resin exports, in accordance with the maximum speed, into the equation (1) to calculate the Reynolds number, whether to accord with the RTM process. 96 calculations the pace of import and export value of the ratio of the diameter of pipes, pipe diameter can be compared and the proportional relationship between flow rates shown in Figure 4. Relationship:

$$Y = -0.47953 + 25.61355X \quad (5)$$

With the change of length of import, export and diameter, the speed of flow changes accordingly. From the experimental data, the speed of export-import has to do with ratio of pipeline diameter, and has not to do with the length of the import and export. Under the assumption that the speed of imports is certain number, and the design of the pipe size, when exports diameter of 6 mm, 10mm, 16mm, can be from Fig5, three equations of export speed and the

Reynolds number are got, as follows:

$$Y = 2.85239E - 6 + 0.00144X \quad (6)$$

$$Y = -1.05055E - 6 + 0.0024X \quad (7)$$

$$Y = 7.97777E - 7 + 0.00384X \quad (8)$$

In accordance with the formula (6), (7), (8), and Reynolds number to be less than 1, it can be got several of the largest diameter pipelines at the Reynolds number and the corresponding size. In this way, it can easily change resin pipes in the future experiment, and better control the resin flow rate.

4. Conclusion

In RTM Process, resin flow in the pipeline must be consistent with the Reynolds number ($Re < 1$), then to conform the requirement to the standard process. By changing the length and diameter of import and export, the speed of the export is simulated and got four equations. Through this four equations, commonly used in pipe size, speed of export and the Reynolds number can be calculated, which ensure compliance with the technical requirements, and the smooth conduct experiments. It is shown that:

(1) Exit velocity had little to do with the length, but the ratio of diameter pipeline.

(2) When the diameter of imports is 6 mm, 10mm, 16mm, 20mm, and if the diameter of export is 6 mm, the speed must be limited range of 0 ~ 694.442 mm/s; if the diameter of export is 10 mm and the speed must be limited the scope of 0 ~ 416.667 mm/s; if the diameter of the export is 16 mm and the speed must be limited the scope of 0 ~ 260.414 mm/s.

Acknowledgements

The authors would like to thank the Tianjin Municipal Science and Technology Commission for the sponsorship of this research in providing funding which aided this research.

References

- Bruschke, M. V., Advani, S. G. (1990). *Polymer Composite*, 11: 398-405.
- Dai, Fuhong, Du, Shanyi, Zhang, Boming and Wan, Dianfu. (2004). *Journal of Materials Science and Technology*, 20:335-340.
- Dai, Fuhong, Zhang, Boming and Du, Shanyi. (2004). *Journal of Composites*, 21:161-167.
- Deng, jie (2005). *Fibre Composites*, 1:50-52.
- FAN, Xiaoqin and WU, Xiaoqing. (2006). *Fibre Reinforced Plastics/Composites*, 3:44-49.
- Li, Hai-chen, Wang, Biao and Lin, Xin. (2003). *Journal of Harbin institute of Technology*, 35:58- 61.
- Liu, Ningsheng. (2005). *Fibre Composites*, 1:40-42.
- Lu, Mingkun, Liu, Yang and Zhang, Boming. (2005). *Fibre Composites*, 2:31-35.
- Martin, G. Q., Son, J. S. (1986). *Dearborn*, 5:149-157.
- Phelan, F. R. Jr. (1992). *Proceedings of the American Society for Composites*, 2:90-102.
- Rudd, C.D., Long, A.C., Kendall, K.N. (1997). Cambridge England: Wood head Publishing Limited. pp. 254-292.
- Rudd, C.D., Long, A.C., Kendall, K.N. and Mangin, C.G.E. (2004). *Liquid molding technologies*. Beijing: Chemical Industry Press.pp.1-8.
- Shojaei and Akbar . (2006). *Composites Part A: Applied Science and Manufacturing*, 37: 1434-1450.
- Simacek, P., Advani, S. G. (2004). *Polymer Composite*, 25:355-367.
- Van, Melick, H. G. H., Haagh, G. A. A. V., Van, de. Vosse. F. N., Peijs, T. (1998). *Advanced Composites Letters*, 7:17-22.
- Wang, Baichen, Huang, Yudong and Liu, Li. (2006). *Journal of Solid Rocket Technology*, 29(4):297-300.
- Wang, Yongxiang, Qiu, Guijie (2005). *Proceedings of 16th Annual Academic conference on FRP/CM*.
- Zhong, Cai (1992). *Journal of Composite Materials*, 26:1310-1338.



Figure 1. Pipeline form



Figure 2. Model of flowing

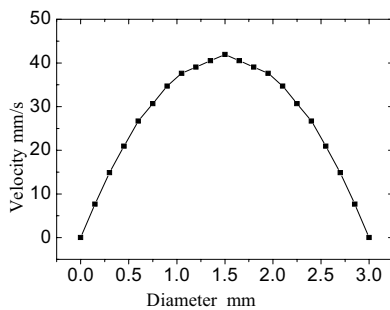


Figure 3. Relationship of diameter and velocity

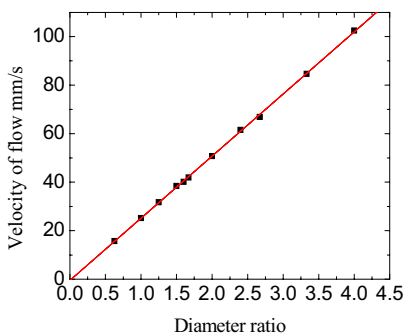


Figure 4. Relationship of diameter ratio and velocity

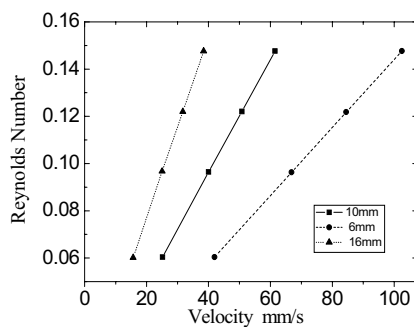


Figure 5. Relationship of exit velocity and Reynolds number

Editorial Board

Ahmad Mujahid Ahmad Zaidi Universiti Tun Hussein Onn Malaysia, Malaysia

Hamimah Adnan Universiti Teknologi MARA, Malaysia

J S Prakash Sri Bhagawan Mahaveer Jain College of Engineering, India

Musa Mailah Universiti Teknologi Malaysia, Malaysia

Sujatha. C.H Cochin University of Science and Technology, India

Sundus H Ahmed Ministry of Science and Technology, Iraq

Susan Sun Canadian Center of Science and Education, Canada

Sutopo Hadi University of Lampung, Indonesia

Wenwu Zhao Macrothink Institute, USA

A journal archived in Library and Archives Canada
A journal indexed in CANADIANA (The National Bibliography)
A journal indexed in AMICUS
A journal indexed in Zentralblatt MATH
A peer-reviewed journal in applied science research

Modern Applied Science

Monthly

Publisher Canadian Center of Science and Education
Address 4915 Bathurst St. Unit# 209-309, Toronto, ON. M2R 1X9
Telephone 1-416-208-4027
Fax 1-416-208-4028
E-mail mas@ccsenet.org
Website www.ccsenet.org
Printer William Printing Inc.
Price CAD.\$ 20.00

